



Nanospectroscopy of thiocyanine dye molecules adsorbed on silver nanoparticle clusters



Uroš Ralević^a, Goran Isić^{a,*}, Dragana Vasić Anicijević^b, Bojana Laban^c, Una Bogdanović^b, Vladimir M. Lazović^d, Vesna Vodnik^b, Radoš Gajić^a

^a Graphene Laboratory of Center for Solid State Physics and New Materials, Institute of Physics, University of Belgrade, Pregrevica 118, 11080 Belgrade, Serbia

^b Vinča Institute of Nuclear Sciences, University of Belgrade, P.O. Box 522, Belgrade, Serbia

^c Faculty of Natural Sciences and Mathematics, University of Priština, 38200 Kosovska Mitrovica, Serbia

^d Institute of Physics, University of Belgrade, Pregrevica 118, 11080 Belgrade, Serbia

ARTICLE INFO

Article history:

Received 29 June 2017

Received in revised form 13 October 2017

Accepted 21 October 2017

Available online 25 October 2017

Keywords:

Surface enhanced Raman scattering

Atomic force microscopy

Citrate capped silver nanoparticles

Thiocyanine dye

ABSTRACT

The adsorption of thiocyanine dye molecules on citrate-stabilized silver nanoparticle clusters drop-cast onto freshly cleaved mica or highly oriented pyrolytic graphite surfaces is examined using colocalized surface-enhanced Raman spectroscopy and atomic force microscopy. The incidence of dye Raman signatures in photoluminescence hotspots identified around nanoparticle clusters is considered for both citrate- and borate-capped silver nanoparticles and found to be substantially lower in the former case, suggesting that the citrate anions impede the efficient dye adsorption. Rigorous numerical simulations of light scattering on random nanoparticle clusters are used for estimating the electromagnetic enhancement and elucidating the hotspot formation mechanism. The majority of the enhanced Raman signal, estimated to be more than 90%, is found to originate from the nanogaps between adjacent nanoparticles in the cluster, regardless of the cluster size and geometry.

© 2017 Elsevier B.V. All rights reserved.

1. Introduction

Dye coated metallic nanoparticles (NPs) exhibit interesting optical properties provided by the interaction between the metal core and dye shell. Depending on the interaction mechanism between the two, the optical properties of dye molecules and NPs can be changed separately or jointly within the adsorbate–NP complex [1]. For example, the NP surface plasmon frequency can be changed by the presence of adsorbate while the dye fluorescence can be quenched or enhanced by the NP [2,3]. Ultimately, under special conditions, these complexes can exhibit unique characteristics different than those of either isolated dye molecules or NPs. Owing to the variety of mechanisms by which dyes can interact with metallic NPs, dye–NP complexes can lead to applications ranging from nanoscale sensing [4] to advanced composite materials for novel active and nonlinear optical devices [5].

Many of the recent studies have been focused on dyes which are able to self-assemble in highly oriented structures called J-aggregates on the surface of the NPs [6–14]. J-aggregates have a

strong and narrow excitonic absorption band that is red-shifted with respect to the monomer absorption band [15]. The special way of molecular stacking, responsible for the formation of Frenkel excitons, has been extensively studied [16–24] as these aggregates are the most famous spectral sensitizers of silver halides for the photographic industry [25]. On the other hand, it has been shown that the combination of J-aggregates and silver or gold NPs provides a platform for the fundamental studies of excitons and their interaction with high electromagnetic fields, as well as a way to utilize optical properties of such a hybrid system for nanoscale optical devices.

A necessary condition for the interaction to occur is that the dye molecules are adsorbed on the surface of the NPs. Therefore, the adsorption process plays one of the key roles in these systems. The most common way in which the dye–NP hybrid systems are prepared is by mixing the appropriate colloid and dye solutions and letting the resulting mixture reach its metastable or stable state in which the NPs have dye molecules adsorbed on their surface. The dynamics of the adsorption process is quite complex as it depends on various factors including the target concentration of the constituents, affinity of the dye molecules to bind to the NP surface and the type of capping anions protecting the surface of the NPs. For instance, the spectrophotometric studies of thiocyanine (TC) dye coated silver nanoparticles (AgNPs) in Refs. [26,12–14]

* Corresponding author.

E-mail address: isicg@ipb.ac.rs (G. Isić).

show that the capping anions can influence the mechanism of the adsorption process and therefore its efficiency.

The influence of capping anions on the adsorption process can be studied on a nanoscopic level by exploiting very strong localized plasmonic fields at the NP surface and employing surface-enhanced Raman scattering (SERS) [27,28]. SERS has already been used for identification of TC J-aggregates and for studying their dynamics on the surface NP clusters in solutions [29–36].

In view of the significance of the dye-to-NP adsorption mechanism, here the mechanism of TC dye adsorption on the surface of AgNP clusters with citrate anion stabilization is investigated. In order to probe the presence of TC dye molecules on the nanoscale (i.e. on individual AgNP clusters), Ag colloids are mixed with TC dye solutions, and subsequently drop-cast onto freshly cleaved mica or SiO₂ substrates and, after drying, investigated using colocalized Raman microspectroscopy and atomic force microscopy (AFM). The key mechanism used for the identification of a small amount of TC dye molecules adsorbed on AgNP clusters is SERS [32]. The measurements are complemented by rigorous numerical simulations of plane wave scattering on AgNP clusters, showing that the electromagnetic enhancement of the Raman signal originates dominantly from the nanogaps between adjacent AgNPs within the clusters. The analysis of the SERS spectra acquired at the AgNP clusters on mica substrate and the fact that the majority of the SERS signal comes from the nanogaps indicate that the citrate anions impede the efficient dye adsorption.

2. Materials and methods

2.1. Chemicals

Silver nitrate (AgNO₃), potassium chloride (KCl), and sodium borohydride (NaBH₄) trisodium citrate (Na₃C₆H₅O₇ × 3H₂O) of the highest purity were purchased from Sigma Aldrich and used as received.

Thiocyanine dye (3,3-disulfopropyl-5,5-dichlorothiocyanine sodium salt, TC) was purchased from Hayashibara Biochemical Laboratories, Okayama, Japan.

2.2. Samples

Aqueous solutions of borate- and citrate-capped AgNPs were synthesized by NaBH₄ reduction of AgNO₃, as described in Refs. [12,14]. For the synthesis of citrate-capped AgNPs, Na₃C₆H₅O₇ × 3H₂O was used as a stabilizing agent. The solution of borate-capped AgNPs was prepared immediately before use as the colloid is stable only up to a few hours. Oppositely, the solution of citrate-capped AgNPs is stable for a longer period of time, measured in months, due to the protective citrate anion mantle. The average diameter of both borate- and citrate-capped AgNPs is around 10 nm (see Section S1 of the Supplementary information). The nominal concentration of citrate-capped AgNPs in water solution is $c_{Ag} = 16$ nM (see Fig. S1 for the related absorption spectra).

Aqueous TC dye solution with nominal concentration $c_{TC} = 50$ μM of TC and 1 mM of KCl was prepared by dissolving the solid TC in water and by adding KCl afterwards. Water purified with a Millipore Milli-Q water system was used in all cases. The absorption spectra of the TC dye is given in Fig. S1 in the Supplementary information.

The Ag colloid and the TC dye solution are mixed, and the resulting mixture (see Fig. S1 in the Supplementary information for the related absorption spectra) is drop-cast on a substrate. The adsorption of TC molecules on the surface of borate-capped AgNPs happens almost instantaneously [13,12], and the mixture was therefore drop-cast on the substrate a few minutes after mix-

ing the two solutions. On the other hand, the adsorption of TC dye on the surface of citrate-capped AgNPs is a much slower process [26,14] and for that reason the mixture was left overnight and afterwards drop-cast on a substrate.

For the investigation of TC/citrate-capped AgNP clusters, as well as for initial characterization of pristine citrate-capped AgNP clusters, mica was used as a substrate. Mica has an atomically flat, hydrophilic surface on which the AgNPs are easily deposited, while its contribution to the total Raman signal is small (see Section S2 of the Supplementary information). In addition to mica, highly oriented pyrolytic graphite (HOPG) and SiO₂ substrates were used as their surfaces are hydrophobic and, therefore, facilitate the formation of large, closely spaced AgNP clusters as well as more efficient aggregation of the TC dye on their surface. In particular, HOPG is used for Raman characterization of concentrated TC dye, since the dye efficiently aggregates on its surface. The SiO₂ is used for the control study of AgNPs having dye/borate anions conformed to their surface, since the large closely spaced AgNP clusters are required for fast Raman/SERS characterization of the initially unstable borate-capped AgNPs. Raman spectra of the TC dye, Mica, Si and HOPG are shown in Fig. S2 in the Supplementary information.

2.3. Methods

The AgNP clusters on a substrate are investigated using colocalized Raman microspectroscopy and AFM. The two techniques are used simultaneously thus providing spatially resolved chemical information of the sample along with its surface topography at the same place. In this way one is able to identify and assert the size of the SERS active AgNP clusters while obtaining the chemical identity of the analyte adsorbed on the surface of AgNPs. The AFM is operated in tapping mode in order to minimize the lateral force between the tip and the sample induced by lateral movements of the tip across the sample. The cantilever-tip system is oscillated at the characteristic first order resonance which is usually in the 90–230 kHz range. For Raman spectroscopy and SERS measurements a linearly polarized semiconductor laser operating at a wavelength of 532 nm is used. The laser power was varied from 2 to 0.2 mW within the $\sim 0.3 \times 0.3$ μm sized focus. The experiments are performed using commercial NTegra Spectra system from NT-MDT.

To numerically solve the classical Maxwell equations we have used the finite element method implemented within the Comsol Multiphysics software package [37]. We consider clusters of AgNPs having a diameter of 10 nm on a substrate under plane wave illumination. The Ag dielectric constant is taken from Rakic et al. [38]. The substrate is assumed to be semi-infinite and isotropic with a dielectric constant of 2.25, which roughly corresponds to the dielectric constants of both mica and SiO₂ at visible frequencies. The surrounding medium is vacuum and its dielectric constant is 1. For purposes of efficient meshing, AgNPs are assumed to lie 1 nm above the substrate. The clusters are formed in the plane which is parallel to the substrate by allowing AgNPs to have random position but enforcing the following conditions: (i) there is a certain minimal allowed distance d between two AgNPs; two AgNPs separated by the minimal distance are said to be adjacent; (ii) each AgNP must be adjacent to at least one other AgNP, thus ensuring that each randomly generated cluster is connected. By imposing these two conditions, we were able to randomly generate various cluster geometries and mimic the lack of control over the clusters morphology in the experiment.

The absorption $\sigma_a(\lambda)$, scattering $\sigma_s(\lambda)$ and extinction $\sigma_{ext}(\lambda)$ cross sections are calculated as a function of wavelength λ , according to their well-known definition [39]. The electric-field enhancement $f(\mathbf{r}, \lambda)$ is defined as the squared ratio of magnitudes of the local electric field $\mathbf{E}_L(\mathbf{r}, \lambda)$ and the incoming electric field $\mathbf{E}_0(\lambda)$, with \mathbf{r} denoting the coordinate at which the former is evaluated.

Following Kerker et al. [40], the SERS enhancement factor is defined as $F(\mathbf{r}, \lambda_{\text{inc}}, \lambda) = f(\mathbf{r}, \lambda_{\text{inc}}) / f(\mathbf{r}, \lambda)$ with λ_{inc} and λ denoting the laser and Stokes wavelength, respectively. Since the measured PL/Raman signal being reported in this paper originates from large (relative to a cluster), diffraction limited, spots of 300 nm approximate diameter, it cannot be directly related to the spatially-resolved field and SERS enhancement factors. Instead, we consider their integrals over the cluster surface S and the corresponding cluster-averaged SERS factor $\langle F(\lambda_{\text{inc}}, \lambda) \rangle$ defined as

$$\langle F(\lambda_{\text{inc}}, \lambda) \rangle = \frac{1}{S} \int_S F(\mathbf{r}, \lambda_{\text{inc}}, \lambda) dS. \quad (1)$$

3. Results and discussion

3.1. Surface-enhanced Raman spectroscopy of pristine citrate-capped AgNPs

Fig. 1(a) shows an AFM topograph of pristine AgNP clusters on mica surface. The corresponding PL/Raman map is shown in Fig. 1(b). The intensity of every pixel in the PL/Raman map is obtained by dividing the sum of PL/Raman intensities across the entire spectral range (100–2000 cm^{-1}) with the number of spectral points. The color bar in panel (b) thus enumerates the average photon count. Bright areas in Fig. 1(b) represent the regions of enhanced signal, henceforth referred to as hotspots. These regions coincide with AgNP clusters consisting of a large number of AgNPs (with diameters in the 10–50 nm range), as seen by comparing the PL/Raman map with the AFM topography image. In fact, we find that the hotspots are dominantly formed within larger AgNP clusters,

such as those in Fig. 1(a), regardless of the substrate which is used (mica, SiO_2 or HOPG).

Fig. 1(d) and (e) shows two sets of consecutively acquired spectra with a 40 s time step taken at two hotspots from Fig. 1(b) using 532 nm laser with intensity of $\approx 200 \mu\text{W}/\mu\text{m}^2$. The spectra in panels (c) and (d) are similar, but cannot be quantitatively compared. Both sets feature a wide background which spreads over the entire spectral range, and a pronounced band blinking in the 1000–1800 cm^{-1} range (shaded region) which hinders a quantitative analysis. Considering that citrate anions are used for stabilizing the AgNPs, our hypothesis is that the blinking spectra is the SERS signal from the citrate anion mantle, sensitive to local heating in hotspots due to the small size of citrate anions, while the wide background is PL coming from the AgNP clusters.

3.2. Numerical simulations of light scattering on random AgNP clusters

In order gain an insight into hotspot formation and assess the Raman enhancement factors, we employ a numerical model to calculate the electromagnetic fields scattered on randomly generated AgNP clusters. The motivation for considering random AgNP clusters is to get an idea on the variability of the electric field enhancement upon changing the cluster geometry and to identify any invariants which could be used to interpret SERS measurements on clusters whose exact geometry is unknown. A typical cluster consisting of 20 AgNPs is shown in Fig. 2(a). In this example we set the minimal AgNP distance at $d = 0.8 \text{ nm}$ while the adjacent AgNPs are indicated by solid (red) lines Fig. 2(a). The extinction cross-section of the AgNP cluster in panel (a) is plotted in Fig. 2(b),

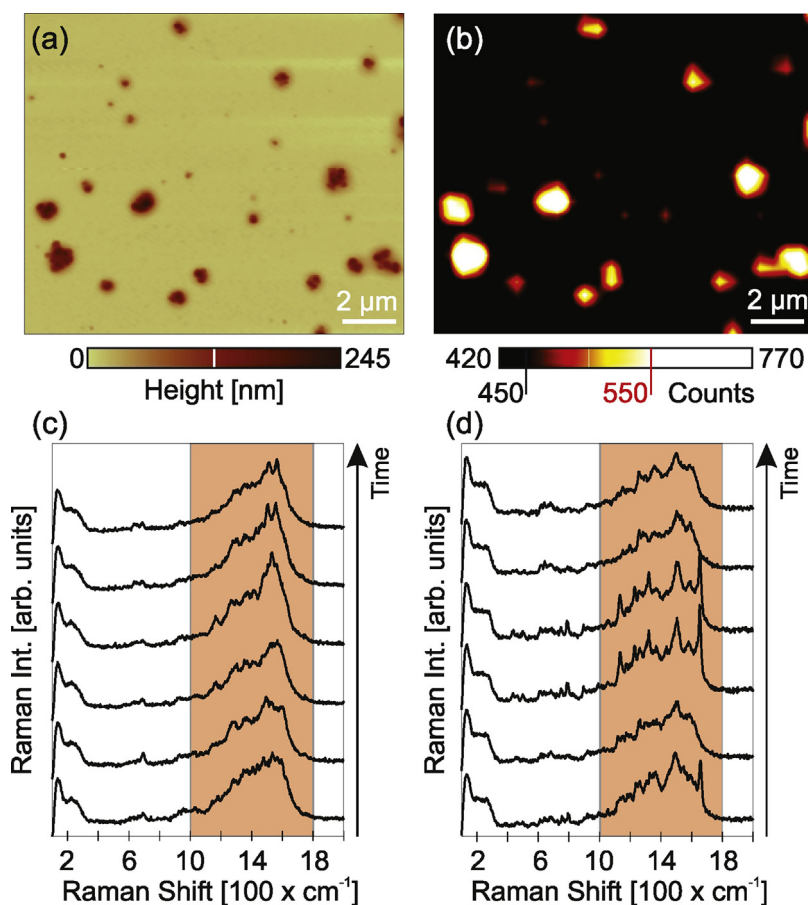


Fig. 1. (a) AFM topograph of pristine AgNP clusters drop-cast onto a freshly-cleaved mica substrate. (b) Corresponding PL/Raman map. (c), (d) Typical SERS spectra acquired within two hot spots in panel (b). The spectra were measured consecutively with a 40 s time step. The excitation laser wavelength is 532 nm.

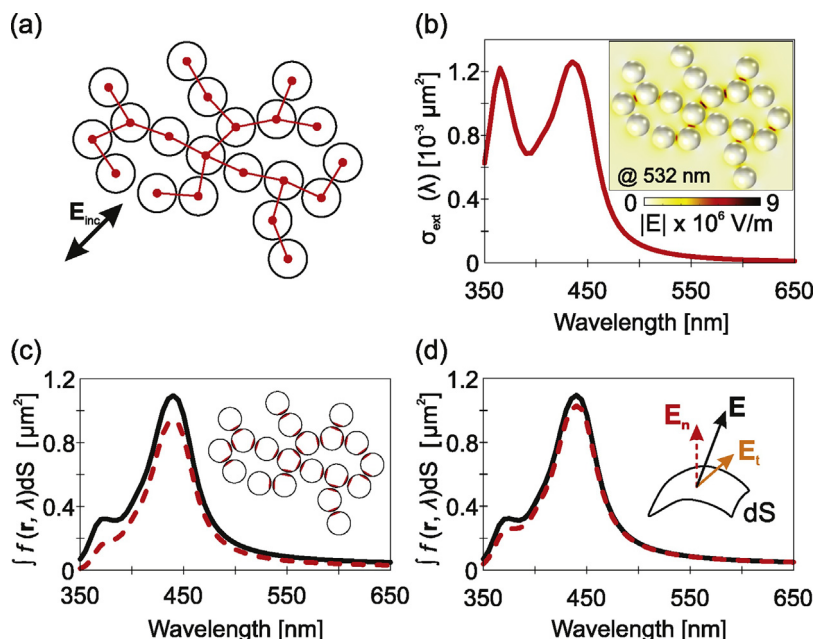


Fig. 2. (a) Sketch of a typical cluster geometry used in the numerical model. Normal incidence is assumed for the incoming wave while its electric field is polarized parallel to the plane of the cluster and oriented as indicated by the arrow. The incident field intensity is set to $200 \mu\text{W}/\mu\text{m}^2$. (b) Extinction spectra of the cluster in panel (a). The inset shows the electric field magnitude distribution at 532 nm. (c) Surface integrals of the intensity enhancement over the entire cluster surface (solid black line) and over the entire gap area (dashed red line) plotted as the function of the wavelength. (d) Surface integrals of the total field enhancement (solid, black) and the ratio of the field component perpendicular to the AgNP surface (dashed, red) both taken over the entire cluster surface. (For interpretation of the references to color in this legend, the reader is referred to the web version of the article.)

as a function of the incident wavelength. For the considered cluster, the scattering cross-section is negligible with respect to the absorption cross-section and therefore $\sigma_{\text{ext}} \approx \sigma_{\text{a}}$. The two peaks observed at 365 and 435 nm, represent the single particle and cluster surface plasmon, respectively. Below we find that the wavelength of the former is virtually independent on the presence of other AgNPs, while the cluster plasmon wavelength redshifts with increasing cluster size. Upon the excitation of a cluster plasmon, the electric field is resonantly enhanced over the entire cluster. Although the distribution of resonant fields is highly dependent on the details of AgNP arrangement [41], the highest enhancement is known [42,43] to be invariably reached within the gaps between adjacent AgNPs, which is corroborated by our numerical simulations of many random AgNP arrangements.

The inset of Fig. 2(b) shows the spatial distribution of the electric field magnitude in the plane containing the NP centers, excited at 532 nm which is far from the cluster plasmon at 435 nm. This hints that the highest field enhancements are reached in NP gaps for any wavelength and not just for resonances. Fig. 2(c) shows the surface integral of the field enhancement evaluated over: (i) the entire cluster surface, consisting of the surfaces of all AgNPs and (ii) over the entire gap area, consisting of the sum of gap areas of individual AgNPs, defined as parts of the NP surface located very close to the adjacent AgNP, as indicated by the (red) shading in Fig. 2(c) inset. According to this definition, the surface over which the (ii) integral is evaluated is a small fraction of the (i) integral. However, the spectra in Fig. 2(c) show that these integrals have virtually the same value away from surface plasmon resonances. The difference around the cluster plasmon wavelength is also not significant, being of the order of 10%. This shows that regardless of the cluster geometry, the majority of the SERS signal of any species adsorbed uniformly on AgNPs is likely to come from the gap region (see also Fig. S3 in the Supplementary information).

Another important question regarding the fields on AgNP clusters is their orientation with respect to the AgNP surface, as

it determines the SERS cross section of vibrational modes of molecules adsorbed on the AgNP surface. To evaluate the extent to which the electric field is perpendicular to the local surface, in Fig. 2(d) we evaluate the surface integrals (taken over the entire cluster) of (i) the square of the normalized total electric field magnitude, which equals $f(\mathbf{r}, \lambda)$ by definition (solid, black), and (ii) the square of the normalized magnitude of the electric field component perpendicular to the AgNP surface (dashed, red). The comparison of the two spectra in Fig. 2(d) shows that the contribution of the tangential component of the local electric field is negligible, indicating that in such clusters the perpendicular component of the electric field is the principal source of the SERS signal.

Having established that for an arbitrarily chosen AgNP cluster the large majority of the SERS signal comes from gaps between AgNPs and is associated with the perpendicular electric field component, we now focus on the cluster-averaged SERS enhancement factor $\langle F(\lambda_{\text{inc}}, \lambda) \rangle$ and investigate how is it affected by the cluster size and geometry. The typical case is illustrated in Fig. 3(a) in which we consider a hierarchy of 3 NP clusters shown in the inset, each having twice as many AgNPs as the previous one. The first one represents a randomly chosen connected arrangement of 5 AgNPs with $d = 0.8$ nm. The second is obtained by adding 5 more AgNPs so that each new AgNP is adjacent to one of the existing AgNPs. Finally, the third and largest cluster is obtained by adding 10 more AgNPs to the second one. The corresponding $\langle F(\lambda_{\text{inc}}, \lambda) \rangle$ spectra in Fig. 3(a) shows two main effects of the cluster size increase. First, the enhancement peaks associated with the cluster plasmon undergoes a gradual redshift. Second, the surface-average enhancement $\langle F(\lambda_{\text{inc}}, \lambda) \rangle$ increases, meaning that the actual SERS signal enhancement given by $S \times \langle F(\lambda_{\text{inc}}, \lambda) \rangle$ will increase even more rapidly with adding new particles to the cluster. For example, a cluster having 5 AgNPs exhibits an average Raman enhancements of the order of 10 in the 532–600 nm range, whereas a cluster having 20 AgNPs yields 10 times higher values in the same range. In previous studies on AuNP chains [44], the increase of particle number has been found

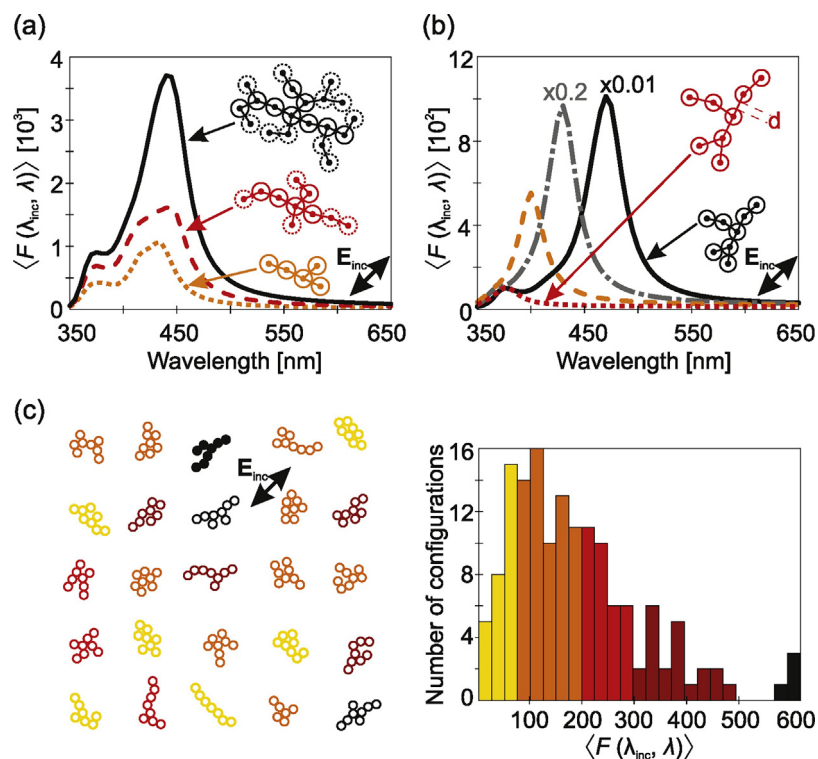


Fig. 3. (a) The average Raman enhancement calculated as a function of the emission wavelength for clusters having 5 particles (dotted orange line), 10 particles (dashed red line) and 20 particles (solid black line). (b) The average Raman enhancement calculated as a function of the emission wavelength for a cluster with 8 particles when the minimal distance between the particles is varied. Particles connected by lines, in the inset, are at the minimal distance d from each other. Solid (black) line corresponds to $d = 0.5$ nm, whereas dash-dotted (gray) line, dashed (orange) line and dotted (red) line correspond to $d = 1$ nm, $d = 2$ nm and $d = 5$ nm, respectively. (c) The left panel shows some of the 150 considered cluster variants and the electric field polarization direction. All the clusters have 8 particles, with the minimal distance $d = 0.8$ nm. The right panel shows a histogram of the average Raman enhancement calculated at the emission wavelength 550 nm for all 150 cluster variants. In all calculations normal incidence at a wavelength 532 nm and the incident field intensity of $200 \mu\text{W}/\mu\text{m}^2$ are assumed. (For interpretation of the references to color in this legend, the reader is referred to the web version of the article.)

to either increase or decrease the average Raman enhancement, depending on the relative position of the incident wavelength and the cluster (chain) plasmon.

In Fig. 3(b) we consider the role of the spacing d between adjacent AgNPs. For a cluster comprising 8 AgNPs decreasing d from 5 nm down to 0.5 nm is seen to result in drastic changes of $\langle F(\lambda_{\text{inc}}, \lambda) \rangle$. The cluster plasmon is rapidly blueshifted and approaches the single-particle plasmon as the AgNPs are moved further apart (see also panel (c) of Fig. S3 in the Supplementary information). Similar conclusions have been previously reported for the AuNP linear chains embedded in a dielectric medium [42,45]. Meanwhile, the peak values of $\langle F(\lambda_{\text{inc}}, \lambda) \rangle$ are seen to decrease very rapidly since the gap field enhancement becomes less effective with increasing d . For example, the lowest considered minimal distance of 0.5 nm yields SERS enhancements as high as 10^4 in the 532–600 nm range.

Lastly, by evaluating the average Raman enhancement at the excitation and Stokes wavelengths of 532 nm and 550 nm, respectively, for a 150 randomly generated 8 AgNP clusters, we evaluate how the cluster morphology affects the non-resonant SERS enhancement value. The variety of clusters that have been considered in the 150 member ensemble, is represented by 25 typical members sketched in the left panel of Fig. 3(c). The histogram of $\langle F(\lambda_{\text{inc}}, \lambda) \rangle$ values is shown in the right panel, where the column colors are selected so that they correspond to the color of the associated cluster in the left panel. The distribution is quite wide, spanning the range from 50 to 600. By comparing the two panels of Fig. 3(c), we see that the highest enhancements are reached in chain shaped clusters having the chain axis aligned with the incident electric field, such as the one illustrated in Fig. 3(c) by filled circles. The effect of disorder of the linear AuNP chain on the Raman

enhancement was studied in Ref. [43], where increasing disorder was found to diminish the Raman enhancement. In this case, the highest Raman enhancements were found for AuNP chains, when the incident electric field is oriented along the chain axis.

The brief numerical analysis of light scattering on random AgNP clusters made in this section shows that the overall SERS enhancement is highly dependent the cluster geometry and its orientation relative to the electric field polarization. The sensitivity of $\langle F(\lambda_{\text{inc}}, \lambda) \rangle$ to fine details, such as the gap spacing, makes its exact evaluation very difficult even when electron microscopy is used for determining the AgNP arrangement with nanometer spatial resolution [46]. In the present case, the possibility of resonant enhancement cannot be excluded, since the cluster plasmon resonances are seen to redshift in elongated clusters with a larger number of particles than the ones considered here [42,43]. However, beside the well elaborated enormous Raman enhancements having a resonant origin [42], we have shown that in the non-resonant case enhancement factors in the range of 10^2 – 10^3 are to be expected.

3.3. Surface-enhanced Raman spectroscopy of TC coated AgNPs I: influence of citrate capping anions on the TC dye adsorption

In the TC/AgNP mixture, the AgNPs may have the J-aggregates or dye monomers or dimers adsorbed on their surface, or even remain pristine. Therefore, it is expected that AgNP clusters drop-cast from the mixture would have a variety of SERS spectra corresponding to those of different dye conformations, citrate anions and even their combinations. To make a clear distinction between the non-aggregated and aggregated molecules one must have an

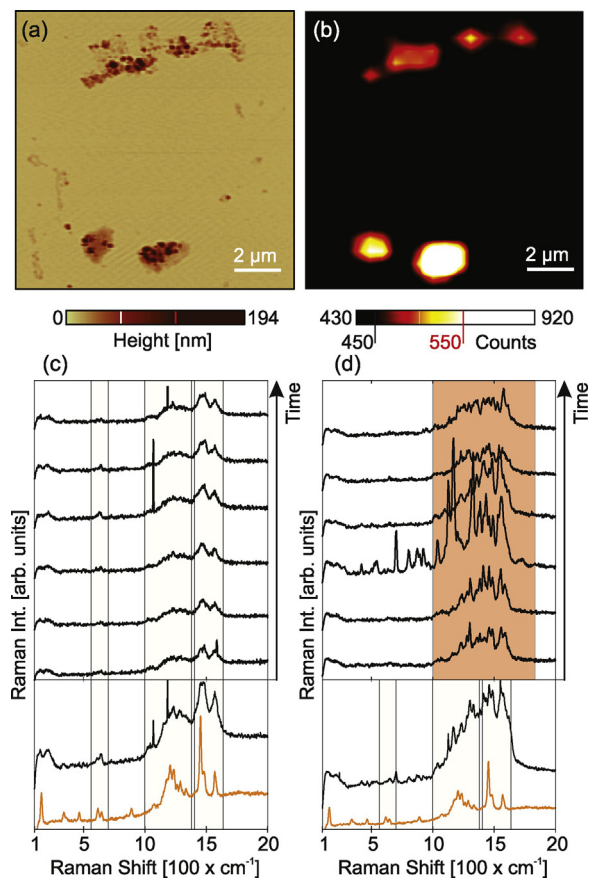


Fig. 4. (a) AFM topograph of TC dye coated Ag NP clusters which are drop-cast on mica. (b) Corresponding PL/Raman map. (c) and (d) Typical SERS spectra acquired within the hot spots, by consecutive measurements with 40 s time step. The excitation laser wavelength is 532 nm. In the lower parts of panels (c) and (d) shown are the SERS spectra obtained by summation of the corresponding consecutively acquired spectra, and the Raman spectra of the drop-cast TC dye. (For interpretation of the references to color in this legend, the reader is referred to the web version of the article.)

excitation resonant with the absorption of either aggregated or non-aggregated dye molecules [32,47]. Here we use a non-resonant laser line at 532 nm which does not allow identification of different dye conformations. However, AgNP clusters are very efficient enhancers at this wavelength, as it is shown in Section 3.1 and thus through the SERS effect alone we are able to determine if the TC dye molecules are adsorbed on AgNPs or not.

Comparison of the AFM topograph and the corresponding Raman map in Fig. 4(a) and (b) reveals that the hot spots are located within the larger AgNP clusters, as in the case of pristine AgNPs in Section 3.1. The SERS spectra acquired at these hot spots can be unambiguously categorized in two groups: one featuring stable Raman bands during successive measurements and the other having blinking Raman bands. The wide background from the AgNP clusters exists in this case as well. Fig. 4(c) and (d) shows the two distinct spectra types. The recording time step is 40 s and the laser intensity is $\approx 200 \mu\text{W}/\mu\text{m}^2$.

The consecutively measured SERS spectra having stable Raman bands are reminiscent of the drop-cast TC dye Raman spectrum. The similarity between the two becomes even more convincing after summation of ten consecutively measured spectra, six of which are displayed in Fig. 4(c). By applying markers to the three wave-number regions, I (300–1000 cm^{-1}), II (1050–1250 cm^{-1}), III (1400–1600 cm^{-1}), where the TC dye has its characteristic Raman bands (see Fig. S2 in the Supplementary information), we find that in region I around 600 cm^{-1} the summed SERS spectrum has

two bands matching those of a drop-cast TC dye, which is plotted again, for clarity, below the summed spectrum. The modes around 400 cm^{-1} and 900 cm^{-1} are, however, absent in the related TC dye SERS. In the remaining regions II and III the two spectra have, more or less, the same Raman bands and even similar backgrounds. Hence, our experiments corroborate the fact that the dye molecules are adsorbed on the surface of the AgNPs, and point out another interesting possibility – the dye molecules drop-cast on the surface of HOPG may be similarly organized as the dye molecules on the surface of the AgNPs.

Panel (d) in Fig. 4 displays SERS spectra characterized by a pronounced band blinking in the 1000–1800 cm^{-1} range, as indicated by gray (orange) region. The resemblance of the spectra in Fig. 4(d) and those of pristine AgNPs in Fig. 1(c) and (d) suggests that the TC dye molecules are not adsorbed on the surface of the AgNPs. However, the sum of the consecutive recordings, shown in the lower part of Fig. 4(d), reveals certain SERS bands in region II and III which are overlapping the drop-cast TC dye bands. Occasional emergence of Raman bands which could belong to the TC dye bands in regions I, II and III, however, is a common event even for the SERS spectra of pristine AgNPs. Having in mind that practically the entire enhanced Raman signal originates from the analyte located in the nanogaps, the blinking SERS signal can be interpreted as a consequence of mixing of the pristine AgNPs blinking SERS and the TC dye SERS which are collected at different nanogaps where the former has the dominant contribution. Consequently, we are unable to conclude whether the AgNP clusters exhibiting blinking SERS bands have the dye molecules adsorbed on their surface or not. However, the existence of the two distinct SERS spectra clearly points out that the AgNPs are partially covered by the TC dye molecules. This further indicates that during the adsorption process, the TC dye molecules are either competing with citrate anions in order to replace them on the surface of AgNPs or that the TC dye molecules have a difficulty conforming over the citrate anion mantle. Hence, we proceed further by changing the concentration of TC dye in the mixture while maintaining the concentration of AgNPs constant at $c_{\text{Ag}} = 16 \text{ nM}$.

The blinking and TC dye SERS spectra observed for $0.01c_{\text{TC}} = 0.5 \mu\text{M}$, $0.1c_{\text{TC}} = 5 \mu\text{M}$, and $0.5c_{\text{TC}} = 25 \mu\text{M}$ of TC, are shown in Fig. 5(a)–(c), respectively. By analyzing spectra at the hotspots within various Raman maps, we find that the AgNP clusters deposited from the solution with the lowest dye concentration yield no clear dye SERS spectra, whereas the AgNP clusters deposited from the solution with the two higher dye concentration provide a number of distinct TC dye SERS spectra at the hotspots, shown in Fig. 5. Comparison of the summed SERS spectra, in the lower parts of panels (a), (b) and (c) in Fig. 5, and the concentrated TC dye Raman spectra corroborates that the SERS spectra in panels (b) and (c) correspond to the one of the TC dye. As expected, using TC dye concentrations of $0.01c_{\text{TC}} = 0.5 \mu\text{M}$, $0.1c_{\text{TC}} = 5 \mu\text{M}$ in the final solution yields either pristine or partially covered AgNP clusters, a fact that concurs with the results in Ref. [14]. However, observation of the blinking type SERS within the AgNP clusters derived from the mixture with the highest TC dye concentration of $0.5c_{\text{TC}} = 25 \mu\text{M}$, for which all of the AgNPs in the solution should be covered by the dye molecules [14], further indicates that the citrate anion mantle impedes the adsorption of the TC dye molecules.

3.4. Surface-enhanced Raman spectroscopy of TC coated AgNPs II: influence of borate and citrate capping anions on the TC dye adsorption

In order to examine if the citrate anions impede the TC dye adsorption, we have performed an additional set of measurements on a control sample – borate-capped AgNPs mixed with the TC dye and deposited on the surface of 300 nm thick SiO_2 , which is thermally grown on the Si wafer. Meanwhile, the borate-capped AgNPs

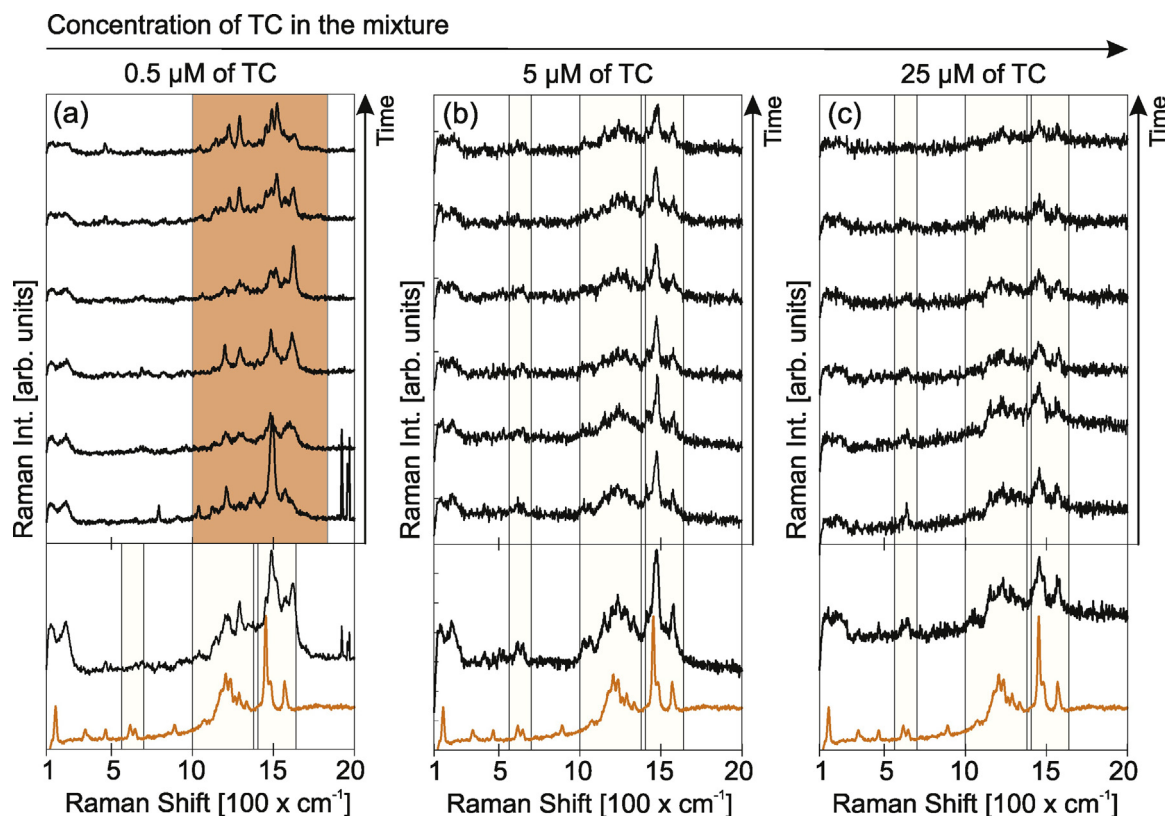


Fig. 5. Blinking and TC dye SERS spectra (acquired by consecutive measurements with 40 s time step) at hotspots on the samples made by varying the TC concentration in TC-Ag NP mixture: (a) 0.5 μM , (b) 5 μM and (c) 25 μM . All shown spectra were taken under the same conditions using 532 nm laser with intensity of 200 $\mu\text{W}/\mu\text{m}^2$.

are unstable with the average lifetimes of the order of couple of hours in the colloid dispersion and are usually stabilized by sodium citrate (or rather by the citrate anions which replace the borate anions while conforming to the surface of the AgNPs), as explained in Ref. [14]. The related lifetimes are much shorter upon deposition of these AgNPs on a substrate. The SiO_2 surface is hydrophobic, and, therefore, promotes formation of closely spaced clusters larger than those observed on mica, since the droplet drop-cast of the former dries over a certain area rather than spreading all over the surface. Such an arrangement, along with the enhanced contrast between the SiO_2 surface and the clusters, is absolutely necessary for fast acquisition of the SERS signal from the unstable, dye/borate-capped AgNP clusters.

Fig. 6(a)–(c) shows the three Raman maps corresponding to: (i) AgNP clusters deposited on mica from a solution having a (citrate-capped) AgNP to the TC dye concentration ratio of 22 nM/17 $\mu\text{M} \approx 1.3 \times 10^{-3}$, (ii) AgNP clusters deposited on mica from a solution having a (citrate capped) AgNP to the TC dye concentration ratio of 16 nM/25 $\mu\text{M} \approx 0.64 \times 10^{-3}$, (iii) AgNP clusters deposited on SiO_2/Si from a solution having a (borate-capped) AgNP to the TC dye concentration ratio of 10 nM/16 $\mu\text{M} \approx 0.63 \times 10^{-3}$, respectively. The (red) diamonds mark the spatial positions within the hotspots where the blinking type of Raman spectra is observed, whereas the (green) squares mark the pixels having the TC dye type of Raman spectra. These maps share the color bar which is located below them. Panels (d), (e) and (f) of Fig. 6 display examples of the spectra collected at the hotspots within the corresponding maps in panels (a), (b) and (c), respectively. For comparison, the concentrated TC dye Raman spectra is plotted in each panel, below all the other spectra.

The dye/borate-capped AgNPs deposited on the SiO_2/Si , form a higher number of larger clusters than the dye/citrate-capped AgNPs on mica, as seen by comparing the Raman maps in panels (a), (b)

and (c), as expected. The SERS spectra acquired at these clusters is exclusively of the TC dye type, as seen in panel (c). In fact, we find this to be the case for every recorded Raman map. In contrast, the dye/citrate-capped AgNP clusters exhibit both the blinking and the TC dye SERS, even when the ratio of the citrate-capped AgNPs and the TC dye concentrations in solution is approximately the same as the one of the borate-capped AgNPs and the TC dye (compare panels (b) and (c) in Fig. 6). The adsorption of the TC dye seems to be more efficient if the AgNPs have borate anions initially conformed to their surface and, therefore, we conjecture that the citrate anions indeed interfere with the adsorption process of the TC dye molecules.

Our findings are in agreement with the previous spectrophotometric study of J-aggregation of TC dye on the surface of AgNPs [26,13,14,12], where is found that the capping anions (borate or citrate), as well as added KCl, have an important role in the adsorption and J-aggregation of the dye molecules. In case of borate-capped AgNPs, the J-aggregation is found to be a fast process ($k_{\text{app}} = 4.97 \text{ s}^{-1}$) whose kinetics can be explained in terms of autocatalysis. Differently, kinetics measurements of J-aggregation on the surface of citrate-capped AgNPs has shown that the J-aggregation occurs via a two-step slower process (adsorption and aggregation, $k_{\text{app1}} = 0.008 \text{ s}^{-1}$ and $k_{\text{app2}} = 0.11 \text{ s}^{-1}$). Also, in the case of citrate-capped AgNPs was found that the quantity of added KCl has an important role in the adsorption of TC dye molecules.

This conclusion is further supported by the analysis of the DFT calculated adsorption energies of the TC dye, borate and citrate anions on the surface of Ag, reported in our previous work [26] (see also Section S4 of the Supplementary information).

4. Summary

In summary, the analysis of SERS enhancement based on rigorous simulations of Maxwell equations for the case of plane wave

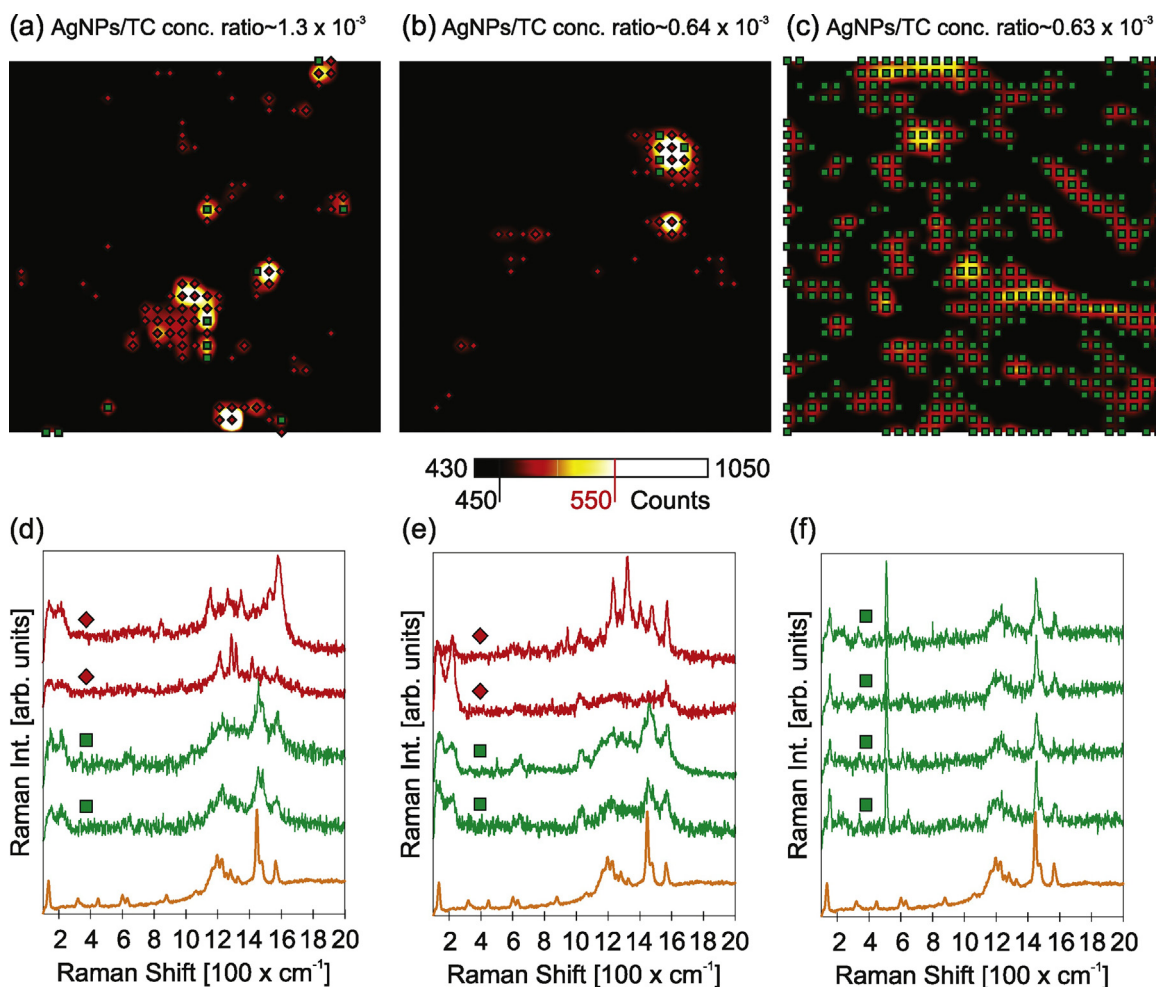


Fig. 6. Raman maps of (a) clusters deposited on mica from a solution having a (citrate capped) NP to the TC dye concentration ratio of $22 \text{ nM}/17 \mu\text{M} \approx 1.3 \times 10^{-3}$, (b) clusters deposited on mica from a solution having a (citrate capped) NP to the TC dye concentration ratio of $16 \text{ nM}/25 \mu\text{M} \approx 0.64 \times 10^{-3}$ (c) clusters deposited on SiO_2/Si from a solution having a (borate capped) NP to the TC dye concentration ratio of $10 \text{ nM}/16 \mu\text{M} \approx 0.64 \times 10^{-3}$. (d)–(f) Examples of the blinking and dye SERS spectra observed in the Raman maps, displayed below the corresponding Raman maps.

scattering on random silver nanoparticle clusters on various substrates has shown that, for the investigated nanoparticles and the 532 nm excitation laser, typical enhancement factors in the range of 10^2 – 10^3 can be expected. The highest field enhancement factors are reached at collective nanoparticle plasmon resonances, which lie in the 400–500 nm range for medium sized clusters (around 20 nanoparticles), and become redshifted in elongated clusters with an increasing number of particles. From an inspection of electromagnetic field distribution on nanoparticle surfaces, a conclusion is reached that at least 90% of the SERS total enhancement originates from nanogaps between adjacent nanoparticles, implying that the experiments are sensitive only to adsorbates located in these gaps.

Combined AFM and PL mapping of citrate-capped AgNP clusters with dye molecules adsorbed from solutions of variable TC concentration have shown that, even at highest TC concentrations, not all hotspots exhibit Raman signatures characteristic of TC dye molecules, indicating that the clusters are only partially covered by dye molecules. In contrast, the control experiment carried out with borate-capped AgNP clusters, with similar nanoparticle and dye concentrations, has shown a complete dye-coverage of AgNP clusters.

These results are a direct demonstration that the citrate anions, while useful for stabilizing the colloid, impede the efficient TC dye adsorption.

Acknowledgements

The research reported in this article was supported by the Serbian Ministry of Education, Science and Technological Development through project Nos. ON171005, ON172023, III45016. This work was performed in the context of COST Action MP 1302 “Nanospectroscopy”.

Appendix A. Supplementary data

Supplementary data associated with this article can be found, in the online version, at <https://doi.org/10.1016/j.apsusc.2017.10.148>.

References

- [1] A. Manjavacas, F.J.G.d. Abajo, P. Nordlander, Quantum plexitronics: strongly interacting plasmons and excitons, *Nano Lett.* 11 (6) (2011) 2318–2323.
- [2] N.T. Fofang, T.-H. Park, O. Neumann, N.A. Mirin, P. Nordlander, N.J. Halas, Plexitonic nanoparticles: plasmon exciton coupling in nanoshell-J-aggregate complexes, *Nano Lett.* 8 (10) (2008) 3481–3487.
- [3] E. Dulkeith, A.C. Morteani, T. Niedereichholz, T.A. Klar, J. Feldmann, S.A. Levi, F.C.J.M. van Veggel, D.N. Reinhoudt, M. Möller, D.I. Gittins, Fluorescence quenching of dye molecules near gold nanoparticles: radiative and nonradiative effects, *Phys. Rev. Lett.* 89 (2002) 203002–203006.
- [4] J. Zhao, X. Zhang, Y.C. Ranjit, A.J. Haes, R.P. Van Duyne, Localized surface plasmon resonance biosensors, *Nanomedicine* 1 (2006) 219–228.

- [5] M.A. Noginov, G. Zhu, A.M. Belgrave, R. Bakker, V.M. Shalae, E.E. Narimanov, S. Stout, E. Herz, T. Suteewong, U. Wiesner, Demonstration of a spaser-based nanolaser, *Nature* 460 (2009) 1110–1112.
- [6] N. Kometani, M. Tsubonishi, T. Fujita, K. Asami, Y. Yonezawa, Preparation and optical absorption spectra of dye-coated Au, Ag, and Au/Ag colloidal nanoparticles in aqueous solutions and in alternate assemblies, *Langmuir* 17 (3) (2001) 578–580.
- [7] A. Yoshida, N. Kometani, Effect of the interaction between molecular exciton and localized surface plasmon on the spectroscopic properties of silver nanoparticles coated with cyanine dye J-aggregates, *J. Phys. Chem. C* 114 (7) (2010) 2867–2872.
- [8] V.S. Lebedev, A.S. Medvedev, D.N. Vasil'ev, D.A. Chubich, A.G. Vitukhnovskiy, Optical properties of noble-metal nanoparticles coated with a dye J-aggregate monolayer, *Quantum Electron.* 40 (3) (2010) 246.
- [9] Y. Kitahama, M. Kashihara, T. Itoh, Y. Ozaki, Surface-enhanced phosphorescence measurement by an optically trapped colloidal Ag nanoaggregate on anionic thiocarbocyanine H-aggregate, *J. Phys. Chem. C* 117 (6) (2013) 2460–2466.
- [10] A. Vujačić, V. Vasić, M. Dramićanin, S.P. Sovilj, N. Bibić, J. Hranisavljević, G.P. Wiederrecht, Kinetics of J-aggregate formation on the surface of Au nanoparticle colloids, *J. Phys. Chem. C* 116 (7) (2012) 4655–4661.
- [11] A. Vujačić, V. Vasić, M. Dramićanin, S.P. Sovilj, N. Bibić, S. Milonjić, V. Vodnik, Fluorescence quenching of 5,5-disulfofopropyl-3,3-dichlorothiacyanine dye adsorbed on gold nanoparticles, *J. Phys. Chem. C* 117 (13) (2013) 6567–6577.
- [12] B.B. Laban, V. Vodnik, A. Vujačić, S.P. Sovilj, A.B. Jokić, V. Vasić, Spectroscopic and fluorescence properties of silver-dye composite nanoparticles, *Russ. J. Phys. Chem. A* 87 (13) (2013) 2219–2224.
- [13] B. Laban, V. Vodnik, M. Dramićanin, M. Novaković, N. Bibić, S.P. Sovilj, V.M. Vasić, Mechanism and kinetics of J-aggregation of thiocyanine dye in the presence of silver nanoparticles, *J. Phys. Chem. C* 118 (40) (2014) 23393–23401.
- [14] B. Laban, V. Vodnik, V. Vasić, Spectrophotometric observations of thiocyanine dye J-aggregation on citrate capped silver nanoparticles, *Nanospectroscopy* 1 (2015) 54–60.
- [15] F. Würthner, T.E. Kaiser, C.R. Saha-Möller, J-aggregates: from serendipitous discovery to supramolecular engineering of functional dye materials, *Angew. Chem. Int. Ed.* 50 (15) (2011) 3376–3410.
- [16] M. Kawasaki, T. Sato, T. Yoshimoto, Controlled layering of two-dimensional J-aggregate of anionic cyanine dye on self-assembled cysteamine monolayer on Au(111), *Langmuir* 16 (12) (2000) 5409–5417.
- [17] R.W. Owens, D.A. Smith, Stm imaging of cyanine dye J-aggregates formed on carboxyl-terminated self-assembled monolayers, *Langmuir* 16 (2) (2000) 562–567.
- [18] H. Yao, S. Kitamura, K. Kimura, Morphology transformation of mesoscopic supramolecular J aggregates in solution, *Phys. Chem. Chem. Phys.* 3 (2001) 4560–4565.
- [19] N. Vranken, P. Foubert, F. Khn, R. Gronheid, I. Scheblykin, M. Van der Auweraer, F.C. De Schryver, Influence of the deposition method on the topography and spectroscopy of J-aggregates of a thiocarbocyanine dye adsorbed to a Langmuir film, *Langmuir* 18 (22) (2002) 8407–8417.
- [20] H. Yao, Y. Kagoshima, S. Kitamura, T. Isohashi, Y. Ozawa, K. Kimura, Superstructures of mesoscopic monomolecular sheets of thiocyanine J aggregates in solution, *Langmuir* 19 (21) (2003) 8882–8887.
- [21] H. Yao, T. Isohashi, K. Kimura, Large birefringence of single J-aggregate nanosheets of thiocyanine dye in solution, *Chem. Phys. Lett.* 396 (4–6) (2004) 316–322.
- [22] S. Özcelik, M.M. Demir, B. Birkan, Probing nanoscale domains of J-aggregates deposited on a mica surface, *J. Phys. Chem. B* 108 (15) (2004) 4679–4683.
- [23] H. Yao, K. Domoto, T. Isohashi, K. Kimura, In situ detection of birefringent mesoscopic H and J aggregates of thiocarbocyanine dye in solution, *Langmuir* 21 (3) (2005) 1067–1073.
- [24] V.V. Prokhorov, O.M. Pereylygina, S.I. Pozin, E.I. Mal'tsev, A.V. Vannikov, A.Y. Tsvadze, Tubular structure of J-aggregates of cyanine dye, *Dokl. Chem.* 460 (1) (2015) 1–4.
- [25] T.H. James, *The Theory of the Photographic Process*, 4th ed., Macmillan, New York, 1977.
- [26] B. Laban, I. Zeković, D. Vasić Aničjević, M. Marković, V. Vodnik, M. Luce, A. Cricenti, M. Dramićanin, V. Vasić, Mechanism of 3,3-disulfofopropyl-5,5-dichlorothiacyanine anion interaction with citrate-capped silver nanoparticles: adsorption and J-aggregation, *J. Phys. Chem. C* 120 (32) (2016) 18066–18074.
- [27] M. Kerker, O. Siiman, L.A. Bumm, D.-S. Wang, Surface enhanced Raman scattering (SERS) of citrate ion adsorbed on colloidal silver, *Appl. Opt.* 19 (19) (1980) 3253–3255.
- [28] O. Siiman, L.A. Bumm, R. Callaghan, C.G. Blatchford, M. Kerker, Surface-enhanced Raman scattering by citrate on colloidal silver, *J. Phys. Chem.* 87 (6) (1983) 1014–1023.
- [29] D.L. Akins, S. Zelik, H.-R. Zhu, C. Guo, Aggregation-enhanced Raman scattering of a cyanine dye in homogeneous solution, *J. Phys. Chem. A* 101 (18) (1997) 3251–3259.
- [30] Y. Kitahama, Y. Tanaka, T. Itoh, Y. Ozaki, Wavelength-dependent surface-enhanced resonance Raman scattering by excitation of a transverse localized surface plasmon, *J. Phys. Chem. C* 113 (27) (2009) 11877–11883.
- [31] Y. Kitahama, Y. Tanaka, T. Itoh, Y. Ozaki, Time-resolved surface-enhanced resonance Raman scattering spectra of thiocyanine molecules in water, *Chem. Lett.* 38 (1) (2009) 54–55.
- [32] Y. Kitahama, Y. Tanaka, T. Itoh, M. Ishikawa, Y. Ozaki, Identification of thiocyanine J-aggregates adsorbed on single silver nanoaggregates by surface-enhanced Raman scattering and emission spectroscopy, *Bull. Chem. Soc. Jpn.* 82 (9) (2009) 1126–1132.
- [33] Y. Kitahama, A. Ogawa, Y. Tanaka, S. Obeidat, T. Itoh, M. Ishikawa, Y. Ozaki, Difference in time dependence of surface-enhanced Raman scattering spectra of thiocarbocyanine J- and H-aggregates adsorbed on single silver nanoaggregates, *Chem. Phys. Lett.* 493 (4–6) (2010) 309–313.
- [34] Y. Kitahama, Y. Tanaka, T. Itoh, Y. Ozaki, Power-law analysis of surface-plasmon-enhanced electromagnetic field dependence of blinking SERS of thiocyanine or thiocarbocyanine adsorbed on single silver nanoaggregates, *Phys. Chem. Chem. Phys.* 13 (2011) 7439–7448.
- [35] C.R. Zamecnik, A. Ahmed, C.M. Walters, R. Gordon, G.C. Walker, Surface-enhanced Raman spectroscopy using lipid encapsulated plasmonic nanoparticles and J-aggregates to create locally enhanced electric fields, *J. Phys. Chem. C* 117 (4) (2013) 1879–1886.
- [36] Y. Kitahama, D. Araki, Y.S. Yamamoto, T. Itoh, Y. Ozaki, Different behaviour of molecules in dark SERS state on colloidal Ag nanoparticles estimated by truncated power law analysis of blinking SERS, *Phys. Chem. Chem. Phys.* 17 (2015) 21204–21210.
- [37] COMSOL MULTIPHYSICS v5.2, COMSOL, Inc.
- [38] A.D. Rakić, A.B. Djurišić, J.M. Elazar, M.L. Majewski, Optical properties of metallic films for vertical-cavity optoelectronic devices, *Appl. Opt.* 37 (22) (1998) 5271–5283.
- [39] C.F. Frontiers, D.R. Huffman, *Absorption and Scattering by an Arbitrary Particle*, Wiley-VCH Verlag GmbH, 2007, pp. 57–81.
- [40] M. Kerker, D.-S. Wang, H. Chew, Surface enhanced Raman scattering (SERS) by molecules adsorbed at spherical particles, *Appl. Opt.* 19 (19) (1980) 3373–3388.
- [41] L.O. Herrmann, V.K. Valev, J. Aizpurua, J.J. Baumberg, Self-sifting of chain plasmons: the complex optics of an nanoparticle clusters, *Opt. Express* 21 (26) (2013) 32377–32385.
- [42] C. Tserkezis, R.W. Taylor, J. Beitner, R. Esteban, J.J. Baumberg, J. Aizpurua, Optical response of metallic nanoparticle heteroaggregates with subnanometric gaps, *Part. Part. Syst. Char.* 31 (1) (2014) 152–160.
- [43] R. Esteban, R.W. Taylor, J.J. Baumberg, J. Aizpurua, How chain plasmons govern the optical response in strongly interacting self-assembled metallic clusters of nanoparticles, *Langmuir* 28 (24) (2012) 8881–8890.
- [44] R.W. Taylor, R. Esteban, S. Mahajan, J. Aizpurua, J.J. Baumberg, Optimizing SERS from gold nanoparticle clusters: addressing the near field by an embedded chain plasmon model, *J. Phys. Chem. C* 120 (19) (2016) 10512–10522.
- [45] N. Harris, M.D. Arnold, M.G. Blaber, M.J. Ford, Plasmonic resonances of closely coupled gold nanosphere chains, *J. Phys. Chem. C* 113 (7) (2009) 2784–2791.
- [46] Y. Ozaki, K. Kneipp, R. Aroca, *Frontiers of Surface-Enhanced Raman Scattering*, John Wiley & Sons Ltd, 2014.
- [47] D.L. Akins, Theory of Raman scattering by aggregated molecules, *J. Phys. Chem.* 90 (8) (1986) 1530–1534.



Green synthesis and characterization of nontoxic L-methionine capped silver and gold nanoparticles

B. Laban^a, U. Ralević^b, S. Petrović^c, A. Leskovac^c, D. Vasić-Aničijević^c, M. Marković^c, V. Vasić^{c,*}

^a Faculty of Sciences, University in Priština – Kosovska Mitrovica, Lole Ribara 29, 38220 Kosovska Mitrovica, Serbia

^b Center for Solid State Physics and New Materials, Institute of Physics, University of Belgrade, Pregrevica 118, 11080 Belgrade, Serbia

^c Vinča Institute of Nuclear Sciences, University of Belgrade, P.O. Box 522, Belgrade, Serbia

ARTICLE INFO

Keywords:

Silver
Gold
Green
Nanoparticles
L-methionine
Toxicity

ABSTRACT

The simple green method for synthesis of stable L-Methionine (L-Met) capped silver (Ag@LM NPs) and gold (Au@LM NPs) nanoparticles (NPs) without adding any additional reduction agent or stabilizer was developed. Colloidal dispersions were characterized by UV–Vis spectrophotometry. The size and spherical shape of NPs were evaluated by transmission electron microscopy. Their surface covering was confirmed by atomic force microscopy, Fourier transform infrared spectroscopy, dynamic light scattering, and zeta potential measurements. Density functional theory calculations pointed that the preferential adsorption mode of L-Met on both Ag and Au surfaces was a vertical binding geometry via $-NH_2$ group, while horizontal binding mode via $-S-$ and $-NH_2$ groups is also possible. The genotoxicity (evaluated by the micronucleus assay) of NPs, as well as their effects on some oxidative stress parameters (catalase activity, malondialdehyde level), were assessed in vitro using human peripheral blood cells as a model system. The influence of NPs on the morphology of lymphocyte cells studied using atomic force microscopy revealed that the membrane of cells remained unaffected after the treatment with NPs. When considering the effects of NPs on catalase activity and malondialdehyde level, neither particle type promoted oxidative stress. However, the treatment of lymphocytes with Ag@LM NPs induced a concentration-dependent enhancement of the micronuclei incidence and suppression of the cell proliferation while Au@LM NPs promoted cell proliferation, with no significant effects on micronuclei formation. The Ag@LM NPs were more prone to induce DNA damage than Au@LM NPs, which makes the latter type more suitable for further studies in nano-medicine.

1. Introduction

During the past decade, noble metal nanoparticles (NPs) have been extensively studied due to their unique optical, chemical and physical properties [1], and have found many applications in different areas, such as electronics, catalysis, and optoelectronic devices. Besides, there is a growing interest in their use in nano-medicine as potential drugs [2,3], in biosensing and drug delivery [4]. There are various physical, chemical, and biological methods for NPs synthesis, including physical vapor deposition, laser ablation, gamma radiation, reduction of metal ions, use of microorganisms, and enzymes [5–7]. For a biomedical application, noble metal NPs are most frequently synthesized in solutions by chemical reduction method [8]. The color of noble metal colloidal dispersions originates from their localized surface plasmon resonance (LSPR) and can be tuned by controlling the NPs size and morphology [8].

Silver and gold NPs (Ag NPs, Au NPs, respectively) are the most frequently studied metal NPs due to their fascinating physical and chemical properties, including the well-defined surface plasmon resonance (SPR). Various amino acids, which are the basic structural units of proteins and also biologically important substances whose activities depend largely on their redox behavior, can be used for the preparation of small-scale metal particles of silver and gold. The application of surfactants and stabilizing ligands on solid matrix [1] determines their size, shape, stability, color, as well as the state of aggregation and physicochemical properties. Amino acids capped NPs have extensive use because of the excellent conductivity, chemical stability, and antimicrobial activity. Especially, Ag NPs and Au NPs have found application in the biomedical field [9,10], and their interactions with various biomolecules have been extensively studied [11]. They are also very promising for medicinal applications in both diagnostics (application of surface enhanced Raman spectroscopy (SERS), cellular imaging,

* Corresponding author.

E-mail address: evasic@vinca.rs (V. Vasić).

<https://doi.org/10.1016/j.jinorgbio.2019.110958>

Received 16 August 2019; Received in revised form 3 December 2019; Accepted 8 December 2019

Available online 11 December 2019

0162-0134/ © 2019 Elsevier Inc. All rights reserved.

biosensors, an assay for Alzheimer's diseases), and therapy (antioxidant and anticancer activity, in photothermal therapy, as drug delivery vehicles) [10,12,13]. With NPs' potential to have a good impact on the human health, there is also a growing need for the development of the green methods for their synthesis [14,15], in order to obtain biocompatible NPs that could find application in nano-medicine [4].

L-Methionine (L-Met) is one of the two sulfur-containing essential amino acids, which is generally found in proteins and has some crucial biological functions in antioxidant defense mechanisms and regulation of cellular function through reversible oxidation and reduction [16,17]. Besides, L-Met has an essential role in cysteine synthesis in the body of healthy persons [18]. In the biochemical processes, it is usually oxidized to methionine sulfoxide [19,20], but in the presence of halogen species, a dehydromethionine form has also been reported [21].

Recently, some papers reported the new green synthesis procedures for obtaining Au NPs, ZnS NPs, and magnetic Fe₃O₄ NPs using L-Met as the biocompatible reducing and capping agent [22–24]. For the synthesis of Ag NPs and gold-coated CoFe₂O₄ NPs, L-Met was used as reducing agent [25,26]. Also, the Ag NPs synthesis in the presence of L-Met by photoreduction method was recently performed [27]. However, in these syntheses, L-Met was used in the presence of other reduction and stabilizing agents (e.g. sodium citrate, NaBH₄, CTAB – cetyltrimethylammonium bromide), which exert additional side effects in biochemical processes. Although there are various reductant agents used, the reaction mechanism for NPs formation is not completely evaluated in many cases, including the nucleation and particle growth [25,28]. However, there is a lack of data concerning L-Met capped NPs green synthesis using no additional reduction or capping agents. Before considering any medical application of NPs in diagnostics or treatment of human diseases, it is necessary to evaluate their biological effects. Though there are numerous studies of metal NPs toxicity [29,30], constant development and improvement of the synthesis methods require a continuous study of the newly synthesized metal NPs biosafety. Physicochemical properties such as size, shape, and surface charge, may influence the penetration of NPs into cells and their interaction with biomolecules [31,32]. Some studies show that free silver ions, which could be present in colloid dispersion after NPs synthesis, also play an important role in the toxicity of Ag colloids [33].

This work aims to develop a new, environmentally friendly, green method for the synthesis of stable Ag NPs and Au NPs, avoiding the application of toxic chemicals for the reduction and stabilization of colloids. For that purpose, the amino acid L-Met was used as reducing and capping agent, in order to obtain the nontoxic NPs, capable of delivering L-Met with its biocompatible properties. Numerous methods (UV–Vis and Fourier transform infrared spectroscopy, transmission electron, and atomic force microscopy, dynamic light scattering, density functional theory calculations) were used to characterize the size, shape, and stability of obtained conjugates, including the optimized geometry of L-Met on NPs surface.

In order to consider the possible diagnostic or therapeutic applications of these NPs in nano-medicine, the biological effects, including the toxicity assessment and oxidative stress effects were performed using human peripheral blood cells as a model system. For this reason, the genotoxic potential and redox modulating activities of newly synthesized NPs were examined, including the morphological study of the untreated and NPs treated lymphocytes carried out using the atomic force microscopy method.

2. Experimental methods

2.1. Chemicals

Silver nitrate (AgNO₃), Hydrogen tetrachloroaurate trihydrate (HAuCl₄ × 3H₂O), L-2-Amino-4-(methylthio)butanoic acid (L-Methionine), and Potassium hydroxide (KOH) were commercial products from Aldrich and Merck and were used as received. All solutions

were prepared using water purified with a Millipore Milli-Q water system. Cytochalasin B, Histopaque-1077 (Lymphocyte separation medium), thiobarbituric acid (TBA), and Giemsa stain were purchased from Merck (Darmstadt, Germany). RPMI-1640 medium, fetal bovine serum, and phytohemagglutinin (PHA-M) were purchased from Fisher Scientific – UK (Leicestershire, UK).

2.2. Ag@LM NPs and Au@LM NPs synthesis

For L-Met capped silver (Ag@LM) NPs synthesis, 1 ml of 10⁻³ M AgNO₃ and 0.5 ml of 10⁻² M L-Met were mixed, and water was added to the final volume of 10 ml, then the reaction mixture was heated to boiling. A few minutes after the mixture started to boiling, the transparent color became dark yellow, indicating the NPs formation. The dispersion was heated for a few minutes, and when it was stopped, the solution was cooled under water.

For L-Met capped gold (Au@LM) NPs synthesis, 10 ml of 10⁻³ M HAuCl₄ was heated to boiling, then 0.5 ml of 10⁻¹ M L-Met and water were added to the final volume of 20 ml. The yellow color of tetrachloroaurate first became transparent than pink due to the formation of NPs. The colloid dispersion was centrifuged, and the precipitate was washed with deionized water. Finally, Au colloid was concentrated in 1 ml. The alkalinity of solutions (pH = 9–11) was adjusted by adding a proper amount of 1 M KOH for both colloids. The Ag and Au NPs working solutions were made by appropriate dilution of stock dispersion.

The concentration of Ag@LM and Au@LM NPs (*c*_{NPs}) in stock dispersion (6.37 × 10⁻⁹ M and 2.25 × 10⁻⁹ M) was approximately determined using Eq. (1):

$$c_{NPs} = \frac{c_M \cdot M_{Ag \text{ (or Au)}}}{\frac{4}{3} r^3 \pi \rho N_o} \quad (1)$$

where *c*_M represents the AgNO₃ or HAuCl₄ molar concentration, *M*_{Ag (or Au)} - the Ag or Au molar mass, *r* - an average particle size radius, *ρ* - the Ag or Au density (10.49 g cm⁻³ and 19.30 g cm⁻³) and *N*_o - the Avogadro number.

2.3. Blood cultures

Blood samples were obtained from healthy, non-smoking young volunteer donors following current regulations [34]. Aliquots of whole heparinized blood (0.5 ml) were added to culture tubes containing 4.5 ml of RPMI-1640 medium supplemented with 15% fetal bovine serum and 2% phytohemagglutinin. The blood cultures were treated with increasing doses of Ag and Au NPs (final concentrations 1 × 10⁻¹³ M - 1 × 10⁻¹¹ M). The untreated cultures served as a control. The adequate number of blood cultures per treatment was established to enable examinations of catalase activity, malondialdehyde (MDA) level, micronuclei incidence, and a cell proliferation index. For the Thiobarbituric acid (TBA) and catalase assays, after 72 h of incubation, the blood cultures were separated using Histopaque-1077; the lymphocytes were collected by centrifugation, washed in physiological saline, and frozen at -80 °C while erythrocytes were hemolyzed in ice-cold deionized water, and frozen at -20 °C for 24 h. For each analysis performed, three independent experiments were carried out. The obtained data were pooled, and the results are expressed as the mean and standard deviation (SD) of the mean.

2.4. Micronuclei analysis

The incidence of micronuclei was estimated employing the cytokinesis-block micronucleus (CB-MN) method of Fenech [35]. Cytochalasin B at a final concentration of 4 µg/ml was added to each sample 44 h after incubation to inhibit cytokinesis. The lymphocyte cultures were incubated for a further 28 h. Cells were collected by centrifugation

and treated with hypotonic solution (0.56% KCl + 0.90% NaCl, mixed in equal volumes) at 37 °C. The cell suspensions were prefixed in methanol/acetic acid 3:1, washed three times with fixative, and dropped onto a clean slide. Slides were air-dried and stained with alkaline Giemsa (2%). For each sample, at least 1000 binucleated (BN) cells were scored, and micronuclei (MN) were evaluated using a microscope with 400× or 1000× magnification. A minimum of 1000 BN cells was scored to evaluate the number of cells with micronuclei.

2.5. Cytokinesis-block proliferation index

A cytokinesis-block proliferation index (CBPI) was calculated according to a method of Surrales et al. [36] as follows: $CBPI = [MI + 2MII + 3(MIII + MIV)]/N$, where MI-MIV represents the number of cells with one to four nuclei, and N is the number of cells scored. For its determination, at least 500 cells per slide were counted. The relative frequencies of mononucleate, binucleate, trinucleate, and tetranucleate cells in the culture provide an accurate method of quantifying the effect on cell proliferation and the cytotoxic or cytostatic activity of a treatment. The cytotoxicity was measured in accordance with the Organization for Economic Cooperation and Development (OECD) Guideline for the Testing of Chemicals 487 [37], by using the CBPI, where:

$\% \text{ Cytostasis} = 100 - 100[(CBPIT - 1)/(CBPIC - 1)]$, where CBPIT is the CBPI of the test compound and CBPIC the CBPI of the untreated control cells. According to Test Guideline, cytotoxicity is identified as a reduction in CBPI. If the maximum concentration is based on cytotoxicity, the highest concentration should aim to achieve $55 \pm 5\%$ cytotoxicity and, i.e. show a reduction in CBPI up to $45 \pm 5\%$ of the concurrent negative control [37].

2.6. Catalase activity assay

The catalase activity was measured using the method of Aebi [38] with minor modifications by following the catalytic reduction of hydrogen peroxide. The decomposition of the substrate H_2O_2 was measured using a Perkin Elmer Lambda 35 Spectrophotometer at 240 nm. The activity was expressed as K – the rate constant of the first-order reaction per minute per mg of hemoglobin (min⁻¹ mg Hb⁻¹). The concentration of hemoglobin was marked by Drabkin's method.

2.7. Thiobarbituric acid (TBA) assay

A thawed lymphocyte suspensions were used for the measurement of malondialdehyde, spectrophotometrically [39] at the 532 nm wavelength. The values are expressed as nmol of thiobarbituric acid-reactive substance (MDA equivalent)/mg protein, using a standard curve of 1,1,3,3-tetramethoxypropane. Protein concentration was determined according to the method of Lowry et al. [40].

2.8. Statistics

Statistical analysis was performed using the Product-Moment and partial correlations and One-way ANOVA followed by post-hoc Tukey test with the software package Statistica 8, for Microsoft Windows. *P* values < .05 were considered significant.

2.9. Apparatus

Absorption spectra of colloidal dispersions were recorded by Perkin Elmer Lambda 35 UV – Vis spectrophotometer using the quartz cuvette with a 1 cm path length.

Transmission electron microscopy (TEM) measurements were carried out using FEI Talos F200X at an operating voltage of 200 kV.

Atomic Force Microscopy (AFM) measurements were performed in air using NTegra Prima from NT-MDT, which was operated in semi-

contact mode. The sample was prepared by placing a drop of colloid (or cell suspension) on a freshly cleaved mica surface. The measurements were done upon drying of the droplet.

Dynamic Light Scattering (DLS) and zeta potential (ZP) measurements were performed using a Nano ZS zetasizer system with 633 nm He–Ne laser (Malvern Instruments, UK) and data were analyzed by the Zetasizer Software Version 6.20.

Fourier transform infrared (FTIR) spectra of Ag and Au colloids were recorded on Nicolet IS 50 FTIR Spectrometer. The samples were prepared by dropping colloids on a clean glass plate and left to dry.

The micronuclei and cell proliferation were analyzed using an Otech microscope (Munich, Germany) with 400× or 1000× magnification.

2.10. Density functional theory calculation details

Density functional theory (DFT) calculations were performed using Pwscf code of Quantum ESPRESSO [41]. Employed Vanderbilt ultrasoft pseudopotentials [42] were based on GGA-PBE approximation for exchange-correlation functional [43]. Cutoff energy for plane waves was set to 25 Ry. For calculations of methionine interactions with one metal atom a supercell of dimensions, 50x50x50 Bohr with Martyna Tuckermann correction was used [44] to assume that the system is isolated. Calculations with one metal atom were performed in a single gamma-point. The electronic convergence criterion was set to 10^{-6} eV. Gaussian smearing was applied. The negative charge of the methionine molecule was modeled through the addition of an excess electron to the supercell, as implemented in Quantum ESPRESSO.

Ag111 and Au111 surfaces were modeled as 3-layer slabs in a 4×4 supercell. Bottom two layers were fixed, and all others were allowed to relax. Space between periodic images was set to at least 15 Å of vacuum to minimize their interaction. The sampling of k-points was performed using the Monkhorst Pack grid [45] of $2 \times 2 \times 1$ k-points. Molecular structures were represented by XCrysDen [46].

3. Results and discussion

3.1. Synthesis of Ag and Au colloids

Ag and Au colloids (Ag@LM NPs and Au@LM NPs, respectively) were prepared by chemical reduction of Ag^+ and Au^{3+} ions by L-Met from their salts. The experiments were performed in excess of L-Met (from 1:5 to 1:10) in the pH range 5–11, at 100 °C, without adding any additional reducing or stabilizing agent. The NPs formation and their time stability were followed spectrophotometrically. Our previous results indicated that Au(III) reduction by L-Met in acidic media and ambient temperature to elemental metal proceeded in multi-step processes [47,48], including also complex formation, but without colloids formation. The in situ reductions of $HAuCl_4$ using $NaBH_4$ as reducing and L-Met as stabilizing agent in an aqueous medium [22,49] led to the formation of L-Met protected Au NPs, including the spherical shape of various particle size (25–100 nm) and flowers. The NPs size and shape depended on pH, concentration of capping, and reducing agents, and they were stable over one week. Besides, the simple, time-saving procedure for gold nanoclusters (Au NCs) formation was published by using L-Met as both reducing and stabilizing ligands [49], which does not require toxic reductants (e.g., $NaBH_4$). The resulting Met-Au NCs exhibit intense yellow fluorescence maximized at 530 nm, the high luminescence quantum yield, wide pH, and time stability (over two months), but the data about their biological effect are still missing.

The Ag@LM and Au@LM colloid dispersions exhibited an intense SPR peak with a maximum at 411 nm (Fig. 1 a), and at 537 nm (Fig. 1 b), respectively. By increasing the molar ratio metal ion: L-Met up 1: 5 in alkaline medium (pH 9–11), the intensity of the characteristic plasmon bands changed, indicating the change of concentration and size of NPs (Fig. S1, SI). Besides, the slight red shifting (3–5 nm) of

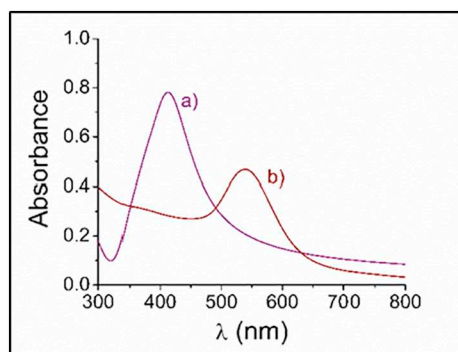


Fig. 1. Absorption spectra of (a) Ag@LM NPs and (b) Au@LM NPs colloids at pH 9–11; 100 °C; $c_{\text{Ag@LM}} = 6.4 \times 10^{-9}$ M; $c_{\text{Au@LM}} = 2.2 \times 10^{-9}$ M; $c_{\text{Met}} = 5 \times 10^{-4}$ M.

plasmon band position was observed, indicating that L-Met was also responsible for interparticle interaction, growth, and cross-linking between the particles. Fig. 1 shows the characteristic absorption spectra of Ag@LM and Au@LM colloids obtained under the controlled conditions (concentration of reactants, pH, molar and volume ratio, temperature, and stirring).

In general, pH of the initial solution, the type of reducing and stabilizing agent, their concentration ratio, and working temperature have a significant influence on NPs size, shape, and stability [50,51]. The red shift of Au@LM NPs absorption band (Fig. S2 a) due to the increase of pH indicated NPs agglomeration in the solution [22].

However, in our synthesis, pH did not have a significant influence on the position of the absorption band of Ag@LM NPs but significantly affected its intensity and width (Fig. S2 b). Similarly, the irradiation of AgNO₃ solution by Xe light promoted the formation of L-Met capped Ag NPs of the size ranging from 15 to 30 nm, with the same position of plasmon band [27], but the increase of pH harms the stability. In our case, the gradual increase in peak intensity with pH increasing indicated that more numbers of particles were present in solution. The highest peak intensity and the narrowest band were obtained at pH > 9.

The use of various surface-active compounds as stabilizers determined the size and shape of NPs. As an example, the reduction of Ag (I) by L-Met in the presence of CTAB resulted in the formation of corn-shaped Ag NPs [25]. By omitting the surface-active compounds from the synthesis in our case, e.g. CTAB, the spherically-shaped NPs of desired size were obtained. Concerning the colloids time stability, both Ag and Au colloidal dispersions were stable for more than one year, in the alkaline medium at pH 9–11. This finding was confirmed by spectrophotometric measurements (Fig. S3).

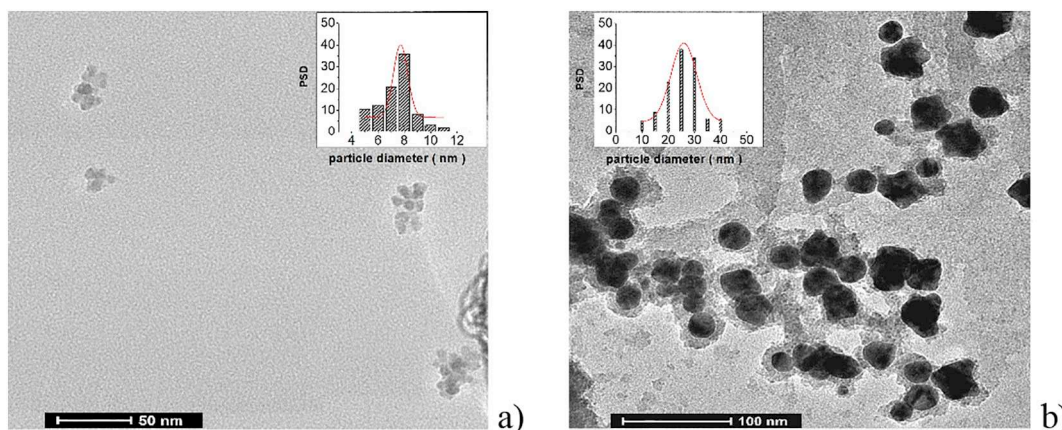
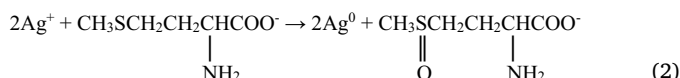


Fig. 2. TEM micrographs of Ag@LM NPs (a) and Au@LM NPs (b). Inset: particle size distribution of NPs.

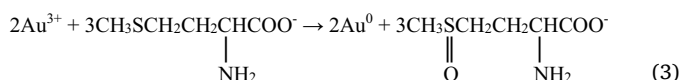
3.2. Reaction mechanism

It seems that L-Met concentration plays a critical role in nucleation and Ag NPs stabilization, together with temperature and time, which control the NPs growth, size, and shape. The reaction steps in Ag⁺ reduction and Ag NPs formation are presented in detail in Supplementary Information. Briefly, the reaction occurred due to Ag⁺-L-Met complex formation, followed by the Ag⁺ reduction and radical cation (Ag⁺-L-Met[•]) formation. It reacted further with Ag⁺ which led to its reduction and another Ag⁺-L-Met sulfoxide complex formation. The formatted of metal nucleation center acted as a catalyst for the reduction of other Ag⁺ ions in solution due to their adsorption on Ag metal surface. The overall reaction can be described by Eq. (2):



For Au NPs formation, the first and fastest step was the [Au³⁺Cl₃(L-Met)]⁻ complex formation resulting from a nucleophilic attack of S-donor from the thioether group and Cl⁻ substitution, as shown in our previous study [47]. In the less acidic media, deprotonated -COOH group enhanced the participation of N-donor from -NH₂ group (zwitter ionic form of L-Met) in the reaction process, resulting in the formation of the more stable chelate. The slow reaction path requires the second L-Met to promote Au³⁺ reduction by forming a linear two-coordinated Au⁺-L-Met complex and methionine sulfoxide.

Moreover, ¹H NMR signal confirmed S-coordination in Au⁺-L-Met complex [47,48]. In this reaction step, L-Met was oxidized in the presence of water to the corresponding sulfoxide, and the disproportionation of aurous species to gold atoms occurred [28]. The reaction steps are given in Supplement Information, and the overall reaction for the formation of elemental gold can be described as follows:



However, the stoichiometric ratio of L-Met to Au required for complete conversion of [AuCl₄]⁻ to elemental Au should be larger than 1.5. The Au atoms adsorb Au⁺, and by further complexation and reduction by L-Met, the large aggregates of Au atoms are formed, as also described for Au NPs formation by using the citrate ions for Au³⁺ reduction [28].

3.3. TEM characterization of Ag@LM and Au@LM NPs

The presence of nanometer-sized particles in colloidal dispersions was confirmed by TEM measurements. TEM micrographs with particle size distribution (PSD) histograms for Ag@LM NPs and Au@LM NPs are

Table 1
The pH, d_{av} , and zeta potential of Ag and Au colloids.

Colloids	d_{av} (nm)				ζ (mV)	PDI	Mobility ($\text{cm}^2 \text{V}^{-1} \text{s}^{-1}$)	Conductivity ($\mu\text{S cm}^{-1}$)
	pH	TEM	AFM	DLS				
Ag@LM	11	7.7 ± 0.2	11.7 ± 1	44 ± 3	-24.6	0.388	-1.93 ± 0.15	0.15 ± 0.001
Au@LM	9.4	25.9 ± 0.6	26.2 ± 1	46 ± 0.2	-33.2	0.258	-2.6 ± 0.16	0.01 ± 0.002

shown in Fig. 2. The mean particle size of NPs was determined by fitting the obtained TEM data with the Gaussian distribution function (Fig. 2, inset) and are given in Table 1.

A TEM study of colloids confirmed the presence of nearly spherical shaped NPs with a layer of film capping their surface in both cases. This film is assumed to be a layer of L-Met adsorbed on NPs surface upon reduction and during the Ag and Au nucleation and aggregation processes. TEM images further indicate that NPs underwent aggregation and cross-linking. It can be concluded that this process was due to the intermolecular binding of adsorbed L-Met molecules by hydrogen bonds formation between its acido-basic functional groups [52].

3.4. AFM study of NPs

The size (diameter) of Ag@LM NPs and Au@LM NPs was assessed from the AFM topography images by evaluating the NPs height. The NPs were identified as bright pixels (yellow-colored areas) within the topography maps. For example, the left images in panels (a) and (b) of Fig. 3 show the raw AFM topography. Next to them are the images in which the color of the pixels identified as NPs represents the value of the assessed NP diameter. The exact diameter values are given in the graphs at the right end of the corresponding panels.

For the particular case illustrated in Fig. 3, the diameter of Ag@LM NPs varies between 9 nm and 26 nm (see panel (a)), whereas the diameter of Au@LM NPs varies between 13 nm and 34 nm (see panel (b)).

The average NPs height was determined by analyzing a series of AFM topography maps (10 maps per NP type, either Ag@LM NPs or Au@LM NPs). Fig. 4 shows the Ag@LM NPs and Au@LM NPs diameter distribution, with the average values given in Table 1.

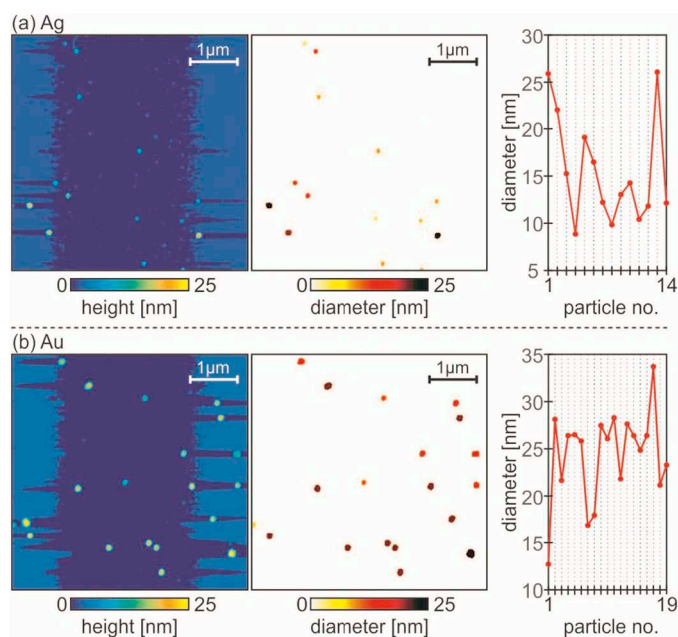


Fig. 3. Raw AFM topography image, color-coded NP diameter image, and a graph showing exact diameter values for every NP assessed from the AFM topography image for (a) Ag@LM NPs and (b) Au@LM NPs.

These values are slightly higher in comparison to those estimated by TEM measurements (Table 1). This is, however, as AFM topography maps show the size of NPs with metal core and adsorption layer. Taking into account the PSD difference between two NPs, it can be concluded that it's approximately equal to the thickness of the adsorbed L-Met layer.

3.5. DLS and zeta potential

DLS analysis enabled us to obtain the hydrodynamic PSD of Ag@LM NPs and Au@LM NPs in colloid suspension. The values obtained by DLS study are presented in Table 1, together with the electrophoretic parameters.

Concerning the PSD, it must be pointed out that the size obtained by DLS was quite bigger compared to TEM and AFM results, as usually obtained for analysis of colloidal solutions [53]. However, DLS provides better size distribution due to the higher number of analyzed particles. Moreover, DLS measures the hydrodynamic radius, i.e., the radius of the hypothetical sphere of the dispersed particles whereas TEM and AFM provide the projected surface area of the corona. It appears that the difference between these various methods represents the thickness of the diffuse layer (capping agent and solvation ions/molecules layer) on the particle corona.

Besides, DLS also provides a polydispersity index (PDI) as a measure of the heterogeneity of NPs size. The values of PDI for both dispersions suggest a high degree of their homogeneity (Table 1). The zeta potential measurements indicated that the surface of NPs was negatively charged. The obtained results were in the range of the values obtained for our previously synthesized citrate and borate capped NPs of similar size [53–55]. According to the classification of NPs based on zeta potential values, both colloid dispersions are highly stable [56]. Concerning the colloids time stability, both Ag and Au colloidal dispersions were stable for more than one year, in the alkaline medium at pH 9–11. This stability was also confirmed by measuring absorption spectra.

The surface conductivity for Ag@LM NPs is higher for more than one order of magnitude compared to Au@LM NPs due to the electro-migration of counter and co-ions of the electrical double layer (EDL) along the surface of the particle. It is in accordance with literature data, which indicates that this value is inversely proportional to the size of the particle [57,58]. Moreover, it is also in accordance with lower zeta potential value compared to Au@LM NPs.

The values of the electrophoretic mobility parameter for both colloids were slightly different, as also found for previously synthesized citrate and borate capped Ag and Au NPs [53–55]. This result is as expected since the migration of charged colloidal particles depends on their size, zeta potential, surface conductivity and stationary medium (ionic strength and pH) [56,59].

3.6. FTIR spectra

Fig. 5 compares the infrared spectra of solid L-Met with the spectra of Ag@LM NPs and Au@LM NPs. The FTIR spectrum of pure L-Met exhibited an intense and broad band at 2910 cm^{-1} assigned to -NH vibrations indicating a zwitter ion form. The bands at 1600 cm^{-1} , 1510 cm^{-1} , 1315 cm^{-1} were assigned to C=O , O-H , and C-O vibrations, respectively. The band at 542 cm^{-1} is assigned to -CSC and

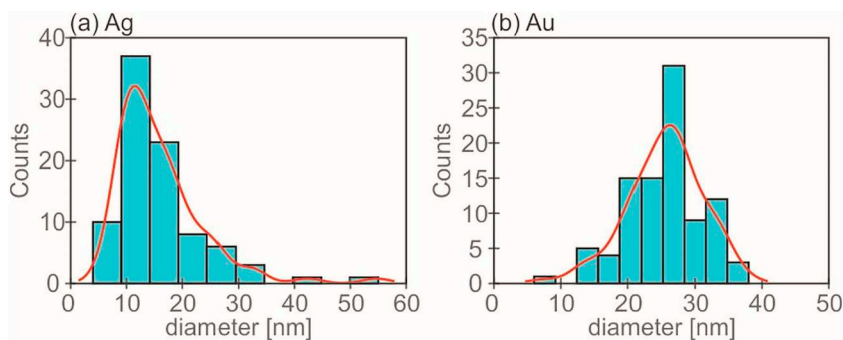


Fig. 4. Diameter distribution of (a) Ag@LM NPs and (b) Au@LM NPs.

the second one, at about 680 cm^{-1} to -SC vibration. Some bands in the range from 700 cm^{-1} to 1300 cm^{-1} were due to coupled -CH_2 vibrations [24,60].

The FTIR spectra of L-Met capped Ag and Au surface (Fig. 5 (b, b')) are identical, indicating the modification of their metal surface due to the same orientation of capping agent for both Ag@LM NPs and Au@LM NPs. They show bands characteristic for -COOH group, as well as for -SC and -CH_2 vibrations. An absence of band characteristic for -NH vibrations indicates that L-Met is attached to Ag and Au surface through an amino group. The broad band at around 3300 cm^{-1} is due to stretching vibration of -OH group, which comes from the water. The 1564 cm^{-1} , 1391 cm^{-1} , 1366 cm^{-1} bands come from a stretch of -COOH group. The band near 1006 cm^{-1} corresponds to S=O stretching vibration from an oxidation product methionine sulfoxide [26].

Bands at 826 cm^{-1} and 971 cm^{-1} were assigned to C-N vibrations

and, at 660 cm^{-1} and 700 cm^{-1} to -SC vibrations. These results indicate that L-Met molecule, more precisely, its oxidation form L-Met sulfoxide, is bound to NPs surface.

3.7. DFT calculations of L-met adsorption on Ag and Au surface

In order to make a more detailed prediction of L-Met orientation on Ag@LM NPs and Au@LM NPs surface in alkaline medium, its adsorption was modeled both as a neutral molecule and a deprotonated anion. The simplest approach, which can be used to predict the binding orientation of the organic molecules on metallic surfaces [53,61], comprises the binding of one metal atom (Ag or Au) to the selected functional groups of the investigated molecule. Calculated one-atom interaction energies are given in Table 2.

Similar trends were observed for both neutral and anionic L-Met molecule. It exhibited the strongest interaction with both Au and Ag

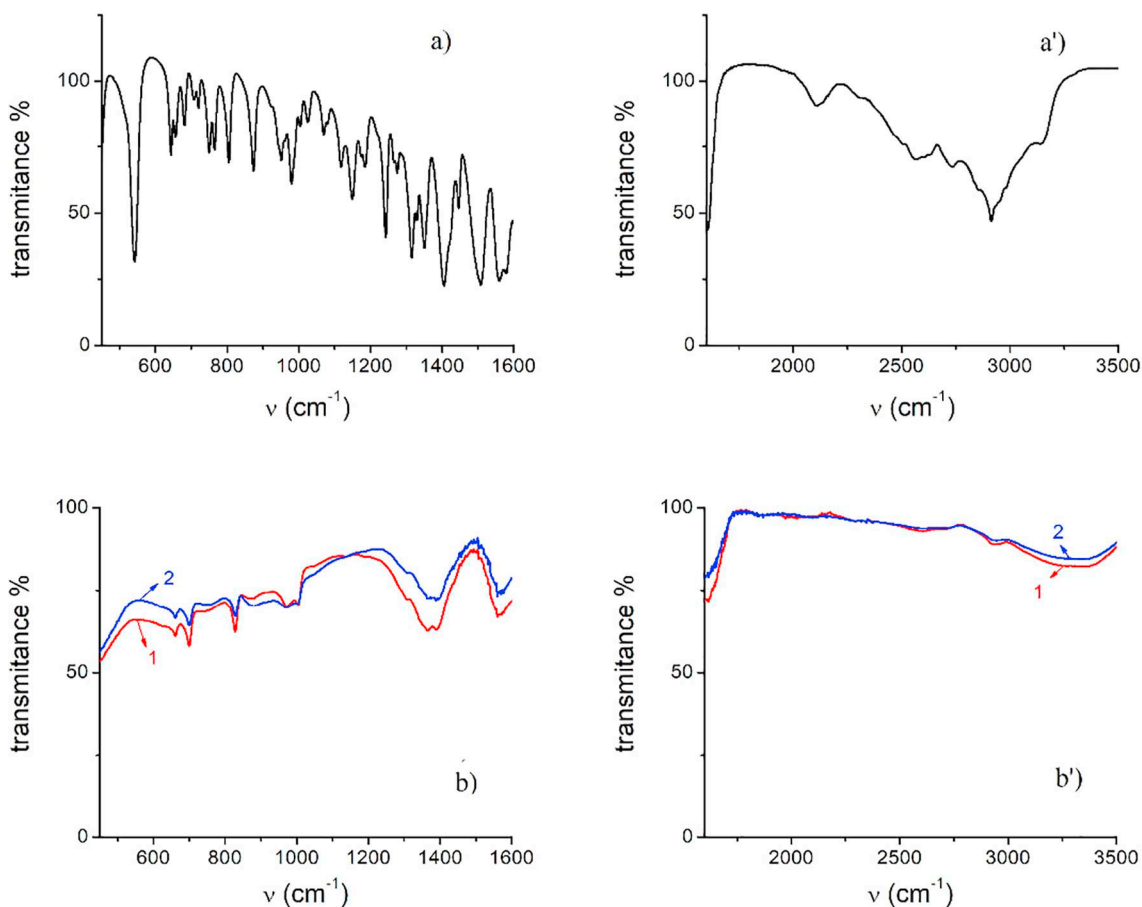


Fig. 5. FTIR spectra of solid L-Met (a, a'), and Ag@LM NPs (1) and Au@LM NPs (2) (b, b').

Table 2
Interaction energies for N, O, and S of neutral and anionic L-Met forms binding with one Ag or Au atom (light blue sphere).

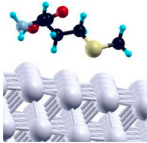
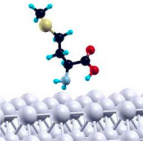
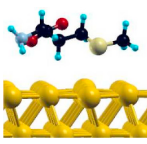
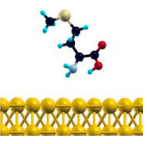
L-Met molecule form	Interaction energy (eV)			
	Ag		Au	
	Neutral	Anionic	Neutral	Anionic
N	-1.22	-1.58	-1.36	-1.63
O	Unstable	-0.33	Unstable	-0.63
S	-0.16	-0.37	-0.64	-0.47

atoms via N- atom of $-NH_2$ group. The thiol group also exhibited a remarkable interaction with one-atom models, which was stronger in the case of the anion. On the other hand, the $-COOH$ group of the neutral molecule did not bind to Ag nor Au atoms, while interaction occurred when it was deprotonated.

According to the observed results two modes for L-Met adsorption on Ag and Au surfaces are proposed on Ag111 and Au111 slabs: (1) a vertical geometry with $-NH_2$ group oriented towards the Ag and Au surface and (2) a horizontal geometry with both $-S-$ and $-NH_2$ groups in contact with the surface. Adsorption on Ag(111) and Au(111) surface slabs was investigated only for the neutral L-Met. Optimized geometries in two proposed adsorption modes and adsorption energies are given in Table 3.

Similar adsorption energies were obtained for both adsorption modes, on both Ag111 and Au111 surfaces. Somewhat weaker adsorption on Au111 compared to Ag111 is expected according to the more noble character of gold. Obtained results, in general, imply that both geometries are probable, and the resulting adsorption mode is dependent on the coverage and presence of other adsorbed species on the surface. However, FTIR results indicate that a vertical geometry with $-NH_2$ group oriented towards the surface is more realistic in both cases. Also, dissociation of the carboxyl group is expected to further increase the number of the possibilities, according to the results of one-atom model calculations that predict a favorable binding between Au

Table 3
Optimized adsorption geometries of L-Met on Ag111 and Au111 surfaces, with corresponding adsorption energies.

Ag111		
Adsorption energy (eV)	-0.43	-0.47
Au111		
Adsorption energy (eV)	-0.23	-0.25

(or Ag) atom and $-COO^-$ group of L-Met.

3.8. Toxicity assessment

The considerable potential for utilizing the Ag@LM NPs and Au@LM NPs for diagnostic and/or therapy in nanomedicine requires their toxicity to be examined. Since most substances are toxic at high doses, it is essential to examine whether they are toxic at a concentration at which they are meant to be used. We examined the toxicity of synthesized NPs in a concentration-dependent manner.

3.8.1. Genotoxic effects of Ag@LM NPs and Au@LM NPs

The genotoxic potential of Ag@LM NPs and Au@LM NPs against normal lymphocytes was determined using the CB-micronucleus assay (CB-MN), which is one of the standard genotoxicity assays recommended by ISO 10993-3 [62]. The CB-MN assay enables a reliable and precise evaluation of the presence and the extent of the DNA damage, cytostasis, and cytotoxicity [63]. In the present study, the lymphocyte cultures were treated with increasing concentrations of Ag@LM NPs and Au@LM NPs. The results obtained for lymphocytes exposed to increasing concentrations of Ag@LM NPs are presented in Table S1 (SI).

The Ag@LM NPs induced a significant concentration-dependent enhancement of the MN incidence (Fig. 6a; $F = 94.83$, $p = .000001$) and decrement of the cell proliferation potential ($F = 37.75$, $p = .000045$) compared to control. Although at investigated concentration range, a mild increase of the CBPI was observed (Fig. 6b), the obtained values were notably lower than that in control. Accordingly, the positive correlation between these parameters was obtained ($r = 0.91$, $p = .0007$). The cytotoxic/cytostatic effects of Ag@LM NPs were evaluated by determining the CBPI. As shown in Table S1, upon treatments with Ag@LM NPs the percentage of cytostasis fluctuated between $8.6 \pm 1.08\%$ (1×10^{-11} M) and $18.28 \pm 2.15\%$ (1×10^{-13} M). In other words, compared to the numbers of cells that have divided to form binucleate and multinucleate cells in the control culture, approximately 91.4% and 81.72% of this number, respectively, were viable cells that have divided in the treated cultures.

The results obtained for lymphocytes exposed to increasing concentrations of Au@LM NPs are presented in Table S2. Upon treatment of lymphocytes with Au@LM NPs, it has been shown that the tested compound did not induce any observable changes in the MN incidence compared to control (Fig. 6a). The Au@LM NPs increased the CBPI in a concentration-dependent manner ($F = 32.07$, $p = .000083$) being the most effective at the highest concentration applied (Fig. 6b). The incidence of micronuclei and cytokinesis-block proliferation index correlated inversely ($r = -0.76$, $p = .017$).

The observed concentration-dependent enhancement of cell proliferation induced by Au@LM NPs implicates a modulation of cell cycle control checkpoints. Since the maintenance of genomic integrity is ensured by DNA repair and cell cycle checkpoints, an impaired fidelity of checkpoint control may result in genomic instability [64]. We hypothesize that Au@LM NPs stimulate cell proliferation by altering the expression and/or function of the proteins that regulate cell cycle progression. These findings are in accordance with our previously published report on citrate-capped gold nanoparticles [31]. As shown in Table S2, the treatment of lymphocytes with Au@LMNPs (1×10^{-13} M) induced a cell growth inhibition in $18.64 \pm 0.62\%$ cells while treatment with other tested concentrations resulted in an increase in the proportion of dividing cells compared to control, as represented by the negative percentage of cytostasis (% cytostasis was up to -12.54%).

Generally, our experimental results show that Ag@LM NPs were more potent MN inducers than Au@LM NPs. At all investigated concentrations, the Ag@LM NPs induced a highly significant enhancement of the MN incidence ($p < .001$) compared to the values induced by Au@LM NPs.

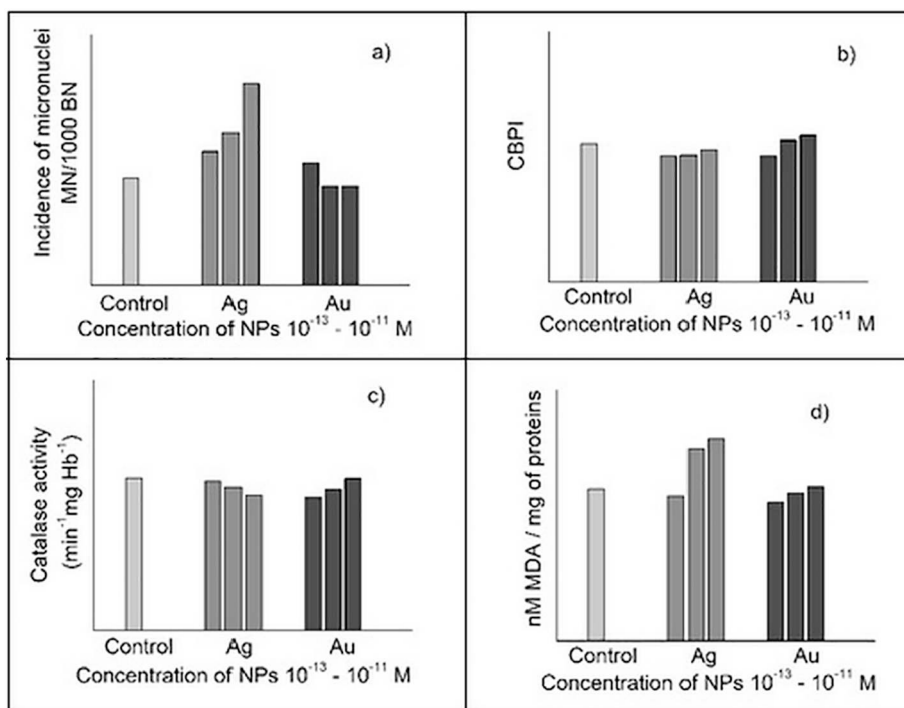


Fig. 6. Diagrams of: incidence of micronuclei (a), cytokinesis-block proliferation index (b), catalase activity (c), and level of malondialdehyde (d) in lymphocyte cultures treated with increasing concentration of Ag@LM NPs and Au@LM NPs (bars from left to right represent increasing concentrations of Ag and Au NPs, respectively).

3.8.2. Effects of Ag@LM NPs and Au@LM NPs on oxidative stress parameters

To investigate whether the Ag@LM NPs and Au@LM NPs affect the antioxidant defense system, we analyzed the activity of erythrocyte catalase in cultures treated with increasing concentrations of investigated compounds. The potency of investigated NPs to induce lipid peroxidation in the cell membrane was estimated by measuring the level of MDA.

As shown in Table S3, upon treatment with Ag@LM NPs, the catalase activity was slightly decreased compared to control (Fig. 6c). Further analysis has shown that Ag@LM NPs induced an increase of MDA levels in a dose-dependent manner, however, without statistical significance.

As shown in Table S4, the Au@LM NPs did not significantly affect the catalase activity as compared to control (Fig. 6c). The catalase activity reached the control value at the highest concentration applied. Statistical analysis of the results showed a significant negative correlation ($p < .05$) between the MN incidence and catalase activity. A concentration-dependent decrease in the MN incidence was followed by an increase in catalase activity.

Similar to the results obtained in treatments with Ag@LM NPs, in all the cultures treated with Au@LM NPs, no significant changes in MDA levels compared to control were observed (Fig. 6d).

3.9. AFM analysis of cells

The AFM measurements of cell suspensions (lymphocytes) were performed (Fig. 7), to analyze the morphology of untreated cells (panel (a)) and those treated with Ag@LM NPs and Au@LM NPs (panels (b) and (c)).

Previous AFM studies of lymphocytes have shown that the membrane of lymphocytes is smooth and the average size of cells can vary from 600 to 1500 nm [65–67]. Our analysis of the AFM measurements reveals that the height of the cells varies between 600 and 900 nm (Fig. 7). If the normal function of the cell is jeopardized (e.g., treatment with drugs or NPs), causing cell apoptosis, the morphology of cells changes, cell diameter changes dramatically, roughness, disruptions, or fragment appearance on membrane occurs [65–67]. As shown in Fig. 7,

the surface of the cell membrane stayed smooth, and there were no visible changes on cells membrane after the cells were treated with NPs.

By comparing our results with previously reported L-Met mediated NPs synthesis [22,24–26] where various additional agents were included in the synthesis process, we show that L-Met can be a good reductant and stabilizing agent at the same time. As a result, NPs with the same morphology and surface modification, both for Ag and Au, can be obtained. Toxicology of NPs with these properties was tested for the first time.

4. Conclusion

In this paper, we report the simple green method for Ag@LM NPs and Au@LM NPs synthesis, using amino acid L-Met as reducing as well as a capping agent. The obtained NPs are spherical with ~8 nm Ag@LM NPs and ~26 nm Au@LM NPs in diameter and with the same surface properties. The NPs shape and size were also confirmed using TEM and AFM measurements. Besides, FTIR and DLS measurements of PSD and electrophoretic properties confirmed the surface morphology, i.e., L-Met binding on Au and Ag surface. The DFT calculations show that the strongest interaction between metal, both Ag and Au, and L-Met is via N-atom of the amino group. The interaction with the thiol group is also noteworthy, proposing vertical and horizontal geometry of L-Met towards metal (Ag and Au) surface.

Toxicity measurements show that Ag@LM NPs induced a concentration-dependent enhancement of the MN incidence and suppression of the cell proliferation, while Au@LM NPs were characterized by concentration-dependent ability to promote cell proliferation, with no effects on MN formation. The cytotoxicity/cytostasis assessments show that treatment with Ag@LM NPs resulted in mild cell growth inhibition while Au@LM NPs treatment stimulated cell growth. The investigated NPs did not induce oxidative stress in human peripheral blood cells as revealed by their insignificant effects on catalase activity and MDA production. AFM studies of lymphocytes upon NPs treatment show that cell membrane stayed unaffected, making these NPs suitable for future studies in nano-medicine.

Further studies are warranted to examine the effects of a broader dose range of synthesized NPs, for a more clear understanding of their

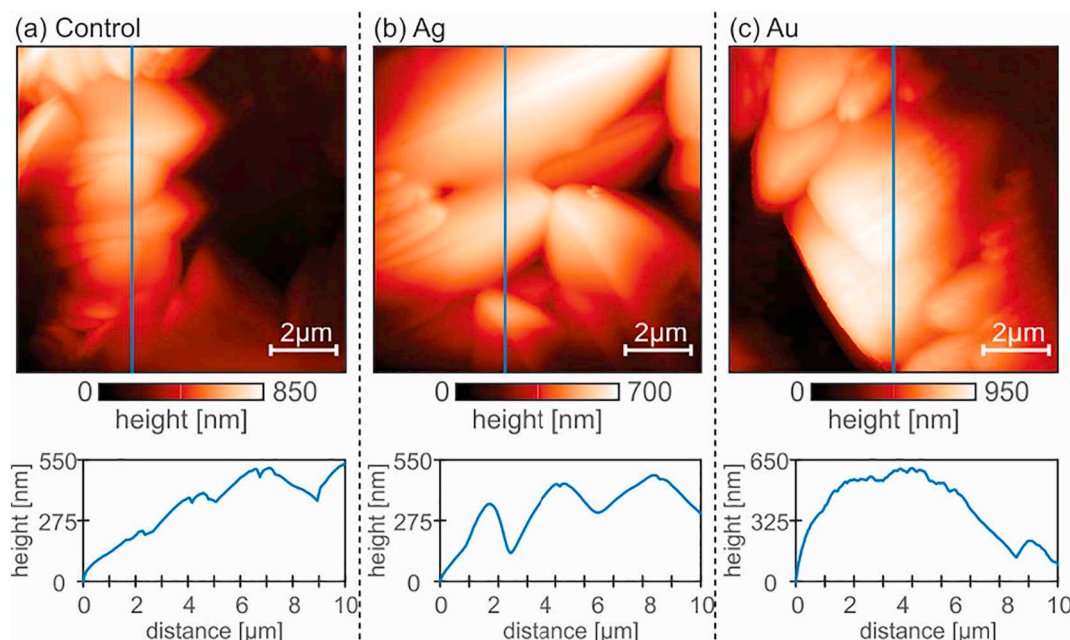


Fig. 7. AFM topography image and the profile is taken along the solid line drawn within the AFM topography image for (a) control cells, (b) cells treated with Ag@LM NPs, and (c) cells treated with Au@LM NPs.

biosafety. Based on the current knowledge, it appears that Au@LM NPs are more suitable for further studies on their potential application in nano-medicine.

Declaration of competing interest

The authors declare that they have no known competing financial interests or personal relationships that could have appeared to influence the work reported in this paper.

Acknowledgment

The authors are grateful to the Ministry of Education and Science of the Republic of Serbia (Project No. 172023 and 172045) Ministry of Education, Science and Technological Development of the Republic of Serbia (Project No. 172023 and 172045) for their financial support.

Appendix A. Supplementary data

Supplementary data to this article can be found online at <https://doi.org/10.1016/j.jinorgbio.2019.110958>.

References

- [1] T.S. Sreepasad, T. Pradeep, R. Vajtai (Ed.), Springer Handbook of Nanomaterials, Noble Metal Nanoparticles, Springer, Berlin, 2013, pp. 303–388.
- [2] X. Huang, M.A. El-Sayed, J. Adv. Res. 1 (2010) 13–28.
- [3] R.R. Arvizo, S. Bhattacharyya, R.A. Kudgus, K. Giri, R. Bhattacharya, P. Mukherjee, Chem. Soc. Rev. 41 (2012) 2943–2970.
- [4] K. Alaqad, T.A. Saleh, J. Environ. Anal. Toxicol. 6 (2016) 384.
- [5] B. Hu, S.B. Wang, K. Wang, M. Zhang, S.H. Yu, J. Phys. Chem. C 112 (2008) 11169–11174.
- [6] K.N. Thakkar, S.S. Mhatre, R.Y. Parikh, Nanomed. Nanotechnol. Biol. Med. 6 (2010) 257–262.
- [7] S. Irvani, H. Korbekandi, S.V. Mirmohammadi, B. Zolfaghari, Res. Pharm. Sci. 9 (2014) 385–406.
- [8] N.E. Motl, A.F. Smith, C.J. DeSantis, S.E. Skrabalak, Chem. Soc. Rev. 43 (2014) 3823–3834.
- [9] L. Ge, Q. Li, M. Wang, J. Ouyang, X. Li, M.M.Q. Xing, Int. J. Nanomedicine 9 (2014) 2399–2407.
- [10] E.C. Dreaden, A.M. Alkilany, X. Huang, C.J. Murphy, M.A. El-Sayed, Chem. Soc. Rev. 41 (2012) 2740–2779.
- [11] A. Rajeshwari, K. Garg, M. Elavarasi, N. Chandrasekaran, A. Mukherjee, Proc. Natl. Acad. Sci., India Sect. B: Biol. Sci. 87 (2017) 23–30.
- [12] E. Boisselier, D. Astruc, Chem. Soc. Rev. 38 (2009) 1759–1782.
- [13] Y. Li, C. Jing, L. Zhang, Y.T. Long, Chem. Soc. Rev. 41 (2012) 632–642.
- [14] F. Pu, Y. Huang, Z. Yang, H. Qiu, J. Ren, ACS Appl. Mater. Interfaces 10 (2018) 9929–9937.
- [15] T. Kunoh, M. Takeda, S. Matsumoto, I. Suzuki, M. Takano, H. Kunoh, J. Takada, ACS Sustain. Chem. Eng. 6 (2018) 364–373.
- [16] P. Bin, R. Huang, X. Zhou, Bio. Med. Res. Int. (2017) (2017) 6.
- [17] R.L. Levine, J. Moskovitz, E.R. Stadtman, IUBMB Life 50 (2008) 301–307.
- [18] L.D. Stegink, L.D. Besten, Science 178 (1972) 514.
- [19] Y. Shechter, Y. Burstein, A. Patchornik, Biochemistry 14 (1975) 4497–4503.
- [20] E.R. Stadtman, J. Moskovitz, R.L. Levine, Antioxid. Redox Signal. 5 (2003) 577–582.
- [21] A.V. Peskin, R. Turner, G.J. Maghzal, C.C. Winterbourn, A.J. Kettle, Biochemistry 48 (2009) 10175–10182.
- [22] A. Raza, S. Javed, M.Z. Qureshi, M.U. Khan, M.S. Khan, App. Nanosci. 7 (2017) 429–437.
- [23] H.V. Ehrlich, T.N. Shcherba, M.P. Zhilenko, G.P. Muraveva, G.V. Lisichkin, Russ. Chem. Bull. 61 (2012) 1705–1710.
- [24] N. Belachew, D.R. Devi, K. Basavaiah, J. Mol. Liq. 224 (2016) 713–720.
- [25] Z. Zaheer, Rafiuddin, J. Exp. Nanosci. 7 (2012) 366–377.
- [26] A. Mikalauskaite, R. Kondrotas, G. Niaura, A. Jagminas, J. Phys. Chem. C 119 (2015) 17398–17407.
- [27] R.A. de Matos, L.C. Courrol, Amino Acids 49 (2017) 379–388.
- [28] S. Kumar, K.S. Gandhi, R. Kumar, Ind. Eng. Chem. Res. 46 (2007) 3128–3136.
- [29] I. Pujalté, I. Passagne, B. Brouillaud, M. Tréguer, E. Durand, C. Ohayon-Courtès, B. L'Azou, Part. Fibre Toxicol. 8 (2011) 10.
- [30] X. Li, L. Wang, Y. Fan, Q. Feng, F. Cui, J. Nanomater. 2012 (2012) 19.
- [31] A. Vujačić, V. Vodnik, G. Joksić, S. Petrović, A. Leskovic, B. Nastasijević, V. Vasić, Digest J. Nanomater. Biostruct. 6 (2011) 1367–1376.
- [32] M.V.D.Z. Park, A.M. Neigh, J.P. Vermeulen, L.J.J. de la Fonteyne, H.W. Verharen, J.J. Briedé, H. van Loveren, W.H. de Jong, Biomaterials 32 (2011) 9810–9817.
- [33] C. Beer, R. Foldbjerg, Y. Hayashi, D.S. Sutherland, H. Autrup, Toxicol. Lett. 208 (2012) 286–292.
- [34] Law on Health Care, Official Gazette of the Republic of Serbia, Parliament of the Republic of Serbia, 2005, pp. 112–161.
- [35] M. Fenech, Mutat. Res. Fundam. Mol. Mech. Mutagen. 285 (1993) 35–44.
- [36] J. Surrallés, N. Xamena, A. Creus, J. Catalán, H. Norppa, R. Marcos, Mutat. Res. Genet. Toxicol. 341 (1995) 169–184.
- [37] Technical guideline Nr., Organization for Economic Cooperation and Development (OECD) Guideline for the Testing of Chemicals, Vitromammalian Cell Micronucleus Test, 2016, p. 487.
- [38] H. Aebi, H.U. Bergmeyer (Ed.), Methods of Enzymatic Analysis, Verlag Chemie, Academic Press Inc, Weinheim, NewYork, 1974, pp. 673–680.
- [39] O.I. Aruoma, B. Halliwell, M.J. Laughton, G.J. Quinlan, J.M.C. Gutteridge, Biochem. J. 258 (1989) 617–620.
- [40] O.H. Lowry, N.J. Rosebrough, A.L. Farr, R.J. Randall, J. Biol. Chem. 193 (1951) 265–275.
- [41] G. Paolo, et al., J. Phys. Condens. Matter 21 (2009) 395502.
- [42] N. Marzari, D. Vanderbilt, A. De Vita, M.C. Payne, Phys. Rev. Lett. 82 (1999) 3296–3299.
- [43] J.P. Perdew, K. Burke, M. Ernzerhof, Phys. Rev. Lett. 77 (1996) 3865–3868.

- [44] G.J. Martyna, M.E. Tuckerman, *J. Chem. Phys.* 110 (1999) 2810–2821.
- [45] H.J. Monkhorst, J.D. Pack, *Phys. Rev. B* 13 (1976) 5188–5192.
- [46] A. Kokalj, *J. Mol. Graphics Modell.* 17 (1999) 176–179.
- [47] A.V. Vujačić, J.Z. Savić, S.P. Sovilj, K. Mészáros Szécsényi, N. Todorović, M.Ž. Petković, V.M. Vasić, *Polyhedron* 28 (2009) 593–599.
- [48] M.D. Đurović, Ž. Bugarčić, F.W. Heinemann, R. van Eldik, *Dalton Trans.* 43 (2014) 3911–3921.
- [49] H.H. Deng, L.N. Zhang, S.B. He, A.L. Liu, G.W. Li, X.H. Lin, X.H. Xia, W. Chen, *Biosens. Bioelectron.* 65 (2015) 397–403.
- [50] M.K. Alqadi, O.A.A. Noqtah, F.Y. Alzoubi, J. Alzoubi, K. Aljarrah, *Mater. Sci.-Poland* 32 (2014) 107–111.
- [51] S.W. Bian, I.A. Mudunkotuwa, T. Rupasinghe, V.H. Grassian, *Langmuir* 27 (2011) 6059–6068.
- [52] Z. Zhong, J. Luo, T.P. Ang, J. Highfield, J. Lin, A. Gedanken, *J. Phys. Chem. B* 108 (2004) 18119–18123.
- [53] B. Laban, I. Zeković, D. Vasić-Aničijević, M. Marković, V. Vodnik, M. Luce, A. Gricenti, M. Dramićanin, V. Vasić, *J. Phys. Chem. C* 120 (2016) 18066–18074.
- [54] B. Laban, V. Vodnik, M. Dramićanin, M. Novaković, N. Bibić, S.P. Sovilj, V.M. Vasić, *J. Phys. Chem. C* 118 (2014) 23393–23401.
- [55] A. Vujačić, V. Vasić, M. Dramićanin, S.P. Sovilj, N. Bibić, S. Milonjić, V. Vodnik, *J. Phys. Chem. C* 117 (2013) 6567–6577.
- [56] S. Bhattacharjee, *J. Control. Release* 235 (2016) 337–351.
- [57] P. Leroy, N. Devau, A. Revil, M. Bizi, *J. Colloid Interface Sci.* 410 (2013) 81–93.
- [58] P. Leroy, C. Tournassat, M. Bizi, *J. Colloid Interface Sci.* 356 (2011) 442–453.
- [59] R. Xu, *Particuology* 6 (2008) 112–115.
- [60] A. Jagminas, A. Mikalauskaitė, V. Karabanovas, J. Vaičiūnienė, *Beilstein J. Nanotechnol.* 8 (2017) 1734–1741.
- [61] R. Binaymotlagh, H. Farrokhpour, H. Hadadzadeh, S.Z. Mirahmadi-Zare, Z. Amirghofran, *J. Phys. Chem. C* 121 (2017) 8589–8600.
- [62] ISO 10993-3, Biological evaluation of medical devices part 3: tests for genotoxicity, carcinogenicity and reproductive toxicity, Retrieved from, 2014. <https://www.iso.org/standard/55614.html>.
- [63] M. Fenech, *Nat. Protoc.* 2 (2007) 1084–1104.
- [64] T. Weinert, *Cell* 94 (1998) 555–558.
- [65] M. Hu, J. Wang, H. Zhao, S. Dong, J. Cai, *J. Biomech.* 42 (2009) 1513–1519.
- [66] Y. Wu, H. Lu, J. Cai, X. He, Y. Hu, H. Zhao, X. Wang, *Nanoscale Res. Lett.* 4 (2009) 942–947.
- [67] X. Huang, J. He, M. Liu, C. Zhou, *Nanoscale Res. Lett.* 9 (2014) 518.



Full Length Article

Low-friction, wear-resistant, and electrically homogeneous multilayer graphene grown by chemical vapor deposition on molybdenum

Borislav Vasić^{a,*}, Uroš Ralević^a, Katarina Cvetanović Zobenica^b, Milče M. Smiljanić^b, Radoš Gajić^a, Marko Spasenović^b, Sten Vollebregt^c

^a Graphene Laboratory of Center for Solid State Physics and New Materials, Institute of Physics Belgrade, University of Belgrade, Pregrevica 118, 11080 Belgrade, Serbia

^b Center of Microelectronic Technologies, Institute of Chemistry, Technology and Metallurgy, University of Belgrade, Njegoševa 12, 11000 Belgrade, Serbia

^c Department of Microelectronics, Delft University of Technology, Feldmannweg 17, 2628CT Delft, the Netherlands



ARTICLE INFO

Keywords:

Graphene
Chemical vapour deposition
Atomic force microscopy
Friction
Wear
Electrical properties

ABSTRACT

Chemical vapour deposition (CVD) is a promising method for producing large-scale graphene (Gr). Nevertheless, microscopic inhomogeneity of Gr grown on traditional metal substrates such as copper or nickel results in a spatial variation of Gr properties due to long wrinkles formed when the metal substrate shrinks during the cooling part of the production cycle. Recently, molybdenum (Mo) has emerged as an alternative substrate for CVD growth of Gr, mainly due to a better matching of the thermal expansion coefficient of the substrate and Gr. We investigate the quality of multilayer Gr grown on Mo and the relation between Gr morphology and nanoscale mechanical and electrical properties, and spatial homogeneity of these parameters. With atomic force microscopy (AFM) based scratching, Kelvin probe force microscopy, and conductive AFM, we measure friction and wear, surface potential, and local conductivity, respectively. We find that Gr grown on Mo is free of large wrinkles that are common with growth on other metals, although it contains a dense network of small wrinkles. We demonstrate that as a result of this unique and favorable morphology, the Gr studied here has low friction, high wear resistance, and excellent homogeneity of electrical surface potential and conductivity.

1. Introduction

Chemical vapour deposition (CVD) is the most dominant method for fabrication of large-area single- and few-layer graphene (Gr) films on various metallic substrates (catalysts) [1–4]. After the growth, Gr films are transferred onto desired substrates that allow practical use [5,6]. The main advantages of CVD over other fabrication techniques are its relative simplicity, low cost, and industrial applicability [7–9]. Still, CVD growth and Gr transfer yield films with defects such as grain boundaries [10–16], wrinkles [17–23] and cracks. Formation of wrinkles, for example, occurs due to a large difference in thermal expansion coefficients of Gr and the catalytic substrate, which results in different shrinking rates during cooling at the end of the CVD growth process. Wrinkles in Gr have been shown to be highly detrimental to the mechanical robustness and electrical homogeneity of graphene [23]. CVD graphene is prone to formation of defects both on most commonly used catalytic metal substrates such as copper [1–3] and nickel [4], as well as on less traditional substrates such as ruthenium, iridium, and platinum [9].

Recently, Gr grown by CVD on thin molybdenum (Mo) films

sputtered on silicon wafers [24–26] has emerged as an alternative to Gr grown on traditional metal substrates. Growth on Mo offers several advantages. Namely, the thermal expansion coefficient of Mo is well matched to that of Gr, supporting wrinkle-free growth [25]. Also, Mo has a high melting point, resulting in less restructuring of the Mo substrate compared to copper during the CVD process. Finally, low solubility of carbon in bulk Mo facilitates easy growth of Gr layers [24], making the process attractive for high-volume applications. In addition to the advantages for growth, graphene on a thin sputtered layer of Mo has advantages for subsequent processing. The Mo layer can be patterned prior to growth, enabling patterning of CVD graphene without post-growth lithography, and the Mo can be easily removed once Gr is grown on it, which allows transfer-free fabrication of Gr devices that is compatible with CMOS processes [27,28]. Graphene grown with this novel process was shown to have applications in anti-corrosion coatings [29–31], gas [27,32] and pressure sensors [28]. Although Gr grown on Mo has high potential for practical use, the relation between microscopic morphology, distribution and geometry of wrinkles, and their influence on the mechanical and electrical properties of the material have not yet been studied.

* Corresponding author.

E-mail address: bvasic@ipb.ac.rs (B. Vasić).

Using atomic force microscopy (AFM) based methods, here we present nanoscale analysis of the morphology, mechanical and electrical properties of few-layer Gr grown by CVD on Mo. We demonstrate that the material contains very few wrinkles and that those wrinkles have dimensions that are much smaller than those typically encountered in Gr grown on copper foils. Gr grown on Mo has low friction and high wear resistance as demonstrated by friction force microscopy and nanoscale wear tests. Using Kelvin probe force microscopy (KPFM) and conductive AFM (c-AFM) we show that this material has high uniformity of the Fermi level (work function) and electrical conductivity, respectively, over large areas. These results allude to strong potential uses of Gr grown on Mo for both mechanical and electrical applications such as ultrathin solid lubricants, electrodes and membranes for nano and microelectromechanical systems.

2. Experimental

2.1. Graphene fabrication and transfer

We studied both Gr on Mo as grown, as well as Gr transferred from Mo to Si/SiO₂. The 50 nm thick Mo catalyst was deposited using magnetron sputter coating on top of a Si/SiO₂ wafer (p-type, 10 cm, (1 0 0) orientation). SiO₂ was approximately 600 nm thick and it was grown using wet thermal oxidation. The Mo target purity was 99.95%. Gr was deposited using an AIXTRON Blackmagic Pro system at 915 °C using 960/40/25 sccm of Ar/H₂/CH₄ at 25 mbar for 30 min and cooled to room temperature under an Ar atmosphere. After this, the wafers were cut into smaller dies for sample preparation. Further details of the CVD growth of Gr on Mo can be found in our previous paper [25].

Graphene was transferred by first immersing dice of Gr on wafer in 30% hydrogen-peroxide for 25 min. Hydrogen peroxide etches away the Mo underneath the Gr layer and Gr is released, floating on the surface of the hydrogen peroxide solution. Gr was transferred into a Petri dish, 5 cm in diameter and 17 ml of volume, with H₂O₂. Hydrogen peroxide was exchanged with deionized (DI) water. The DI water was exchanged three times to ensure complete removal of peroxide. Gr was then carefully picked up onto a Si/SiO₂ wafer die. The sample was dried at room temperature for 25 min, and was put under a glass bell for the next 24 h to dry completely.

2.2. AFM and Raman characterization

All AFM measurements were performed with an NTEGRA Spectra system at ambient conditions. Morphology was measured in tapping AFM mode with NSG01 probes. The surface roughness was measured across ten 50 × 50 μm² areas, calculated as the root-mean square of the height distributions, and then averaged. Phase lag of the AFM probes was measured simultaneously with topography in order to achieve better contrast of small topographic features and to check for possible changes in material contrast on the sample surface.

Wear tests were done in contact AFM mode on 5–10 different 10 × 10 μm² areas with diamond coated probes DCP20. In order to initiate Gr wear, the normal load was kept constant during scanning within 1 μm wide parallel stripes and increasing in steps of around 1 μN from stripe to stripe, for a total range between 0.5 μN and 5 μN [23]. During the wear tests, we recorded the lateral forces in both forward and backward directions. These forces correspond to the lateral torsion of the AFM cantilever due to the AFM tip-Gr friction. The friction force was determined as the half-difference between the lateral force in the forward and backward direction. The normal force was calculated according to force–displacement curves, whereas the friction force was calibrated on a standard Si grating [33].

Kelvin probe force microscopy (KPFM) and Pt coated NSG01/Pt probes were employed in order to measure local electrical surface potential. KPFM is a two-pass AFM-based measurement technique which returns a local contact potential difference (CPD) between a metallic

AFM tip and the sample surface. The topographic profile of the sample was measured in the first pass. In the second pass, the AFM probe was lifted by 20 nm and scanned along the same topographic line as in the first pass, while a sum of DC and variable AC voltages was applied between the probe and the sample. The role of the AC voltage was to electrically excite probe oscillations, while the DC voltage was controlled by the AFM feedback loop in order to nullify these oscillations. The value of DC voltage which nullifies AFM probe oscillations is equal to the local CPD between the AFM tip and the sample.

Since CPD is equal to the difference between the work functions of the AFM tip (WF_{tip}) and the sample (WF_{sample}), in order to find the absolute value of WF_{sample}, the WF_{tip} of the Pt coated AFM probes was calibrated on a HOPG sample with a well known work function of 4.6 eV [34]. Measurements on HOPG yielded WF_{tip} = 5 eV. The work functions of the Gr samples were calculated as WF_{Gr} = CPD – WF_{tip}. As in the case of the surface roughness and wear tests, the CPD was measured on 5–10 different areas (50 × 50 μm² in the case of Gr grown on Mo, and 30 × 30 μm² on Gr transferred on SiO₂) and then averaged.

Conductive AFM (C-AFM) with highly doped diamond coated probes DCP20 was used for characterization of local conductivity. In C-AFM, during standard topographic imaging in AFM contact mode, a DC voltage in a range between 1 V and 2 V was applied between the probe and the sample. The resulting DC current through the AFM probe, proportional to the local conductivity of Gr samples, was simultaneously measured with a built-in current amplifier. In order to avoid wear of AFM tips and achieve reliable current measurements, C-AFM was done using diamond coated DCP20 probes which were heavily doped by nitrogen. The diamond coating provides the robustness and wear resistance of AFM tips, while the high doping makes them highly conductive. As a result, these probes enabled reliable current mapping in contact AFM mode.

Raman imaging of CVD Gr transferred on Si/SiO₂ was performed on the same NTEGRA Spectra module equipped with a confocal Raman system (NA 0.7). Raman maps were measured with a step of 0.5 μm. The wavelength of the excitation laser was 532 nm.

3. Results and discussion

3.1. Morphology

3.1.1. CVD Gr on Mo

The topography of CVD Gr on Mo is depicted in Fig. 1 on two different length scales. One of the main motivations and potential benefits of CVD on Mo is the growth of wrinkle-free Gr since the thermal expansion coefficient of Mo is much better matched to that of Gr than the thermal expansion coefficients of copper or nickel. Indeed, in these topographic images there are no long wrinkles typically observed in traditional CVD Gr grown on copper.

Still, very short wrinkles can sometimes be observed on small-scale

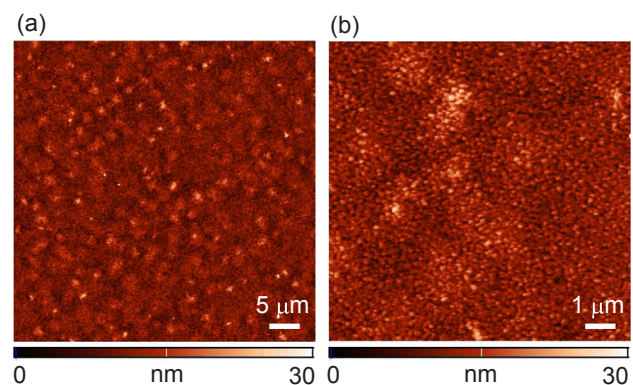


Fig. 1. Morphology of CVD Gr on Mo: (a) 50 × 50 μm² and (b) 10 × 10 μm² area.

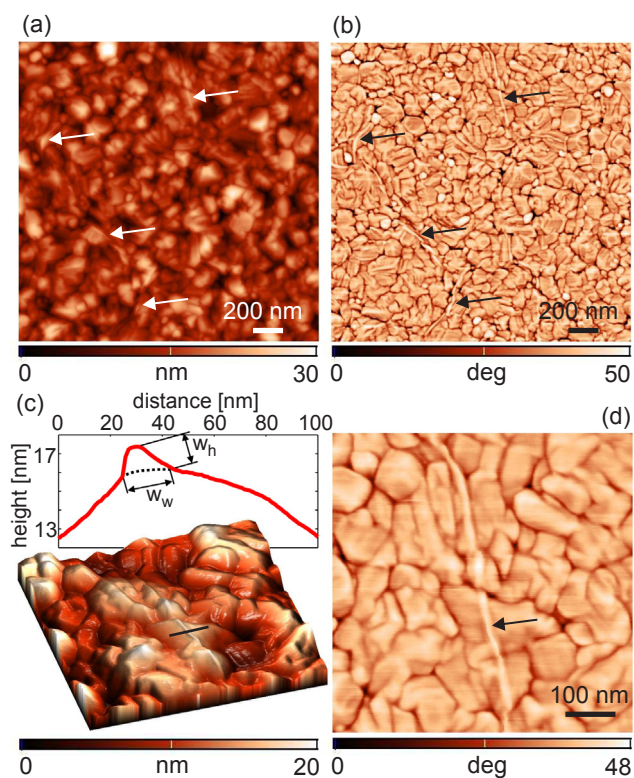


Fig. 2. Wrinkles in CVD Gr on Mo: (a) topography and (b) phase of $2 \times 2 \mu\text{m}^2$ area. (c) Three-dimensional topography and (d) phase of $0.6 \times 0.6 \mu\text{m}^2$ area. Wrinkles are marked by arrows. The inset in part (c) depicts the topographic cross-section across the wrinkle, along the solid line. The dotted line is a guide to the eye which follows the surface of the grain in order to emphasize the wrinkle geometry.

images. A typical example is presented in the topographic and phase images in Figs. 2(a) and 2(b), respectively. Usually it is difficult to recognize wrinkles in topographic images since they are very small. On the other hand, wrinkles can be resolved in the phase image as elongated, curved lines, several hundreds of nanometers long (denoted by arrows). By using the position of wrinkles found from the phase image to carefully search the topographic map, one can identify bright and narrow lines indicating that here Gr is locally wrinkled. The local Gr wrinkling is best visualized if we further zoom into an area containing a single wrinkle, as illustrated in Figs. 2(c) and 2(d), with the three-dimensional topographic and phase image, respectively. The inset in part (c) depicts the height profile across the wrinkle. Its width w_w and height w_h are around 20 nm and 1.5 nm, respectively.

Surface roughness of Gr calculated from large-scale images such as from Fig. 1(a) was 2.9 ± 0.1 nm (averaged over ten $50 \times 50 \mu\text{m}^2$ areas). Lower roughness could be achieved by using Mo foils as substrates [26], but foils are not compatible with semiconductor technologies. Therefore, we have considered Gr grown on thin films such as sputtered Mo, which is fully compatible with CMOS processing [27,28].

The roughness of Gr originates from patches with slightly increased height and from the grain structure of the underlying substrate. Gr patches in topographic images in Fig. 1 look like brighter domains, with a lateral size of several microns, and a height of several nanometers. A high-resolution image of an $2 \times 2 \mu\text{m}^2$ area, depicted in Fig. 2(a), reveals that Gr follows the morphology of the underlying Mo substrate while the grain structure of Mo is imprinted and replicated onto Gr. As a result, the grain structure of Mo dominates the measured topography thus contributing to increased surface roughness. It should be emphasized that as deposited Mo is very flat with sub-nm roughness. However, the Mo turns into Mo_2C upon exposure to CH_4 before the Gr formation starts [26], and due to this recrystallization into Mo_2C , the roughness

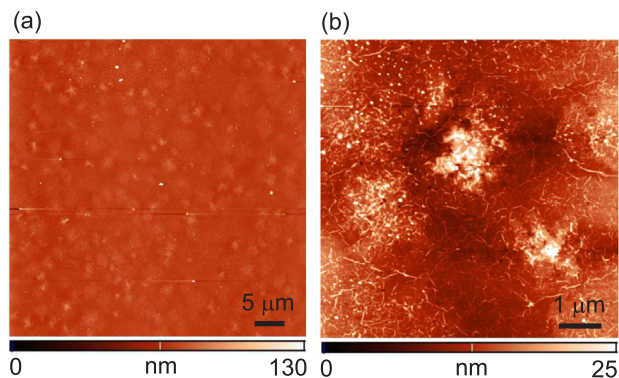


Fig. 3. Morphology of CVD Gr on SiO_2 : (a) $50 \times 50 \mu\text{m}^2$ and (b) $7 \times 7 \mu\text{m}^2$ area.

increases.

Grain structure and especially grain boundaries are even better visualized in the corresponding phase image in Fig. 2(b). Since the phase signal is generally very sensitive to sudden and sharp topographic features such as hills (grains) or narrow holes (grain boundaries), it can be used for their visualization with even better resolution than in pure topographic images. As can be seen, the shape of grains is rather irregular, with an average grain diameter of around 100 nm. The auto-correlation function of the height distribution (not-shown here) is isotropic, indicating that on average, there is no preferential in-plane anisotropy of the grain structure.

3.1.2. CVD Gr on SiO_2

The morphology of CVD Gr transferred on SiO_2 is presented in Fig. 3. The calculated surface roughness was 3.8 ± 1 nm (averaged over ten $50 \times 50 \mu\text{m}^2$ areas). Therefore, the roughness slightly increased after the transfer mainly because micron-size patches with a slightly increased height were more evident than in the previous case of Gr on Mo. In addition, Gr on SiO_2 has a rather dense network of short wrinkles as depicted in Fig. 3 and it contains nano-particles, represented by bright, isolated point-like features in Fig. 3(a), which are most probably residues from the transfer process.

As mentioned above, Mo thin films as substrates allow transfer-free Gr fabrication, thus making the fabrication simpler and compatible with semiconductor technologies [27,28]. Here we consider Gr transferred on SiO_2 because it facilitates characterization and analysis, but it should be emphasized that the chemical treatment is the same in both cases (i.e. Gr is immersed in hydrogen-peroxide in both cases, the only difference is that in the transfer-free approach, the original growth substrate is reused, whereas during the transfer, another substrate is used for picking Gr up). Therefore, the results presented here hold for transfer-free Gr as well.

Short Gr wrinkles observed in Fig. 3(b) are better visualized in the small-scale images in Fig. 4(a) and 4(b). The typical height profile of a wrinkle is depicted in Fig. 3(c), whereas the distributions of wrinkle widths and heights are given in Fig. 4(d). The height can be fitted with a linear function of the width. According to Ref. [20], there are three classes of wrinkle geometry: ripples, standing collapsed wrinkles and folded wrinkles. Since the wrinkle width in our case is less than ~ 50 nm, they have the geometry of ripples, while higher wrinkles are most probably standing collapsed ones. This is a significant difference compared to CVD Gr grown on copper [23] where thermally induced wrinkles are much wider, up to several hundreds of nanometers, and belong to the class of folded wrinkles. On the Gr studied here, wrinkles are generally short, most of them with lengths in the range 100 – 200 nm. They do not have any preferential direction, while shorter wrinkles are usually curved. These wrinkles appear during transfer onto SiO_2 . According to wrinkle lengths, shapes, and their mutual distances, it seems that they correspond to grain boundaries of Gr on Mo - narrow, irregular and curved domains along which Gr on Mo

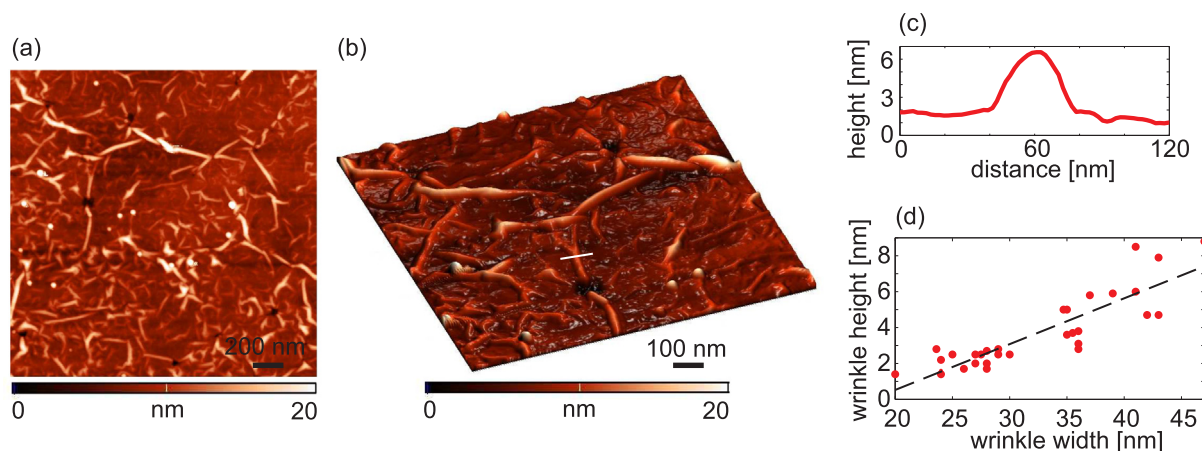


Fig. 4. Wrinkles in CVD Gr on SiO₂: (a) two-dimensional topographic image of $2 \times 2 \mu\text{m}^2$ area, and (b) three-dimensional $1 \times 1 \mu\text{m}^2$ area, (c) the height profile of the wrinkle along the solid line in part (b), and (d) the distribution of wrinkle widths and heights from part (c). The dashed line in the distribution plot is a linear fit.

was locally bent and corrugated. The different wrinkle type of Gr grown on Mo compared to that grown on copper is the most probable reason for improved mechanical and electrical properties, as will be discussed in the following sections.

3.2. Raman analysis

Further characterization of CVD Gr transferred on SiO₂ was done by combined AFM and Raman mapping. The results are presented in Fig. 5 with the topography (part (a)), integrated Raman intensity (part (b)), the ratio between the intensity of G and 2D Raman modes (part (c)), and Raman spectra taken at three representative points (part (d)). As can be seen, the characteristic Raman modes of Gr, G (around

1586 cm^{-1}) and 2D (around 2700 cm^{-1}) modes are clearly resolved. Still, the appearance of the defect mode D (around 1350 cm^{-1}) indicates non-negligible defects in CVD Gr. The 2D peak is slightly shifted to longer wavenumbers which indicates that the considered CVD Gr is multi-layered. The ratio G/2D is in the range between 0.5 and 0.7, which corresponds to a thickness of 4–6 layers [35]. The same thickness is confirmed by AFM measurements as shown in Fig. S1 of Supplementary material. By comparing encircled domains in all maps, most of the patches with increased height correspond to domains with decreased total Raman intensity and increased G/2D ratios. Therefore, the number of Gr layers is locally increased within those patches. Still, some patches where the G/2D ratio is not increased (or has even slightly decreased) likely contain just locally wrinkled and/or folded layers. Raman spectra

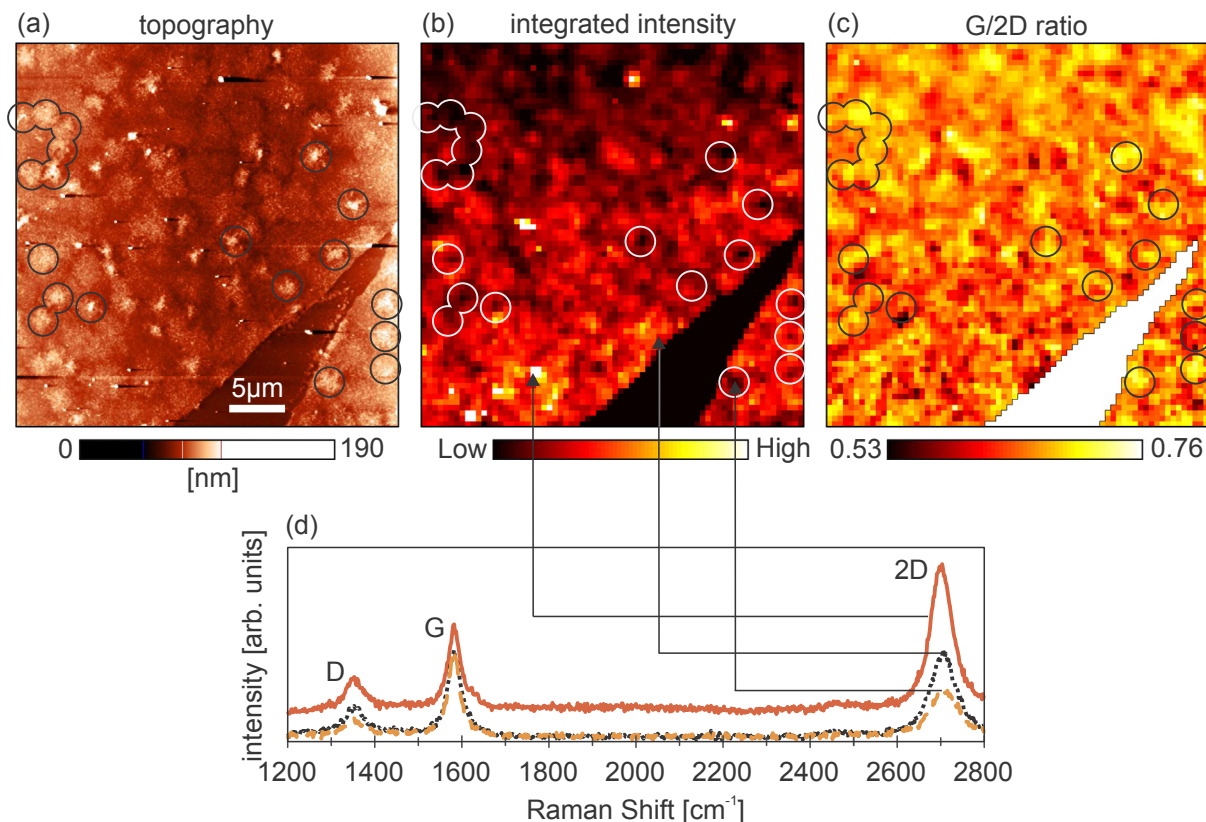


Fig. 5. (a) Topography, (b) total Raman intensity integrated between 1200 cm^{-1} and 2800 cm^{-1} , (c) the ratio between the intensity of G and 2D Raman modes, and (d) Raman spectra measured at three points marked in part (b).

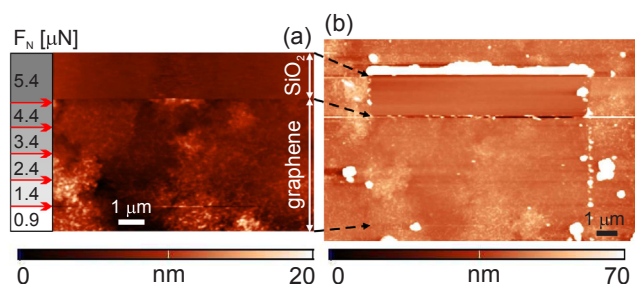


Fig. 6. Wear test: (a) topography during scratching in AFM contact mode, and (b) topography of enlarged area measured in tapping AFM mode after scratching. The value of the normal load is presented on the left side of part (a). The arrows in part (a) mark positions where the normal load was increased.

of samples stored in ambient conditions for over two years reveal no deterioration due to aging.

3.3. Friction and wear properties

Wear tests were done by scratching CVD Gr on SiO₂ in contact AFM mode. The results are presented in Figs. 6(a) and 6(b), that depict topography obtained during scratching and an enlarged topographic image recorded in tapping mode after scratching, respectively. The scratching was done from the bottom to the top. The normal load was increased in a range starting from 0.9 μN applied to the bottom Gr stripe with 1 μm width, to 5.4 μN applied on the top of the image where tearing occurred. The points where the normal load was increased are marked by arrows in Fig. 6(a). When the normal load reached a threshold value of 5.4 μN, Gr started to tear. The moment of tearing is clearly visible as a sudden change in the contrast of both topographic images in Fig. 6. The normal load was then kept at a high value, while Gr was peeled off by the AFM probe within the scan area. The area where Gr was peeled off is apparent in Fig. 6(b) as a rectangular stripe with bare SiO₂. Peeled Gr was rolled and deposited at the top of this domain, where scratching was stopped, and it is visible as a bright and narrow horizontal stripe.

The same wear experiment was repeated on five different areas of the Gr sample. The results were similar in all cases - sudden Gr tearing at a high enough normal load, while the threshold normal force needed for Gr tearing varied in the range 3.4 – 5.4 μN. The mechanism of Gr tearing can be explained in the following way. High normal forces applied by the AFM tip during wear test lead to plastic deformations of Gr beneath the tip [36]. The plastic deformations are characterized with various defects, mostly by vacancy defects, which degrade the mechanical properties of Gr and its breaking strength [37]. By increasing normal force, Gr becomes more defective while the breaking strength of Gr becomes very small, which results in Gr fracture and tearing. The average threshold force for the tearing of CVD Gr considered here is around 4 μN and it is much higher, at least by an order of magnitude, than in CVD Gr grown on copper and transferred on SiO₂, where Gr tearing was always initiated from long and wide, thermally grown wrinkles, for normal loads less than 0.5 μN [23] and sometimes already at around 100 nN [38]. Although in the former cases single-layer Gr samples were considered, the wear resistance of CVD Gr grown on Mo seems to be higher because of the different type of wrinkles in CVD Gr grown on Mo. Here they are small and narrow (simple ripples [20]) and can be easily pressed by the AFM tip without tearing, while the Gr sheet is simultaneously just locally flattened.

The lateral force recorded during the scratching test is displayed in Fig. 7(a). The force increases with the normal load in stepwise fashion before Gr tearing. The friction force was calculated according to the lateral force recorded in forward and backward directions. The friction map is depicted in Fig. 7(b), whereas the corresponding histogram is presented in Fig. 7(c). The friction map is characterized by two distinct

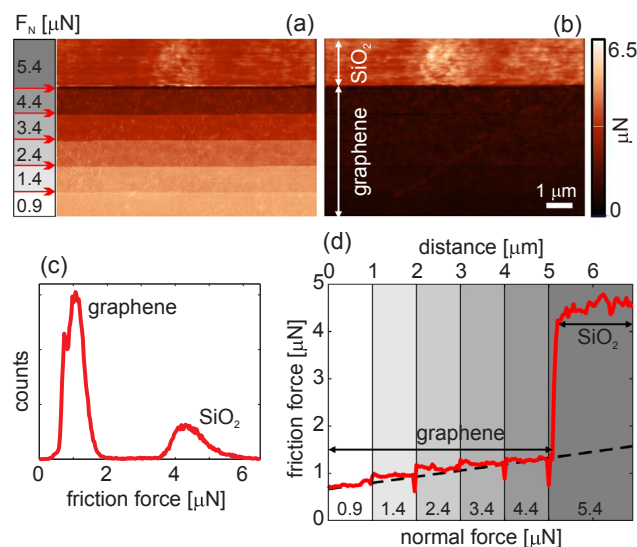


Fig. 7. Friction during the wear test: (a) lateral force map and (b) corresponding friction map during the scratching experiment from Fig. 6, (c) histogram of the friction map, and (d) the average vertical profile of the friction force map. The averaging was applied in order to filter out noise and better present stepwise increase of the friction force. The dashed line in part (d) is a linear fit to the stepwise increasing friction force during the scratching of Gr. The slope of this curve corresponds to the friction coefficient of Gr.

domains: the bottom part with low friction on Gr covered SiO₂ and the top part with high friction on bare SiO₂. According to the histogram, friction on Gr is more than 4 times smaller than on SiO₂, indicating good lubrication properties of Gr.

The average profile of the friction map along the vertical direction is given in Fig. 7(d). The friction force increases stepwise with the normal load. When the threshold force for Gr tearing is reached, the friction increases abruptly and stays at a constant level representing friction on bare SiO₂. The initial stepwise increase of the friction can be approximated by a linear function represented by the dashed line in Fig. 7(d). The slope of this linear curve is the ratio between the friction force and applied normal load and it yields a friction coefficient of Gr of only 0.13. This value is similar to that obtained earlier for Gr grown on copper and nickel [39]. Friction is also influenced by defects in Gr [40], mainly by exposed Gr edges and wrinkles, which lead to increased friction [38,41]. As mentioned above, the considered CVD graphene is almost free of cracks and exposed edges. At the same time, friction maps (the typical one shown in Fig. 7(b)) do not show increased friction due to Gr wrinkles, because they are small and narrow and could be easily pressed by the AFM tip. According to these results, CVD Gr grown on Mo could be an excellent choice for making large-scale and ultrathin solid lubricants with increased wear resistance for friction [39,42,43] and wear reduction [36,44–46] of underlying substrates.

3.4. Electrical surface potential

3.4.1. CVD Gr on Mo

Homogeneity of electrical surface potential was investigated by KPFM. Topography of CVD Gr on Mo and the corresponding CPD map are given in Figs. 8(a1) and (a2), respectively, whereas the histogram of the CPD map is shown in Fig. 8(a3). The histogram contains a single, narrow peak indicating that the measured CPD is rather uniform over a wide 50 × 50 μm² area. Averaged CPD (taking into account 10 different areas) was 352 ± 6 mV. The absolute value of the work function of the considered CVD Gr on Mo is thus 4.66 eV. The maximal half-width of all CPD maps measured on 50 × 50 μm² areas was only around 5 mV, indicating a very uniform electrical surface potential distribution. Still, CPD maps clearly show irregularly shaped potential puddles. The

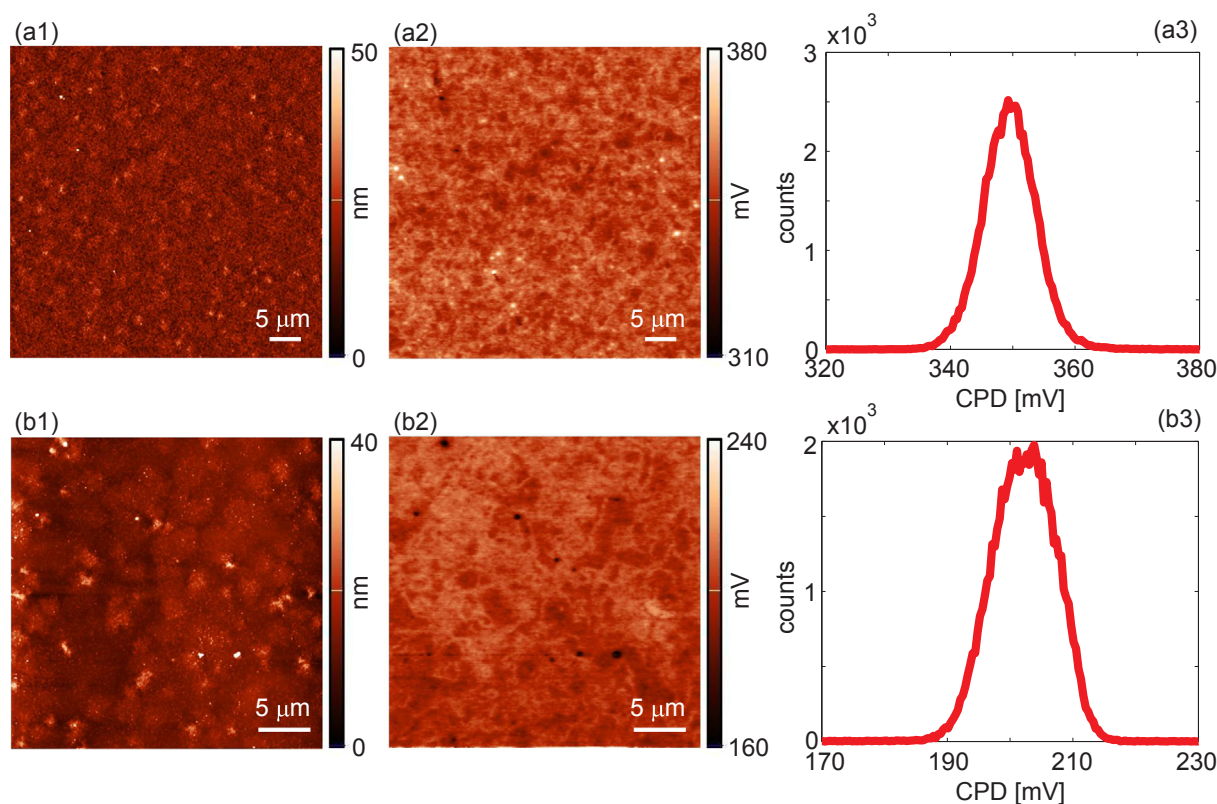


Fig. 8. (a1) Morphology of CVD Gr on Mo, (a2) the corresponding CPD map measured by KPFM, and (a3) the histogram of the CPD map. (b1) Morphology of CVD Gr transferred on SiO₂, (b2) the corresponding CPD map measured by KPFM, and (b3) the histogram of the CPD map.

potential between adjacent puddles varies by several mV, while their lateral shapes can not be related to any morphological features such as patches with increased height. Similar electron-hole puddles have been already observed in graphene [47–50] due to charge impurities in the substrate, intercalated between Gr and the substrate, or due to intrinsic ripples in Gr.

3.4.2. CVD Gr on SiO₂

Similar analysis of the distribution of electrical surface potential was done for CVD Gr transferred on SiO₂. The results are given in Fig. 8(b) representing 30 × 30 μm² topographic and KPFM images (parts (b1) and (b2), respectively), and the CPD histogram (part (b3)). CPD maps exhibit similar features as in the previous case, with a very flat surface potential, implying that CVD Gr on SiO₂ is electrically homogeneous. Since wrinkles are narrow and small, Gr is free of wrinkle-induced potential variations previously observed in other forms of CVD Gr [23,21,22]. However, small and irregular charge puddles are still present, as in the case on Mo. The average CPD was 205 ± 4 mV, thus giving the absolute value of the work function of Gr transferred on SiO₂ of 4.8 eV. Therefore, there was a small difference of around 0.14 eV between the work functions of Gr on Mo and SiO₂. In the former case, Gr was most probably not thick enough to completely screen an electric field originating from the underlying Mo with a lower work function than Gr. As a result, the work function of Gr on Mo was slightly decreased. A second possibility is that Mo dopes the Gr by charge transfer, again lowering its work function [51,52].

The work function of a material or surface is a key property that determines its behavior in an electronic circuit. Energy level differences between different constituent layers of a device dictate functionality ranging from Ohmic contacts to Schottky barriers. One of the primary strengths of silicon and other materials of choice in the semiconductor industry is their uniform work function, or surface potential. Bare silicon surfaces, typically used as references for KPFM measurements,

have RMS uniformity on the order of 3 mV [53]. Aside from their use in integrated electronics, surfaces with flat topography and surface potential are also of interest as substrates for self-assembly. The quality of molecular self-assembly is critically determined by the electronic structure of the substrate surface and by variations of its surface potential due to charge transfer between the substrate and adsorbed molecules. As a result, highly homogeneous metal surfaces are often the substrate of choice due to well-defined molecule-metal interactions [54–57].

Here we show that few-layer Gr grown by CVD on sputtered Mo films has an extremely uniform surface potential profile over large areas, as measured by KPFM. In addition, such Gr that has been transferred, keeps the excellent uniformity, with RMS variability in surface potential in the order of 4 mV for areas as large as 30 × 30 μm². This is an improvement compared to the epitaxial Gr grown on SiC which has surface potential with RMS uniformity on the order of ~10 mV, however domains of few-layer Gr and steps in the SiC spoil this homogeneity in the surface potential at scales larger than 1 μm [58]. Monolayer Gr grown by CVD on copper contains wrinkles that also introduce inhomogeneity in surface potential on the order of ~20 mV [23]. Even metal films, such as sputtered gold, display larger variability of surface potential over large areas [59], whereas films deposited with atomic layer deposition display variability on the order of ~10 mV [60].

3.5. Electrical conductivity

3.5.1. CVD Gr on Mo

Homogeneity of electrical conductivity was studied by C-AFM. Topography and corresponding current maps are presented in Figs. 9(a) and 9(b), respectively. The current map exhibits rather homogeneous and high current. The corresponding histogram is displayed in Fig. 9(c). As can be seen, the current distribution is characterized with a single peak around 14.5 nA, with a half-width of around 1 nA. The broadening

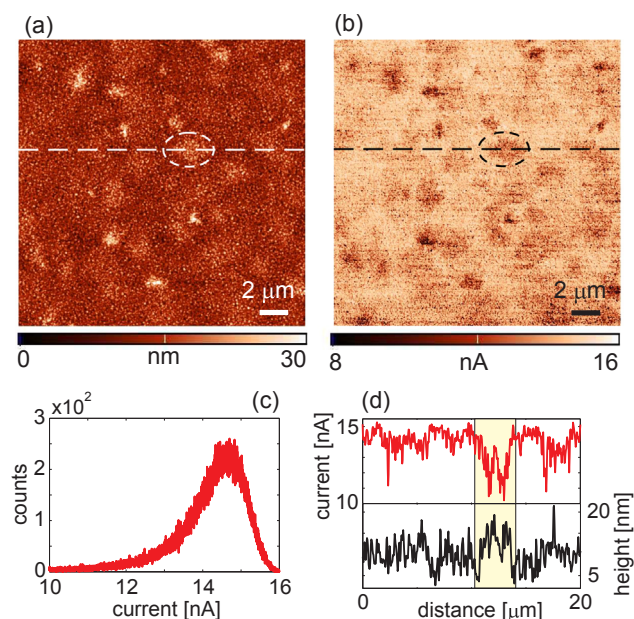


Fig. 9. (a) Morphology of CVD Gr on Mo and (b) corresponding current map measured by C-AFM. (c) Histogram of the current distributions in map (b). (d) Height and current profiles along the dashed lines in parts (a) and (b), respectively. Dashed circles in (a) and (b) correspond to the region with lower current which is highlighted by yellow in (d). (For interpretation of the references to colour in this figure legend, the reader is referred to the web version of this article.)

of the current peak appears due to decreased conductivity on the patches with increased thickness. The height and current profiles across one such patch (along the dashed lines indicated in Figs. 9(a) and 9(b)) are depicted in Fig. 9(d). As can be seen from these profiles, the current drops by several nA on the patch. In addition, small current drops (shown in Fig. S2 of Supplementary material) are visible along narrow Mo grain boundaries (imprinted in Gr as well) because of unstable contact with the AFM tip.

3.5.2. CVD Gr on SiO₂

As in the previous case for the electrical surface potential, a similar analysis of the current distribution was conducted for CVD Gr on SiO₂. The conductivity exhibits the same characteristics as previously observed for Gr on Mo: homogeneous and high current except on thicker patches (results presented in Fig. S3 of Supplementary material).

The small-scale images with topographic and current maps are presented for two cases: Figs. 10(a1) and 10(a2) for flat Gr (without patches) and Figs. 10(b1) and 10(b2) across a Gr patch. Both current images show homogeneous current despite of a dense network of Gr wrinkles. As we discussed above, wrinkles in the considered case have the geometry of simple, small and narrow ripples [20]. Then, during scanning in AFM contact mode, such wrinkles are pressed by the AFM tip leading to local Gr flattening, which finally gives a constant and high current. At the same time, Gr is wear resistive, so this local mechanical deformation does not result in Gr tearing. This is a significant improvement compared to CVD Gr grown on copper, where wrinkles are much wider and folded [20], leading to a more pronounced current drop. In the worst case, an AFM tip going across such wrinkles easily initiates local Gr tearing thus producing narrow and insulating trenches in a Gr sheet with zero current [23].

Still, the current map in Fig. 10(b2) contains local, point-like domains, represented by dark contrast, with a slightly decreased current. Reduced conductivity across patches indicates possible irregularities in the growth of these additional layers. However, the current drops only along patch edges or at pronounced topographic features such as point-

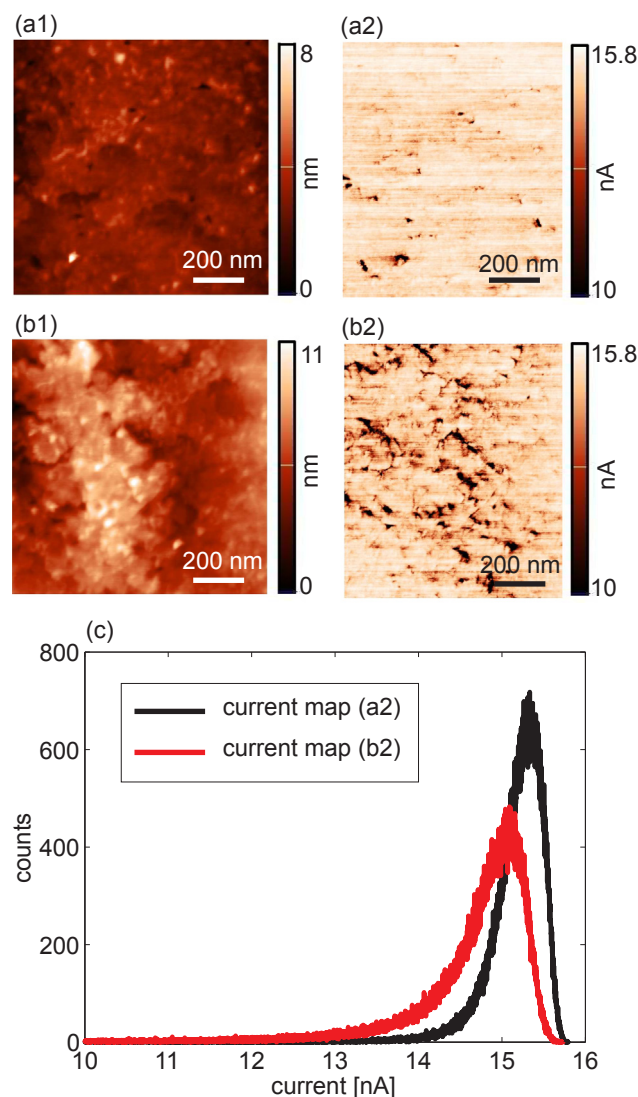


Fig. 10. (a1) Morphology and (a2) current map of CVD Gr transferred on SiO₂ without patches. (b1) Morphology and (b2) current map of Gr with a patch. (c) Histograms of the current distributions from parts (a2) and (b2).

like bumps. Therefore, one possible reason of decreased current on these parts is a less stable electrical contact between the AFM tip and Gr. Further improvement in the Gr growth process is needed in order to avoid these imperfections. Current histograms for both Gr with and without patches are given in Fig. 10(c). As can be seen, due to a slightly decreased conductivity of the domain with patches, the current peak is shifted by around 0.2 nA to a lower value.

4. Conclusion

In summary, we have demonstrated that although few-layer Gr grown on Mo does contain wrinkles with a height of several nanometers, the wrinkles are much narrower than in CVD Gr grown on copper, and they do not have a detrimental effect on uniformity of wear and electrical properties. It is shown that few-layer Gr grown by CVD on sputtered Mo films is characterized with a very low friction coefficient of around 0.13. Its wear resistance is improved compared to CVD Gr grown on copper, giving the threshold normal load for wear of around 4 μN. The considered Gr has very uniform surface potential over large areas, with RMS variability on the order of 5 mV for areas as large as 50 × 50 μm². The uniformity of electrical properties is better than in other types of Gr and is on par with industrial-grade materials such as

silicon and metals deposited by atomic layer deposition. The local conductivity of the Gr films is also uniform, although with small variations at the edges of Gr patches with varying thickness. The patches are a result of the growth process which should be further optimized in order to overcome this issue.

We thus propose that few-layer Gr grown on Mo holds strong potential for use as an ultrathin solid lubricant for friction and wear reduction. It can also be used as an ultrathin electrode in integrated electronics, allowing wafer-scale device uniformity and reproducibility. Furthermore, the material holds potential as a substrate for self-assembly and for other uses that require uniform and well-defined electrical properties over large areas.

Declaration of Competing Interest

There are no conflict of interest in this work.

Acknowledgements

We would like to acknowledge support of the Ministry of Education, Science and Technological Development of the Republic of Serbia through projects OI171005 and TR32008. We acknowledge the Innovation Fund project no 50038 and the Graphene Flagship.

Appendix A. Supplementary material

Supplementary data associated with this article can be found, in the online version, at <https://doi.org/10.1016/j.apsusc.2019.144792>.

References

- [1] X. Li, W. Cai, J. An, S. Kim, J. Nah, D. Yang, R. Piner, A. Velamakanni, I. Jung, E. Tutuc, S.K. Banerjee, L. Colombo, R.S. Ruoff, Large-area synthesis of high-quality and uniform graphene films on copper foils, *Science* 324 (2009) (2009) 1312–1314.
- [2] A.N. Obraztsov, E.A. Obraztsova, A.V. Tyurnina, A.A. Zolotukhin, Chemical vapor deposition of thin graphite films of nanometer thickness, *Carbon* 45 (2007) (2007) 2017–2021.
- [3] H. Zhou, W.J. Yu, L. Liu, R. Cheng, Y. Chen, X. Huang, Y. Liu, Y. Wang, Y. Huang, X. Duan, Chemical vapour deposition growth of large single crystals of monolayer and bilayer graphene, *Nat. Comm.* 4 (2013) (2013) 2096.
- [4] K.S. Kim, Y. Zhao, H. Jang, S.Y. Lee, J.M. Kim, K.S. Kim, J.-H. Ahn, P. Kim, J.-Y. Choi, B.H. Hong, Large-scale pattern growth of graphene films for stretchable transparent electrodes, *Nature* 457 (2009) (2009) 706–710.
- [5] X. Li, Y. Zhu, W. Cai, M. Borysiak, B. Han, D. Chen, R.D. Piner, L. Colombo, R.S. Ruoff, Transfer of large-area graphene films for high-performance transparent conductive electrodes, *Nano Lett.* 9 (2009) (2009) 4359–4363.
- [6] J. Kang, D. Shin, S. Bae, B.H. Hong, Graphene transfer: key for applications, *Nanoscale* 4 (2012) (2012) 5527–5537.
- [7] C. Mattevi, H. Kim, M. Chhowalla, A review of chemical vapour deposition of graphene on copper, *J. Mater. Chem.* 21 (2011) (2011) 3324–3334.
- [8] Y. Zhang, L. Zhang, C. Zhou, Review of chemical vapor deposition of graphene and related applications, *Acc. Chem. Res.* 46 (2013) (2013) 2329–2339.
- [9] C.-M. Seah, S.-P. Chai, A.R. Mohamed, Mechanisms of graphene growth by chemical vapour deposition on transition metals, *Carbon* 70 (2014) (2014) 1–21.
- [10] C.S. Ruiz-Vargas, H.L. Zhuang, P.Y. Huang, A.M. van der Zande, S. Garg, P.L. McEuen, D.A. Muller, R.G. Hennig, J. Park, Softened elastic response and unzipping in chemical vapor deposition graphene membranes, *Nano Lett.* 11 (2011) (2011) 2259–2263.
- [11] G.-H. Lee, R.C. Cooper, S.J. An, S. Lee, A. van der Zande, N. Petrone, A.G. Hammerberg, C. Lee, B. Crawford, W. Oliver, J.W. Kysar, J. Hone, High-strength chemical-vapor-deposited graphene and grain boundaries, *Science* 340 (2013) (2013) 1073–1076.
- [12] H.I. Rasool, C. Ophus, W.S. Klug, A. Zettl, J.K. Gimzewski, Measurement of the intrinsic strength of crystalline and polycrystalline graphene, *Nat. Commun.* 4 (2013) (2013) 2811.
- [13] J.C. Koepke, J.D. Wood, D. Estrada, Z.-Y. Ong, K.T. He, E. Pop, J.W. Lyding, Atomic-scale evidence for potential barriers and strong carrier scattering at graphene grain boundaries: a scanning tunneling microscopy study, *Nano Lett.* 7 (2013) (2013) 75–86.
- [14] K.W. Clark, X.-G. Zhang, I.V. Vlassiok, G. He, R.M. Feenstra, A.-P. Li, Spatially resolved mapping of electrical conductivity across individual domain (grain) boundaries in graphene, *Nano Lett.* 7 (2013) (2013) 7956–7966.
- [15] P. Nemes-Incze, P. Vancsó, Z. Osváth, G.I. Márk, X. Jin, Y.-S. Kim, C. Hwang, P. Lambin, C. Chapelier, L.B. Biró, Electronic states of disordered grain boundaries in graphene prepared by chemical vapor deposition, *Carbon* 64 (2013) (2013) 178–186.
- [16] A.W. Cummings, D.L. Duong, V.L. Nguyen, D. Van Tuan, J. Kotakoski, J.E. Barrios Vargas, Y.H. Lee, S. Roche, Charge transport in polycrystalline graphene: challenges and opportunities, *Adv. Mater.* 26 (2014) (2014) 5079–5094.
- [17] K. Xu, P. Cao, J.R. Heath, Scanning tunneling microscopy characterization of the electrical properties of wrinkles in exfoliated graphene monolayers, *Nano Lett.* 9 (2009) (2009) 4446–4451.
- [18] N. Liu, Z. Pan, L. Fu, C. Zhang, B. Dai, Z. Liu, The origin of wrinkles on transferred graphene, *Nano Res.* 4 (2011) (2011) 996–1004.
- [19] M. Ahmad, H. An, Y.S. Kim, J.H. Lee, J. Jung, S.-H. Chun, Y. Seo, Nanoscale investigation of charge transport at the grain boundaries and wrinkles in graphene film, *Nanotechnology* 23 (2012) (2012) 285705.
- [20] W. Zhu, T. Low, V. Perebeinos, A.A. Bol, Y. Zhu, H. Yan, J. Tersoff, P. Avouris, Structure and electronic transport in graphene wrinkles, *Nano Lett.* 12 (2012) (2012) 3431–3436.
- [21] S. Ladak, J.M. Ball, D. Moseley, G. Eda, W.R. Branford, M. Chhowalla, T.D. Anthopoulos, L.F. Cohen, Observation of wrinkle induced potential drops in biased chemically derived graphene thin film networks, *Carbon* 64 (2013) (2013) 35–44.
- [22] P. Willke, C. Möhle, A. Sinterhauf, T. Kotzot, H.K. Yu, A. Wodtke, M. Wenderoth, Local transport measurements in graphene on SiO₂ using Kelvin probe force microscopy, *Carbon* 102 (2016) (2016) 470–476.
- [23] B. Vasić, A. Zurutuza, R. Gajić, Spatial variation of wear and electrical properties across wrinkles in chemical vapour deposition graphene, *Carbon* 102 (2016) (2016) 304–310.
- [24] Y. Wu, G. Yu, H. Wang, B. Wang, Z. Chen, Y. Zhang, B. Wang, X. Shi, X. Xie, Z. Jin, X. Liu, Synthesis of large-area graphene on molybdenum foils by chemical vapor deposition, *Carbon* 50 (2012) (2012) 5226–5231.
- [25] Y. Grachova, S. Vollebregt, A.L. Lacaita, P.M. Sarro, High quality wafer-scale CVD graphene on molybdenum thin film for sensing application, *Proc. Eng.* 87 (2014) (2014) 1501–1504.
- [26] Z. Zou, L. Fu, X. Song, Y. Zhang, Z. Liu, Carbide-forming groups IVB-VIB metals: a new territory in the periodic table for CVD growth of graphene, *Nano Lett.* 14 (2014) (2014) 3832–3839.
- [27] C. Schiattarella, S. Vollebregt, T. Polichetti, B. Alfano, E. Massera, M.L. Miglietta, G. Di Francia, P.M. Sarro, CVD transfer-free graphene for sensing applications, *Beilstein J. Nanotechnol.* 8 (2017) (2017) 1015–1022.
- [28] S. Vollebregt, R.J. Dolleman, H.S.J. van der Zant, P.G. Steeneken, P.M. Sarro, Suspended graphene beams with tunable gap for squeeze-film pressure sensing, 2017 19th International Conference on Solid-State Sensors, Actuators and Microsystems (TRANSDUCERS), 2017, pp. 770–773.
- [29] S. Naghdi, I. Jevremović, V. Mišković-Stanković, K.Y. Rhee, Chemical vapour deposition at atmospheric pressure of graphene on molybdenum foil: effect of annealing time on characteristics and corrosion stability of graphene coatings, *Corros. Sci.* 113 (2016) (2016) 116–125.
- [30] S. Naghdi, K. Nešović, V. Mišković-Stanković, K.Y. Rhee, Comprehensive electrochemical study on corrosion performance of graphene coatings deposited by chemical vapour deposition at atmospheric pressure on platinum-coated molybdenum foil, *Corros. Sci.* 130 (2018) (2018) 31–44.
- [31] S. Naghdi, K.Y. Rhee, S.J. Park, Oxidation resistance of graphene-coated molybdenum: Effects of pre-washing and hydrogen flow rate, *Int. J. Refract. Metals Hard Mater.* 65 (2017) (2017) 29–33.
- [32] F. Ricciardella, S. Vollebregt, T. Polichetti, M. Miscuglio, B. Alfano, M.L. Miglietta, E. Massera, G. Di Francia, P.M. Sarro, Effects of graphene defects on gas sensing properties towards NO₂ detection, *Nanoscale* 9 (2017) (2017) 6085–6093.
- [33] D.K. Hong, S.A. Han, J.H. Park, S.H. Tan, N. Lee, Y. Seo, Frictional force detection from lateral force microscopic image using a Si grating, *Colloids Surf. A* 313–314 (2008) (2008) 567–570.
- [34] Y.-J. Yu, Y. Zhao, S. Ryu, L.E. Brus, K.S. Kim, P. Kim, Tuning the graphene work function by electric field effect, *Nano Lett.* 9 (2009) (2009) 3430–3434.
- [35] D. Graf, F. Molitor, K. Ensslin, C. Stampfer, A. Jungen, C. Hierold, L. Wirtz, Spatially resolved Raman spectroscopy of single- and few-layer graphene, *Nano Lett.* 7 (2007) (2007) 238–242.
- [36] B. Vasić, A. Matković, U. Ralević, M. Belić, R. Gajić, Nanoscale wear of graphene and wear protection by graphene, *Carbon* 120 (2017) (2017) 137–144.
- [37] A. Zandiatashbar, G.-H. Lee, S.J. An, S. Lee, N. Mathew, M. Terrones, T. Hayashi, C.R. Picu, J. Hone, N. Koratkar, Effect of defects on the intrinsic strength and stiffness of graphene, *Nat. Commun.* 5 (2014) (2014) 3186.
- [38] M. Tripathi, F. Awaja, R.A. Bizzo, S. Signetti, E. Iacob, G. Paolicelli, S. Valeri, A. Dalton, N.M. Pugno, Friction and adhesion of different structural defects of graphene, *ACS Appl. Mater. Inter.* 10 (2018) (2018) 44614–44623.
- [39] K.-S. Kim, H.-J. Lee, C. Lee, S.-K. Lee, H. Jang, J.-H. Ahn, J.-H. Kim, H.-J. Lee, Chemical vapor deposition-grown graphene: the thinnest solid lubricant, *ACS Nano* 5 (2011) (2011) 5107–5114.
- [40] S. Zhang, T. Ma, A. Erdemir, Q. Li, Tribology of two-dimensional materials: from mechanisms to modulating strategies, *Mater. Today* 26 (2019) (2019) 67–86.
- [41] A. Vasić, B. Matković, R. Gajić, I. Stanković, Wear properties of graphene edges probed by atomic force microscopy based lateral manipulation, *Carbon* 107 (2016) (2016) 723–732.
- [42] D. Berman, A. Erdemir, A.V. Sumant, Graphene: a new emerging lubricant, *Mater. Today* 17 (2014) (2014) 31–42.
- [43] P. Egberts, G.H. Han, X.Z. Liu, A.T.C. Johnson, R.W. Carpick, Frictional behavior of atomically thin sheets: hexagonal-shaped graphene islands grown on copper by chemical vapor deposition, *ACS Nano* 8 (2014) (2014) 5010–5021.
- [44] M.-S. Won, O.V. Penkov, D.-E. Kim, Durability and degradation mechanism of graphene coatings deposited on Cu substrates under dry contact sliding, *Carbon* 54 (2013) (2013) 472–481.

- [45] D. Berman, S.A. Deshmukh, S.K.R.S. Sankaranarayanan, A. Erdemir, A.V. Sumant, Extraordinary macroscale wear resistance of one atom thick graphene layer, *Adv. Funct. Mater.* 24 (2014) (2014) 6640–6646.
- [46] A. Klemenz, L. Pastewka, S.G. Balakrishna, A. Caron, R. Bennewitz, M. Moseler, Atomic scale mechanisms of friction reduction and wear protection by graphene, *Nano Lett.* 14 (2014) (2014) 7145–7152.
- [47] J. Martin, N. Akerman, G. Ulbricht, T. Lohmann, J.H. Smet, K. von Klitzing, A. Yacoby, Observation of electron-hole puddles in graphene using a scanning single-electron transistor, *Nat. Phys.* 4 (2007) (2007) 144.
- [48] Y. Zhang, V.W. Brar, C. Girit, A. Zettl, M.F. Crommie, Origin of spatial charge inhomogeneity in graphene, *Nat. Phys.* 5 (2009) (2009) 722.
- [49] S.C. Martin, S. Samaddar, B. Sacépé, A. Kimouche, J. Coraux, F. Fuchs, B. Grévin, H. Courtois, C.B. Winkelmann, Disorder and screening in decoupled graphene on a metallic substrate, *Phys. Rev. B* 91 (2015) (2015) 041406.
- [50] A. Deshpande, W. Bao, F. Miao, C.N. Lau, B.J. LeRoy, Spatially resolved spectroscopy of monolayer graphene on SiO₂, *Phys. Rev. B* 79 (2009) (2009) 205411.
- [51] G. Giovannetti, P.A. Khomyakov, G. Brocks, V.M. Karpan, J. van den Brink, P.J. Kelly, Doping graphene with metal contacts, *Phys. Rev. Lett.* 101 (2008) (2008) 026803.
- [52] A. Matković, M. Chhikara, M. Milićević, U. Ralević, B. Vasić, D. Jovanović, M. Belić, G. Bratina, R. Gajić, Influence of a gold substrate on the optical properties of graphene, *J. Appl. Phys.* 117 (2015) (2015) 015305.
- [53] C. Leung, H. Kinns, B.W. Hoogenboom, S. Howorka, P. Mesquida, Imaging surface charges of individual biomolecules, *Nano Lett.* 9 (2009) (2009) 2769–2773.
- [54] L. Bartels, Tailoring molecular layers at metal surfaces, *Nat. Chem.* 2 (2010) (2010) 87–95.
- [55] J. Wyrick, D.-H. Kim, D. Sun, Z. Cheng, W. Lu, Y. Zhu, K. Berland, Y.S. Kim, E. Rotenberg, M. Luo, P. Hyldgaard, T.L. Einstein, L. Bartels, Do two-dimensional noble gas atoms produce molecular honeycombs at a metal surface? *Nano Lett.* 11 (2011) (2011) 2944–2948.
- [56] A.S. DeLoach, B.R. Conrad, T.L. Einstein, D.B. Dougherty, Coverage dependent molecular assembly of anthraquinone on Au(111), *J. Chem. Phys.* 147 (2017) (2017) 184701.
- [57] C. Krull, M. Castelli, P. Hapala, D. Kumar, A. Tadich, M. Capsoni, M.T. Edmonds, J. Hellerstedt, S.A. Burke, P. Jelinek, A. Schiffrin, Iron-based trinuclear metal-organic nanostructures on a surface with local charge accumulation, *Nat. Commun.* 9 (2018) (2018) 3211.
- [58] O. Kazakova, V. Panchal, T.L. Burnett, Epitaxial graphene and graphene-based devices studied by electrical scanning probe microscopy, *Crystals* 3 (2013) (2013) 191–233.
- [59] S. Hormeño, M. Penedo, C.V. Manzano, M. Luna, Gold nanoparticle coated silicon tips for Kelvin probe force microscopy in air, *Nanotechnology* 24 (2013) (2013) 395701.
- [60] R. Huang, S. Ye, K. Sun, K.S. Kiang, C.H.K. de Groot, Fermi level tuning of ZnO films through supercycled atomic layer deposition, *Nanoscale Res. Lett.* 12 (2017) (2017) 541.



Plasmon – Phonon interaction in $\text{ZnSnSb}_2 + \text{Mn}$ semiconductors

Maja Romcevic^{a,*}, Novica Paunovic^a, Uros Ralevic^a, Jelena Pesic^a, Jelena Mitric^a, Jelena Trajic^a, Lukasz Kilanski^b, Witold Dobrowolski^b, Irina Valentinovna Fedorchenko^{c,d}, Sergej Fedorovich Marenkin^{c,d}, Nebojsa Romcevic^a

^a Institute of Physics, University of Belgrade, Belgrade, Serbia

^b Institute of Physics, Polish Academy of Sciences, Warsaw, Poland

^c Kurnakov Institute of General and Inorganic Chemistry, Russian Academy of Science, Moscow, Russian Federation

^d College of New Materials and Nanotechnologies, National University of Science and Technology, Moscow, Russian Federation

ARTICLE INFO

Keywords:

Semiconductors
Lattice defects
Optical properties
Phonon properties
Plasmon - phonon interaction

ABSTRACT

Semiconductors of II-IV-V₂ type with chalcopyrite structure have been studied for several decades. Due to advances in materials synthesis technologies, and doping with various elements, the possibilities of their application have expanded. In this paper, polycrystalline $\text{ZnSnSb}_2 + \text{Mn}$ was examined with the aim to explain the connection of its high free carrier concentration with the material structure and influence on optical properties. Two samples of $\text{Zn}_{1-x}\text{Mn}_x\text{SnSb}_2$ with different compositions ($x = 0.027$ and $x = 0.076$) and significant difference in carrier concentrations were analyzed. Their structural properties were examined by x-ray diffraction, optical microscopy, and AFM. The existence of several different phases - ZnSnSb_2 , ZnSb , SnSb , and small amounts of Sn and MnSb , as well as very complex microstructures, were registered. It was found that the high free carrier concentrations are caused by a large number of defects, especially zinc vacancies. Optical properties were analyzed using IR spectroscopy at room temperature. Based on the analysis of IR reflection spectra, the presence of plasmon - phonons interaction was registered. It was determined that three ZnSnSb_2 phonons of B₂ symmetry interact with plasma, which then leads to the change of their positions. A detailed analysis of this interaction provides insight into the behavior of some other material parameters. Also, vibration modes of ZnSb and SnSb phases were registered on the spectra. Knowledge of phonon behavior and their interaction with plasma is important for possible applications, especially as a thermoelectric material.

1. Introduction

Semiconductors have been widely used thanks to the ability to adapt to different requirements. The II-IV-V₂ chalcopyrite semiconductors have been intensively studied in recent decades [1]. The fields of their application are considerably expanded by doping with various impurities. A significant breakthrough was achieved by the addition of magnetic impurities, whereby ferromagnetism at room temperature was achieved [2,3]. The synthesis technology of this class of compounds has been developed, but it is still adapting to new requirements [4]. Zn-Sn-Sb based alloys have required thermoelectric properties and find application as low-toxic thermoelectric materials [5,6,7]. The engineering of structural, transport, electrical, optical, magnetic properties as well as other material parameters, goes along with the increasing application of this class of semiconductors.

ZnSnSb_2 is II-IV-V₂ type material with the tetragonal chalcopyrite structure, narrow gap of 0.7 eV at room temperature, high

concentration of free carriers (10^{21} – 10^{22} cm⁻³) and inhomogeneous structure [8,9]. In this paper we analyzed ferromagnetic semiconductor $\text{ZnSnSb}_2 + \text{Mn}$, which has interesting magnetic properties, such as paramagnet-ferromagnet transition with the Curie temperature about 522 K and the cluster-glass behavior with the transition temperature about 465 K, caused by the formation of MnSb clusters in the material [10]. The $\text{Zn}_{1-x}\text{Mn}_x\text{SnSb}_2$ samples were obtained using direct fusion method, and characterization of their structural, magnetic, optical and phonon properties were done [9]. We chose two samples with different chemical contents, $x = 0.027$ and $x = 0.076$, which we labeled as samples A and B respectively, with the aim to examine their properties in more detail. Main reason was a ten times difference in their free-carrier concentrations ($p_A = 13 \times 10^{21}$ cm⁻³ and $p_B = 1.2 \times 10^{21}$ cm⁻³). We wanted to determine what the cause of this difference in concentration is, and whether there is a reaction between the free carriers and the crystal lattice. The question of plasmon-phonon interaction is particularly interesting in the study of thermoelectric

* Corresponding author.

E-mail address: romcevic@ipb.ac.rs (M. Romcevic).

<https://doi.org/10.1016/j.infrared.2020.103345>

Received 3 February 2020; Received in revised form 23 April 2020; Accepted 25 April 2020

Available online 28 April 2020

1350-4495/ © 2020 Elsevier B.V. All rights reserved.

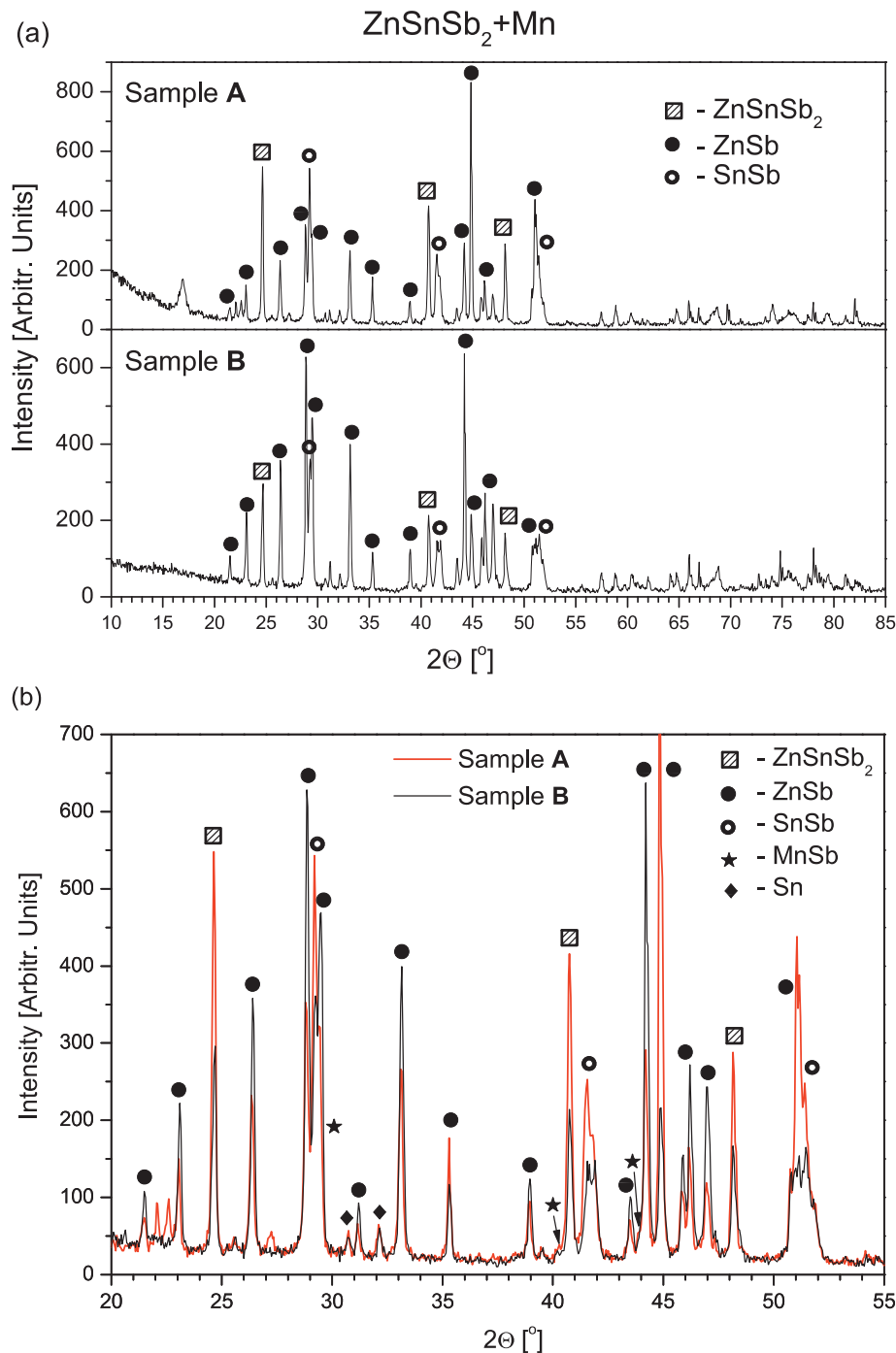


Fig. 1. (a) X-ray diffraction pattern for ZnSnSb₂ + Mn samples which contain different amounts of Mn. The registered crystal phases are marked; (b) The two spectra are overlapped to compare their relative intensities.

materials, as well as their electrical and thermal conductivity, and their interdependence.

ZnSnSb₂ is not a homogeneous material, and the consequence is that even two samples from the same crystal can have significantly different properties. This is not surprising given the complicated ZnSnSb₂ microstructure. Our goal was to analyze the relationship between microstructures, their phonons and free carriers, their conditionality and interactions. For this purpose we used x-ray diffraction, optical microscopy, AFM and IR spectroscopy measurements. Obtained results were analyzed by applying the model for plasmon-phonon interaction.

2. Samples and characterization

ZnSnSb₂ semiconductor has a chalcopyrite structure, spatial group I42d, with lattice parameters $a \approx 6.275$ Å and $c \approx 12.55$ Å and ratio c/a close to 2. ZnSnSb₂ melts by a peritectic reaction at $T = 362$ °C with a possible phase transformation of the cubic modification into a tetragonal one at $T = 348$ °C [11,12]. The ZnSnSb₂ + Mn ferromagnetic semiconductors were synthesized using the method that makes it possible to obtain single crystals at temperatures below the temperature of the peritectic reaction.

The analyzed samples of Zn_{1-x}Mn_xSnSb₂ were synthesized by the direct fusion method. High purity components were used for the

synthesis: zinc single crystals (99.999%), shots of tin (99.999%), anti-mony single crystals (99.999%), and manganese powder (99.999%). They were mixed in stoichiometric ratios.

The reaction mixture was put into a quartz glass tube and heated up to 631 °C. After that, ampoules were quenched to 355 °C and then annealed at 355 °C. This is described in more detail in the papers [12,13]. The synthesized crystals were cut into slices of about 1.5 mm thickness.

The chemical composition of the samples (x) was determined using the energy dispersive x-ray fluorescence method (EDXRF) [10]. Obtained results showed that average Mn content (x) in the samples is between 0.027 and 0.138. All the studied crystals had the correct stoichiometry of $Zn_{1-x}Mn_xSnSb_2$ alloy equal to $1-x : x : 1 : 2$, within our measurement accuracy of about 10% of the x value.

Based on the magnetotransport measurements [10] it was found that electrical and magnetotransport parameters, such as resistivity, carrier concentration, and carrier mobility, do not depend linearly on composition, i.e. on the Mn content. Therefore, as mentioned above, two samples with a considerable difference in free-carrier concentrations were selected. The sample with $x = 0.027$ and $p = 13 \times 10^{21} \text{ cm}^{-3}$ was labeled as sample A and the one with $x = 0.076$ and $p = 1.2 \times 10^{21} \text{ cm}^{-3}$ as sample B. In this way we wanted to determine the connection between the free carriers and the structural and optical properties of the alloy.

The structural properties of these samples were investigated by the XRD powder technique. Measurements were done using a Philips PW 1050 diffractometer equipped with a PW 1730 generator, 40 kV \times 20 mA, using Ni filtered Co K α radiation of 0.1778897 nm at room temperature. The x-ray diffraction patterns were collected during 2 h in the range of 10–100° with a scanning step of 0.05° and 10 s scanning time per step. Phase analysis showed that besides the main phase of chalcopyrite $ZnSnSb_2$, the orthorhombic $ZnSb$, rhombohedral $SnSb$, and hexagonal $MnSb$ phases are present in the samples. This is consistent with the literature [8,10].

An optical microscope was used to get an insight into the distribution of different phases of the material along the surface. Images were captured using Olympus BH series modular microscope with UIS objective lenses with 50x and 400x enhancement.

The surfaces of $ZnSnSb_2 + Mn$ samples were examined in detail using Atomic Force Microscope (AFM), NTEGRA prima from NTMDT. The topography and phase images were acquired simultaneously by operating the AFM in semi-contact mode. NSG01 probes with a typical resonant frequency of 150 kHz and 10 nm tip apex curvature radius were used.

The far-infrared (FIR) reflectivity measurements were done with a BOMEM DA-8 Fourier-transform infrared spectrometer in the spectral range from 40 to 450 cm^{-1} at room temperature. A Hyper beamsplitter and deuterated triglycine sulfate (DTGS) pyroelectric detector were used.

3. Results and discussion

It is known that during the preparation of $ZnSnSb_2$ the polycrystalline material is formed, consisting of the main phase and $ZnSb$, $SnSb$ and β - Sn inclusions [11].

The structure of the two selected samples was investigated by X-ray diffraction measurements. Obtained results with marked phases are presented in Fig. 1. In Fig. 1(b) the overlap of the results is shown, with the aim to compare their relative intensities. The list of XRD peaks positions and their corresponding Miller indices and phases is given in Table 1 in Supplementary Materials.

Besides the chalcopyrite $ZnSnSb_2$ phase the orthorhombic $ZnSb$, rhombohedral $SnSb$, Sn have also been registered, as well as weak lines from hexagonal $MnSb$ inclusions. The idea was to detect differences in the structures of these two samples. It is obvious that diffraction lines corresponding to the $ZnSnSb_2$ phase (squares) are stronger for sample A

Table 1
Expected values of $ZnSnSb_2$ phonons of B_2 and E symmetries, from literature [26].

Phonon	B_2^1	B_2^2	B_2^3	E^1	E^2	E^3	E^4	E^5	E^6
Estimated value [cm^{-1}]	189	199	70	189	185	195	111	88	54

as well as lines of $SnSb$ phase (open circles). Also, it is clear that lines corresponding to $ZnSb$ (black circles) are mostly stronger for sample B. Existence of the Sn phase is evident, but lines corresponding $MnSb$ phase are barely visible.

In order to examine the spatial distribution of the existing different crystal phases, the samples were recorded by an optical microscope with two different magnifications (50 \times and 400 \times). Obtained micrographs are presented in Fig. 2.

Existing phases are clearly visible and they form multiphase structures. It should be noted that this is a very non-homogeneous material and that images from different parts of the samples differed, so the characteristic ones are selected and shown in Fig. 2.

In our previous work [9] is determined that gray fields are $ZnSnSb_2$ crystal, white ones correspond $SnSb$ phase and that dark parts consist of $ZnSb$. Micrometric crystals of $MnSb$ in the shape of dark circles were registered also.

Although microstructures of similar shapes have been formed in both samples, it is apparent that the surfaces significantly differ. Based on previous work [8,9,14], it can be concluded that these spherical and needle like microcrystals are $ZnSb$, $MnSb$, Sn , and Sb phases formed during crystallization of the material. As can be seen from Fig. 2. the sample B contains a lot of micron-sizes phases relatively evenly distributed over the surface (volume).

In order to more accurately examine the surface of the samples, we used atomic force microscopy (AFM) measurements. The characteristic results are presented in Fig. 3.

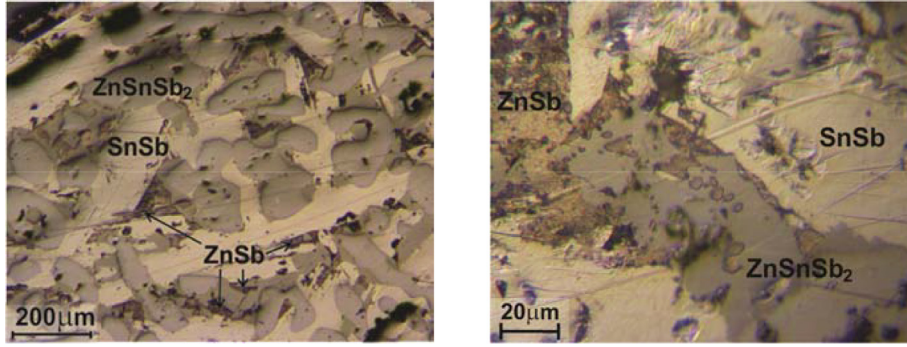
The surfaces of both samples have a granular structure. The sample A has evenly distributed grains over the entire surface with a few larger clusters and an average grain height of around ~ 100 nm (see Fig. 3(a) and the profile in Fig. 3(c)). The phase contrast in Fig. 3(b) originates exclusively from the abrupt changes in the height, indicating that the material properties of the sample A surface are homogeneous. The grains on the surface of the sample B are exclusively arranged into clusters which are not evenly distributed over the surface. The majority of the clusters reach several tens of nm in height, with a few exceptions having a height of ~ 100 nm (see Fig. 3(d) and the profile in Fig. 3(f)). The phase contrast of the sample B surface shows that the larger clusters have a distinct phase shift, seen as dark and white regions in Fig. 3(e), so that clusters have different material properties than the remainder of the surface.

This material is known to be difficult to synthesize and beside $ZnSnSb_2$ the $ZnSb$ and $SnSb$ phases are formed [11,15]. The series of $Zn_{1-x}Mn_xSnSb_2$ samples were synthesized under the same conditions with the only difference being the starting amounts of manganese and zinc [10]. Obviously, the small variation in the starting mixture causes rather different structures and properties of the materials.

It was found that a large concentration of lattice defects, especially in the cation sublattice, in $ZnSnSb_2$, as well as in other II-IV-V₂ semiconductors [16,17], causes a high hole concentration. In particular, Zn vacancies are those defects that lead to a very high concentration of holes [18,19,20]. Typical hole concentration in $ZnSnSb_2$ is 10^{20} cm^{-3} [15–20], in two-component p-type $ZnSb$ it is 10^{19} cm^{-3} [18,19], while $SnSb$ is a n-type material with metallic character and electron concentration of about 10^{22} cm^{-3} at 1.8 K [21]. Evidently, the electronic structure is very complex in this material.

It is difficult to say exactly what is the cause of different hole concentrations in the $Zn_{1-x}Mn_xSnSb_2$ samples, but it could be assumed that Zn vacancies are the main reason. Sample A has a higher content of

Sample A



Sample B

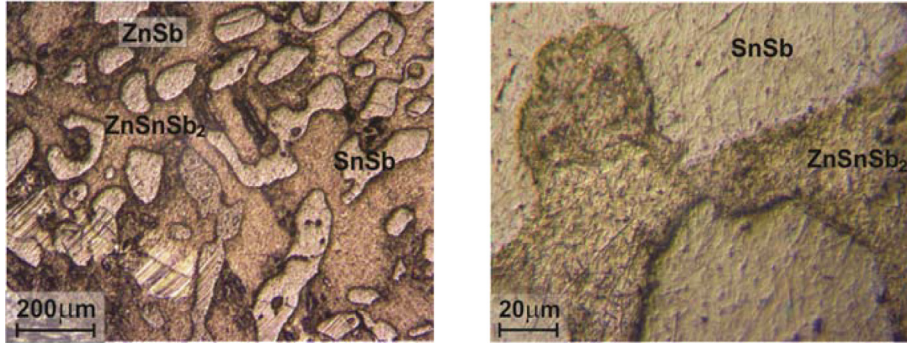


Fig. 2. Micrographs of the ZnSnSb₂ + Mn samples surfaces with magnifications of 50 × and 400 ×.

SnSb, which is related to a higher deficiency of Zn atoms, and therefore higher hole concentration. So, the different concentrations of free carriers in the samples are a consequence of various defects and microstructures which are formed.

In order to examine the interaction of free carriers and a lattice, the far-infrared reflectivity spectra in the range 40–450 cm⁻¹ at room temperature have been recorded. Obtained spectra are shown in Fig. 4.

It is obvious that the most distinct difference between the spectra relates to wave numbers above 220 cm⁻¹, where the high carrier concentration has a main influence. Also, in the range from 120 to 180 cm⁻¹ the spectrum for sample B (black line) contains some phonon lines which are absent or attenuated in the spectrum for sample A (red line).

A detailed analysis of the obtained results was necessary. For the analysis of the spectra the fitting procedure which includes plasmon-phonon interaction was applied.

4. Plasmon - phonon interaction

In materials with high free carrier concentration a plasmon-phonon interaction should be taken into account, as it significantly affects the properties of the material. Its influence on the dielectric properties of the material is important for the analysis of the reflection spectra.

A theoretical model of the dielectric function in bulk materials [22] has been applied. The dielectric function $\epsilon(\omega)$ describes dielectric properties of single crystal and includes classical oscillators corresponding to the TO-modes, and Drude part which takes into account the free carrier contribution:

$$\epsilon(\omega) = \epsilon_{\infty} + \sum_{k=1}^l \frac{\epsilon_{\infty}(\omega_{LOk}^2 - \omega_{TOk}^2)}{\omega_{TOk}^2 - \omega^2 - i\gamma_{TOk}\omega} - \frac{\epsilon_{\infty}\omega_p^2}{\omega(\omega + i\Gamma_p)} \quad (1)$$

In this equation ϵ_{∞} is the high-frequency dielectric constant, ω_{TOk} and ω_{LOk} are the transverse and longitudinal optical-phonon frequencies, l is the number of phonons, ω_p is the plasma frequency, γ_{TOk}

and Γ_p are the phonon and plasmon damping. The use of such a dielectric function is valid in multiphase materials, since it is based on a phenomenological approach where the effective values of the material parameters are used, e.g. $\omega_p^2 = \omega_{p1}^2 + \omega_{p2}^2 + \omega_{p3}^2 + \dots$.

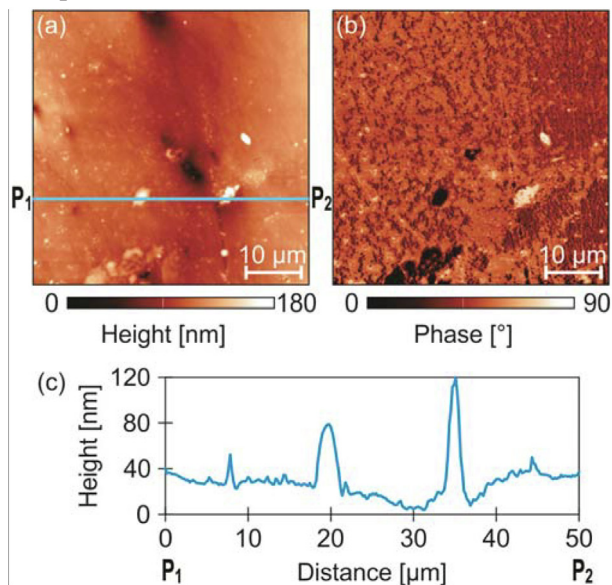
As our ZnSnSb₂ + Mn samples have high concentration of free-carriers (p), and therefore high values of ω_p ($\omega_p^2 \sim p$), it is expected that plasma interacts with phonons. As a result the phonon frequencies are changed, i.e. their positions are shifted from the expected values. The phonon lines observed at the reflection spectra are these shifted modes i.e. coupled plasmon-phonon modes. So, the situation is much clearer if the dielectric function which takes a plasmon-phonon interaction in advance is used [23,24]. It also allows the possibilities that more than one phonon interact with plasma as well as existence of uncoupled phonons. That dielectric function is:

$$\epsilon(\omega) = \epsilon_{\infty} \frac{\prod_{j=1}^{n+1} (\omega^2 + i\gamma_{ij}\omega - \omega_{ij}^2)}{\omega(\omega + i\Gamma_p) \prod_{i=1}^n (\omega^2 + i\gamma_{ii}\omega - \omega_{ii}^2)} \cdot \prod_{k=1}^s \frac{\omega^2 + i\gamma_{LOk}\omega - \omega_{LOk}^2}{\omega^2 + i\gamma_{TOk}\omega - \omega_{TOk}^2} \quad (2)$$

The first fraction in Eq. (2) describes coupling of a plasmon and n LO phonons, where parameters ω_{ij} and γ_{ij} are eigenfrequencies and damping coefficients of the longitudinal component of the coupled phonons. ω_{ii} and γ_{ii} are frequencies and damping of transverse component of these phonons. Γ_p is the plasma damping. The second factor in Eq. (2) represents s uncoupled phonons of the crystal, wherein ω_{LOk} (ω_{TOk}) and γ_{LOk} (γ_{TOk}) are LO (TO) frequencies and damping coefficients of the k -th uncoupled phonon of the crystal.

The analysis of the obtained reflection spectra was performed by a fitting procedure, by adjusting the parameters of Eq. (2) in order to obtain a match between the experimental and theoretical curves. The values of ω_{ij} and ω_{ii} are directly obtained in this way while the ω_p and ω_{LO} values are calculated [25]. It can be seen that the positions of the ω_{l2} and ω_{l4} are significantly different for samples A and B. The behavior of phonons and interactions with plasma were analyzed based on the data thus obtained.

Sample A



Sample B

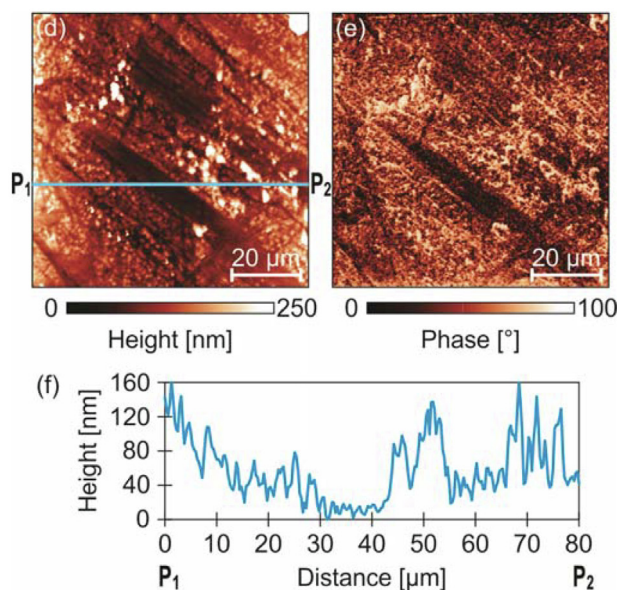


Fig. 3. (a) AFM topography and (b) corresponding phase-contrast image of sample A; (c) Height profile taken along the straight solid line in (a) from point P_1 to point P_2 ; Figures (d), (e), and (f) refer to sample B in the same way.

The phonons of ZnSnSb_2 which are IR active are known from literature [26], and they are of B_2 and E symmetries. Their estimated values are given in Table 1.

Plasmon - phonon interaction commonly refers to the coupling of the plasma and one phonon [27]. In that case two coupled modes appear ω_{11} and ω_{12} , often labeled as ω_+ and ω_- . In the case of ZnSnSb_2 , based on data obtained by fitting procedure, it was established that the plasma interacts with three phonons of B_2 symmetry [28,29,30]. As a result of that their positions are shifted and instead three B_2 modes there are four coupled modes ω_{11} , ω_{12} , ω_{13} and ω_{14} . Obtained values are shown as black points in Fig. 6. Their positions are different for the two samples because of the different influences of the plasma ($\omega_p^2 \sim p$). Because of the high plasma frequency of sample A, the ω_{14} has high value of 675 cm^{-1} which is outside of the measured range.

For ease of analysis, it is common to draw a dependency diagram of obtained parameters (ω_{ij} , ω_b , ω_{TO} , ω_{LO}) on plasma frequency ω_p , as

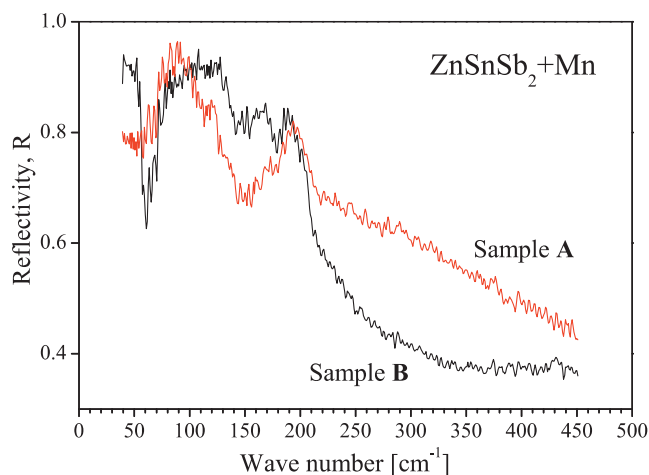


Fig. 4. Far-infrared reflectivity spectra of $\text{ZnSnSb}_2 + \text{Mn}$.

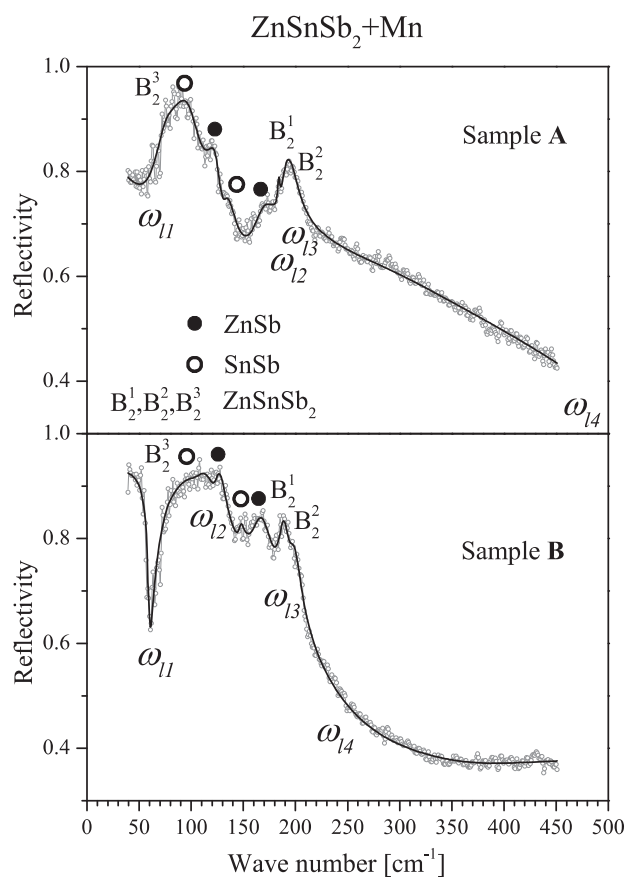


Fig. 5. Analyzed reflection spectra; experimental data are represented by circles while black lines are theoretical curves; registered optical phonons are indicated on the spectra.

shown in Fig. 6. The full lines are solutions of $\text{Re}\{\epsilon(\omega)\} = 0$ from Eq. (1). It should be noted that line ω_{13} between B_2^1 and B_2^2 phonons is barely visible because they are very close. The lines are calculated for five different values of plasma damping Γ_p (Fig. 6) ($\Gamma_p = 1/\tau$, where τ is a lifetime of plasmon). This was done to determine Γ_p interdependence with plasmon - phonon interaction.

The obtained values of plasma damping and plasma frequency of samples A and B are: $\Gamma_{pA} = 500 \text{ cm}^{-1}$, $\Gamma_{pB} = 375 \text{ cm}^{-1}$, $\omega_{pA} = 837 \text{ cm}^{-1}$ and $\omega_{pB} = 405 \text{ cm}^{-1}$. It should be noted that these parameters represent the effective values that describe the sample as a

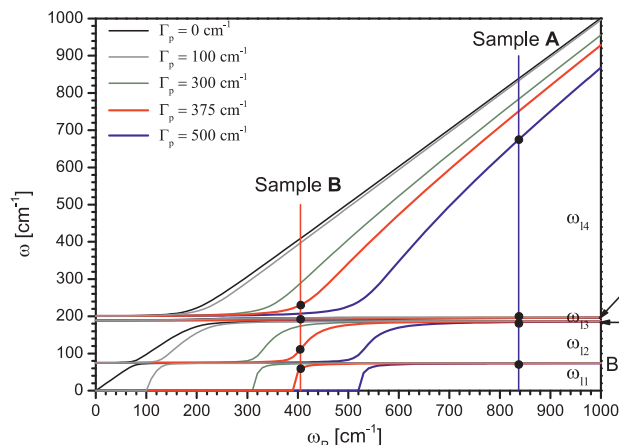


Fig. 6. Analysis of plasmon - three-phonons interaction; Full lines are obtained from Eq. (1), as the solutions of $\text{Re}\{\epsilon(\omega)\} = 0$, for various values of Γ_p ; Black points represent experimentally obtained data for ω_{ij} for both samples (Eq. (2)).

whole. It could be expected (based on p_A and p_B values and $\omega_p^2 \sim p$) that ω_{pA} and ω_{pB} differ about three times, which was not established. Plasma frequency is defined as $\omega_p^2 = (n_p e^2) / (\epsilon_0 \epsilon_\infty m_h^*)$, i.e. it includes other parameters of the material. Thus, by determining the plasma frequency and plasma damping the other properties of the material can be analyzed.

Besides phonons of B_2 symmetry which interact with plasma, other ZnSnSb_2 phonons are not registered on the IR reflectivity spectra. However, characteristic phonons of the other phases can be identified, as can be seen in Fig. 5. It was necessary that these phonons are not covered by the plasmon - phonon interaction. ZnSb modes are noticed at about 125 and 165 cm^{-1} , which is in agreement with results from the literature [31]. Two modes that correspond to SnSb phase are at about 94 and 145 cm^{-1} , which matches the previously obtained data [9,32]. The appearance of these modes is expected due to the significant presence of ZnSb and SnSb phases in the samples. MnSb phonons are not registered, i.e. it was not possible to discern them due to the small amount of that phase.

Based on the performed analyses, it can be seen that different microstructures formed in the investigated samples lead to high concentrations of free carriers, but which are ten times different from each other. Those high values cause plasmon - B_2 phonons interaction. That can be used to analyze optical and electrical properties of the materials, as well as other parameters, such as dielectric constants, effective mass of charge carriers and phonon lifetimes. In this way, the multiphase material with different microstructures was analyzed as a whole.

Investigation of thermoelectric properties of ZnSnSb_2 is a current issue [5,15,33]. The analysis of plasmon - phonon interaction performed in this paper can significantly assist in the study and understanding of thermoelectric processes in this as in other semiconducting polycrystalline materials [34].

5. Conclusion

Two samples of $\text{ZnSnSb}_2 + \text{Mn}$ with different amounts of manganese were analyzed in this paper. The small difference in the initial composition of the material led to a difference of ten times in the free carrier concentrations. Their structural properties were examined by x-ray diffraction, optical microscopy, and AFM. Several different phases were registered - ZnSnSb_2 , ZnSb , SnSb , and small amounts of Sn and MnSb . These phases form different microstructures, which is related to the large irregularities of the lattice. It was found that the high free carrier concentrations are caused by a large number of defects, especially zinc vacancies.

The optical characteristics of these multiphase materials were

examined, whereby the samples were considered as a whole. Based on the analysis of IR reflection spectra the presence of a plasmon - phonons interaction was confirmed. It was determined that three ZnSnSb_2 phonons of B_2 symmetry interact with plasma, which led to the change of their positions. It is clear that strong plasmon - phonon interaction modifies optoelectronic properties of the $\text{ZnSnSb}_2 + \text{Mn}$ samples, and that phonon positions depend on a free carrier concentration. A detailed analysis of this interaction also provides insight into the behavior of other material parameters, such as dielectric constants, effective mass of charge carriers and phonon lifetimes. Also, vibration modes of ZnSb and SnSb phases were registered on the spectra. Knowledge of phonon behavior in a material, as well as interaction with plasma, is very important for studying its thermoelectric properties.

Declaration of competing interest

The authors declare that there is no conflict of interest in this paper.

Acknowledgement

This work was supported under the Agreement of Scientific Collaboration between Polish Academy of Science and Serbian Academy of Sciences and Arts. The work in Serbia was supported by the Serbian Ministry of Education, Science and Technological Development through Project 45003.

Appendix A. Supplementary material

Supplementary data to this article can be found online at <https://doi.org/10.1016/j.infrared.2020.103345>.

References

- [1] J.L. Shay, J.H. Wernick, Ternary Chalcopyrite Semiconductors: Growth, Electronic Properties, and Applications, Chapter 3 - Electronic Structure of II-IV-V₂ Compounds, Pergamon Press, New York, 1975, pp. 79–109 <https://doi.org/10.1016/B978-0-08-017883-7.50008-1>.
- [2] W. Dobrowolski, J. Kossut, T. Story. II–VI and IV–VI Diluted Magnetic Semiconductors – New Bulk Materials and Low-Dimensional Quantum Structures. Handbook of Magnetic Materials 15 (2003) pp. 289–377, (Elsevier, Amsterdam, 2003). [https://doi.org/10.1016/S1567-2719\(03\)15003-2](https://doi.org/10.1016/S1567-2719(03)15003-2).
- [3] L. Kilanski, M. Górska, W. Dobrowolski, E. Dynowska, M. Wójcik, B.J. Kowalski, J.R. Anderson, C.R. Rotundu, D.K. Maude, S.A. Varnavskiy, I.V. Fedorchenko, S.F. Marenkin, Magnetism and magnetotransport of strongly disordered $\text{Zn}_{1-x}\text{Mn}_x\text{GeAs}_2$ semiconductor: The role of nanoscale magnetic clusters, J. Appl. Phys. 108 (2010) 073925, <https://doi.org/10.1063/1.3490231>.
- [4] S.F. Marenkin, A.D. Izotov, I.V. Fedorchenko, V.M. Novotortsev, Manufacture of magnetic granular structures in semiconductor-ferromagnet systems, Russ. J. Inorg. Chem. 60 (2015) 295300, <https://doi.org/10.1134/S0036023615030146>.
- [5] M. Ito, Y. Ohishi, H. Muta, K. Kurosaki, S. Yamanaka, Thermoelectric properties of Zn-Sn-Sb based alloys, Mater. Res. Soc. Symp. Proc. 1314 (2011), <https://doi.org/10.1557/opl.2011.618>.
- [6] P. Balasubramanian, M. Battabyal, D. Sivaprasasam, R. Gopalan, On the formation of phases and their influence on the thermal stability and thermoelectric properties of nanostructured zinc antimonide, J. Phys. D: Appl. Phys. 50 015602 (11 (2017) pp), <https://doi.org/10.1088/1361-6463/50/1/015602>.
- [7] G. Coquil, B. Fraisse, S. Biscaglia, D. Ayme-Perrot, M.T. Sougrati, L. Monconduit, ZnSnSb_2 anode: A solid solution behavior enabling high rate capability in Li-ion batteries, J. Power Sour. 441 (2019) 227165, <https://doi.org/10.1016/j.jpowsour.2019.227165>.
- [8] O. Zobac, J. Sopousek, J. Bursik, A. Zemanova, P. Roupceva, Experimental Study of the Sb-Sn-Zn Alloy System, Metall. Mater. Trans. 45A (2014) 1181–1188, <https://doi.org/10.1007/s11661-013-2104-1>.
- [9] M. Romcevic, M. Gilic, L. Kilanski, W. Dobrowolski, I.V. Fedorchenko, S.F. Marenkin, N. Romcevic, Phonon properties of $\text{ZnSnSb}_2 + \text{Mn}$ semiconductors: Raman spectroscopy, J. Raman Spectrosc. 49 (2018) 1678–1685, <https://doi.org/10.1002/jrs.5421>.
- [10] L. Kilanski, M. Górska, A. Slawska-Waniewska, S. Lewinska, R. Szymczak, E. Dynowska, A. Podgorni, W. Dobrowolski, U. Ralevic, R. Gajic, N. Romcevic, I.V. Fedorchenko, S.F. Marenkin, High temperature magnetic order in $\text{Zn}_{1-x}\text{Mn}_x\text{SnSb}_2 + \text{MnSb}$ nanocomposite ferromagnetic semiconductors, J. Phys.:Condens. Matter. 28 (2016) 336004, <https://doi.org/10.1088/0953-8984/28/33/336004>.
- [11] A. Tenga, F.J. Garcia-Garcia, A.S. Mikhaylushkin, B. Espinosa-Arronte, M. Andersson, U. Haussermann, Sphalerite – Chalcopyrite Polymorphism in Semimetallic ZnSnSb_2 , Chem. Mater. 17 (2005) 6080–6085, <https://doi.org/10.1021/cm042048a>.

- 1021/cm0516053.
- [12] A. Tenga, F.J. Garcia-Garcia, Y. Wu, N. Newman, U. Hausermann, Metal-nonmetal transition in the sphalerite-type solid solution $[\text{ZnSnSb}_2]_{1-x}[\text{InSb}]_x$, *J. Solid State Chem.* 182 (2009) 1438–1442, <https://doi.org/10.1016/j.jssc.2009.03.015>.
- [13] M. Bostrom, S. Hovmoller, Preparation and Crystal Structure of the Pseudo-Decagonal Approximant Mn_3Ga_5 , *J. Solid State Chem.* 153 (2000) 398–403, <https://doi.org/10.1006/jssc.2000.8790>.
- [14] C. Wang, Y. Xu, S. Yang, H. Jiang, J. Li, J. Zhu, S. Yang, X. Liu, Experimental Determination of Phase Equilibria in the Sn-Zn-Sb System, *J. Phase Equil. Diff.* 36 (2015) 350–356, <https://doi.org/10.1007/s11669-015-0387-1>.
- [15] A. Nomura, S. Choi, M. Ishimaru, A. Kosuga, T. Chasapis, S. Ohno, G.J. Snyder, Y. Ohishi, H. Muta, S. Yamanaka, K. Kurosaki, Chalcopyrite ZnSnSb_2 : A Promising Thermoelectric Material, *ACS Appl. Mater. Interf.* 10 (2018) 43682–43690, <https://doi.org/10.1021/acsami.8b16717>.
- [16] V.N. Brudnyi, Electronic properties and pinning of the Fermi level in irradiated II–IV–V₂ semiconductors, *Semiconductors* 43 (2009) 1146–1154, <https://doi.org/10.1134/S1063782609090085>.
- [17] V.G. Voevodin, S.N. Grinyaev, O.V. Voevodina, Nonstoichiometry and point defects in nonlinear optical crystals $\text{A}^2\text{B}^4\text{C}_2^5$, *Mater. Sci. Semicond. Proces.* 6 (2003) 385–388, <https://doi.org/10.1016/j.mssp.2003.07.006>.
- [18] X. Song, M. Schrade, N. Maso, T.G. Finstad, Zn vacancy formation, Zn evaporation and decomposition of ZnSb at elevated temperatures: Influence on the microstructure and the electrical properties, *J. Alloys Comp.* 710 (2017) 762–770, <https://doi.org/10.1016/j.jallcom.2017.03.339>.
- [19] L.V. Prokofieva, P.P. Konstantinov, A.A. Shabal'din, On the tin impurity in the thermoelectric compound ZnSb : Charge-carrier generation and compensation, *Semicond* 50 (2016) 741–750, <https://doi.org/10.1134/S1063782616060208>.
- [20] L. Bjerg, G.K.H. Madsen, B.B. Iversen, Ab initio Calculations of Intrinsic Point Defects in ZnSb , *Chem. Mater.* 24 (2012) 2111–2116, <https://doi.org/10.1021/cm300642t>.
- [21] B. Liu, J. Wu, Y. Cui, H. Wang, Y. Liu, Z. Wang, Z. Ren, G. Cao, Superconductivity in SnSb with a natural superlattice structure, *Supercond. Sci. Technol.* 31 (2018) 7, <https://doi.org/10.1088/1361-6668/aae6fe> 125011.
- [22] Abstreiter G., Cardona M., Pinczuk A. Light scattering by free carrier excitations in semiconductors. In: Cardona M., Güntherodt G. (eds) *Light Scattering in Solids IV*. Topics in Applied Physics, vol 54. Springer, Berlin, Heidelberg. (1984) https://doi.org/10.1007/3-540-11942-6_20.
- [23] A.A. Kukharskii, Plasmon-phonon coupling in GaAs, *Solid State Commun.* 13 (1973) 1761–1765, [https://doi.org/10.1016/0038-1098\(73\)90724-2](https://doi.org/10.1016/0038-1098(73)90724-2).
- [24] N. Romcevic, M. Romcevic, W.D. Dobrowolski, L. Kilanski, M. Petrovic, J. Trajic, B. Hadzic, Z. Lazarevic, M. Gilic, J.L. Ristic-Djurovic, N. Paunovic, A. Reszka, B.J. Kowalski, I.V. Fedorchenko, S.F. Marenki, Far-infrared spectroscopy of $\text{Zn}_{1-x}\text{Mn}_x\text{GeAs}_2$ single crystals: Plasma damping influence on plasmon – Phonon interaction, *J. Alloys Comp.* 649 (2015) 375–379, <https://doi.org/10.1016/j.jallcom.2015.07.087>.
- [25] J. Trajic, N. Romcevic, M. Gilic, M. Petrovic Damjanovic, M. Romcevic, V.N. Nikiforov, Optical properties of $\text{PbTe}_{0.95}\text{S}_{0.05}$ single crystal at different temperatures: Far - infrared study, *Optoelec. Adv. Mater. Rap. Comm.* 6 (2012) 543–546.
- [26] F.W. Ohrendorf, H. Haeuselner, Lattice Dynamics of Chalcopyrite Type Compounds. Part I. Vibrational Frequencies, *Cryst. Res. Technol.* 34 (1999) 339–349, [https://doi.org/10.1002/\(SICI\)1521-4079\(199903\)34:3<339::AID-CRAT339>3.0.CO;2-E](https://doi.org/10.1002/(SICI)1521-4079(199903)34:3<339::AID-CRAT339>3.0.CO;2-E).
- [27] Klein M.V. Electronic Raman Scattering. In: Cardona M. (eds) *Light Scattering in Solids*. Topics in Applied Physics, vol 8. Springer, Berlin, Heidelberg (1975). https://doi.org/10.1007/978-3-540-37568-5_4.
- [28] M. Petrovic, N. Romcevic, J. Trajic, W.D. Dobrowolski, M. Romcevic, B. Hadzic, M. Gilic, A. Mycielski, Far-infrared spectroscopy of $\text{CdTe}_{1-x}\text{Se}_x(\text{In})$: Phonon properties, *Infrared Phys. Tech.* 67 (2014) 323–326, <https://doi.org/10.1016/j.infrared.2014.08.010>.
- [29] M. Romcevic, N. Romcevic, W. Dobrowolski, L. Kilanski, J. Trajic, D.V. Timotijevic, E. Dynowska, I.V. Fedorchenko, S.F. Marenkin, Optical properties and plasmon – Two different phonons coupling in $\text{ZnGeAs}_2 + \text{Mn}$, *J. Alloys Comp.* 548 (2013) 33–37, <https://doi.org/10.1016/j.jallcom.2012.09.017>.
- [30] I.J. Luxmoore, C.H. Gan, P.Q. Liu, F. Valmorra, P. Li, J. Faist, G.R. Nash, Strong coupling in the far-infrared between graphene plasmons and the surface optical phonons of silicon dioxide, *ACS Photonics* 1 (2014) 1151, <https://doi.org/10.1021/ph500233s>.
- [31] D.V. Smirnov, D.V. Mashovets, S. Pasquier, J. Leotin, P. Puech, G. Landa, Yu.V. Roznovan, Long-wavelength optical phonons of $\text{Cd}_x\text{Zn}_{1-x}\text{Sb}$ mixed crystals, *Semicond. Sci. Technol.* 9 (1994) 333–337.
- [32] P. Nithyadharseni, M.V. Reddy, B. Nalini, M. Kalpana, B.V.R. Chowdari, Sn-based Intermetallic Alloy Anode Materials for the Application of Lithium Ion Batteries, *Electrochim. Acta* 161 (2015) 261–268, <https://doi.org/10.1016/j.electacta.2015.02.057>.
- [33] Yu M. BasalaeV, Ab Initio Study of the ZnSnSb_2 Semiconductor, *Semiconductors* 52 (2018) 1715–1720, <https://doi.org/10.1134/S1063782618130043>.
- [34] Q. Xu, J. Zhou, T.H. Liu, G. Chen, Effect of electron-phonon interaction on lattice thermal conductivity of SiGe alloys, *Appl. Phys. Lett.* 115 (2019) 023903, <https://doi.org/10.1063/1.5108836>.



Contents lists available at ScienceDirect

Spectrochimica Acta Part A: Molecular and Biomolecular Spectroscopy

journal homepage: www.elsevier.com/locate/saa

Influence of chemical fixation process on primary mesenchymal stem cells evidenced by Raman spectroscopy

J.J. Lazarević^a, U. Ralević^a, T. Kukolj^b, D. Bugarski^b, N. Lazarević^{a,*}, B. Bugarski^c, Z.V. Popović^{a,d}

^aCenter for Solid State Physics and New Materials, Institute of Physics Belgrade, University of Belgrade, Pregrevica 118, Belgrade 11080, Serbia

^bLaboratory for Experimental Hematology and Stem Cells, Institute for Medical Research, University of Belgrade, Belgrade 11000, Serbia

^cDepartment of Chemical Engineering, Faculty of Technology and Metallurgy, University of Belgrade, Karnegijeva 4, Belgrade 11060, Serbia

^dSerbian Academy of Sciences and Arts, Knez Mihailova 35, Belgrade 11000, Serbia

ARTICLE INFO

Article history:

Received 7 December 2018

Received in revised form 6 March 2019

Accepted 6 March 2019

Available online 9 March 2019

Keywords:

Raman spectroscopy

Stem cells

Chemical fixation

ABSTRACT

In investigation of (patho)physiological processes, cells represent frequently used analyte as an exceptional source of information. However, spectroscopic analysis of live cells is still very seldom in clinics, as well as in research studies. Among others, the reasons are long acquisition time during which autolysis process is activated, necessity of specified technical equipment, and inability to perform analysis in a moment of sample preparation. Hence, an optimal method of preserving cells in the existing state is of extreme importance, having in mind that selection of fixative is cell lineage dependent. In this study, two commonly used chemical fixatives, formaldehyde and methanol, are used for preserving primary mesenchymal stem cells extracted from periodontal ligament, which are valuable cell source for reconstructive dentistry. By means of Raman spectroscopy, cell samples were probed and the impact of these fixatives on their Raman response was analyzed and compared. Different chemical mechanisms are the core processes of formaldehyde and methanol fixation and certain Raman bands are shifted and/or of changed intensity when Raman spectra of cells fixed in that manner are compared. In order to get clearer picture, comprehensive statistical analysis was performed.

© 2019 Elsevier B.V. All rights reserved.

1. Introduction

Mesenchymal stem cells (MSCs) are heterogenous group of adult stem cells originally discovered in bone marrow, but present in all tissues and organs, with the purpose to keep tissue homeostasis, regeneration and renewal. These acts are performed not only through multipotent differentiation potential (toward chondrogenic, adipogenic, and osteogenic lineages), but also through their ability to modulate immune response (directly or indirectly) [1–5]. Although MSCs possess common cellular features, it is overall accepted that these cells still exhibit variable regenerative capacity due to different tissue origin, donor diversity, and variations in culture conditions [6,7]. Human MSCs investigated in this study originate from periodontal ligament, a fibrous, cellular, and vascular soft connective tissue. The main role of periodontal ligament is to anchor tooth to the alveolar bone, maintain mineralisation level and alleviate mechanical forces associated with the process of mastication [8–10]. Previously, it was demonstrated that human periodontal ligament

stem cells (hPDLSCs) investigated in this experiment fulfill criteria for MSCs identification and characterization, set by The International Society for Cell Therapy (ISCT) [11,12]. Minimal criteria for characterization of human MSCs, set by ISCT, include plastic adhesion, with expression of CD73, CD90, CD105 surface markers and lack of hematopoietic markers CD34–, CD45–, CD14–, CD79 α –, HLA-DR–; and multilineage differentiation potential into osteoblasts, adipocytes, and chondroblasts [13]. However, MSCs nature, including hPDLSCs, is still elusive. Therefore, the exploration of hPDLSCs, as a cell source for reconstructive dentistry, is of great importance for the novel therapeutic strategies related to recovery of periodontium and curing dental defects [14].

Taking into account the heterogeneity of MSCs, it is crucial for these cells to be adequately characterized during the lifespan, before further manipulation. Although many techniques are available in this field, including mass spectroscopy, flow cytometry, and immunocytochemistry, most of them are destructive, invasive, time consuming or require expensive cell-specific labels [15,16]. However, a light scattering technique, Raman spectroscopy, is able to overrun these issues due to its unique properties: it is non-invasive, non-destructive, fast, label-free, and complex sample preparation is not required. It operates with low sample volume even in aqueous

* Corresponding author.

E-mail address: nenadl@ipb.ac.rs (N. Lazarević).

solutions and provide a plenty of biochemical information as an outcome. Raman spectroscopy is a type of vibrational spectroscopy, based on Raman effect [17], in which an inelastically scattered component of the visible light bears the information of the analyte. Raman scattering experiment results in vibrational spectrum, a fingerprint of a sample, which carries the information about chemical composition and structure of a sample, on a submolecular level. Typically, it comprises vibrational modes of the highest Raman scattering cross section [16, 18–20].

Spectroscopic analysis of live cells is still very seldom, both in clinical and research conditions, particularly due to the longevity of the processes, when autolysis is inevitable. On the other hand, it is not always possible to investigate a sample in a moment of acquiring. The crucial and fundamental step in cell biology, for obtaining sensitive and reproducible results, is a process called fixation, which maintain the localization of biomolecules. It is used for preserving a cell in a physiological state, by preventing cell shrinkage or swelling caused by osmotic pressure initiated with air-drying, as well as autolysis by activating lysosomal enzymes, which includes denaturation of proteins, dephosphorylation of mononucleotides, phospholipids and proteins, chromatin compaction, nuclear fragmentation, and cytoplasmic condensation and fragmentation [21]. However, it is known that selection of a fixative is very much dependent on a cell nature when it comes to Raman spectroscopy and can significantly distort experimental data [22]. In the past decade, investigations of different fixatives' influence on Raman spectra of numerous cell lineages were reported, with an aim to clarify the best option for each cell lineage. One of the studies investigated the effect of formaldehyde and ethanol fixation on CARS (Coherent Anti-Stokes Raman Spectroscopy) signal of proteins and lipids in different cellular compartments of glial and neuronal cells, concluding that formaldehyde fixation is preferable method of preservation of these cells [22]. Also, the effect of chemical fixation procedures on the Raman spectra of normal and leukemia cells was characterized [23]. When compared to the spectra of unfixed cells, the fixed cell spectra showed changes in the intensity of specific Raman markers, and latter statistical analysis suggested that methanol provokes greater changes in Raman spectra when compared to paraformaldehyde. Further, micro-Raman spectroscopy was employed for chemical fixation mechanism study in three cell lines (normal skin, normal bronchial epithelium, and lung adenocarcinoma) [24]. Nucleic acid degradation, protein denaturation, and lipid leaching was observed with all fixatives (formalin, Carnoy's fixative, and methanol-acetic acid) and for all cell lines, but to varying degrees. Also, the authors suggested that formalin best preserves cellular integrity and gives the closest spectral content to that in live cells. The next study monitored the impact of fixation by formalin, desiccation, and air-drying on *in vitro* cell culture lines [25]. The results indicate that the choice of fixation methodology significantly influences the quality and reproducibility of the resulting spectral data. Formalin showed inconsistency in sample preservation and a loss of signal intensity, while air-drying appears to be inconsistent in terms of spectral reproducibility. Desiccation showed good spectral reproducibility and good signal-to-noise ratio [25].

Although numerous Raman studies of fixative process' spectral influence have been performed [22–25], according to our knowledge, no such research has been performed on primary mesenchymal stem cells originating from periodontal ligament. We used micro-Raman spectroscopy in order to probe fixed hPDLSCs and investigate the effects of two most frequently used chemical fixatives which have different chemical mechanisms of preservation (formaldehyde and methanol), and then compared those effects. Formaldehyde reacts extensively with amino groups to form methylene bridges and cross-links molecules, which alters, but stabilizes them [26]. Further, formaldehyde does not appear to perturb tertiary structure very much. On the other hand, methanol replaces water in cell environment, disrupts hydrophobic and hydrogen bonding, and

consequently alters tertiary structure of proteins [27,28]. Although fixation substantially alters composition and appearance, it is possible to produce consistent chemical and physical properties by selection of suitable preparation conditions. Nevertheless, standardization of Raman spectroscopy regarding fixative selection could provide valuable additional information in many biological tests that require cell fixation and also indicate the existence of fine differences in the fixative effect that are necessary to be taken into consideration during standard biological protocols.

2. Experiment

2.1. Isolation and Cultivation of Human Periodontal Ligament Stem Cells

After getting the informed consent from healthy patients (age 18), subjected to the procedure of tooth extraction for orthodontic reasons, at the Department of Oral Surgery of the Faculty of Dental Medicine, the University of Belgrade, human periodontal ligament tissues from normal impacted third molars were collected. Immediately after, tissues were placed in sterile cell culturing conditions. As previously reported [11], human PDLSCs were isolated, characterized and expanded. For hPDLSCs isolation, periodontal tissues were carefully detached from the mid-third of the root surface, cut into small pieces and placed in a 25 cm² flask with Dulbecco's modified Eagle's medium (DMEM; Sigma-Aldrich St. Louis, MO, USA) supplemented with 10% fetal bovine serum (FBS; Capricorn-Scientific, Germany), 100 U/ml penicillin and 100 mg/ml streptomycin (Gibco, Thermo Fisher Scientific, USA). Standard cultivation conditions included 37 °C temperature, humidified atmosphere containing 5% CO₂, while medium was exchanged two times per week. After reaching 80% to 90% confluence, cells were detached regularly in growth medium (GM-DMEM with 10% FBS) using 0.05% trypsin with 1 mM EDTA (Gibco, Thermo Fisher Scientific, USA). In order to demonstrate the universality of experimental results for MSCs, cells from third and sixth passages were used, divided into two batches. Moreover, hPDLSCs were characterized based on immunophenotype and multipotent differentiation potential toward osteogenic, chondrogenic and adipogenic lineages as it has been described before [11]. All treatments were performed according to the approved ethical guidelines set by Ethics Committee of the Faculty of Dental Medicine, University of Belgrade and Declaration of Helsinki.

2.2. Sample Preparation

For the Raman experiment, hPDLSCs were seeded on rounded CaF₂ slides in 24-well plate (5 × 10³ cells per slide) and cultivated in GM in standard cultivation conditions during 24 h. Following the adhesion, hPDLSCs were washed with saline buffer and fixed with 3.7% formaldehyde or methanol for 10 min at room temperature. Right before Raman spectroscopy was performed, samples were washed with distilled water.

2.3. μ -Raman Spectroscopy

In most of the cases, the Raman spectroscopy independently probes single vibrations within a molecule or a crystal, but in a complex biological systems composed of various types of macromolecules, only vibrational bands consisting of numerous vibrations of the same type, rather than a single vibration, could be distinguished. Consequently, the changes of biological system composition may result with a change of certain Raman bands line-shapes and/or intensities.

The Raman scattering experiment was performed using NTegra Spectra from NTMDT. The 532 nm line of a semiconductor laser was used as an excitation source. The laser power was set to 2 mW

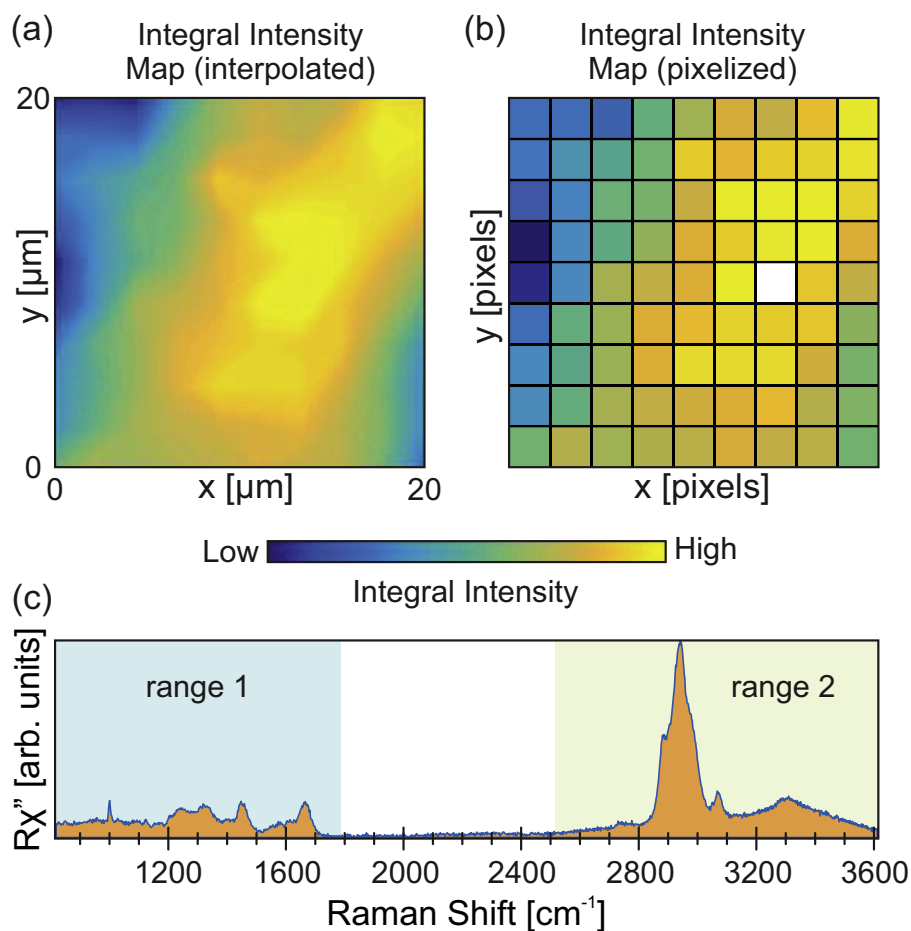


Fig. 1. A single PDLSC Raman (a) interpolated integral intensity map, and (b) pixelized integral intensity map. (c) Human PDLSC Raman scattering spectrum acquired on a pixel marked in white.

and focused on the area of about $1\ \mu\text{m}$, in order to provide a reasonable Raman intensity for a 60 s long acquisition. Under these conditions, the sample associated Raman bands, acquired sequentially at the same position, were found to be stable in terms of both the band intensity and spectral position. In other words, no visible laser induced modifications of the cells were observed upon repeating the signal acquisition for a few times at any of the acquisition points.

Due to very complex inner structure of a cell, there may be small variations in Raman spectra for the data collected at different positions. Consequently, suitable methodology must be applied in order to achieve the needed level of sample representation. In other words, the applied method has to be robust. Here, two batches of cells treated with methanol and formaldehyde were examined by spatially mapping the Raman scattering signal on 20 cells per batch. The spectra were collected at 10×10 or 11×11 matrices of spatial points separated by a distance larger than the estimated focus diameter of $\approx 1\ \mu\text{m}$. The distance between adjacent spatial points, or the spatial resolution, was varied between $2\ \mu\text{m}$ and $3\ \mu\text{m}$ depending on the cell size. The example of an interpolated spectral map of a single methanol fixed cell is presented in Fig. 1(a). Fig. 1(b) shows the same map with the actual pixels omitting the interpolation for clarity. The x and y represent spatial coordinates in which a spectrum is acquired. The intensity of a pixel, labeled white in Fig. 1(b), is obtained by integrating the Raman spectra collected at that pixel. The value of the integral is equal to the area below the acquired signal as illustrated by shaded (orange) area below the typical hPDLSC

Raman spectra in Fig. 1(c). It is characterized by clearly visible Raman bands in two spectral regions marked in Fig. 1(c). The first spectral region spans from $800\ \text{cm}^{-1}$ to $1770\ \text{cm}^{-1}$, whereas the second starts at $2500\ \text{cm}^{-1}$ and ends at $3600\ \text{cm}^{-1}$.

2.4. Data Processing and Analysis

In addition to typical PDLSCs Raman spectra [Fig. 1(c)], a few (in total) significantly different spectra, having an extremely high

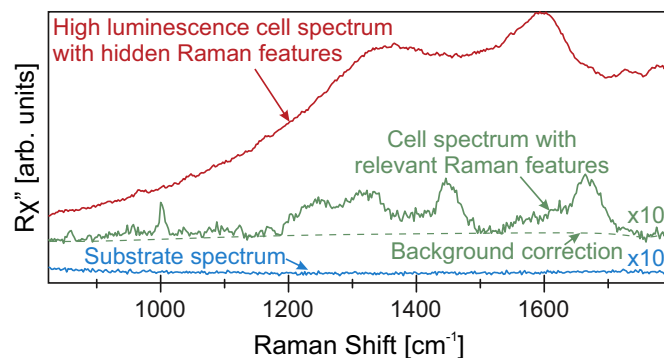


Fig. 2. A typical PDLSCs, substrate, and high luminescence points Raman spectra in the range from $800\ \text{cm}^{-1}$ to $1800\ \text{cm}^{-1}$, depicting spectral selection and preprocessing.

luminescence contribution, were observed as well. The example of such a spectrum truncated to the spectral region from 800 cm^{-1} to 1770 cm^{-1} is shown in Fig. 2. Clearly, extremely strong luminescence masks the relevant Raman bands, making them misleading. Consequently, the high luminescence spectra were omitted from the analysis. The relevant Raman spectra were preprocessed before further manipulation. In the initial step, the background, modelled as a polynomial function of the fourth degree, was subtracted (see Fig. 2). Upon background removal, the spectra were normalized to the value of the integral intensity, calculated within the considered spectral region and then subjected to the analysis.

Besides the direct comparison of the Raman spectra of the cells fixed with formaldehyde and methanol, a multivariate statistical method, principal component analysis (PCA), was applied [15,18,29,30]. Thereby, the dimensionality of the experimental data set is reduced, by transforming to a new set of variables, the principal components, which are uncorrelated and ordered in a way that the first few retain most of the variation present in all of the original variables [31]. The outcome of this analysis is distinct grouping of Raman spectra based on their mutual features [18,29].

3. Results and Discussion

Regarding biological background of our samples, it is well known that primary mesenchymal stem cell cultures represent heterogenic cellular populations, thus the intrinsic heterogeneity of primary cells should be taken into consideration. Moreover, cellular features of

these cells are highly prone to modifications during standard cultivation process [32,33]. Therefore, in order to get reproducible results, we analyzed cells from different passages (passage 3 in Batch 1 and passage 6 in Batch 2).

It is known that the effect of fixation process is cell type and fixative dependent [25]. Different chemical mechanisms may result in variations of the respective Raman spectra. Whereas depletion of certain component will result in reduction of corresponding Raman bands' intensities, various perturbations of the electronic cloud will lead to the changes of bands energy and linewidth. The second does not exclude the possibility of variations of the Raman intensities since the change in electronic structure may impact probability of the inelastic light scattering processes. In our data, the most pronounced changes are occurring in two spectral regions [Fig. 1], ranging from 800 cm^{-1} to 1770 cm^{-1} and from 2500 cm^{-1} to 3600 cm^{-1} . In the statistical treatment, these regions were analyzed independently due to the intrinsic imperfections of the spectrometer.

In Fig. 3, 2D Raman spectra map, averaged spectra, their difference and PCA of Batch 1 and Batch 2 of formaldehyde and methanol fixed PDLSCs, are presented respectively, for spectral region between 800 cm^{-1} and 1770 cm^{-1} . Closer inspection of formaldehyde and methanol fixed PDLSCs 2D Raman spectra map [Fig. 3(a) and (c)] already reveals significant difference between two groups. Relative change of intensity and/or energy shift can be clearly observed for multiple Raman bands. This is even more evident in the difference of formaldehyde and methanol fixed PDLSCs average Raman spectra [Fig. 3(a) and (c)]. It can be seen that phenylalanine peaks at 1002 cm^{-1} and 1030 cm^{-1} are of higher intensity in methanol fixed PDLSCs Raman spectra compared to formaldehyde fixed ones.

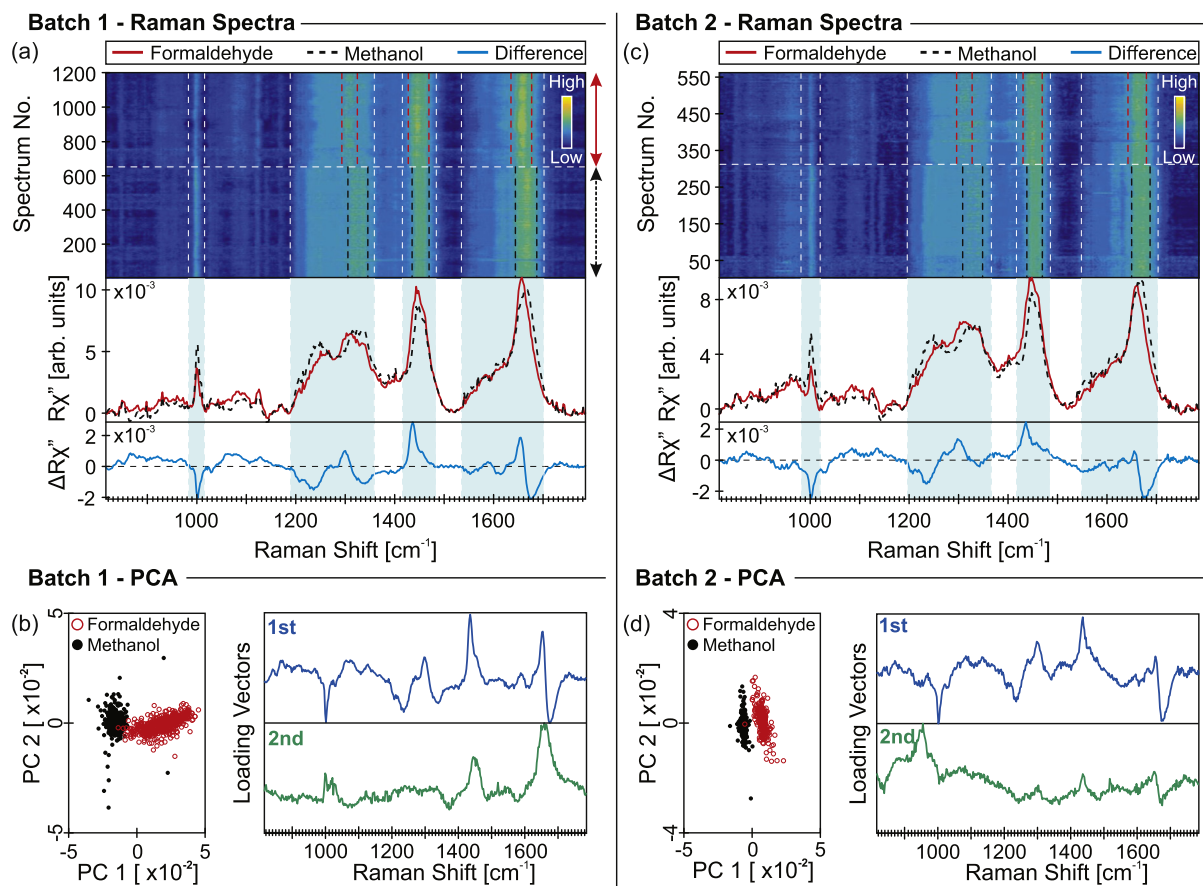


Fig. 3. 2D Raman spectra map obtained from PDLSCs (see Supplementary information), fixed with formaldehyde and methanol, their mean spectra, as well as their difference for the spectral region from 800 cm^{-1} to 1770 cm^{-1} ; PCA score plots calculated for these two groups of cells, and PCA loading vectors for (a)–(b) Batch 1 and (c)–(d) Batch 2, respectively. Percentage of variance PC1–PC2: for Batch 1 19.85%–5.76%; for Batch 2 17.95%–7.43%.

The DNA bands at 1095 cm^{-1} , 1130 cm^{-1} , and 1330 cm^{-1} are of higher intensity in formaldehyde fixed PDLSCs spectra whereas the band at about 1330 cm^{-1} is also slightly shifted. Amide III band at about 1260 cm^{-1} is significantly shifted and of higher intensity in methanol fixed spectra. When it comes to lipid band at 1450 cm^{-1} , it is of noticeable higher intensity and shifted in formaldehyde fixed spectra, as well as the Amide I band at about 1660 cm^{-1} .

The observed behaviour is consistent with the biochemical picture in which the protein content is larger in methanol fixed cells. This is evidenced by more pronounced phenylalanine peak. On the other hand, the secondary structure is more preserved in formaldehyde fixed samples (Amide I band). Modification of native proteins by formaldehyde does not perturb the secondary structure very much. Lipid content is maintained greatly in formaldehyde fixed sample, which is in a good agreement with the literature, due to methanol-caused leaching of lipids through deteriorated cell membrane. As a consequence of cross-linking mechanism of fixation, DNA level is maintained in greater moiety in formaldehyde fixed PDLSCs Raman spectrum [27,28,34].

Spectra of averaged formaldehyde and methanol fixed PDLSCs spectra, and their difference spectrum, from Batch 2 are given in Fig. 3(c). The only observable difference, in comparison to Batch 1, is lower intensity of Amide I band at 1660 cm^{-1} in formaldehyde fixed PDLSCs Raman spectrum, relative to methanol fixed PDLSCs spectrum.

The same procedure is repeated for spectral region from 2500 cm^{-1} to 3600 cm^{-1} . In Fig. 4, 2D Raman spectra map, averaged

spectra, their difference, and PCA of Batch 1 and Batch 2 of formaldehyde and methanol fixed PDLSCs, are presented respectively. Again, formaldehyde and methanol fixed PDLSCs Raman spectra are compared in this spectral region which reflects protein, lipid, and water content. In Fig. 4(a) and (c), it is observable from averaged spectra of difference that the bands at 2860 cm^{-1} and 2890 cm^{-1} , are more intense in formaldehyde fixed PDLSCs Raman spectra. These two bands present CH_2 and CH_3 symmetric stretch in lipids and proteins [35]. Raman band at 2940 cm^{-1} is assigned to CH vibrations in lipids and proteins and is more pronounced in methanol fixed PDLSCs Raman spectra. This confirms above-mentioned statements that formaldehyde better maintains the level of lipids with regard to methanol. On the other hand, methanol keeps protein levels.

Further, PCA is applied for the treatment of the spectral data, and the outcome is presented in Figs. 3 (b), (d) and 4(b), (d) for Batch 1 and Batch 2, respectively. Analyzing PCA score plots, clear assemblage of cells fixed with the same fixative is observable and, as expected, in all cases, PC1 is the component that makes the difference [Figs. 3(b), (d), and 4(b), (d)]. Only a few overlapping points have been observed due to the heterogeneity of the samples and/or variable signal-to-noise ratio. For illustration, PC2s and corresponding loading vectors are also presented. They represent intra- and inter-cellular variations, within the group of cells fixed with the same fixative. PC1 loading vectors are consistent with discrepancies directly observable in Raman spectra of differences, as discussed above. This is not surprising, having in mind the nature of this principal component and the algorithms applied.

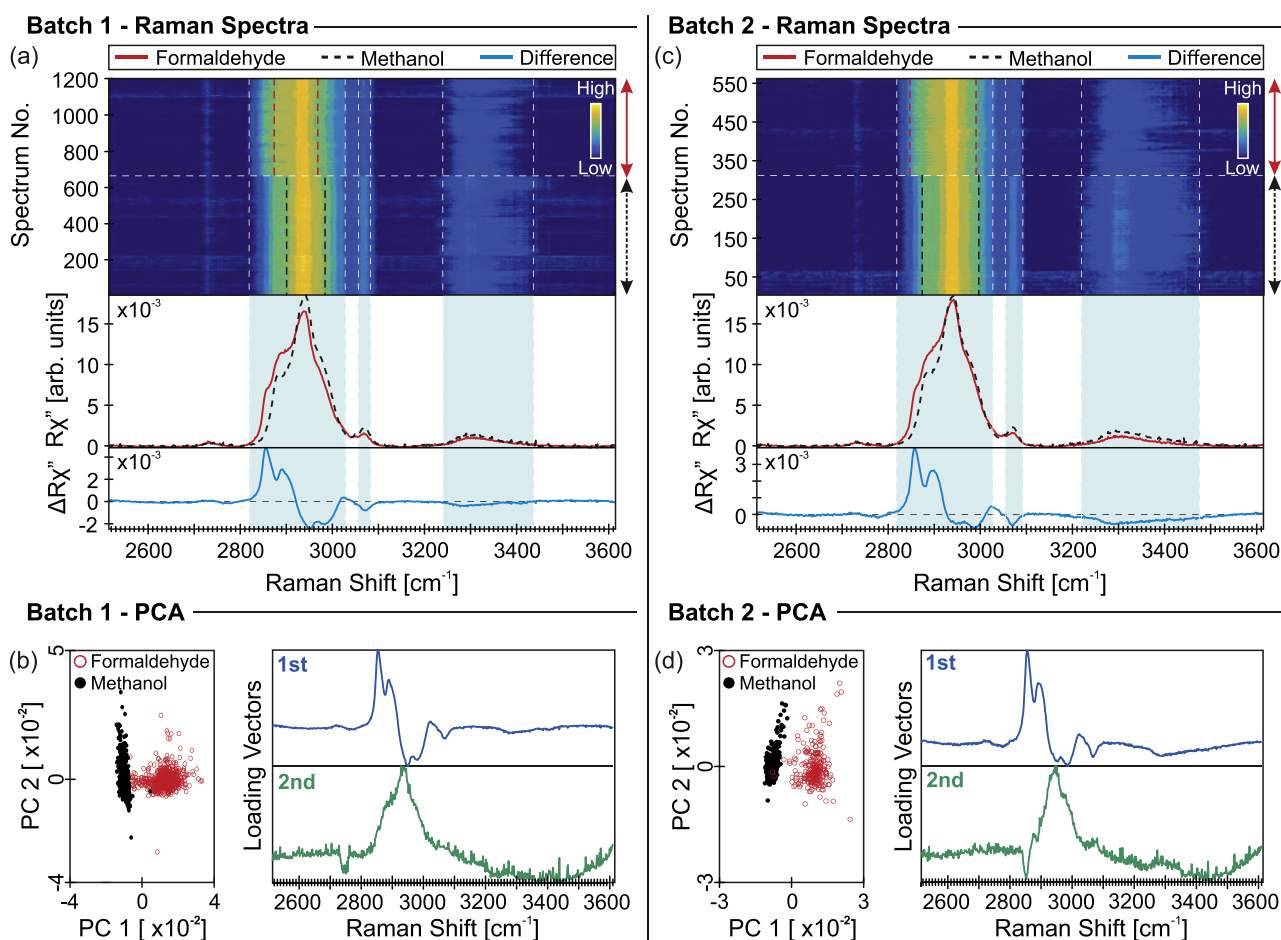


Fig. 4. 2D Raman spectra map obtained from PDLSs (see Supplementary information), fixed with formaldehyde and methanol, their mean spectra, as well as their difference for spectral region from 2500 cm^{-1} to 3600 cm^{-1} ; PCA score plots calculated for these two groups of cells, and PCA loading vectors for (a)–(b) Batch 1 and (c)–(d) Batch 2, respectively. Percentage of variance PC1–PC2: for Batch 1 64.09%–12.59%; for Batch 2 60.08%–14.64%.

Closer inspection of PCA score plots [Figs. 3(b), (d), and 4(b), (d)] reveals greater spread along PC1 for Batch 1, in particular for the spectral region from 800 cm^{-1} to 1770 cm^{-1} of formaldehyde fixed cells. This is most likely a consequence of heterogeneity of these primary cells. Depending on the nature of the inter-/intracellular variations, fixation process may enhance and/or suppress their Raman spectra signatures [22–26]. Detailed comparison between batches for both fixatives is presented in the Supplementary information.

4. Conclusion

Fixatives cause dramatic changes for all cell types but to varying extent. It is crucial to have a clear idea of what is expected from the sample when choosing the fixative agent. Preservation of cells by formaldehyde and methanol treatment represents standard procedures in most laboratory protocols. In this study, we investigated the effects of these two chemicals on Raman spectra of primary cell lineage, PDLSCs. Both procedures provided quantitatively and qualitatively close Raman spectra that can be considered as fingerprint spectra for this cell lineage. Through the direct comparison of the Raman spectra, as well as the statistical treatment, subtle differences have been observed between two groups that can be traced back to the variations in lipid and protein content. Consequently, when choosing the fixation method, the purpose of investigation has to be kept in mind. When it comes to Raman spectroscopy of hPDLSCs, both formaldehyde and methanol are acceptable choices, but with unlike sensitivity for tracing different biochemical composition.

Acknowledgments

We gratefully acknowledge M. Miletić and M. Andrić for supplying the periodontal ligament tissue. This work was supported by the Ministry of Education, Science, and Technological Development of the Republic of Serbia under Projects Nos. III46010, III45018, ON175062, and OI171005.

Appendix A. Supplementary Data

Supplementary data to this article can be found online at <https://doi.org/10.1016/j.saa.2019.03.012>.

References

- [1] M. Gazdic, V. Volarevic, N. Arsenijevic, M. Stojkovic, Mesenchymal stem cells: a friend or foe in immune-mediated diseases, *Stem Cell Rev. Rep.* 11 (2) (2015) 280–287.
- [2] Y. Sato, H. Araki, J. Kato, K. Nakamura, Y. Kawano, M. Kobune, T. Sato, K. Miyayoshi, T. Takayama, M. Takahashi, et al. Human mesenchymal stem cells xenografted directly to rat liver are differentiated into human hepatocytes without fusion, *Blood* 106 (2) (2005) 756–763.
- [3] R.O. Oreffo, C. Cooper, C. Mason, M. Clements, Mesenchymal stem cells, *Stem Cell Rev.* 1 (2) (2005) 169–178.
- [4] A.R. Williams, J.M. Hare, Mesenchymal stem cells biology, pathophysiology, translational findings, and therapeutic implications for cardiac disease, *Circ. Res.* 109 (8) (2011) 923–940.
- [5] J. Lazarević, T. Kukulj, D. Bugarski, N. Lazarević, B. Bugarski, Z. Popović, Probing primary mesenchymal stem cells differentiation status by micro-Raman spectroscopy, *Spectrochim. Acta A Mol. Biomol. Spectrosc.* 213, 384–390.
- [6] R. Hass, C. Kasper, S. Böhm, R. Jacobs, Different populations and sources of human mesenchymal stem cells (msc): a comparison of adult and neonatal tissue-derived msc, *Cell Commun. Signal* 9 (1) (2011) 12.
- [7] D.G. Phinney, Functional heterogeneity of mesenchymal stem cells: implications for cell therapy, *J. Cell. Biochem.* 113 (9) (2012) 2806–2812.
- [8] I.C. Gay, S. Chen, M. MacDougall, Isolation and characterization of multipotent human periodontal ligament stem cells, *Orthod. Craniofacial Res.* 10 (3) (2007) 149–160.
- [9] S. Ivanovski, S. Gronthos, S. Shi, P. Bartold, Stem cells in the periodontal ligament, *Oral Dis.* 12 (4) (2006) 358–363.
- [10] M. Shimono, T. Ishikawa, H. Ishikawa, H. Matsuzaki, S. Hashimoto, T. Muramatsu, K. Shima, K.I. Matsuzaka, T. Inoue, Regulatory mechanisms of periodontal regeneration, *Microsc. Res. Tech.* 60 (5) (2003) 491–502.
- [11] A. Miletić, S. Mojsilović, I. Okić-Djordjević, T. Kukulj, A. Jauković, J. Santibanez, G. Jovčić, D. Bugarski, Mesenchymal stem cells isolated from human periodontal ligament, *Arch. Biol. Sci.* 66 (1) (2014) 261–271.
- [12] T. Kukulj, D. Trivanović, I.O. Djordjević, J. Mojsilović, J. Krstić, H. Obradović, S. Janković, J.F. Santibanez, A. Jauković, D. Bugarski, Lipopolysaccharide can modify differentiation and immunomodulatory potential of periodontal ligament stem cells via ERK1, 2 signaling, *J. Cell. Physiol.* 233 (1) (2018) 447–462.
- [13] A. Klimczak, U. Kozłowska, Mesenchymal stromal cells and tissue-specific progenitor cells: their role in tissue homeostasis, *Stem Cells Int.* 2016 (2016) 1–11.
- [14] H. Egusa, W. Sonoyama, M. Nishimura, I. Atsuta, K. Akiyama, Stem cells in dentistry—part II: clinical applications, *J. Prosthodont. Res.* 56 (4) (2012) 229–248.
- [15] A. Downes, R. Mouras, A. Elfick, Optical spectroscopy for noninvasive monitoring of stem cell differentiation, *BioMed Res. Int.* 2010 (2010) 1–10.
- [16] A. Downes, R. Mouras, P. Bagnaninchi, A. Elfick, Raman spectroscopy and CARS microscopy of stem cells and their derivatives, *J. Raman Spectrosc.* 42 (10) (2011) 1864–1870.
- [17] C.V. Raman, K.S. Krishnan, A new type of secondary radiation, *Nature* 121 (3048) (1928) 501.
- [18] J.W. Chan, D.K. Lieu, Label-free biochemical characterization of stem cells using vibrational spectroscopy, *J. Biophotonics* 2 (11) (2009) 656–668.
- [19] A.F. Palonpon, J. Ando, H. Yamakoshi, K. Dodo, M. Sodeoka, S. Kawata, K. Fujita, Raman and SERS microscopy for molecular imaging of live cells, *Nat. Protoc.* 8 (4) (2013) 677–692.
- [20] I. Notingher, I. Bisson, A.E. Bishop, W.L. Randle, J.M. Polak, L.L. Hench, In situ spectral monitoring of mRNA translation in embryonic stem cells during differentiation in vitro, *Anal. Chem.* 76 (11) (2004) 3185–3193.
- [21] F. Lyng, E. Gazi, P. Gardner, Preparation of Tissues and Cells for Infrared and Raman Spectroscopy and Imaging, *Biomedical Applications of Synchrotron Infrared Microspectroscopy: A Practical Approach*, Royal Society of Chemistry, Cambridge, 2010, 147–191.
- [22] S.M. Levchenko, X. Peng, L. Liu, J. Qu, The impact of cell fixation on CARS signal intensity in neuronal and glial cell lines, *J. Biophotonics* (2018) e201800203.
- [23] J.W. Chan, D.S. Taylor, D.L. Thompson, The effect of cell fixation on the discrimination of normal and leukemia cells with laser tweezers Raman spectroscopy, *Biopolymers Original Res. Biomol.* 91 (2) (2009) 132–139.
- [24] A.D. Meade, C. Clarke, F. Draux, G.D. Sockalingum, M. Manfait, F.M. Lyng, H.J. Byrne, Studies of chemical fixation effects in human cell lines using Raman microspectroscopy, *Anal. Bioanal. Chem.* 396 (5) (2010) 1781–1791.
- [25] M.M. Mariani, P. Lampen, J. Popp, B.R. Wood, V. Deckert, Impact of fixation on in vitro cell culture lines monitored with Raman spectroscopy, *Analyst* 134 (6) (2009) 1154–1161.
- [26] E.A. Hoffman, B.L. Frey, L.M. Smith, D.T. Auble, Formaldehyde crosslinking: a tool for the study of chromatin complexes, *J. Biol. Chem.* (2015) jbc-R115.
- [27] M. Noguchi, J.S. Furuya, T. Takeuchi, S. Hirohashi, Modified formalin and methanol fixation methods for molecular biological and morphological analyses, *Pathol. Int.* 47 (10) (1997) 685–691.
- [28] J. Shaham, Y. Bomstein, A. Meltzer, Z. Kaufman, E. Palma, J. Ribak, DNA-protein crosslinks, a biomarker of exposure to formaldehyde-in vitro and in vivo studies, *Carcinogenesis* 17 (1) (1996) 121–126.
- [29] T. Ichimura, K.F. Liang-da Chiu, S. Kawata, T.M. Watanabe, T. Yanagida, H. Fujita, Visualizing cell state transition using Raman spectroscopy, *PLoS One* 9 (1) (2014) 1–8.
- [30] E. Brauchle, K. Schenke-Layland, Raman spectroscopy in biomedicine—non-invasive in vitro analysis of cells and extracellular matrix components in tissues, *Biotechnol. J.* 8 (3) (2013) 288–297.
- [31] I. Jolliffe, Principal component analysis, *International Encyclopedia of Statistical Science*, Springer, 2011, pp. 1094–1096.
- [32] W. Wagner, P. Horn, M. Castoldi, A. Diehlmann, S. Bork, R. Saffrich, V. Benes, J. Blake, S. Pfister, V. Eckstein, et al. Replicative senescence of mesenchymal stem cells: a continuous and organized process, *PLoS One* 3 (5) (2008) e2213.
- [33] Y.H.K. Yang, C.R. Ogando, C.W. See, T.Y. Chang, G.A. Barabino, Changes in phenotype and differentiation potential of human mesenchymal stem cells aging in vitro, *Stem Cell Res. Ther.* 9 (1) (2018) 131.
- [34] E. Gazi, J. Dwyer, N.P. Lockyer, J. Miyan, P. Gardner, C. Hart, M. Brown, N.W. Clarke, Fixation protocols for subcellular imaging by synchrotron-based Fourier transform infrared microspectroscopy, *Biopolymers Original Res. Biomol.* 77 (1) (2005) 18–30.
- [35] A.C.S. Talari, Z. Movasaghi, S. Rehman, I.U. Rehman, Raman spectroscopy of biological tissues, *Appl. Spectrosc. Rev.* 50 (1) (2015) 46–111.



Surface optical phonon – Plasmon interaction in nanodimensional CdTe thin films

J. Mitric^{a,*}, N. Paunovic^a, M. Mitric^b, B. Vasic^a, U. Ralevic^a, J. Trajic^a, M. Romcevic^a,
W.D. Dobrowolski^c, I.S. Yahia^{d,e}, N. Romcevic^a

^a Institute of Physics, University of Belgrade, Pregrevica 118, 11080 Belgrade, Serbia

^b Institute Vinca, University of Belgrade, P.O. Box 522, 11001 Belgrade, Serbia

^c Institute of Physics, Polish Academy of Science, al. Lotnikow 32/46, 02-668 Warsaw, Poland

^d Department of Physics, Faculty of Science, King Khalid University, P.O. Box 9004, Abha, Saudi Arabia

^e Nano-Science & Semiconductor Labs, Department of Physics, Faculty of Education, Ain Shams University, Roxy, Cairo, Egypt

ARTICLE INFO

Keywords:

Thin film

Surface optical phonon

Raman spectroscopy

Far-infrared spectroscopy

Plasmon-phonon interaction

ABSTRACT

Structural and optical properties of CdTe thin films were investigated applying atomic force microscopy (AFM), XRD powder technique, Raman spectroscopy and far-infrared spectroscopy. CdTe thin films were prepared by using thermal evaporation technique. In the analysis of the far – infrared reflection spectra, numerical model for calculating the reflectivity coefficient for system which includes films and substrate has been applied. Effective permittivity of film mixture (CdTe and air) was modeled by Maxwell – Garnet approximation. We reveal the existence of surface optical phonon (SOP) mode and coupled plasmon-SOP modes (CPSOPM).

1. Introduction

II – VI semiconductor compounds, especially thin films, have become very popular because of their applications in numerous electronic and optoelectronic devices. Due to low production cost, thin films nowadays enjoy great attention in basic research and solid state technology.

The interest in various properties of photonic CdTe is well justified, as this material plays an important role in expanding variety of applications as in: integrated optics, optoelectronics, or solar energy conversion [1].

Two main properties of CdTe thin film are its high optical absorption coefficient (a thin film of CdTe with thickness of approximately 2 μm will absorb nearly 100% of the incident solar radiation) and its near ideal band gap for photovoltaic conversion efficiency of 1.45eV [2]. Also, its ease of film fabrication and low cost make it a representative material among II – VI semiconductors.

For fabrication of the CdTe films, various techniques have been applied: RF magnetron sputtering [3], molecular beam epitaxy (MBE) [4], pulsed laser deposition (PLD) [5], successive ionic layer adsorption and reaction method (SILAR) [6], metal organic chemical vapor deposition [7], screen printing [8], thermal evaporation method [9] etc. Thermal evaporation method shows some advantages such as: minimization of impurities proportional to the growing layer, reduced

chances of oxidation and direction of propagation (occurs from the source to the substrate) [9,10]. This makes thermal evaporation technique the most suitable method, thanks to very high deposition rate, low material consumption and low cost of fabrication [11].

In the case of crystal with relatively small dimension, in the frequency range between bulk longitudinal optical phonon frequency (ω_{LO}) and transversal optical phonon frequency (ω_{TO}), a new mode known as a surface phonon mode appears [12,13]. It is known for the case of real crystal, that when its dimension is relatively small, surface modes and effects of dimension will be manifested in addition to the normal modes of infinite lattice. But, when crystal is reduced to extremely small dimensions, only the surface mode will persevere [12–14].

On the other side, electron – phonon interaction takes an important place in semiconducting materials [15]. In our earlier work we have registered plasmon (collective electron excitation) and LO phonons interaction in different systems [16–19]. Besides that, we have studied the impact of damping on interaction appearance [20], interaction between plasmon and different phonons [21,22], as well as interaction between plasmon and impurity local phonons [23–25].

In this work we report experimental studies of CdTe thin films prepared by thermal evaporation technique. Existence of nanodimensional structures in these thin films enabled us to observe effects associated with interactions between surface optical phonon (SOP) and

* Corresponding author.

E-mail address: jmitric@ipb.ac.rs (J. Mitric).

<https://doi.org/10.1016/j.physe.2018.07.021>

Received 27 April 2018; Received in revised form 5 July 2018; Accepted 16 July 2018

Available online 18 July 2018

1386-9477/ © 2018 Elsevier B.V. All rights reserved.

plasmon for the first time.

Samples characterization was performed using atomic force microscopy (AFM). Structural properties were analyzed using XRD powder technique, and optical properties were characterized using Raman and far-infrared spectroscopy.

2. Sample preparation and characterization methods

CdTe single crystal was grown by the Bridgman technique. Different thickness of CdTe thin films were deposited by thermal evaporation from a resistance heating quartz glass crucible onto glass substrates using high vacuum coating unit type Edward 306 A. Films were grown at a pressure of 106 Pa. The mechanical rotation of the substrate holder during deposition produced homogeneous film. The distance between the source heater and substrates holder is 21 cm, in order to avoid any heat flow from the source to the substrates.

The morphology of the four CdTe thin films of different thicknesses was investigated by Atomic force microscopy (AFM). Atomic force microscopy measurements were performed using NT-MDT system NTEGRA Prima. Imaging was done in tapping mode using NSG01 probes. All AFM measurements were done at ambient conditions. For the sake of statistical analysis of sample surface, we calculated histograms and bearing ratios for each topographic image. The histogram represents a height distribution density of all points in a two-dimensional topographic image, or in other words, it is a number of points with height given on x-axis. On the other hand, the bearing ratio curve gives a percent of points in a corresponding two-dimensional topographic image with a height less than the number given on x-axis.

The structural characteristics were obtained by the XRD powder technique. All samples were examined under the same conditions, using a Philips PW 1050 diffractometer equipped with a PW 1730 generator, 40 kV \times 20 mA, using Ni filtered Co K α radiation of 0.1778897 nm at room temperature. Measurements were carried out in the 2 h range of 10–100° with a scanning step of 0.05° and 10 s scanning time per step. Crystallite size was determined by using XFIT computing program which is based on Fundamental Parameter convolution approach [26].

Raman measurements were performed using commercial NTEGRA Spectra system from NT-MDT. A linearly polarized semiconductor laser operating at a wavelength of 532 nm was used. All the spectra were obtained by setting the laser power to 2 mW within the $\sim 0.5 \times 0.5 \mu\text{m}$ sized focus with exposure time of 600 s.

The far-infrared (FIR) reflectivity measurements were performed at room temperature with a BOMEM DA-8 Fourier-transform infrared spectrometer. A Hyper beamsplitter and deuterated triglycine sulfate (DTGS) pyroelectric detector were used to cover the wave number region from 80 to 650 cm^{-1} .

3. Results and discussion

3.1. Atomic force microscopy

Three dimensional topographic images of all four samples are shown in the left side of Fig. 1. As can be seen, sample surfaces are rather flat, but still they are characterized with bright protrusions and dark holes (which represent air) resulting in a small surface roughness of several nanometers.

In order to characterize fraction of both observed topographic features, the statistical analysis have been performed by calculating histograms and bearing ratios from two dimensional topographic images. The results for all four samples are given in the right side of Fig. 1. They show that the peaks in the histograms are positioned in the middle of bearing ratio curves. Therefore, from these curves we can conclude that the fraction of holes and protrusions are rather similar, around 50%.

In order to estimate thicknesses of studied films, their step edges were measured by AFM. 3D AFM topographic images of the step edges are depicted in Fig. 2(a1-d1). The films are brighter and the substrates

are dark in the images, while the step edges are clearly resolved. Based on the AFM images, height distributions were calculated and presented in Fig. 2 (a2-d2). In all histograms, there are two characteristic peaks: a lower one corresponds to the substrate, while a higher one corresponds to the film. Therefore, the film height can be then approximately calculated as a difference between these two peaks. Estimated film thicknesses are given in Fig. 2 (a2-d2). The best resolved height peaks were found on CdTe 1 in Fig. 2 (a2) due to a smooth sample surface as can be seen in Fig. 2 (a1).

3.2. XRD

Structures of four synthesized CdTe thin films with different thicknesses were identified by XRD pattern as shown in Fig. 3. The diffractograms confirm that all samples are monophased, and that they crystallized in sphalerite type structure in 216. space group, $F\bar{4}3m$. All of the observed diffraction peaks are indexed according to this space group. Therefore, in our thin film samples there is no other structures other than CdTe. In this structural type, Cd ions occupy 4a Wyckoff positions, $[[0, 0, 0]]$ with local symmetry $\bar{4}3m$, while Te ions occupy 4c Wyckoff positions $[[1/4, 1/4, 1/4]]$ with the same local symmetry. Cd ions are in tetrahedral surrounding of Te ions (and vice versa). The tetrahedrons are regular and share common vertices. Crystallite size (R) is determined and presented in Fig. 2 and Table 1.

3.3. Raman spectroscopy

The cubic face-centered structure of bulk crystal CdTe is characterized by the 216. space group $F\bar{4}3m$ and contains four formula units, while the primitive cell is one fourth as many. Optical modes consist of one three fold-degenerated mode F_2 which is active in IR and Raman spectra. The dipole mode F_2 is split into the transverse (TO) and longitudinal (LO) modes in the vibrational spectra. It is very well known that reduction of the particle dimensions to nanoscale results in a breakdown of phonon selection rules and allows phonons with $l \neq 0$ to contribute to Raman scattering [27–31]. Consequently, some new forbidden vibration modes (low frequency region, acoustic modes, and high frequency region, surface optical modes) occur due to imperfections, impurity, valence band mixing and/or nonspherical geometry of the nanostructures [14].

TO (142 cm^{-1}) and LO (170.5 cm^{-1}) modes for the CdTe bulk crystal are both active in the Raman spectra. Also, the modes in band near 120 cm^{-1} correspond to phonons of Te on the CdTe surface and can be seen in the Raman spectra [32].

Raman spectra of CdTe thin films of different thickness at room temperature are presented in Fig. 4.

For analyzing obtained spectra Lorentz profiles were used. Solid lines are their sums. In the top right corner Raman spectra of bulk CdTe crystal for ambient conditions is presented [32]. The observed Raman spectra for all samples among characteristic CdTe TO mode at 142 cm^{-1} and phonon of Te of the CdTe surface (127 cm^{-1}), show the LO phonon like frequency shift from 170.5 cm^{-1} to 164 cm^{-1} . That can be attributed to the surface optical phonon (SOP) mode effect [33–38]. It is clear that SOP phonon is wider compared to LO phonon of bulk crystal, as well as when it's compared to phonon of nanodimensional film. This effect is associated with interaction between SOP and plasmon, which will be mentioned later on.

In order to analyze the surface optical phonon we have to take into account that a part of crystallites are surrounded by air. We will analyze the dependence of the SOP mode position on filling factor (f) of the mixed material.

Surface phonon modes can be detected in systems where particle size is much smaller when compared to wavelength of exciting light source [39]. These modes can be obtained for in the case of polar crystals [40], so we consider expression for dielectric function which describes optical properties of polar semi-insulating semiconductor in

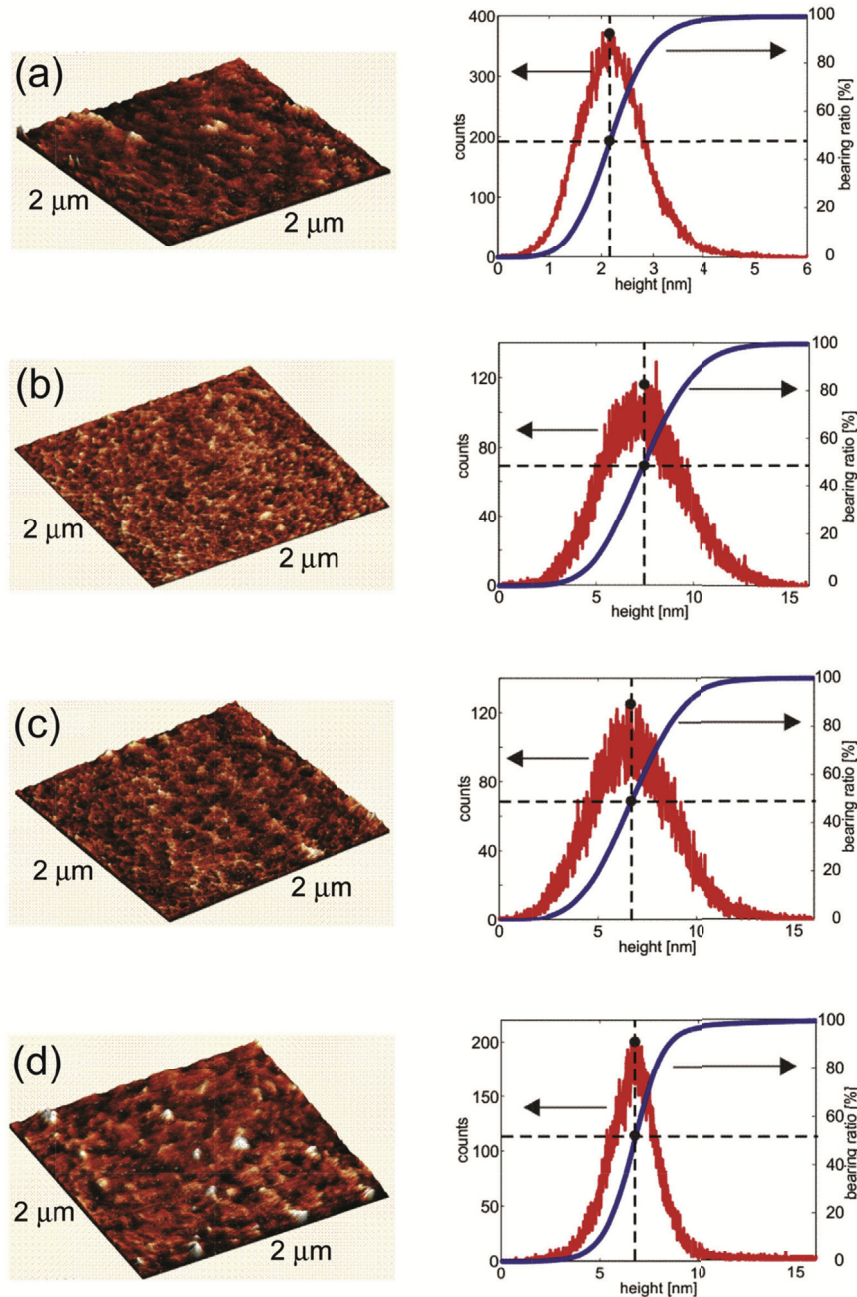


Fig. 1. Three-dimensional topographic image (left) and corresponding histogram and bearing ratio (right) for (a) CdTe 1, (b) CdTe 2, (c) CdTe 3, and (d) CdTe 4. Scan size is 2 μm .

IR region [24]:

$$\epsilon_2(\omega) = \epsilon_\infty \left(1 + \sum_{k=1}^n \frac{\omega_{LOk}^2 - \omega_{TOk}^2}{\omega_{TOk}^2 - \omega^2 - i\gamma_{TOk}\omega} - \frac{\omega_P^2}{\omega(\omega + i\Gamma)} \right) \quad (1)$$

ω_{TO} and ω_{LO} represent transverse and longitudinal optical bulk phonons, respectively; ϵ_∞ is the dielectric constant at high frequencies, ω_P is plasma frequency and γ and Γ are the damping constants. Surface phonons can be considered similarly to phonons in infinite crystals, but with adapted wave functions to the geometry of the small particle.

Here, we will apply effective medium theory: Because the size of semiconducting nanoparticles, L , (with dielectric function ϵ_2 , and are distributed in a medium with dielectric constant ϵ_1) is considerably

smaller than the interacting wavelength of visible light, λ ($\lambda \gg L$), we treat the heterogeneous composite as a homogeneous medium.

Even though there are numerous models for the effective dielectric permittivity for these kinds of mixtures [41], we decided to use Maxwell – Garnet model, because all our samples are thin films with well defined and separated nanosized grains. According to the Maxwell – Garnet mixing rule [42,43], effective permittivity of mixture, including spherical geometry of particles is given with:

$$\epsilon_{eff} = \epsilon_1 + 3f\epsilon_1 \frac{\epsilon_2 - \epsilon_1}{\epsilon_2 + 2\epsilon_1 - f(\epsilon_1 - \epsilon_2)} \quad (2)$$

In this case, nanoparticles are spheres with permittivity ϵ_2 and are randomly distributed in homogeneous environment, with permittivity

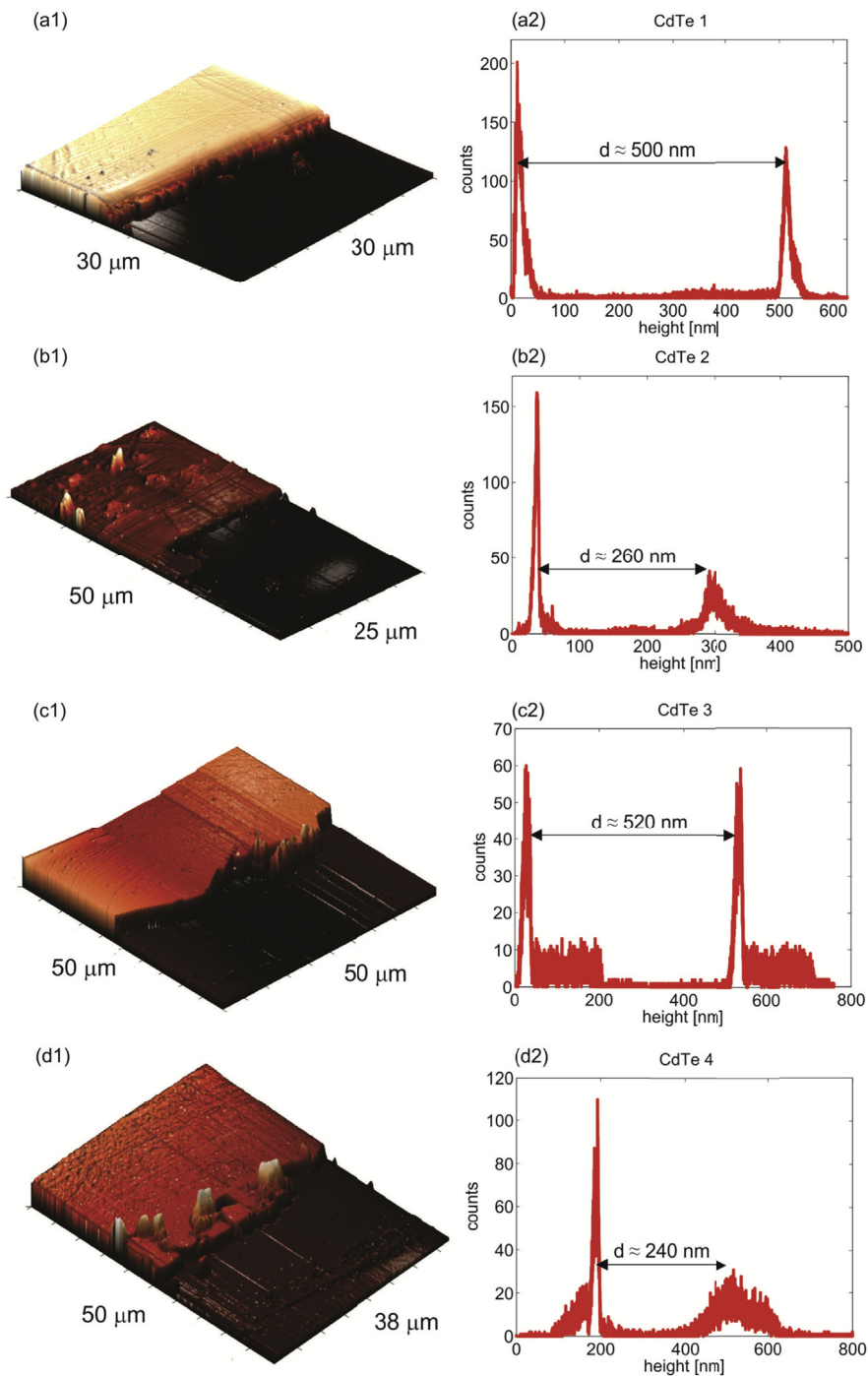


Fig. 2. (a1-d1) 3D AFM topographic images of step edges of studied films, and (a2-d2) corresponding height histograms. Average films thicknesses are denoted in the histograms.

ϵ_1 and occupy a volume fraction f .

Position surface optical phonon (SOP) mode frequencies are obtained from Ref. [44]:

$$\omega_{SOP} = \max \left(I_m \left(-\frac{1}{\epsilon_{eff}} \right) \right) \quad (3)$$

The result is shown in Fig. 5. The practical liner dependence of the position of the SOP mode on the filling factor f has been obtained. For the frequency of the SOP mode determined in Fig. 4 we have $f = 0.53$. This result is in accordance with the one obtained from the AFM measurements.

3.4. Far-infrared spectroscopy

Thicknesses of our films, as we will see, are in a range from $\sim 0.39 \mu\text{m}$ to $\sim 0.72 \mu\text{m}$, so reflectivity spectra contain information about CdTe films together with information about substrate. Representative scheme of our layered structure can be presented in Fig. 6 [45]. Medium 1 is air, medium 2 is thin bulk CdTe crystal layer and medium 3 is substrate glass, with dielectric functions ϵ_1 ($\epsilon_1 = 1$), ϵ_2 and ϵ_3 , respectively. We can now write [46]:

$$R_A = \frac{A_r}{A_i} = \frac{n_2 e^{-i\alpha} + r_{23} e^{i\alpha}}{e^{-i\alpha} + n_2 r_{23} e^{i\alpha}} \quad (4)$$

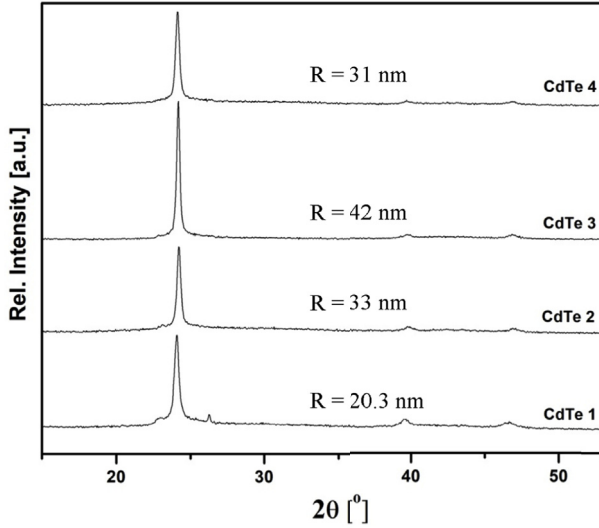


Fig. 3. XRD analysis of CdTe thin films of different thickness. Obtained crystallite sizes (R) are presented too.

Table 1

Parameters obtained from XRD measurements and FIR reflection spectroscopy. Thin films thickness - d , Crystallite size - R .

Name	d [μm]	R [nm]	ω_{11} (ω_+) [cm^{-1}]	ω_{12} (ω_-) [cm^{-1}]	ω_p [cm^{-1}]	ω_t [cm^{-1}]	f
CdTe 4	0.39	31.0	187	103	137.5	140.0	0.53
CdTe 2	0.43	33.0	174	78	96.6	140.5	0.53
CdTe 3	0.71	42.0	170	65	79.5	139	0.53
CdTe 1	0.72	20.3	165	30	35.2	140.5	0.53

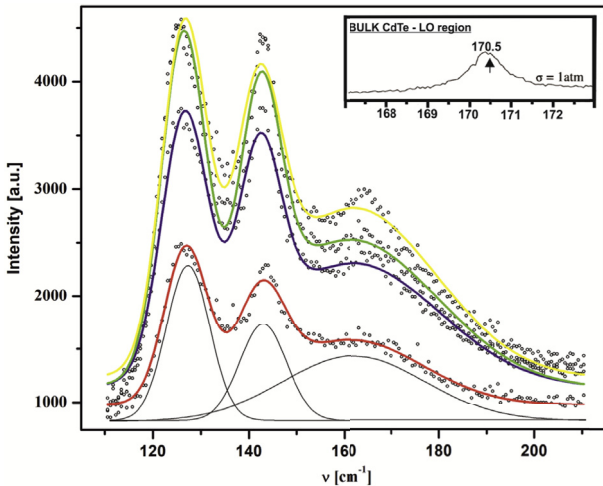


Fig. 4. Raman spectra of CdTe thin films of different thickness. Experimental spectra are shown by open dots. Solid lines are sums of three Lorentz profiles as it shown for spectrum of CdTe 1. In the top right corner LO region of bulk CdTe is presented, taken from the literature [32].

$r_{ij} = (n_i - n_j)/(n_i + n_j) = (\sqrt{\epsilon_i} - \sqrt{\epsilon_j})/(\sqrt{\epsilon_i} + \sqrt{\epsilon_j})$ describe Fresnel coefficients, A_i and A_r represent amplitudes of incident and reflection beams, n is complex index of refraction, ϵ is the dielectric constant and $\alpha = 2\pi\omega d(\epsilon_2)^{1/2}$ is the complex phase change related to the absorption in the crystal layer with the thickness d .

Reflectance, R , is given with:

$$R = |R_A|^2 \quad (5)$$

In this case we decided to use dielectric function which takes into

consideration the existence of plasmon – phonon interaction in advance.

The dielectric function of the CdTe crystal layer is:

$$\epsilon_2(\omega) = \epsilon_{\infty \text{CdTe}} \prod_{j=1}^2 \frac{\omega^2 + i\gamma_j\omega - \omega_{lj}^2}{\omega(\omega + i\Gamma_p)(\omega^2 + i\gamma_l\omega - \omega_l^2)} \quad (6)$$

The ω_{lj} and γ_{lj} ($j = 1, 2$), parameters of the first numerator are the eigenfrequencies and damping coefficients of the longitudinal plasmon-phonon (LP + LO) waves, that arise as a result of the interaction of the initial phonon ($\omega_{LO, \text{CdTe}} = 170.5 \text{ cm}^{-1}$) and plasmons (ω_p) modes. The parameters of the denominator correspond to the similar characteristics of the transverse vibrations (ω_b, γ_t) and plasmon damping Γ_p . As a result of the best fit, we obtain coupled mode frequencies (ω_{l1} and ω_{l2}).

The dielectric function of the glass substrate is:

$$\epsilon_s(\omega) = \epsilon_{\infty \text{sup}} \prod_{k=1}^n \frac{\omega_{LOk}^2 - \omega^2 + i\gamma_{LOk}\omega}{\omega_{TOk}^2 - \omega^2 + i\gamma_{TOk}\omega} \quad (7)$$

where ω_{TO} and ω_{LO} are the transversal and longitudinal optical vibrations, and γ_{TO} and γ_{LO} are damping parameters, respectively.

In our case, layer 2 consists of a CdTe crystals and air (see Fig. 6). The size of the crystallites (R) is given in Fig. 2 and Table 1. These crystallites are described by a dielectric function given in Eq. (1) or Eq. (6) and located randomly in homogeneous environment ϵ_1 (air) and occupy a volume fraction f , so we can use effective medium theory and Maxwell - Garnet mixing rule, given with Eq. (2).

The far – infrared reflectivity spectrum of the glass substrate is shown in Fig. 7(e). The calculated spectrum, presented by solid line, was obtained using the dielectric function given by equation (7). As a result of the best fit we obtained three modes, whose characteristic frequency are $\omega_{TO1} = 60 \text{ cm}^{-1}$, $\omega_{LO1} = 140 \text{ cm}^{-1}$, $\omega_{TO2} = 441 \text{ cm}^{-1}$, $\omega_{LO1} = 443 \text{ cm}^{-1}$ and $\omega_{TO3} = 471 \text{ cm}^{-1}$, $\omega_{LO3} = 522 \text{ cm}^{-1}$. Frequency values of these modes have remained the same during the fitting procedure for all CdTe thin film samples.

The parameters obtained by the best fit between the experimental results and the models for CdTe film described earlier are also given in Table 1. The far-infrared spectra of CdTe thin films, in the spectral range of 80–600 cm^{-1} , at room temperature, are presented in Fig. 7. Experimental data are presented by circles, while the solid lines are calculated spectra obtained by a fitting procedure based on the previously presented model. Experimental and theoretical spectra show an excellent match.

The thicknesses of our films obtained by Far – infrared spectroscopy are 20% greater, which is within the limits of error for both techniques. When using Far – infrared spectroscopy for calculating thickness of layered structured, we bring errors in absolute measurements, because we calculate effective thickness. The important thing is, the trend is the same, the films does not differ in the relative thickness, i.e. thickness ratios between films are the same.

We note that the thickness (d) of the film changes in the range of $\sim 0.39 - \sim 0.7 \mu\text{m}$. While the thickness of the film is in the $0.40 \mu\text{m}$ region, the crystallite size is about 32 nm, and for a film thickness of about $0.72 \mu\text{m}$, we have two sizes of crystallites different for a factor of 2. In addition, from Table 1, we have for thicker films CdTe 1 and CdTe 3, that the position of the coupled plasmon-phonon mode ω_{11} is below the values of $\omega_{LO, \text{CdTe}} = 170.5 \text{ cm}^{-1}$. On the other hand, these values are above $\omega_{LO, \text{CdTe}}$ for thin films CdTe 2 and CdTe 4. In both cases plasmon damping (Γ_p) is relatively low. The obtained eigenfrequencies of the plasmon – phonon coupled modes for CdTe thin films are presented in Fig. 8. As a result of the best fit from Fig. 7, we obtained the frequencies of coupled modes (ω_{l1} and ω_{l2}) marked by open circles and transverse mode frequencies which are denoted by - x. Value of ω_p are calculated by Refs. [16–18]:

$$\omega_p = \frac{\omega_{l1}\omega_{l2}}{\omega_t} \quad (8)$$

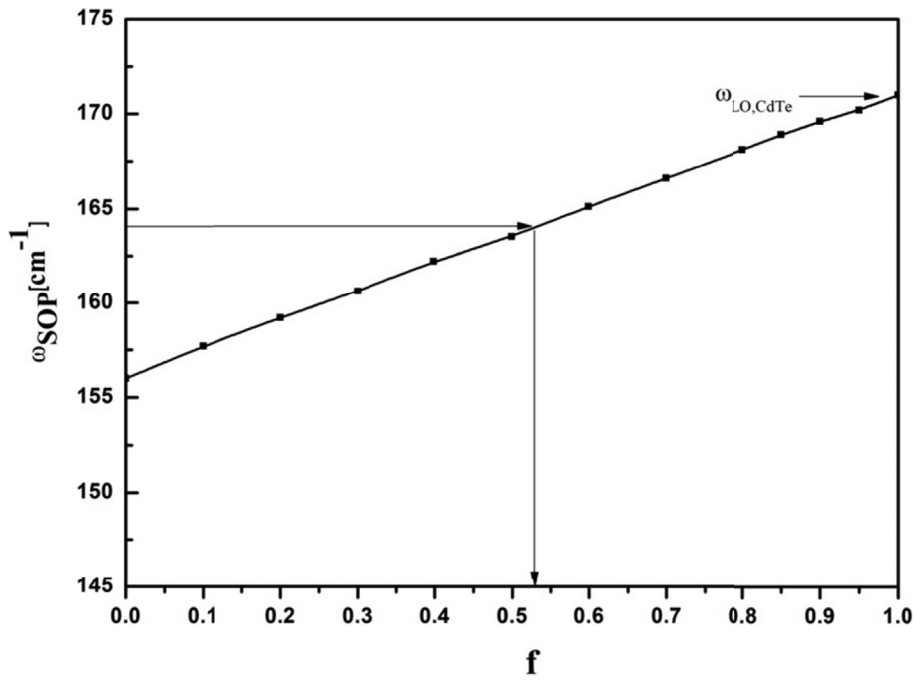


Fig. 5. Surface optical phonon (SOP) mode position vs. filling factor.

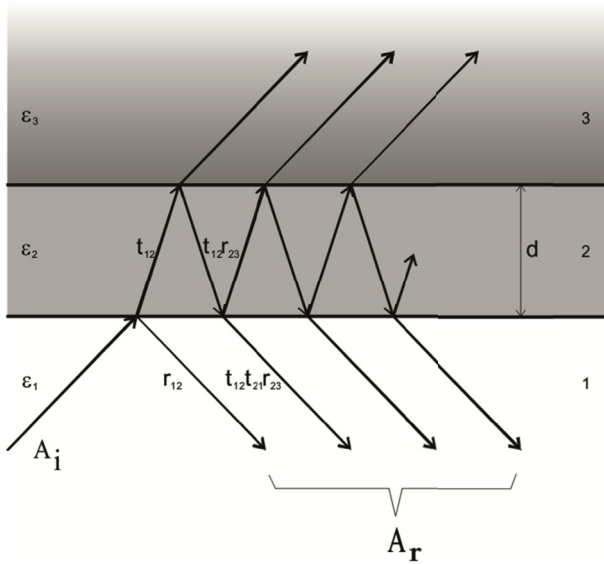


Fig. 6. Schematic presentation of a three layer structure [46].

The calculated lines at Fig. 7 are solution of a real part of uncoupled dielectric function (Eq. (1)). However, for plasma-phonon modes positions are obtained:

$$\omega_{\pm} = \frac{\omega_p^2 + \omega_{LO}^2}{2} \pm \sqrt{\frac{(\omega_p^2 + \omega_{LO}^2)^2 - \omega_p \omega_{TO}}{4}} \quad (9)$$

The full lines in Fig. 7 were obtained for the case $\omega_{LO, CdTe} = 170.5 \text{ cm}^{-1}$. It is clear that all values of ω_{11} and ω_{12} are out of this theoretical model. Best fit, dashed lines in Fig. 7, was obtained for $\omega_{SOP} = 164 \text{ cm}^{-1}$ which in Eq. (9) plays a role ω_{LO} . Shift of about 7 cm^{-1} is registered in relation to $\omega_{LO, CdTe}$, just like in the case of Raman spectra. As we said earlier, the LO phonon shift of CdTe crystal is attributed to the surface optical phonon (SOP) mode effect.

Based on these results, it is clear that in the case of CdTe thin films, prepared by using thermal evaporation technique, the filling factor is constant and does not depend on film thickness, crystallite size and

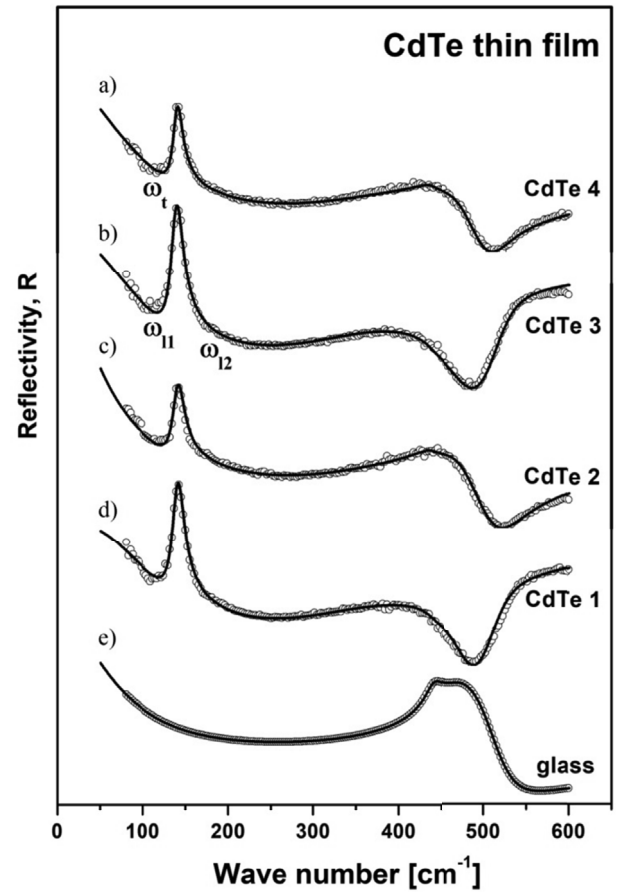


Fig. 7. Far – infrared reflection spectra of: CdTe thin films with thickness of (a) $0.39 \mu\text{m}$, (b) $0.71 \mu\text{m}$, (c) $0.43 \mu\text{m}$, (d) $0.72 \mu\text{m}$, and glass substrate (e). Experimental spectra are presented by circles while solid lines are calculated spectra obtained by a fitting procedure based on the model given by Eqs. (2) and (4)–(7).

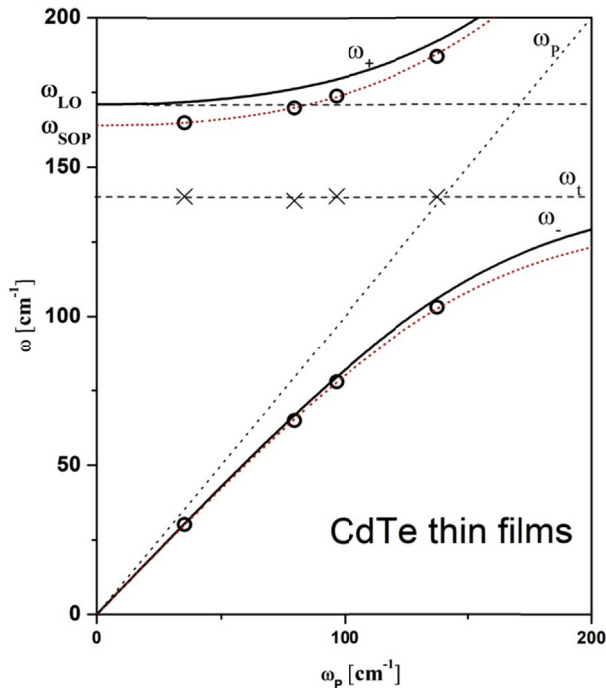


Fig. 8. The eigenfrequencies of the plasmon–phonon modes for CdTe thin films. The lines are calculated spectra [$\text{Re}\{\epsilon_2\} = 0$; ϵ_2 is given by Eq. (1)]: solid line with $\omega_{LO,CdTe} = 170.5 \text{ cm}^{-1}$; dashed line with $\omega_{SOP} = 164 \text{ cm}^{-1}$; \circ - ω_{l_1} , ω_{l_2} ; \times - ω_t .

concentration of free carriers. On the other hand, the reflection spectra depend on the thickness of the film and the concentration of free carriers in the film, which is expected. In general, thin films have a higher concentration of free carriers ($\sim \omega_p$) (see Table 1). The linear dependence of the position of the SOP mode on the filling factor causes the existence of a modified plasmon – phonon interaction, where the SOP has the role of the LO phonon.

Of course, there are many models that can describe the registered frequency shift of the LO phonon in CdTe e.g. a continuum model of the optical phonon confinement [47,48] would also give a shift of 7 cm^{-1} , but for spherical nanoparticles of about 5 nm, which is far from our case.

4. Conclusion

In this paper, we present results of investigation of CdTe thin films prepared with thermal evaporation technique, with different thicknesses. Sample's surfaces are rather flat, but still they are characterized with bright protrusions and dark holes (air) resulting in a small surface roughness of several nanometers. We showed that, when using thermal evaporation technique we get high quality thin films, especially for thicker films with greater crystallite size. We conclude that the filling factor of our thin films is constant and does not depend on film thickness, crystallite size or concentration of free carriers, but yet has linear dependence on SOP position. This kind of morphology, with filling factor of $\sim 50\%$ causes existence of surface optical phonon and its interaction with plasmon, because of the free surface around nanoparticles. A numerical model for calculating the reflectivity coefficient for complex system, which includes films and substrate, has been applied, and CdTe thin film were treated as a mixture of homogenous spherical inclusion in air modeled by Maxwell – Garnet formula.

Acknowledgements

This research was financially supported by the Serbian Ministry of

Education and Science (Project 45003) and in Poland by National Science Center granted under decision No. DEC-2011/01/B/ST5/06602. The authors would like to express their gratitude to King Khalid University, Saudi Arabia for providing administrative and technical support.

References

- [1] S. Chandra Ray, K. Mallick, Int. J. Chem. Eng. Appl. 4 (2013) 183–186.
- [2] C.S. Ferekides, U. Balasubramanian, R. Mamazza, V. Viswanathan, H. Zhao, D.L. Morel, Sol. Energy 77 (2004) 823–830.
- [3] R. Kulkarni, et al., Energy Procedia 110 (2017) 188–195.
- [4] A. Arnoult, J. Cibert, Appl. Phys. Lett. 66 (1995) 2397–2399.
- [5] P. Bhattacharya, D.N. Bose, Semicond. Sci. Technol. 6 (1991) 384–387.
- [6] A.U. Ubale, D.K. Kulkarni, Indian J. Pure Appl. Phys. 44 (2006) 254–259.
- [7] T.L. Chu, S.S. Chu, C. Ferekides, J. Britt, C.Q. Wu, J. Appl. Phys. 71 (1992) 3870.
- [8] A. Nakano, et al., Sol. Cell. 17 (1986) 233.
- [9] K.S. Rahman, F. Haque, 3rd International Conference on the Developments in Renewable Energy Technology (ICDRET), 2014, pp. 29–31.
- [10] S. Lalitha, S. Zh Karazhanov, P. Ravindran, S. Senthilarasu, R. Sathyamoorthy, J. Janabergenov, Physica B 387 (2007) 227–238.
- [11] S. Singh, et al., Thin Solid Films 519 (2010) 1078–1081.
- [12] D.S. Chuu, C.M. Dai, W.F. Hsieh, C.T. Tsai, J. Appl. Phys. 69 (1991) 12.
- [13] A. Singha, B. Satpati, P.V. Satyam, A. Roy, J. Phys. Condens. Mater. 17 (2005) 5708–5967.
- [14] M. Gilić, J. Trajić, N. Romčević, M. Romčević, D.V. Timotijević, G. Stanišić, I.S. Yahia, Opt. Mater. 35 (2013) 1112–1117.
- [15] M. Cardona (Ed.), Top. Appl. Phys., vol. 8, Springer, Berlin, 1975.
- [16] N. Romčević, M. Romčević, A. Golubović, Le Van Khoi, A. Mycielski, Đ. Jovanović, D. Stojanović, S. Nikolić, S. Đurić, J. Alloy. Compd. 397 (2005) 52–57.
- [17] M. Romčević, N. Romčević, V.N. Nikiforov, Infrared Phys. Technol. 42 (2001) 541–545.
- [18] N. Romčević, M. Romčević, A. Milutinović, S. Kostić, J. Alloy. Compd. 478 (2009) 41–44.
- [19] J. Trajić, M. Romčević, N. Romčević, B. Babić, B. Matović, P. Balaž, Opt. Mater. 57 (2016) 225–230.
- [20] N. Romčević, M. Romčević, W.D. Dobrowolski, L. Kilanski, M. Petrović, J. Trajić, B. Hadžić, Z. Lazarević, M. Gilić, J.L. Ristic-Djurović, N. Paunović, A. Reszka, B.J. Kowalski, I.V. Fedorchenko, S.F. Marenkin, J. Alloy. Compd. 649 (2015) 375–379.
- [21] J. Trajić, N. Romčević, M. Romčević, V.N. Nikiforov, Mater. Res. Bull. 42 (2007) 2192–2201.
- [22] M. Romčević, N. Romčević, W. Dobrowolski, L. Kalinski, J. Trajić, D.V. Timotijević, E. Dynowska, I.V. Fedorchenko, S.F. Marenkin, J. Alloy. Compd. 548 (2013) 33–37.
- [23] N. Romčević, J. Trajić, T.A. Kuznetsova, M. Romčević, B. Hadžić, D.R. Khokhlov, J. Alloy. Compd. 442 (2007) 324–327.
- [24] J. Trajić, N. Romčević, M. Romčević, D. Stojanović, R. Rudolf, T.A. Kuznetsova, D.R. Khokhlov, J. Alloy. Compd. 493 (2010) 41–46.
- [25] J. Trajić, N. Romčević, M. Romčević, D. Stojanović, L.I. Ryabova, D.R. Khokhlov, J. Alloy. Compd. 602 (2014) 300–305.
- [26] R.W. Cheary, A. Coelho, J. Appl. Crystallogr. 25 (1992) 109–121.
- [27] R. Triboulet & P. Siffert, first ed., Elsevier, 2010.
- [28] H. Zeng, W. Cai, B. Cao, J. Hu, Y. Li, P.S. Liu, Appl. Phys. Lett. 88 (2006) 181905.
- [29] A. Ghosh, R.N.P. Chodhary, J. Phys. D Appl. Phys. 42 (2009) 075416.
- [30] F. Friedrich, N.H. Nickel, Appl. Phys. Lett. 91 (2007) 111903.
- [31] J. Xu, W. Ji, X.B. Wang, H. Shu, Z.X. Shen, S.H. Tang, J. Raman Spectrosc. 29 (1998) 613.
- [32] V.C. Stergiou, Y.S. Raptis, E. Anastassakis, N. Pelekaneos, A. Nahmani, J. Cibert, Phys. Status Solidi 223 (2001) 237.
- [33] J.F. Scott, T.C. Damem, Optic Commun. 5 (1972) 410.
- [34] R. Rossetti, S. Nakahara, L.E. Bru, J. Chem. Phys. 79 (1983) 1086.
- [35] B.F. Variano, N.E. Schlotter, D.M. Hwangand, C.J. Sandroff, J. Chem. Phys. 88 (1988) 2848.
- [36] A.V. Baranov, Y.S. Bobovich, N.I. Grebenshchikova, V.I. Petrov, M.Y. Tsenter, Optic Spectrosc. 60 (1986) 685.
- [37] H. Jerominek, M. Pigeon, S. Patela, Z. Jakubczk, C. Delisle, R.J. Tremblay, Appl. Phys. 63 (1986) 957.
- [38] E.F. Hilinski, P.A. Lucas, J. Chem. Phys. 89 (1988) 3435.
- [39] J. Trajić, M. Gilić, N. Romčević, M. Romčević, G. Stanišić, B. Hadžić, M. Petrović, Y.S. Yahia, Sci. Sinter. 47 (2015) 145–152.
- [40] G. Irmer, J. Raman Spectrosc. 38 (2007) 634.
- [41] K. Karkkainen, A. Saviola, K. Nikoskinen, IEEE Trans. Geosci. Rem. Sens. 39 (5) (2001) 1013.
- [42] J.C.M. Garnett, Trans. Roy. Soc. Can. CIII (1904) 385420.
- [43] A. Saviola, I. Lindell, A. Priou (Ed.), Dielectric Properties of Heterogeneous Materials PIER 6 Progres in Electromagnetic Research, Elsevier, Amsterdam, 1992, pp. 101–115 1.
- [44] B. Hadžić, N. Romčević, M. Romčević, I. Kuryliszyn-Kudelska, W. Dobrowolski, J. Trajić, D.V. Timotijević, U. Narkiewicz, D. Sibera, J. Alloy. Compd. 540 (2012) 49–56.
- [45] M. Gilić, et al., Infrared Phys. Technol. 76 (2016) 276–284.
- [46] J. Trajić, M. Gilić, N. Romčević, M. Romčević, G. Stanišić, Z. Lazarević, D. Joksimović, I.S. Yahia, Phys. Scr., T 162 (2014) 014031.
- [47] R. Roca, C. Trallero-Giner, M. Cardona, Phys. Rev. B 49 (1994) 13704.
- [48] M.P. Chamberlain, C. Trallero-Giner, M. Cardona, Phys. Rev. B 51 (1995) 1680.

Article

Characterization of Flexible Copper Selenide Films on Polyamide Substrate Obtained by SILAR Method—Towards Application in Electronic Devices

Gediminas Jakubauskas¹, Martina Gilic^{2,3}, Edita Paluckiene¹, Jelena Mitric², Jovana Cirkovic⁴, Uros Ralevic², Egle Usoviene¹, Egidijus Griskonis¹  and Neringa Petrasauskiene^{1,*} 

¹ Department of Physical and Inorganic Chemistry, Kaunas University of Technology, Radvilenu 19, 50254 Kaunas, Lithuania

² Institute of Physics Belgrade, University of Belgrade, Pregrevica 118, 11080 Belgrade, Serbia

³ Institut of Experimental Physics, Freie Universität Berlin, Arnimallee 14, 14195 Berlin, Germany

⁴ Institute for Multidisciplinary Research, University of Belgrade, Kneza Visaslava 1, 11000 Belgrade, Serbia

* Correspondence: neringa.petrasauskiene@ktu.lt

Abstract: Thin copper selenide films were synthesized on polyamide sheets using the successive ionic layer adsorption and reaction (SILAR) method at three different temperatures. It was found that elevating the temperature of the solution led to the creation of copper selenide films with different features. X-ray diffraction characterization revealed that all films crystallized into a cubic Cu_{2-x}Se , but with different crystallinity parameters. With elevating the temperature, grain size increased (6.61–14.33 and 15.81 for 40, 60 and 80 °C, respectively), while dislocation density and the strain decreased. Surface topology was investigated with Scanning Electron Microscopy and Atomic Force Microscopy, which revealed that the grains combined into agglomerates of up to 100 nm (80 °C) to 1 μm (40 °C). The value of the direct band gap of the copper selenide thin films, obtained with UV/VIS spectroscopy, varied in the range of 2.28–1.98 eV. The formation of Cu_{2-x}Se was confirmed by Raman analysis; the most prominent Raman peak is located at 260 cm^{-1} , which is attributed to binary copper selenides. The thin Cu_{2-x}Se films deposited on polyamide showed *p*-type conductivity, and the electrical resistivity varied in the range of 20–50 Ω . Our results suggest that elevated temperatures prevent large agglomeration, leading to higher resistance behavior.

Keywords: copper selenide; polyamide; SILAR method



Citation: Jakubauskas, G.; Gilic, M.; Paluckiene, E.; Mitric, J.; Cirkovic, J.; Ralevic, U.; Usoviene, E.; Griskonis, E.; Petrasauskiene, N.

Characterization of Flexible Copper Selenide Films on Polyamide Substrate Obtained by SILAR Method—Towards Application in Electronic Devices. *Chemosensors* **2022**, *10*, 313. <https://doi.org/10.3390/chemosensors10080313>

Academic Editor: Vardan Galstyan

Received: 22 June 2022

Accepted: 1 August 2022

Published: 5 August 2022

Publisher's Note: MDPI stays neutral with regard to jurisdictional claims in published maps and institutional affiliations.



Copyright: © 2022 by the authors. Licensee MDPI, Basel, Switzerland. This article is an open access article distributed under the terms and conditions of the Creative Commons Attribution (CC BY) license (<https://creativecommons.org/licenses/by/4.0/>).

1. Introduction

Copper selenide can be formed in various stoichiometric compositions, such as CuSe , Cu_2Se , CuSe_2 , Cu_3Se_2 , Cu_7Se_4 , Cu_5Se_4 , Cu_3Se_4 , and non-stoichiometric compositions Cu_{2-x}Se [1–3]. The stoichiometric composition of copper selenide strongly influenced its crystalline structure and electronic behavior—it alters its electronic, chemical, and thermal properties [4,5]. Copper-deficient Cu_{2-x}Se is an intrinsic *p*-type semiconductor with direct bandgap energies in the range of 2.0 to 2.4 eV, the work function of 4.17 eV, and high photo-electrochemical conversion efficiency (~14.6%) [3,5–8]. These features of Cu_{2-x}Se can be used as Schottky diodes [9], self-repairable electrodes [10], and photovoltaic devices [8]. Furthermore, the Cu_{2-x}Se columnar superstructures are used as low-cost and highly efficient counter electrodes in quantum dot sensitized solar cells [11,12].

Several decades ago, due to concerns about homeland security, medical and environmental monitoring as well as food safety, a large interest was shown in the development of gas sensors for detecting volatile and toxic gases. Cu_{2-x}Se exhibits good sensitivity and short response and recovery times to Hg^{2+} [13], and organic gases such as ethanol and acetone [14].

Many works have been reported on the formation of Cu_{2-x}Se on substrates, such as glass [1,6,15], and fluorine-doped tin oxide [8,11,12,16].

Flexible electronics is a growing field that is promising to develop various new commercial products such as displays, solar cells, flexible photovoltaics, and biomedical sensors due to their lightweight and low cost [17–21]. Flexible polymer substrates possess unique features such as low cost, low thickness, low mass, and excellent mechanical deformability. They can remain in the environmental, chemical, and thermal environments required for the construction of electronic circuits while maintaining their mechanical flexibility [22,23]. Recently, ferroelectric semiconductors have been increasingly studied [24,25].

When Cu_{2-x}Se is deposited on a flexible transparent polymer substrate (polyvinylchloride, polyvinyl alcohol), the possibility of using thin flexible polymer substrates appears in the fabrication of flexible optoelectronic devices [26]. Cu_{2-x}Se films on polyester sheets can be used as a transparent electrode for inorganic and organic hybrid light emitters, as a possible replacement for indium tin oxide or fluorine-doped tin oxide [7].

This work reports the preparation and characterization of electrically conductive copper selenide onto polyamide 6 (PA) sheets. Polyamide 6 was chosen as a cheap, chemically stable, and flexible substrate. Flexibility is the ability of the material to be bent without mechanical failures such as fracture and plastic deformation. One of the few mechanical parameters that describe the deformation of a material is Young's modulus, which characterizes the resistance of a material to elastic deformation. Young's moduli of polyamide 6 are lower than those of other polymers. For example, polyimide and polyethylene terephthalate have a Young's modulus of 4 GPa and 3 GPa, respectively, while the Young's modulus of polyamide 6 is 2.4 GPa [17,27,28]. As a semihydrophilic flexible polymer, PA is capable of adsorbing molecules or ions of various electrolytes from nonaqueous and aqueous solutions [29,30]. Unlike glass and fluorine-doped tin oxide substrates, on which copper selenide builds a thin film, polymer allows the material to partially diffuse in it, so the final product is a conductive composite (PA with copper selenide nanocrystals embedded in it).

Cu_{2-x}Se films can be prepared by chemical bath deposition [1,7,31], combined electrochemical followed by chemical bath deposition [8], sonochemical synthesis [32], ion beam sputtering deposition [33], electrochemical [12], successive ionic layer adsorption and reaction [15,34], and other methods.

Here, copper selenide nanocrystals were formed on the surface as well as inside the polyamide using the simple and versatile successive ionic layer adsorption and reaction (SILAR) method. The method used differs from other chemical methods, as it does not require specialized equipment or conditions; it is quite inexpensive and simple, convenient for large area deposition, and it can be used at room temperature [34]. As a low-temperature process, it also avoids oxidation [35]. The SILAR method consists of two stages: first, copper ions are adsorbed on the polyamide surface from a precursor solution containing copper ions; second, copper selenide thin films are formed by treating the layer formed in the first stage with a solution containing selenium ions. To the best of our knowledge, the copper selenide/PA composite by employing the SILAR method has never been obtained before. We suggest that slightly elevated solution temperatures could facilitate crystalline formation in the polymer matrix and therefore improve the optical and electric properties of the as-obtained composites. Combined with the natural abundance of material and the low cost of composite production, the copper selenide/PA composite could be a possibility for printable electronics on flexible substrates or in sensors in the future.

Structural characterization of the composites was performed with the help of X-ray diffraction, Scanning electron microscopy combined with Energy-dispersive X-ray spectroscopy, and Raman Spectroscopy, while the optical properties were characterized with UV/VIS spectroscopy. The surface morphology of the films was investigated with Atomic Force Microscopy. The conductivity of the composites was checked with a multimeter.

2. Materials and Methods

2.1. Materials and Film Preparation

The reactive solutions were made with just pure analytical reagents and purified water. All reagents were obtained from Sigma-Aldrich and used as received. Only freshly prepared solutions were used for experiments and were not de-aerated during the experiments.

Thin copper selenide films were deposited on a PA sheet (PA 6, Tecamid 6, density 1.13 g/cm^{-3} , thickness $500 \text{ }\mu\text{m}$, surface resistance $\sim 1 \text{ k}\Omega/\text{m}^2$), which was obtained from Ensinger GmbH (Germany). Before the experiments, the PA films were boiled in distilled water for 2 h to remove the remaining unpolymerized monomer residues. Then, they were dried with filter paper and incubated over anhydrous CaCl_2 for 24 h.

The copper sulfate solution (CuSO_4) was used as the cationic solution and the freshly prepared sodium selenosulfate solution (Na_2SeSO_3) was used as the anionic solution for the deposition of a thin film of copper selenide on PA using the SILAR method.

To prepare the Na_2SeSO_3 solution, selenium powder (99% purity) and anhydrous sodium sulfite were dissolved in distilled water for 8 h at $80 \text{ }^\circ\text{C}$ with constant stirring. It was kept for 24 h in a sealed container, to allow undissolved selenium to settle. A clear solution was obtained after it was filtered [34].

In one SILAR cycle, the substrate was immersed separately in solutions of anionic and cationic precursors. The substrate was washed with an ion exchange solution (distilled water) to avoid a homogeneous deposition between each immersion.

Thin copper selenide films on polyamide substrate were grown by repeating these cycles 30 times at different temperatures ($40 \text{ }^\circ\text{C}$, $60 \text{ }^\circ\text{C}$, and $80 \text{ }^\circ\text{C}$). The proposed reaction mechanism of the obtained film could be found in [34].

2.2. Characterization of Copper Selenide Films

X-ray diffraction (XRD) measurements were performed using a Philips PW 1050 diffractometer equipped with a PW 1730 generator, $40 \text{ kV} \times 20 \text{ mA}$, using Ni filtered $\text{Co K}\alpha$ radiation of 0.1778897 nm at room temperature. Measurements were carried out in the 2θ range of 10 to 70° with a scanning step of 0.05° and a scan time of 10 s per step. The experimental values of d (lattice spacing) for copper selenide are determined using the Bragg relation [36]. The average grain size (D) was calculated based on the full width at the half-maximum intensity (FWHM) of the main reflections by applying Scherrer's formula [37,38]. Furthermore, to have more information on the number of defects in the films, the dislocation density (δ) [34] and the strain (ϵ) values were calculated [39].

Scanning electron microscopy (SEM) was performed using a Raith GMBH e-Line instrument equipped with a field emission gun operating at 10 kV accelerating voltage, magnification: $20,000 \times$. A secondary electron signal was used for imaging. Energy-dispersive X-ray spectroscopy (EDX) imaging was performed using QUANTAX EDS with an X-Flash Detector 3001 and ESPRIT software.

The UV/VIS absorbance and diffusion reflectance spectra were recorded in the wavelength range of 200 – 800 nm on a Shimadzu UV-2600 spectrophotometer equipped with an integrated sphere. The diffuse reflectance and absorbance spectra were measured relative to a reference sample of BaSO_4 . The optical band gap from the diffuse reflectance measurements was calculated using the Tauc plot [40,41]. The acquired diffuse reflectance spectra are converted to Kubelka–Munk function [42]. The optical band gap was estimated by extrapolating the linear portion of a plot of $(\alpha h\nu)^2$ versus $h\nu$ to $\alpha = 0$. Using this function, a plot of $(\alpha h\nu)^2$ against $h\nu$ is obtained.

Raman measurements were performed using TriVista 557 micro-Raman system in backscattering configuration, equipped with a nitrogen-cooled CCD detector. The 514.5 nm line of Ar^+/Kr^+ ion laser was used as the excitation source. The measurements were performed with low laser power to prevent a local overheating of the sample.

The surface morphology of copper selenide samples was investigated by atomic force microscopy (AFM). AFM imaging was performed using the NTEGRA Prima system from NT MDT. AFM measurements were performed at room temperature and under ambient

conditions. The AFM topography and phase images were acquired simultaneously using NSG01 probes with a typical resonant frequency of 150 kHz and a 10 nm curvature radius of the tip apex.

The constant current resistivity of the copper selenide films was measured using a multimeter MS8205F (Mastech, Shenzhen, China) with special electrodes. The electrodes were produced from two nickel-plated copper plates with a 1 cm spacing and the dielectric material between them.

3. Results

3.1. XRD Characterization of Copper Selenide Thin Films

The crystal structures and orientations of the thin copper selenide films on the PA substrate were investigated by X-ray diffraction patterns and are shown in Figure 1. The XRD results revealed that all films have a polycrystalline structure.

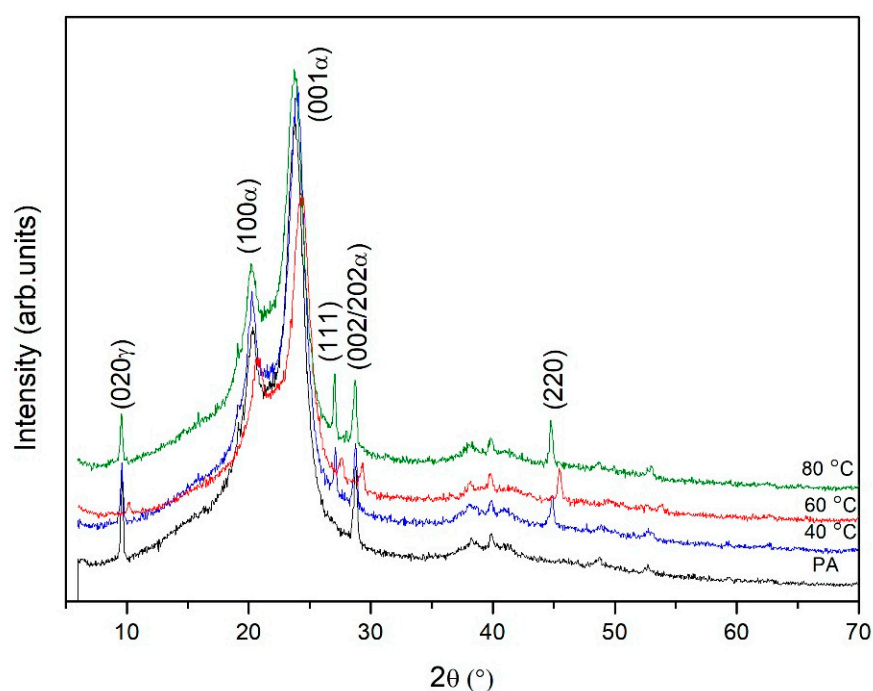


Figure 1. XRD patterns of the initial PA and copper selenide thin films.

Semicrystalline peaks of polyamide were observed between 9° and 30° (in 2θ). These peaks, according to JCPDS 12-923, appear at 20.3° and 23.8° with the corresponding d-spacing of 4.36 and 3.74, respectively. They are attributed to the (100α) and (001α) crystal planes, respectively, showing the presence of a dominant crystalline α -phase [28,43,44]. Two reflections were also observed at around $2\theta = 9.6^\circ$ (020γ) and 28.8° ($002/202\alpha$). XRD analysis showed that the temperature of the solutions of anionic and cationic precursors used in the experiment influenced the composition of the obtained thin films. The X-ray peaks on diffractograms are more intense when the solutions' temperature is higher. The peaks at 28° and 45° are absent in the spectrum of pure PA and they correspond to planes (111) and (220) of a cubic phase of Cu_{2-x}Se Berzelianite (JCPDS 6-680). It is common Cu_{2-x}Se phase [12,15]. The experimental values of the Miller indices d , 2θ and (hkl) of PA and copper selenide thin films are given in Table 1.

Table 1. Values of the Miller indices d , 2θ and (hkl) of PA and copper selenide thin films.

Miller Indices (hkl)		Temperature							
		PA		40 °C		60 °C		80 °C	
		(2 θ)	d (Å)	(2 θ)	d (Å)	(2 θ)	d (Å)	(2 θ)	d (Å)
PA	(020 γ)	9.6	9.21	9.65	9.16	10.2	8.67	9.6	9.21
	(100 α)	20.35	4.36	20.3	4.37	20.95	4.24	20.25	4.38
	(001 α)	23.8	3.74	24	3.70	24.3	3.66	23.75	3.74
Cu _{2-x} Se	(111)	–	–	27.15	3.28	27.7	3.22	27.1	3.28
PA	(002/202 α)	28.75	3.10	28.8	3.10	29.4	3.04	28.75	3.10
Cu _{2-x} Se	(220)	–	–	44.95	2.02	45.5	1.99	44.8	2.02

Changes in the intensities and full width at half maximum (FWHM) values of these peaks were observed with the use of different temperatures of solutions. The intensities of the diffraction peak increased slightly with changing temperature of the solution temperature from 40 to 80 °C. The structural parameters for the (220) peak such as FWHM (β), grain size (D), dislocation density (δ), and strain (ϵ) for all films were evaluated by XRD patterns and presented in Table 2. As shown, grain size increases, while dislocation density and strain decrease with the change in the deposition temperature.

Table 2. Grain size (D), dislocation density (δ), strain (ϵ) and full width at half maximum (FWHM, β) values of copper selenide thin films.

Temperature	2 θ (°)	β (°)	D (nm)	$\delta \cdot 10^{-3}$ (nm ⁻²)	$\epsilon \cdot 10^{-3}$ (nm ⁻²)
40 °C	44.95	1.30	6.61	22.89	13.72
60 °C	45.5	0.60	14.33	4.86	6.25
80 °C	44.8	0.54	15.81	4.00	5.76

These changes can be attributed to the improvement in film crystallization and to the inductive lattice matching, which has a strong impact on structural parameters. The higher values of D , and the smaller β , δ and ϵ values indicate better crystallization of thin films. Regarding the values of D , β , and δ , the best results were obtained for the film made at 80 °C, suggesting that a higher temperature facilitates the crystallization of the film.

3.2. Scanning Electron Microscopy and Energy Dispersive X-ray Analysis

Scanning electron microscopy was used to evaluate the changes in surface morphology of the copper selenide layer on the PA substrate, with the changes in synthesis parameters. The SEM micrographs of the samples are presented on the left-hand side of Figure 2, with a magnification of 20,000 k. The images clearly show that the polymer is well-covered with copper selenide thin films.

Copper selenide grains grow in irregular shapes and sizes. By changing temperature, it could be seen that when the temperature increases, the copper selenide film becomes denser, coated with tightly packed spherical grains that, in turn, were combined into agglomerates of 100 nm to 1 μ m. Micrographs show a compact structure composed of single types of small, densely packed microcrystals. The thin copper selenide films on surface of PA are well dispersed, relatively uniform, and consist of randomly oriented particles. Such morphological forms can produce a very rough surface with high porosity, which leads to increased catalytic activity.

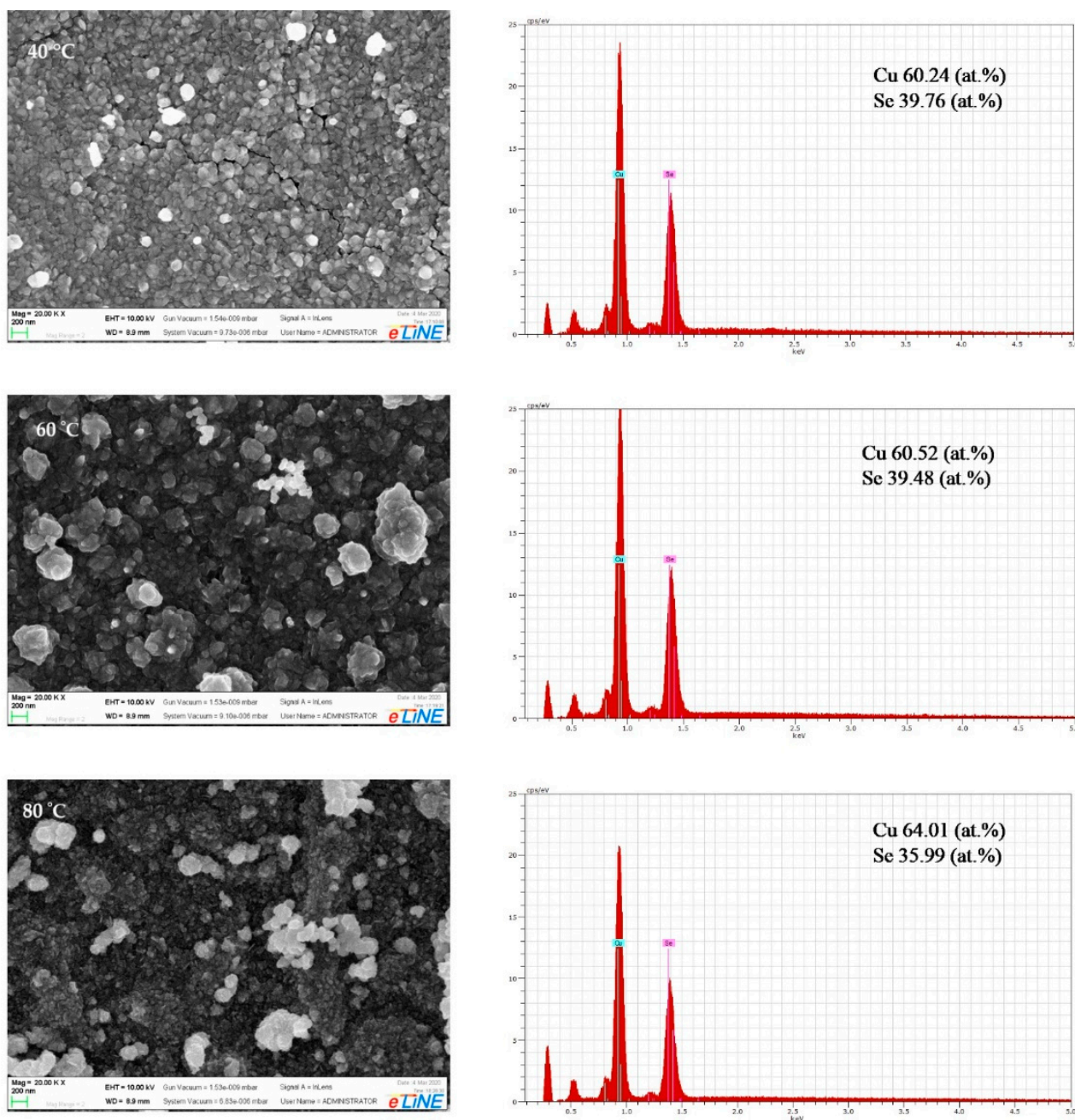


Figure 2. SEM micrographs and EDX spectra of copper selenide/PA thin films.

The elemental analysis of the copper selenide thin films was performed using an EDX micro-analytic unit attached with scanning electron microscopy and shown on the right-hand side of Figure 2. The presence of emission lines in the investigated energy range indicates that copper selenide films were successfully deposited on the polyamide substrates and the expected elements (selenium and copper) were detected. The element analysis revealed the presence of Cu and Se with the average atomic percentages shown on the right side of Figure 2. All films show a higher atomic presence of Cu than Se, which confirms the presence of Cu_{2-x}Se . The Cu/Se ratio measured by EDX analysis was 1.52–1.78, which is in good agreement with the XRD results.

3.3. Measurements of Electrical Resistivity

The resistance of thin films of copper selenide formed on PA plotted in Figure 3 is measured from the close contact up to the 1 cm distance of electrodes, and it includes the contact resistance of the electrode contacts. On the contrary, the pure PA substrate shows no electrical conductivity—the material is a pure insulator.

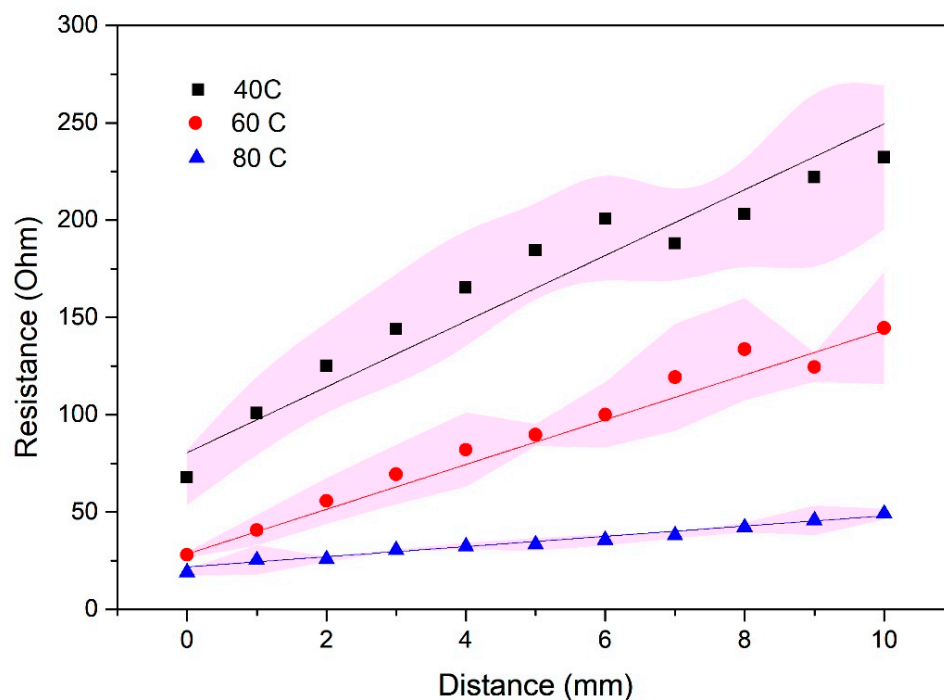


Figure 3. Resistance vs. distance graph for copper selenide films on PA. The results are the averaged values of 4 measurements, and error bars are indicated as the pink area.

At a distance of 1 cm between the electrodes, the resistances of films obtained at 40 °C, 60 °C and 80 °C are 270 Ω, 124 Ω and 49 Ω, while the values for the close contact between the electrodes were obtained to be 50 Ω, 26 Ω and 20 Ω, respectively. The corresponding slopes are 16, 11, and 2.6, which implies that the electrical properties of the film improve with elevating the temperature. Compared to XRD results, the sample obtained at 80 °C has the best crystallinity, which is directly connected with higher conductivity (i.e., lower resistivity). As it can be seen in the graph, the error bar values are minimal for the sample obtained at 80 °C, and they increase with decreasing the temperature.

3.4. Optical Analysis of Copper Selenide Thin Films

The absorbance and diffuse reflectance spectra of thin films of copper selenide on PA in the wavelength range of 200–800 nm are presented in Figure 4. An increase in the absorbance of the copper selenide films is observed with the increased temperature of solutions, as well as the opposite effect of the reflectance.

The determination of band gaps in semiconductors is significant for obtaining basic solid-state physics.

In this study, we used the Tauc plot for the determination of the optical band gap from diffuse reflectance measurements [40–42]. The experimental values of energy gaps for copper selenide thin films are determined to be 2.28 eV for the sample obtained at 80 °C, 2.14 eV for the sample at 60 °C, and 1.98 eV for the sample obtained at 40 °C (Figure 5). This is in good agreement with the values of the reported data [3,5,6].

The obtained band gap values are also consistent with AFM data, according to the rule—the smaller particle size, the bigger the band gap.

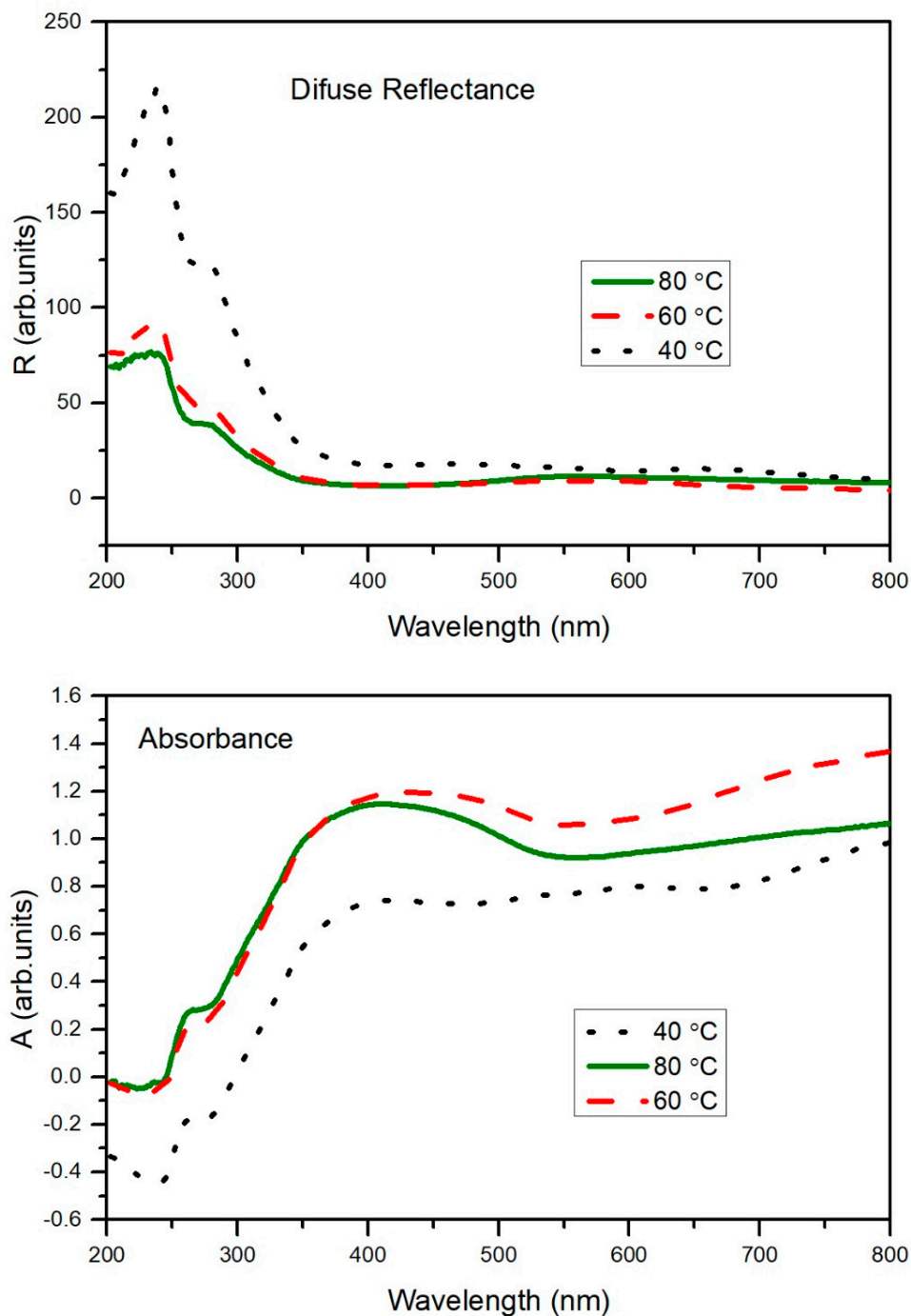


Figure 4. Diffuse reflectance and absorbance spectra of copper selenide/PA thin films.

3.5. Raman Analysis of Copper Selenide Thin Films

Raman spectroscopy is a useful spectroscopic technique for detecting the vibration energy levels of compounds and for further confirming the crystal structure.

Consequently, further clarity on the crystalline phase of the copper selenide thin films was explored by Raman analysis. As shown in Figure 6, the typical Raman spectra of three copper selenide film samples (deposited at different temperatures) exhibit similar peak positions.

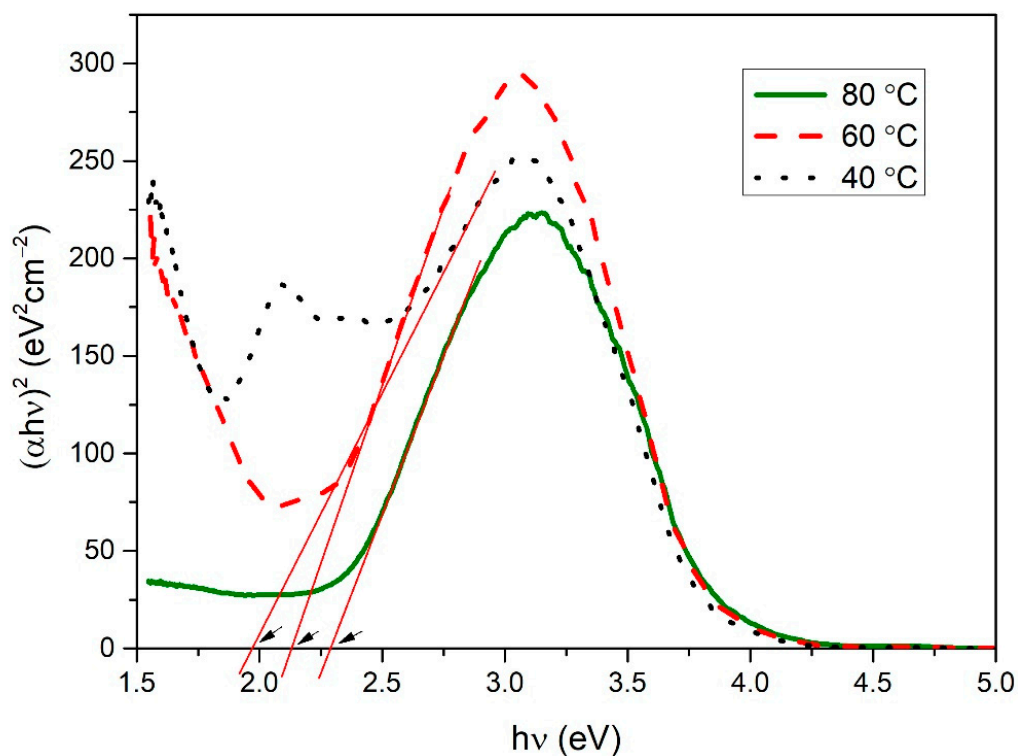


Figure 5. Plots of $(\alpha h\nu)^2$ versus $h\nu$ for copper selenide/PA thin films.

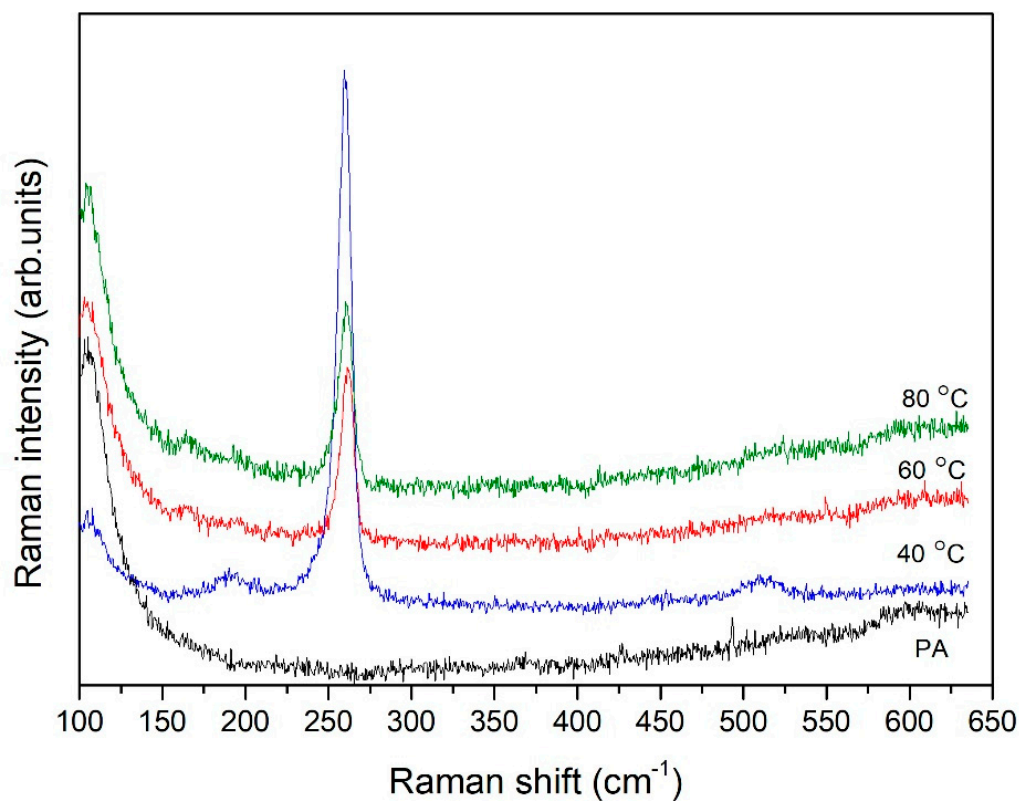


Figure 6. Raman spectra of the copper selenide/PA thin films.

The only strong peak, observed at 260 cm^{-1} , can be assigned to the Se–Se stretching vibration in Cu_{2-x}Se and is consistent with the previous reports [11,45], while the peak at 187 cm^{-1} corresponds to the Cu–Se vibration [46]. The peak at 520 cm^{-1} is the first overtone

of the intensive peak at 260 cm^{-1} . Raman analysis confirms the composition of the copper selenide/PA films. There are no modes of elemental selenium or copper. The background at the beginning of the spectra comes from PA.

3.6. AFM Analysis of Copper Selenide Thin Films

Atomic force microscopy is a very suitable method for visualizing the surface morphology and quantitative analysis of surface roughness. 2D and 3D images, as well as histograms of $5 \times 5\ \mu\text{m}$ areas of copper selenide/PA films, are presented in Figure 7. The height and surface morphology of the copper selenide thin films formed on PA depend on the temperature of the solutions of anionic and cationic precursors used in the experiment: the microstructure of the thin film changes according to the deposition temperature. The surface image shows that the surface of the film is rough with particles gathered into agglomerates. The typical parameters of the quantitative analysis of AFM images are presented in Table 3. With an increase in the precursor solution temperature, the surface roughness decreases and the film becomes more compact and dense. Average roughness is $\sim 194\text{ nm}$ at a precursor solution temperature of $40\text{ }^\circ\text{C}$ and decreases to $\sim 16\text{ nm}$ and $\sim 13\text{ nm}$ in case of the temperature of $60\text{ }^\circ\text{C}$ and $80\text{ }^\circ\text{C}$. As can be seen, a thin film of copper selenide deposited at $80\text{ }^\circ\text{C}$ temperature solution has greater uniformity and homogeneity than other films.

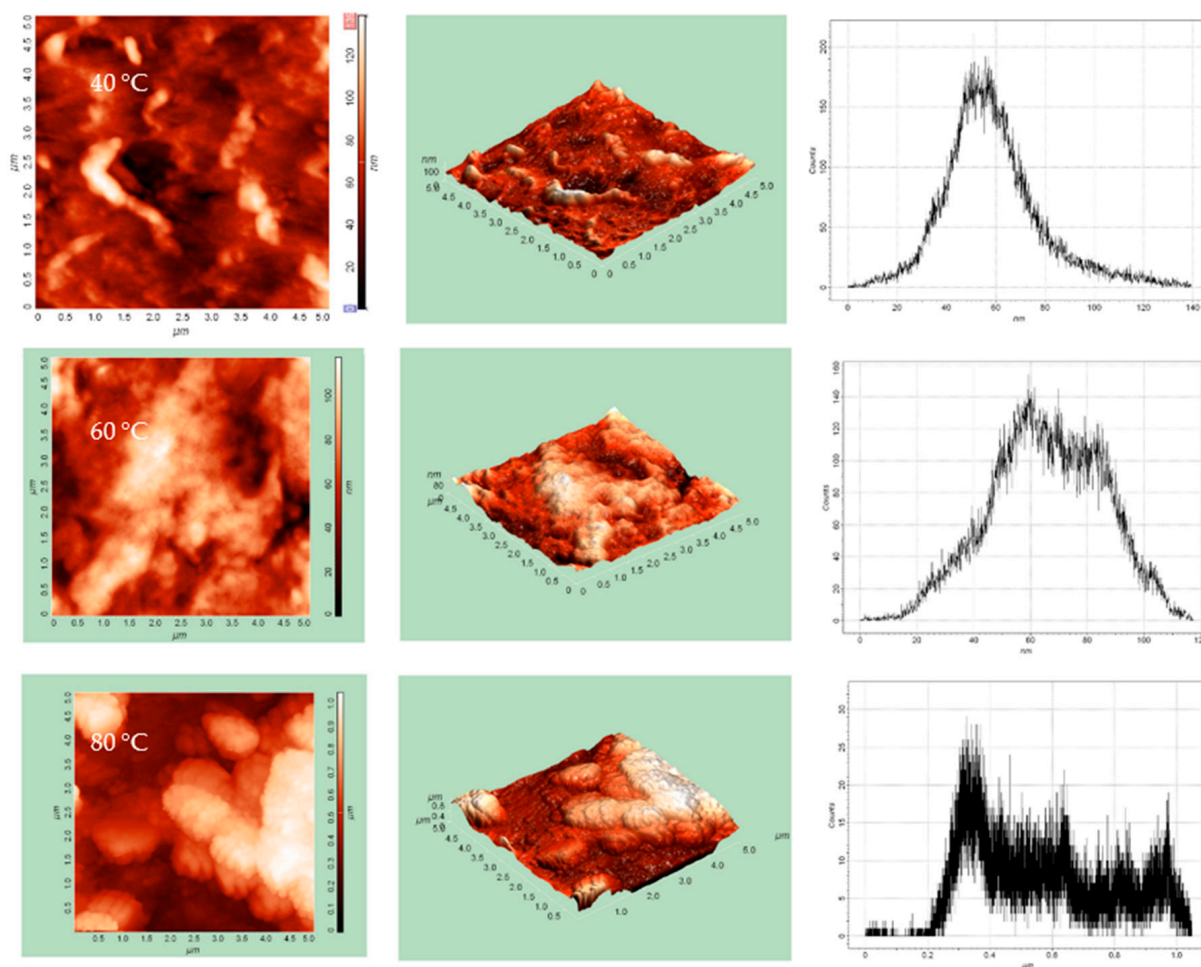


Figure 7. 2D and 3D AFM images and histograms of copper selenide/PA films.

Table 3. Surface roughness parameters of copper selenide thin films.

Parameters	Temperature		
	40 °C	60 °C	80 °C
Maximum height of peaks, h_{max} , nm	1048.41	117.32	123.16
Average height, h_{mean} , nm	565.57	65.64	49.99
Average Roughness, R_a , nm	194.62	16.24	13.32
RMS Roughness, R_q , nm	227.76	19.90	17.21
Surface skewness, R_{sk}	0.42	−0.13	0.58

4. Conclusions

$Cu_{2-x}Se$ thin films can be deposited on a flexible polyamide substrate by using the SILAR method, while by adjusting the temperature of precursor solutions we can affect and tune the optical, structural, and electrical properties of as obtained films. XRD analysis revealed that $Cu_{2-x}Se$ exists in the cubic crystal structure. The band gap energy of $Cu_{2-x}Se$ films was found to be in the order of 1.98–2.28 eV. Raman analysis confirmed the formation of the $Cu_{2-x}Se$ phase (260 cm^{-1}) without any elemental selenium or copper phase. A thin film of copper selenide deposited at 80 °C temperature solution has greater uniformity and homogeneity than other films, the largest grain size, but with the smallest agglomerates, the largest band gap value, and the best conductivity.

Author Contributions: Conceptualization, N.P. and G.J.; methodology, N.P., G.J. and E.P.; validation, M.G., N.P. and G.J.; formal analysis, N.P., G.J. and E.P.; investigation, G.J., J.M., J.C. and U.R.; data curation, M.G., J.C., U.R. and E.G.; writing—original draft preparation, G.J. and N.P.; writing—review and editing, N.P., M.G. and E.P.; visualization, G.J. and E.U.; supervision, N.P. and M.G. All authors have read and agreed to the published version of the manuscript.

Funding: This research received no external funding.

Institutional Review Board Statement: Not applicable.

Informed Consent Statement: Not applicable.

Data Availability Statement: Not applicable.

Conflicts of Interest: The authors declare no conflict of interest.

References

- García, V.M.; Nair, P.K.; Nair, M.T.S. Copper Selenide Thin Films by Chemical Bath Deposition. *J. Cryst. Growth* **1999**, *203*, 113–124. [[CrossRef](#)]
- Tyagi, K.; Gahtori, B.; Bathula, S.; Jayasimhadri, M.; Singh, N.K.; Sharma, S.; Haranath, D.; Srivastava, A.K.; Dhar, A. Enhanced Thermoelectric Performance of Spark Plasma Sintered Copper-Deficient Nanostructured Copper Selenide. *J. Phys. Chem. Solids* **2015**, *81*, 100–105. [[CrossRef](#)]
- Thirumavalavan, S.; Mani, K.; Sagadevan, S. Investigation of the Structural, Optical and Electrical Properties of Copper Selenide Thin Films. *Mater. Res.* **2015**, *18*, 1000–1007. [[CrossRef](#)]
- Zhao, L.; Wang, X.; Yun, F.F.; Wang, J.; Cheng, Z.; Dou, S.; Wang, J.; Snyder, G.J. The Effects of Te^{2-} and I^- Substitutions on the Electronic Structures, Thermoelectric Performance, and Hardness in Melt-Quenched Highly Dense $Cu_{2-x}Se$. *Wiley Online Libr.* **2015**, *1*, 1400015. [[CrossRef](#)]
- Hussain, R.A.; Hussain, I. Copper Selenide Thin Films from Growth to Applications. *Solid State Sci.* **2020**, *100*, 106101. [[CrossRef](#)]
- Hankare, P.P.; Khomane, A.S.; Chate, P.A.; Rathod, K.C.; Garadkar, K.M. Preparation of Copper Selenide Thin Films by Simple Chemical Route at Low Temperature and Their Characterization. *J. Alloy. Compd.* **2009**, *469*, 478–482. [[CrossRef](#)]
- Silva, S.F.C.; Zanatta, B.S.; Rabelo, A.C.; Bottecchia, O.L.; Tozoni, J.R.; Oliveira, O.N.; Marletta, A. Flexible and Transparent Electrodes of $Cu_{2-x}Se$ with Charge Transport via Direct Tunneling Effect. *Adv. Electron. Mater.* **2021**, *7*, 2001189. [[CrossRef](#)]
- Zyoud, A.; Murtada, K.; Kwon, H.; Choi, H.J.; Kim, T.W.; Helal, M.H.S.; Faroun, M.; Bsharat, H.; Park, D.H.; Hilal, H.S. Copper Selenide Film Electrodes Prepared by Combined Electrochemical/Chemical Bath Depositions with High Photo-Electrochemical Conversion Efficiency and Stability. *Solid State Sci.* **2018**, *75*, 53–62. [[CrossRef](#)]
- Kalenga, M.P.; Govindraju, S.; Airo, M.; Moloto, M.J.; Sikhwivhilu, L.M.; Moloto, N. Fabrication of a Schottky Device Using CuSe Nanoparticles: Colloidal versus Microwave Digestive Synthesis. *J. Nanosci. Nanotechnol.* **2015**, *15*, 4480–4486. [[CrossRef](#)]
- Singh, S.C.; Li, H.; Yao, C.; Zhan, Z.; Yu, W.; Yu, Z.; Guo, C. Structural and Compositional Control in Copper Selenide Nanocrystals for Light-Induced Self-Repairable Electrodes. *Nano Energy* **2018**, *51*, 774–785. [[CrossRef](#)]

11. Xu, J.; Yang, Q.; Kang, W.; Huang, X.; Wu, C.; Wang, L.; Luo, L.; Zhang, W.; Lee, C.S. Water Evaporation Induced Conversion of CuSe Nanoflakes to Cu_{2-x}Se Hierarchical Columnar Superstructures for High-Performance Solar Cell Applications. *Part. Part. Syst. Charact.* **2015**, *32*, 840–847. [[CrossRef](#)]
12. Zhou, R.; Huang, Y.; Zhou, J.; Niu, H.; Wan, L.; Li, Y.; Xu, J.; Xu, J. Copper Selenide (Cu₃Se₂ and Cu_{2-x}Se) Thin Films: Electrochemical Deposition and Electrocatalytic Application in Quantum Dot-Sensitized Solar Cells. *Dalton Trans.* **2018**, *47*, 16587. [[CrossRef](#)] [[PubMed](#)]
13. Zhang, H.; Xia, Y. Ratiometry, Wavelength, and Intensity: Triple Signal Readout for Colorimetric Sensing of Mercury Ions by Plasmonic Cu_{2-x}Se Nanoparticles. *ACS Sens.* **2016**, *1*, 384–391. [[CrossRef](#)]
14. Wang, Z.; Peng, F.; Wu, Y.; Yang, L.; Zhang, F.; Huang, J. Template Synthesis of Cu_{2-x}Se Nanoboxes and Their Gas Sensing Properties. *Cryst. Eng. Comm.* **2012**, *14*, 3528–3533. [[CrossRef](#)]
15. Astam, A.; Akaltun, Y.; Yildirim, M. Conversion of SILAR Deposited Cu₃Se₂ Thin Films to Cu_{2-x}Se by Annealing. *Mater. Lett.* **2016**, *166*, 9–11. [[CrossRef](#)]
16. Bhuse, V.M.; Hankare, P.P.; Garadkar, K.M.; Khomane, A.S. A Simple, Convenient, Low Temperature Route to Grow Polycrystalline Copper Selenide Thin Films. *Mater. Chem. Phys.* **2003**, *80*, 82–88. [[CrossRef](#)]
17. Li, X.; Li, P.; Wu, Z.; Luo, D.; Yu, H.-Y.; Lu, Z.-H. Review and Perspective of Materials for Flexible Solar Cells. *Mater. Rep. Energy* **2021**, *1*, 100001. [[CrossRef](#)]
18. Yoon, H.; Kang, S.M.; Lee, J.K.; Choi, M. Hysteresis-Free Low-Temperature-Processed Planar Perovskite Solar Cells with 19.1% Efficiency. *Energy Environ. Sci.* **2016**, *9*, 2262–2266. [[CrossRef](#)]
19. Aernouts, T.; Vanlaeke, P.; Geens, W.; Poortmans, J.; Heremans, P.; Borghs, S.; Mertens, R.; Andriessen, R.; Leenders, L. Printable Anodes for Flexible Organic Solar Cell Modules. *Thin Solid Film.* **2004**, *451–452*, 22–25. [[CrossRef](#)]
20. Fonrodona, M.; Escarré, J.; Villar, F.; Soler, D.; Asensi, J.M.; Bertomeu, J.; Andreu, J. PEN as Substrate for New Solar Cell Technologies. *Sol. Energy Mater. Sol. Cells* **2005**, *89*, 37–47. [[CrossRef](#)]
21. Chen, H.; Gu, Z.G.; Zhang, J. Chiral-Induced Ultrathin Covalent Organic Frameworks Nanosheets with Tunable Circularly Polarized Luminescence. *J. Am. Chem. Soc.* **2022**, *144*, 7245–7252. [[CrossRef](#)] [[PubMed](#)]
22. Hassan, M.; Abbas, G.; Li, N.; Afzal, A.; Haider, Z.; Ahmed, S.; Xu, X.; Pan, C.; Peng, Z. Significance of Flexible Substrates for Wearable and Implantable Devices: Recent Advances and Perspectives. *Adv. Mater. Technol.* **2022**, *7*, 2100773. [[CrossRef](#)]
23. Wang, K.; Cheng, S.; Hu, Q.; Yu, F.; Cheng, Y.; Huang, K.; Yuan, H.; Jiang, J.; Li, W.; Li, J.; et al. Vertical Graphene-Coated Cu Wire for Enhanced Tolerance to High Current Density in Power Transmission. *Nano Res.* **2021**, *14*, 1–7. [[CrossRef](#)]
24. Chen, Y.; Gao, C.; Yang, T.; Li, W.; Xu, H.; Sun, Z.; Chen, Y.; Gao, C.; Yang, T.; Li, W.; et al. Research Advances of Ferroelectric Semiconductors of 2D Hybrid Perovskites toward Photoelectronic Applications. *Chin. J. Struct. Chem.* **2022**, *41*, 2204001–2204011. [[CrossRef](#)]
25. Chang, H.B.; Liu, J.B.; Dong, Z.; Wang, D.D.; Xin, Y.; Jiang, Z.L.; Tang, S.S. Enhancement of Photocatalytic Degradation of Polyvinyl Chloride Plastic with Fe₂O₃ Modified AgNbO₃ Photocatalyst under Visible-Light Irradiation. *Jiegou Huaxue* **2021**, *40*, 1595–1603. [[CrossRef](#)]
26. Vikulov, S.; di Stasio, F.; Ceseracciu, L.; Saldanha, P.L.; Scarpellini, A.; Dang, Z.; Krahne, R.; Manna, L.; Lesnyak, V. Fully Solution-Processed Conductive Films Based on Colloidal Copper Selenide Nanosheets for Flexible Electronics. *Adv. Funct. Mater.* **2016**, *26*, 3670–3677. [[CrossRef](#)]
27. Qu, C.; Hu, J.; Liu, X.; Li, Z.; Ding, Y. Morphology and Mechanical Properties of Polyimide Films: The Effects of UV Irradiation on Microscale Surface. *Materials* **2017**, *10*, 1329. [[CrossRef](#)]
28. Parodi, E.; Peters, G.W.M.; Govaert, L.E. Structure-Properties Relations for Polyamide 6, Part 1: Influence of the Thermal History during Compression Moulding on Deformation and Failure Kinetics. *Polymers* **2018**, *10*, 710. [[CrossRef](#)]
29. Janickis, V.; Petraškauskienė, N.; Žalėnkiene, S.; Morkvenaite-Vilkociene, I.; Ramanavicius, A. Morphology of CdSe-Based Coatings Formed on Polyamide Substrate. *J. Nanosci. Nanotechnol.* **2018**, *18*, 604–613. [[CrossRef](#)]
30. Ivanauskas, R.; Milasiene, D. Fabrication of Polyamide-Ag₂Se Composite Films with Controllable Properties by an Adsorption-Diffusion Method. *J. Phys. Chem. Solids* **2020**, *145*, 109533. [[CrossRef](#)]
31. Lakshmi, M.; Bindu, K.; Bini, S.; Vijayakumar, K.P.; Sudha Kartha, C.; Abe, T.; Kashiwaba, Y. Chemical Bath Deposition of Different Phases of Copper Selenide Thin Films by Controlling Bath Parameters. *Thin Solid Film.* **2000**, *370*, 89–95. [[CrossRef](#)]
32. Xu, S.; Wang, H.; Zhu, J.J.; Chen, H.Y. Sonochemical Synthesis of Copper Selenides Nanocrystals with Different Phases. *J. Cryst. Growth* **2002**, *234*, 263–266. [[CrossRef](#)]
33. Li, Y.D.; Fan, P.; Zheng, Z.H.; Luo, J.T.; Liang, G.X.; Guo, S.Z. The Influence of Heat Treatments on the Thermoelectric Properties of Copper Selenide Thin Films Prepared by Ion Beam Sputtering Deposition. *J. Alloy. Compd.* **2016**, *658*, 880–884. [[CrossRef](#)]
34. Güzeldir, B.; Sağlam, M. Using Different Chemical Methods for Deposition of Copper Selenide Thin Films and Comparison of Their Characterization. *Spectrochim. Acta Part A Mol. Biomol. Spectrosc.* **2015**, *150*, 111–119. [[CrossRef](#)]
35. Pathan, H.M.; Lokhande, C.D. Deposition of Metal Chalcogenide Thin Films by Successive Ionic Layer Adsorption and Reaction (SILAR) Method. *Bull. Mater. Sci.* **2004**, *27*, 85–111. [[CrossRef](#)]
36. Bragg, W.H.; Bragg, W.L.; Bragg, B.W.; Professor of Physics, C. The Reflection of X-Rays by Crystals. *Proc. R. Soc. London. Ser. A Contain. Pap. A Math. Phys. Character* **1913**, *88*, 428–438. [[CrossRef](#)]
37. Patterson, A.L. The Scherrer Formula for X-Ray Particle Size Determination. *Phys. Rev.* **1939**, *56*, 978. [[CrossRef](#)]

38. Nath, D.; Singh, F.; Das, R. X-Ray Diffraction Analysis by Williamson-Hall, Halder-Wagner and Size-Strain Plot Methods of CdSe Nanoparticles—A Comparative Study. *Mater. Chem. Phys.* **2020**, *239*, 122021. [[CrossRef](#)]
39. Ashraf, M.; Akhtar, S.M.J.; Khan, A.F.; Ali, Z.; Qayyum, A. Effect of Annealing on Structural and Optoelectronic Properties of Nanostructured ZnSe Thin Films. *J. Alloy. Compd.* **2011**, *509*, 2414–2419. [[CrossRef](#)]
40. Tauc, J.; Grigorovici, R.; Vancu, A. Optical Properties and Electronic Structure of Amorphous Germanium. *Phys. Status Solidi (B)* **1966**, *15*, 627–637. [[CrossRef](#)]
41. Makuła, P.; Pacia, M.; Macyk, W. How To Correctly Determine the Band Gap Energy of Modified Semiconductor Photocatalysts Based on UV-Vis Spectra. *J. Phys. Chem. Lett.* **2018**, *9*, 6814–6817. [[CrossRef](#)] [[PubMed](#)]
42. Petrović, M.; Gilić, M.; Ćirković, J.; Romčević, M.; Romčević, N.; Trajić, J.; Yahia, I. Optical Properties of CuSe Thin Films—Band Gap Determination. *Sci. Sinter.* **2017**, *49*, 167–174. [[CrossRef](#)]
43. Banerjee, S.S.; Janke, A.; Gohs, U.; Heinrich, G. Electron-Induced Reactive Processing of Polyamide 6/Polypropylene Blends: Morphology and Properties. *Eur. Polym. J.* **2018**, *98*, 295–301. [[CrossRef](#)]
44. Zhao, X.Y.; Zhang, B.Z. The Effects of Annealing (Solid and Melt) on the Time Evolution of the Polymorphic Structure of Polyamide 6. *J. Appl. Polym. Sci.* **2010**, *115*, 1688–1694. [[CrossRef](#)]
45. Minceva-Sukarova, B.; Najdoski, M.; Grozdanov, I.; Chunnillal, C.J. Raman Spectra of Thin Solid Films of Some Metal Sulfides. *J. Mol. Struct.* **1997**, *410–411*, 267–270. [[CrossRef](#)]
46. Malavekar, D.B.; Bulakhe, R.N.; Kale, S.B.; Patil, U.M.; In, I.; Lokhande, C.D. Synthesis of Layered Copper Selenide on Reduced Graphene Oxide Sheets via SILAR Method for Flexible Asymmetric Solid-State Supercapacitor. *J. Alloy. Compd.* **2021**, *869*, 159198. [[CrossRef](#)]



Article

A Single-Cell Raman Spectroscopy Analysis of Bone Marrow Mesenchymal Stem/Stromal Cells to Identify Inter-Individual Diversity

Tamara Kukolj ^{1,*},[†] , Jasmina Lazarević ^{2,†}, Ana Borojević ³, Uroš Ralević ², Dragana Vujić ^{3,4}, Aleksandra Jauković ¹, Nenad Lazarević ² and Diana Bugarski ¹

- ¹ Group for Hematology and Stem Cells, Institute for Medical Research, National Institute of Republic of Serbia, University of Belgrade, 11129 Belgrade, Serbia; aleksandra@imi.bg.ac.rs (A.J.); dianab@imi.bg.ac.rs (D.B.)
² Center for Solid State Physics and New Materials, Institute of Physics Belgrade, University of Belgrade, Pregrevica 118, 11080 Belgrade, Serbia; jasminal@ipb.ac.rs (J.L.); uros.ralevic@ipb.ac.rs (U.R.); nenad.lazarevic@ipb.ac.rs (N.L.)
³ Mother and Child Health Care Institute of Serbia “Dr Vukan Čupić”, 11000 Belgrade, Serbia; ana.stojanovic.89@gmail.com (A.B.); vujicdbg@gmail.com (D.V.)
⁴ School of Medicine, University of Belgrade, 11000 Belgrade, Serbia
* Correspondence: tamara.kukolj@imi.bg.ac.rs; Tel.: +381-11-2685-788
† These authors contributed equally to this work.

Abstract: The heterogeneity of stem cells represents the main challenge in regenerative medicine development. This issue is particularly pronounced when it comes to the use of primary mesenchymal stem/stromal cells (MSCs) due to a lack of identification markers. Considering the need for additional approaches in MSCs characterization, we applied Raman spectroscopy to investigate inter-individual differences between bone marrow MSCs (BM-MSCs). Based on standard biological tests, BM-MSCs of analyzed donors fulfill all conditions for their characterization, while no donor-related specifics were observed in terms of BM-MSCs morphology, phenotype, multilineage differentiation potential, colony-forming capacity, expression of pluripotency-associated markers or proliferative capacity. However, examination of BM-MSCs at a single-cell level by Raman spectroscopy revealed that despite similar biochemical background, fine differences in the Raman spectra of BM-MSCs of each donor can be detected. After extensive principal component analysis (PCA) of Raman spectra, our study revealed the possibility of this method to diversify BM-MSCs populations, whereby the grouping of cell populations was most prominent when cell populations were analyzed in pairs. These results indicate that Raman spectroscopy, as a label-free assay, could have a huge potential in understanding stem cell heterogeneity and sorting cell populations with a similar biochemical background that can be significant for the development of personalized therapy approaches.

Keywords: human bone marrow mesenchymal stem/stromal cells (BM-MSCs); Raman spectroscopy; single cell; inter-individual heterogeneity



Citation: Kukolj, T.; Lazarević, J.; Borojević, A.; Ralević, U.; Vujić, D.; Jauković, A.; Lazarević, N.; Bugarski, D. A Single-Cell Raman Spectroscopy Analysis of Bone Marrow Mesenchymal Stem/Stromal Cells to Identify Inter-Individual Diversity. *Int. J. Mol. Sci.* **2022**, *23*, 4915. <https://doi.org/10.3390/ijms23094915>

Academic Editor:
Sébastien Bonhommeau

Received: 30 March 2022
Accepted: 25 April 2022
Published: 28 April 2022

Publisher's Note: MDPI stays neutral with regard to jurisdictional claims in published maps and institutional affiliations.



Copyright: © 2022 by the authors. Licensee MDPI, Basel, Switzerland. This article is an open access article distributed under the terms and conditions of the Creative Commons Attribution (CC BY) license (<https://creativecommons.org/licenses/by/4.0/>).

1. Introduction

In the field of regenerative medicine, mesenchymal stem/stromal cells (MSCs) are reported to be the most frequently investigated stem cells (SCs) in clinical trials [1]. This type of SCs is capable of self-renewing and differentiating toward mature cells [2–4], whereby their potential therapeutic application is also based on their abilities to produce a wide variety of bioactive factors that support tissue remodeling and exhibit immunoregulatory features as well [5–7]. MSCs are a particularly convenient type of SCs for therapeutic use, since they can be isolated from almost all adult and postnatal tissues obtained after regular medical procedures. Along with minimal invasiveness and accessibility, MSCs are easy to expand, thus providing sufficient yield for use in potential therapy treatments [4,8,9]. However, the main challenge for their wide therapeutic usage is the heterogeneity of

biological properties between different MSCs populations [10], as there is no specific cellular marker to identify MSCs [11–13]. Following isolation, MSCs identification is based on minimal requirements evinced under in vitro conditions. These criteria include the fibroblast-like shape of cells adherent to the plastic surface, a phenotype that considers the expression of mesenchymal markers (CD44, CD73, CD90, CD105, etc.), with the lack of hematopoietic markers (CD34, CD45, CD14, etc.) and differentiation potential toward at least three lineages (osteogenic, chondrogenic or adipogenic) [14,15]. However, despite the morphological, phenotypical and functional similarities between MSCs populations, specific intrinsic properties related to the MSCs tissue source have been documented [16–19]. Moreover, other factors such as culture conditions, donor specificity or age can also have a significant influence on the variability of results related to the MSCs population description [10,20]. All these factors significantly disable the standardization of conditions necessary to establish therapeutic procedures. Therefore, in the field of MSCs research and MSCs-based therapy, the key issue today is still the precise characterization of MSCs that evidently requires the use of more sensitive tests.

In order to fully describe a certain population of cells, the most advanced technologies with the competence to provide data on each analyzed cell (i.e., single cell analysis) are needed. However, most of the cell and molecular biology techniques are very demanding in terms of sample preparation and duration of the process, with cell destruction or perturbation as a common consequence [21–23]. In basic research, there is a strong benefit to utilizing technologies that would allow simple, fast, reproducible, non-destructive and information-rich characterization of each cell within the MSCs population.

Raman spectroscopy of a single cell provides a one-of-a-kind vibrational spectrum in which macromolecules of large light scattering cross-section (e.g., proteins, nucleic acids, carbohydrates and lipids) and their interactions are present as characteristic vibrational modes, as a unique imprint of the analyzed sample. Having in mind the advantages of Raman spectroscopy, it is indicative that it can be a method of choice for the analysis of MSCs properties at a single-cell level. It should also be highlighted that a large number of data on the biochemical composition at the level of a single cell in a short time interval can be analyzed [24,25], thus providing a prompt and unambiguous interpretation of cell populations compositions which is not possible by applying currently available bioassays.

Although Raman spectroscopy has been applied in stem cell analysis [26–31], the subject of these research studies was mostly related to the examination of SCs differentiation processes [29,32–39]. In this study, we showed the potential of Raman spectroscopy to assess the heterogeneity of undifferentiated MSCs through the diversification of bone marrow MSCs (BM-MSCs) populations from different individuals. BM-MSCs from five healthy pediatric donors were isolated and characterized according to the minimal criteria for their characterization set by the International Society for Stem Cells (ISCT). Standard biological tests did not reveal donor-dependent variations of MSC features (adherence, phenotype, clonogenicity, and multilineage differentiation potential). In addition, no differences were detected in terms of their proliferative capacity and expression of pluripotency-associated markers. Raman spectroscopy analysis of BM-MSCs at the single-cell level revealed a similar biochemical background of the tested samples. However, after extensive principal component analysis (PCA), a clustering of MSCs populations was observed, particularly when the samples were analyzed in pairs.

2. Results

2.1. Comparison of Bone Marrow Mesenchymal Stem/Stromal Cell Features Isolated from Five Pediatric Donors

Following the isolation and in vitro expansion of BM-MSCs of each donor, we were guided by the minimal criteria for MSCs identification set by the International Society for Cellular Therapies (ISCT) [14] to confirm the BM-MSC identity of isolated cells. For that purpose, we analyzed the morphology of adherent cells, their immunophenotype and differentiation potential comparing in parallel these features between different donors. At the

fifth passage, as well as during long-term cultivation, isolated adherent BM-MSCs derived from all five donors retained a fibroblast-like morphology with a similar cytoskeleton organization of F-actin (Figure 1A). Further on, flow cytometry analysis showed that BM-MSCs exhibited typical immunophenotype since the surface antigens related to the MSCs were highly expressed, while the rate of hematopoietic stem cell markers expression was low as determined by flow cytometry (Figure 1B). Namely, the expression of MSCs-positive markers between donors ranged from 97.89% to 99% for CD29, from 84.6% to 98.05% for CD73, from 78.5% to 97.78% for CD90, and from 96.1% to 98.13% for CD105. A slightly lower expression of CD73 and CD90 markers was observed for BM-MSCs of D5, indicating the inter-individual heterogeneity of BM-MSCs populations. On the other side, less than 2.3% of BM-MSCs expressed CD45, while in less than 1.73% of cells, HLA-DR expression was detectable. Based on these results, no significant difference in immunophenotype at the fifth passage between the BM-MSCs of pediatric donors was detected.

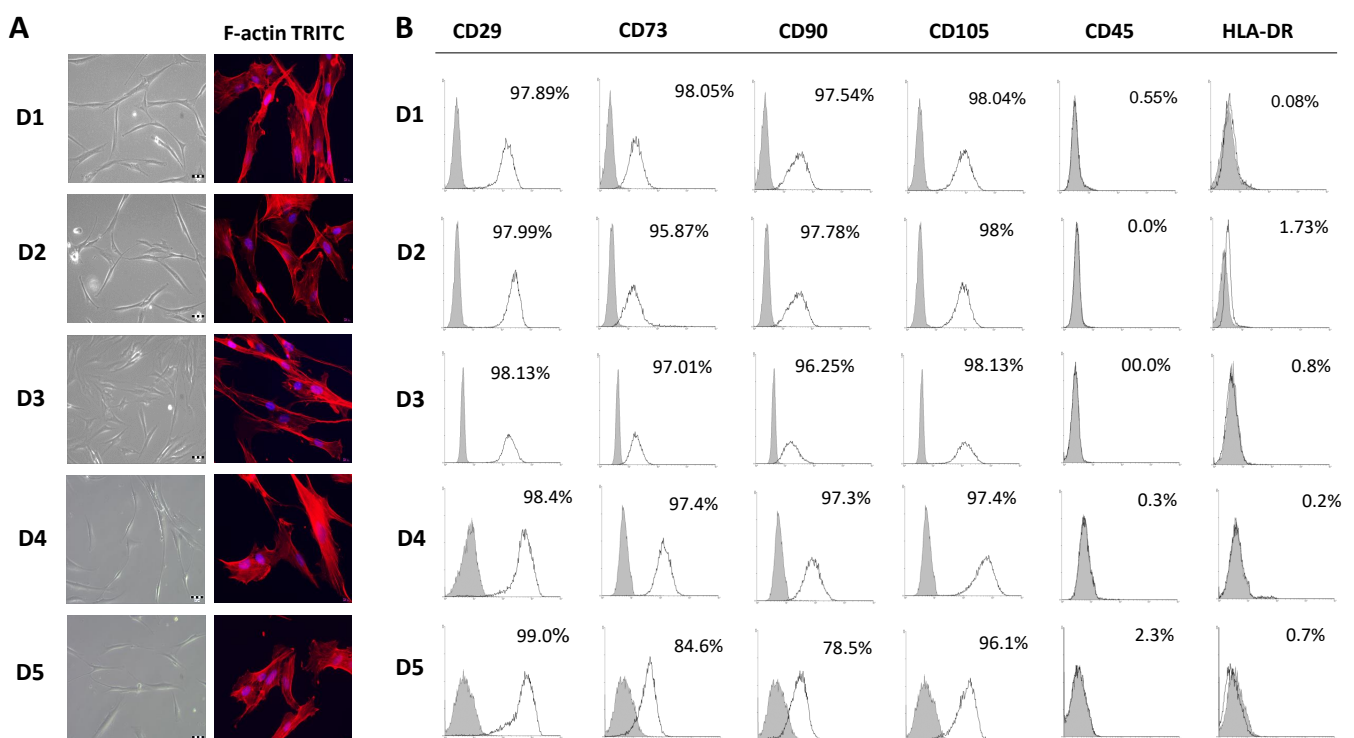


Figure 1. Morphology and immunophenotype of BM-MSCs derived from pediatric donors. (A) Adherent BM-MSCs from five donors (D1–D5) with fibroblast-like shape grown in GM under standard conditions for 3 days (scale bars: 50 μ M); Fluorescent images of TRITC-conjugated phalloidin labeled F-actin (red) merged with DAPI (4',6-diamidino-2-phenylindole) nuclear staining (blue) (scale bars: 20 μ M). (B) Immunophenotypic characteristics of BM-MSCs estimated by follow cytometry. Representative histograms for each donor presenting percentages of cells positive (empty peaks) for mesenchymal markers (CD29, CD73, CD90, CD105) and hematopoietic markers (CD45, HLA-DR) in comparison to isotype control (shaded peaks).

Regarding the functional analysis related to the potential of MSCs to differentiate toward more mature cells, we examined the ability of isolated BM-MSCs to differentiate toward osteogenic, chondrogenic and adipogenic lineages, to further define the identity features of MSCs. As shown in Figure 2, the obtained results demonstrate that the BM-MSCs of each donor possess tri-lineage differentiation capacity, while no spontaneous differentiation was observed. Namely, the activity of the ALP enzyme was significantly increased in BM-MSC cultivated in the osteogenic medium in comparison to the control cells. In accordance with early osteogenesis increase, BM-MSCs achieved complete osteoblast differentiation through matrix mineralization production, as determined

by Alizarin red staining. Thus, the osteogenic differentiation of BM-MSCs of all five donors was confirmed, with no significant differences observed among donors. Similarly, BM-MSCs of each donor were able to differentiate into chondrocytes under chondrogenic inductive conditions, since the significant increase in cartilage-related proteoglycans was observed by Safranin O staining in comparison to the control cells. Along with osteogenesis and chondrogenesis, the BM-MSCs of each donor showed a similar ability to differentiate into adipocytes after cultivation in an adipogenic medium. In these cells, the significant formation of intracellular lipid droplets was evidenced via Oil Red O staining, which was not observed in the control group.

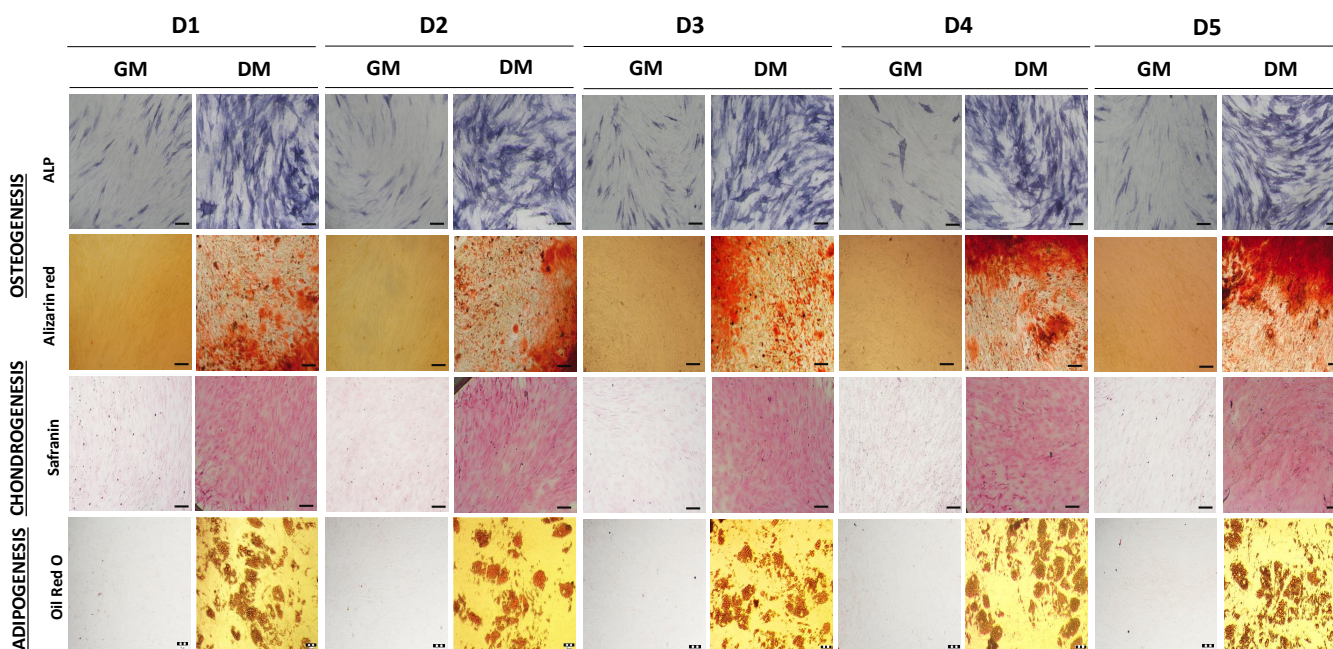


Figure 2. Multilineage differentiation potential of BM-MSCs. Representative images of cells cultivated in GM or differentiation medium (DM) are shown. Osteogenic differentiation detected after 7 days of cultivation by staining for alkaline phosphatase (ALP) activity, and after 21 days for calcium depositions by Alizarin red staining (Scale bar: 50 μ M). Chondrogenic differentiation detected with Safranin O staining of proteoglycans after 21 days cultivation (scale bar: 50 μ M). Adipogenic differentiation determined based on the presence of intracellular lipid droplets by Oil Red O staining after 21 days (scale bar: 20 μ M).

Overall, these data confirm that the BM-MSCs of each pediatric donor exhibit characteristics related to mesenchymal stem cells, while no significant differences between donors were detected.

2.2. Self-Renewal of BM-MSCs and Expression of Markers Associated with Pluripotency

Further on, we evaluated the self-renewal potential of BM-MSCs by using Colony Forming Unit–Fibroblast (CFU-F) assay. Results shown in Figure 3A demonstrate that the BM-MSCs of each donor have comparable clonogenic potential, since the average efficiency for each donor was approximately 3%. It can also be noticed that the morphology of CFU-F was heterogenic but similar amongst donors.

Along with clonogenic capacity, we examined the expression of markers associated with pluripotency via immunofluorescent labeling. The results presented in Figure 3B revealed the constitutive expression of pluripotency-related markers including OCT4A, SOX2 and NANOG in the BM-MSCs of each donor observed both in cytoplasmic and in the nuclear region. However, slight differences between donors were noticed. As for OCT4A, a more dominant expression was detected in the nuclear/perinuclear region of cells derived from donors D3, D4, and D5, while weaker cytoplasmatic expression was

observed for the BM-MSCs of donors D1 and D2. The expression of SOX2 was highest in the nuclear/perinuclear region of D3 and D5, whereas D1, D2, and D4 exhibited a lower expression of this transcription factor, which was localized mainly in the perinuclear and cytoplasmic compartment. Considering NANOG expression, some differences in protein localization were detected among donors, since nuclear localization was determined in D4 and perinuclear/cytoplasmic in donors D1, D2, D3, and D5.

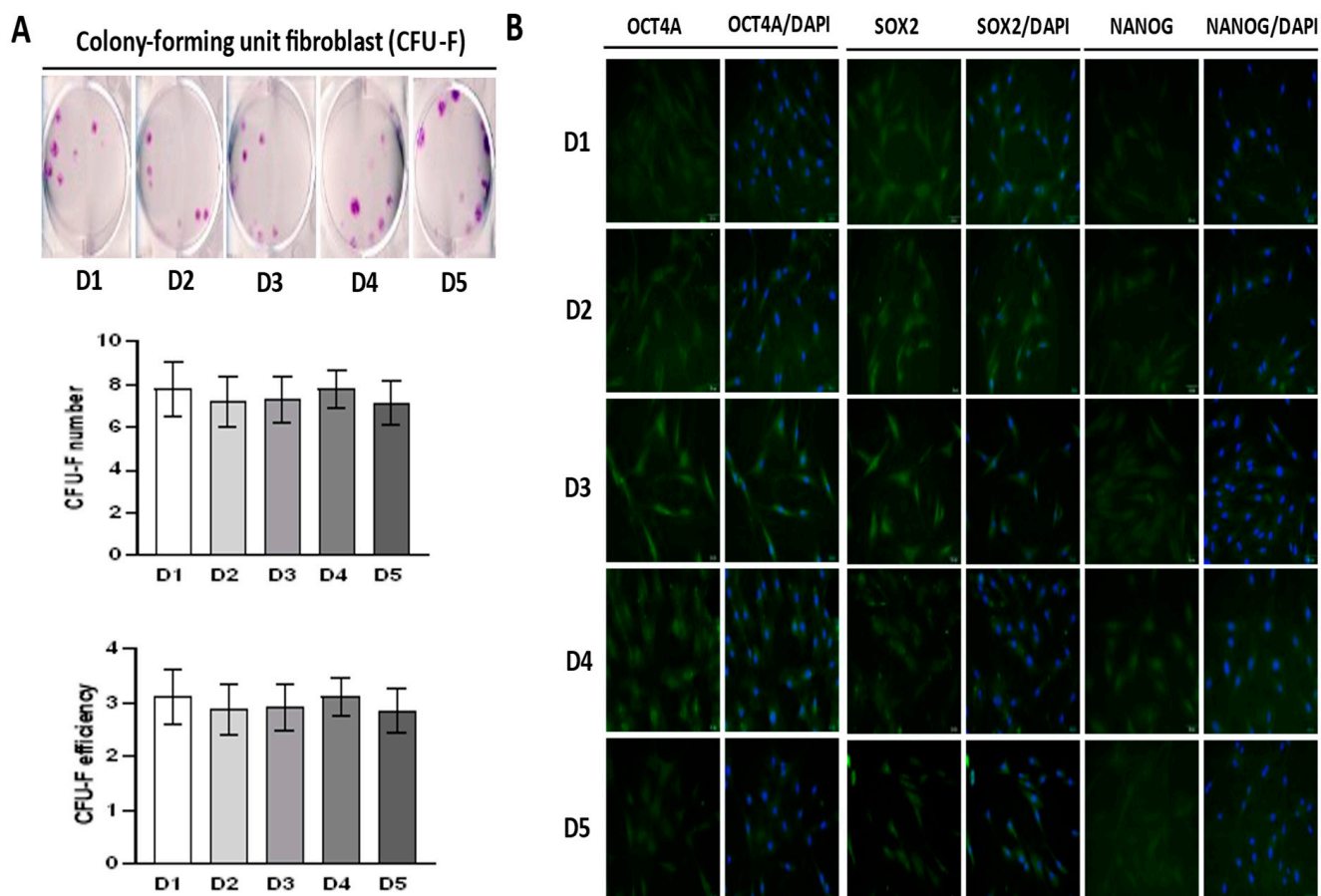


Figure 3. Clonogenic capacity and expression of pluripotency-associated markers in BM-MSCs. (A). Representative images of colony-forming unit–fibroblast (CFU-F) stained by crystal violet are shown. CFU-F number and efficiency (number of colonies relative to number of seeded cells) of BM-MSCs are presented as mean \pm SEM of three independent experiments. (B) Expression of pluripotency-associated transcription factors (OCT4, SOX-2 and NANOG) determined by indirect immunofluorescence labeling with FITC-conjugated corresponding secondary antibodies. Cell nuclei were stained with DAPI (4',6-diamidino-2-phenylindole). Representative images are shown (scale bars: 50 μ m).

2.3. Growth Characteristics of BM-MSCs

A comparison of BM-MSC viability performed by MTT test revealed equivalent metabolic activity between donors following 24 h (Figure 4A). With a slight increase, this trend was retained after 48 h as well (Figure 4A). In accordance with this result, analysis of the population doubling time (PDT) demonstrated that the BM-MSCs of each donor possess a uniform growth rate (Figure 4B). The active proliferative abilities of all donors were further confirmed by investigation of cellular senescence via the determination of β -galactosidase expression that showed a very low number of β -gal-positive cells among all donors (Figure 4C), which is in agreement with MTT and PDT data. These results were also supported on a molecular level by the evidence of strong constitutive expression of the intracellular proliferation marker Ki67 (Figure 4D).

Interestingly, the highest expression of Ki67 was detected for D5, whereby cellular localization varied between donors. BM-MSCs of D1, D2, and D3 expressed Ki67 in the cytoplasm and nucleus, while the Ki67 expression of D4 and D5 was predominantly cytoplasmic (Figure 4D). Analysis of p53 protein, as a regulator of cell proliferation and senescence, revealed similar basal expression in BM-MSCs with differences in its localization. p53 was detected in the cytoplasm and nucleus in D1, D2 and D3 BM-MSCs, while in donors D4 and D5, p53 was detected only within the nucleus contrary to the Ki67 localization pattern (Figure 4D).

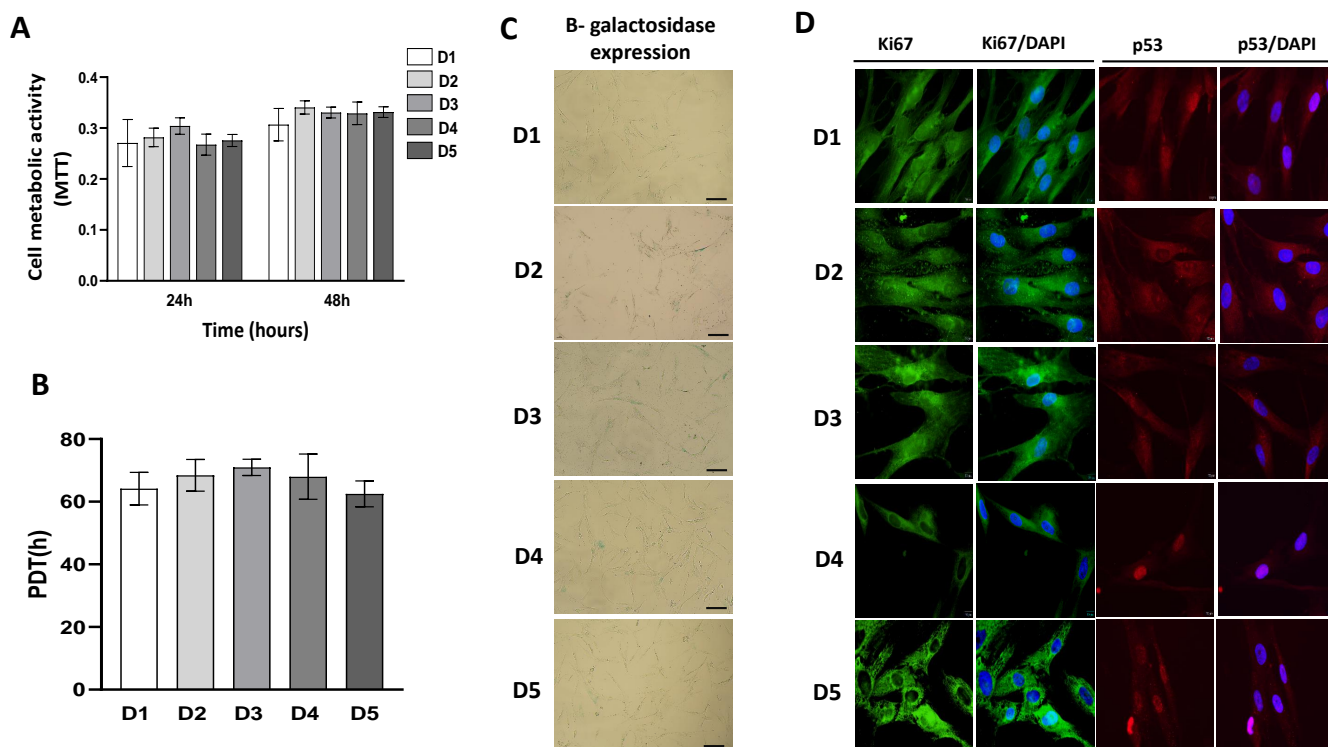


Figure 4. Growth characteristics of BM-MSCs. (A) Metabolic activity of cells isolated from 5 donors during 24 h and 48 h estimated by MTT test. (B) Population doubling time (PDT) of BM-MSCs. Cells were cultivated in standard conditions, passaged at 90% confluency, and enumerated at each passage (up to 6th passage). For PDTs calculation, the formula described in Material and Methods was applied. Results on the graph are presented as \pm SEM of independent experiments. (C) Representative images of BM-MSCs stained for β -galactosidase expression after one day of cultivation under standard conditions (scale bar: 50 μ M). (D) Expression of proliferation-associated marker Ki67 and p53 detected by indirect immunofluorescence labeling with corresponding FITC-conjugated or AlexaFluor555-conjugated secondary antibodies. Cell nuclei were stained with DAPI (4',6-diamidino-2-phenylindole). Representative images are shown (scale bars: 10 μ m).

2.4. Raman Spectra Analyses

The Raman spectra of human cells, depending on their origin, nature or physiological state, have numerous mutual features whose Raman shifts are used as spectral markers. Cells under observation, as primary MSCs cultures, naturally, present a heterogeneous entity highly susceptible to modifications of the intrinsic chemical structure, and consequently, spectral features, by standard culture conditions, among others. As the analyzed cells were fixed to provide a less variable system, it was ensured that physiological processes within the cells were interrupted at the same (desired) stage. In addition, to keep the system out of the additional extrinsic influence, the investigated cells were of the same 5th passage.

The main contribution to BM-MSCs Raman spectra comes from nucleic acids (singled out purine and/or pyrimidine bases and DNA/RNA backbone structure), proteins (individual amino acids, amide groups of proteins' secondary structure and various vibrations within C-C or C-N bonding), and lipids (vibrations within the hydrocarbon chain), as shown in Table 1 [27,36,40–44].

Table 1. Vibrations in BM-MSCs and their energies noticed in obtained Raman spectra. Adapted from [27,36,40–44].

Energy (cm ⁻¹)	Biomolecule Assignment
940	Skeletal modes in polysaccharides
957	O-P-O symmetric stretch in adenosine-monophosphate
1003	Symmetric ring breathing mode in phenylalanine (Phe)
1010	Ring breathing in benzene ring of tryptophan (Trp)
1033	C-H in plane bend (Phe)
1050	C-O and C-N stretch in proteins
1080	O-P-O symmetric stretch
1100	PO ₂ ⁻ symmetric stretching in RNA and phosphatidylinositol
1123	Cytochrome C; C-C asymmetric stretch in fatty acids
1155	C-C and C-N stretch in proteins
1165	C-O stretch, C-OH bending, C=C stretch in lipids, C-C stretch in proteins
1173	G-ring stretch, C-C-H bending in phenol ring (DNA)
1206	C-C stretch in phenol ring of tyrosine (Tyr)
1245	NH ₂ bending in Amide III _β
1266	Amide III _α
1310	C-H deformation (saturated. lipids)
1335	DNA purine bases (CH ₃ CH ₂ wagging mode of polynucleotide chain)
1450	CH ₂ scissoring in lipids
1554	Amide II
1604	Phe, Tyr
1655	Amide I _α
1669	Amide I _β

The averaged Raman spectra of BM-MSCs for each donor are presented in Figure 5A, while PCA score plots (PC1–PC2 and PC1–PC3) are shown in Figure 5B, confirming the similar biochemical background of analyzed samples. Regarding the significant similarity of all Raman spectra (Figure 5), to obtain a comprehensive insight into the biomolecular content of cells originating from different donors, the averaged Raman spectra, as well as statistical analysis, are analyzed and presented in pairs (Figures 6 and 7).

Figure 6A shows the Raman spectra of cell populations from D1 (red) and D2 (blue) and their ratio. By direct spectral reading, which on some occasions may be a formidable task due to various overlapping contributions, a phenylalanine mode at 1003 cm⁻¹ is of significantly higher intensity in the D1 spectrum. However, the mode assigned to RNA at 1100 cm⁻¹ is of higher intensity in the D2 spectrum and broader, implying higher content of nucleic acids or their enhanced activity. A biochemical discrepancy between D1 and D2 is confirmed statistically when the PCA score plot is considered, which is the one that represents PC1–PC3. The distinct grouping of red and blue dots per mutual spectral features is observed, indicating that the cells from one population have different biomolecular imprint than cells from another.

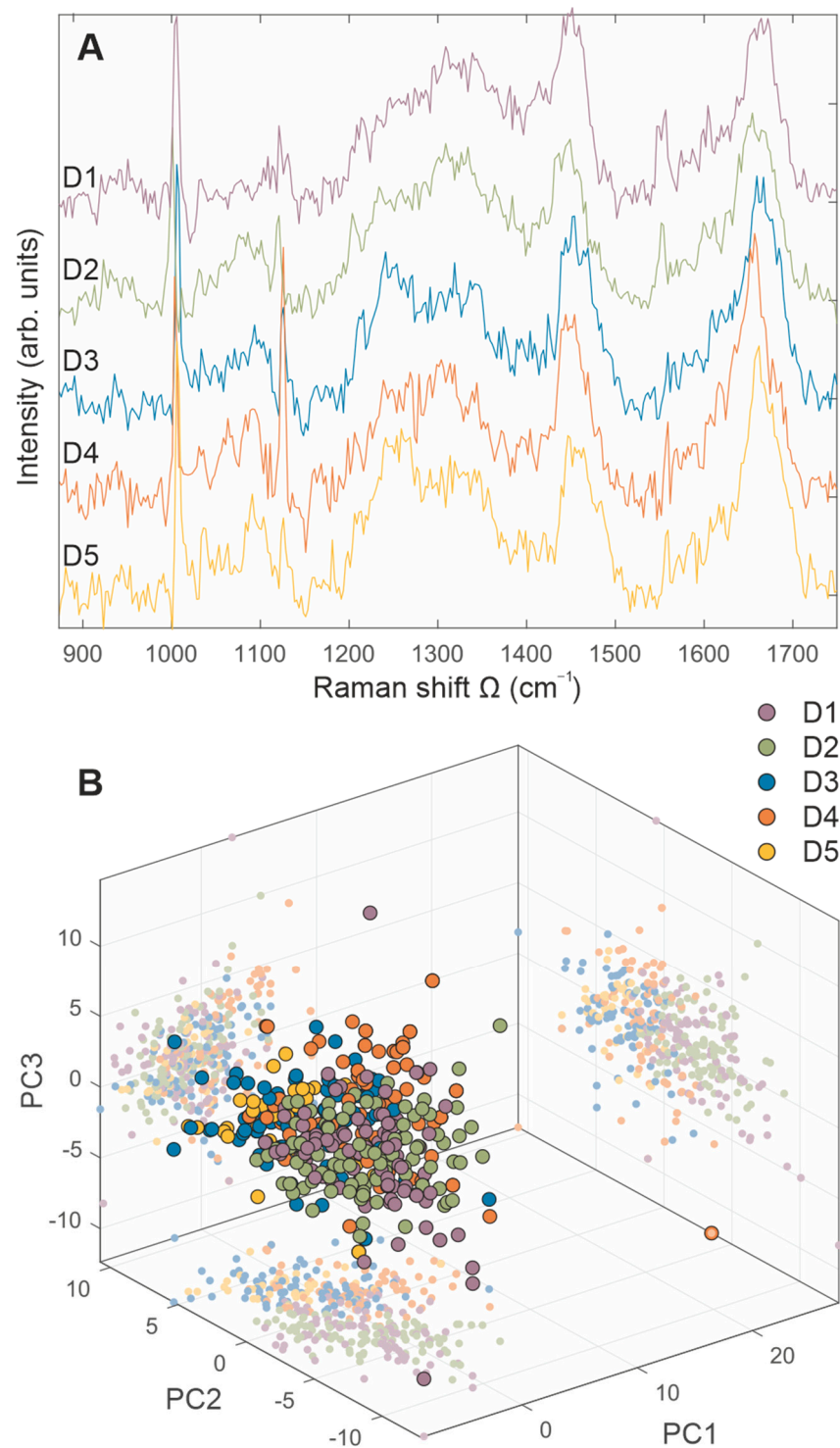


Figure 5. Comparative representation of BM-MSCs Raman spectra, derived from five donors. BM-MSCs were seeded on rounded CaF₂ slides (Raman grade quality) and cultivated under standard conditions during 24 h. Before Raman scattering experiments, cells were washed with saline buffer and fixed with methanol for 10 min at the room temperature. On average, 50 to 100 cells per each cell population were analyzed. (A) Averaged Raman spectra of BM-MSCs for each donor are presented with purple (D1), green (D2), blue (D3), orange (D4), and yellow (D5) lines. (B) 3D PCA score plots (PC1–PC2 and PC1–PC3) are presented with purple (D1), green (D2), blue (D3), orange (D4), and yellow (D5) dots.

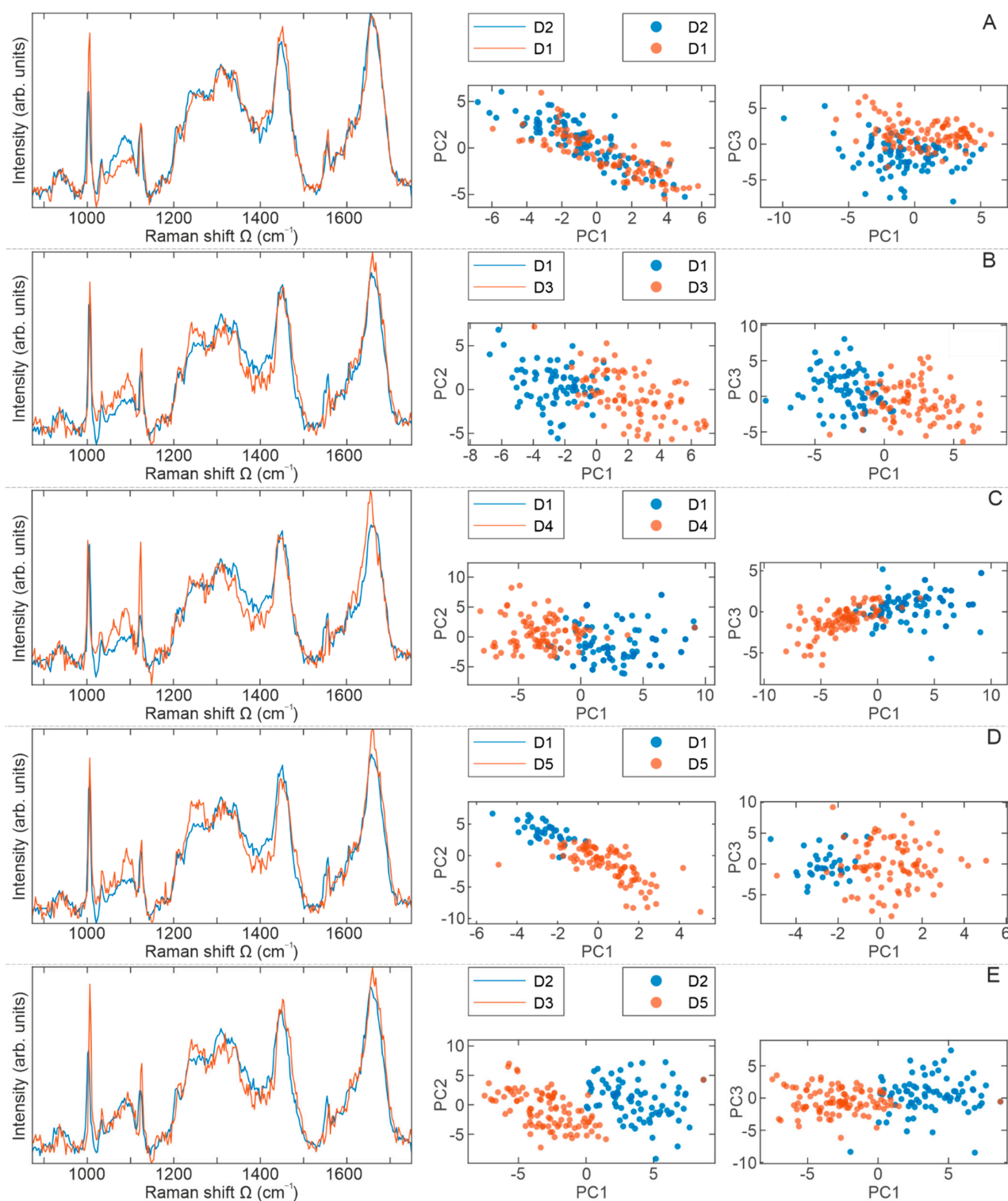


Figure 6. Comparative representation of BM-MSCs Raman spectra presented in pairs. BM-MSCs were seeded on rounded CaF₂ slides (Raman grade quality) and cultivated under standard conditions during 24 h. Before Raman scattering experiments, cells were washed with saline buffer and fixed with methanol for 10 min at the room temperature. On average, 50 to 100 cells per each cell population were analyzed. A comparative display of the averaged Raman spectra (red and blue lines) per cell populations: (A) D1–D2, (B) D1–D3, (C) D1–D4, (D) D1–D5, and (E) D2–D3. Principal component analysis (PCA) score plots are represented with red and blue dots.

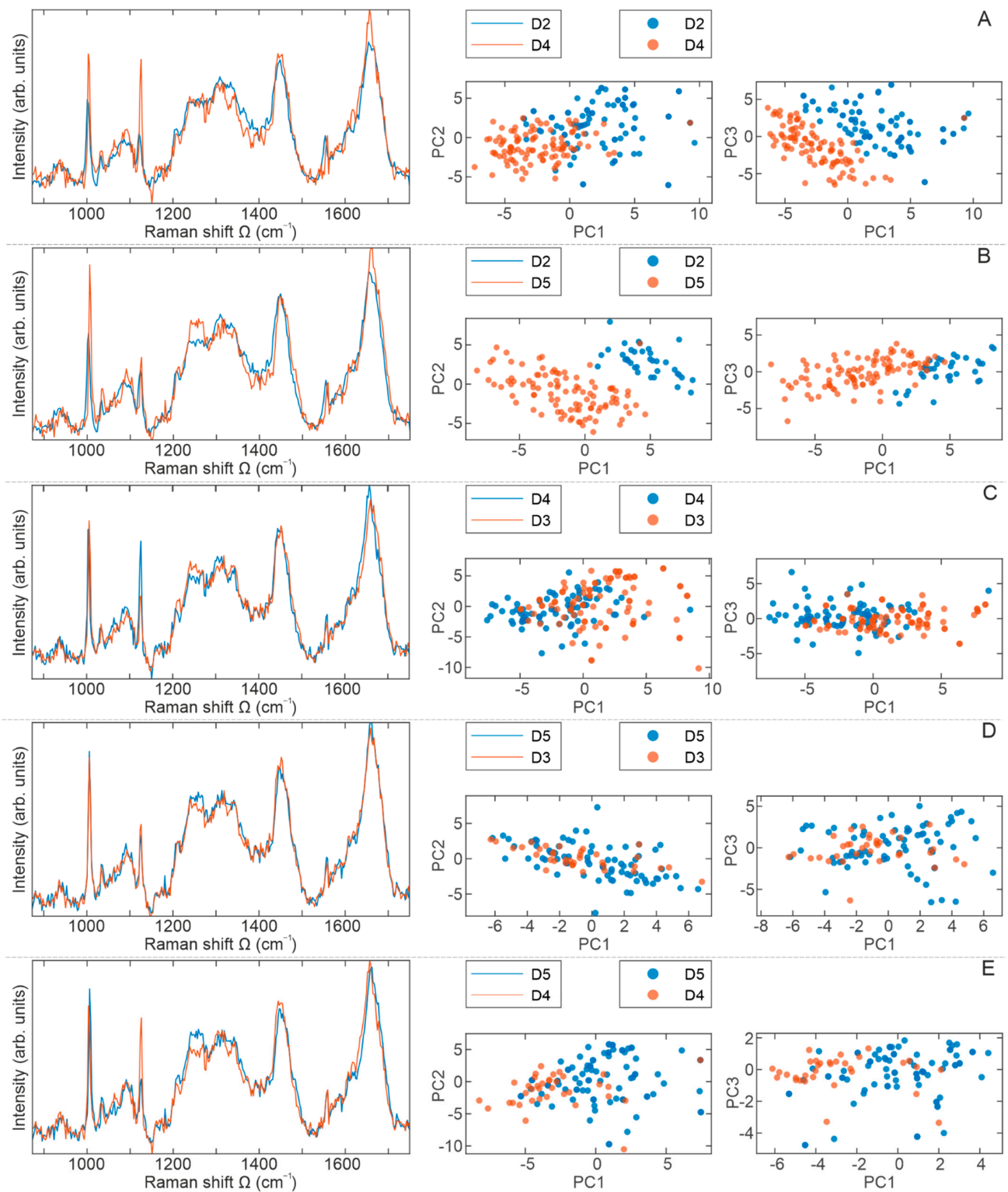


Figure 7. Comparative representation of BM-MSCs Raman spectra presented in pairs. BM-MSCs were seeded on rounded CaF₂ slides (Raman grade quality) and cultivated under standard conditions for 24 h. Prior Raman scattering experiments cells were washed with saline buffer and fixed with methanol for 10 min at the room temperature. On average, 50 to 100 cells per each cell population were analyzed. A comparative display of the averaged Raman spectra (red and blue lines) per cell populations: (A) D2–D4, (B) D2–D5, (C) D3–D4, (D) D3–D5, and (E) D4–D5. PCA score plots are represented with red and blue dots.

The averaged Raman spectra of cell populations D1 (blue) and D3 (red) are presented in Figure 6B. Clearly noticeable are modes of higher intensities in the D3 spectrum: at 1100 cm^{-1} (assigned to RNA), 1124 cm^{-1} (cytochrome c), and at about 1250 cm^{-1} (protein content in the Amide III $_{\beta}$ form). Statistically, both PCA score plots (PC1–PC2 and PC1–PC3) show distinct clustering of Raman spectra of BM-MSCs from donors D1 and D3 based on their intrinsic biomolecular contents, confirming the D1–D3 biochemical variability.

A comparison of an averaged Raman spectra of cells from D1 and D4 is shown in Figure 6C. Evidently, a higher intensity of Raman modes at about 1050 cm^{-1} , 1080 cm^{-1} , 1100 cm^{-1} , 1127 cm^{-1} and 1660 cm^{-1} is observed in D4 Raman spectrum. Biomolecular interpretation of this assignment indicates a higher content of proteins, DNA, and RNA respectively, as well as cytochrome c and proteins in their secondary structure. Furthermore, somewhat more dominant is a Raman mode at 1604 cm^{-1} , which is assigned to amino acids Phe and Tyr. Both PCA score plots designate clear and unequivocal grouping of Raman spectra per mutual spectral features, i.e., a biomolecular fingerprint.

Figure 6D presents BM-MSCs' averaged Raman spectra of cell populations D1 and D5, where the D5 (red) spectrum shows few Raman modes of higher intensity: at 1080 cm^{-1} , 1250 cm^{-1} , and 1660 cm^{-1} indicating more nucleic acids and proteins in Amide III form. To some extent, the lipid mode at about 1450 cm^{-1} is broader and of higher intensity in the D1 (blue) spectrum, pointing to the higher lipid content in these cells. Clearly, the PCA score plots show disjunction between these two cell populations, indicating the biochemical discrepancy between D1 and D5.

From the spectra in Figure 6E, it is obvious that the D3 (red) spectrum shows a higher content of amino acids (proteins), cytochrome c, and proteins in Amide III and Amide I form (see Table 1). The Raman peak at about 1310 cm^{-1} shows a greater content of saturated lipids in the D2 (blue) spectrum. Based on the PCA score plots shown in Figure 6, the maximum separation is noticed for D2–D3 cell populations (Figure 6E), while the minimal clustering was observed for D1–D2 cell populations (Figure 6A).

When analyzing the averaged Raman spectra displayed in Figure 7, the results are mostly in a good accordance with those presented in Figure 6, meaning that all changes come from differences in intensities, with no new modes detected in the spectra.

Figure 7A shows the averaged Raman spectra of cell populations D2 (blue) and D4 (red). Of significantly higher intensities are modes at 1003 cm^{-1} (Phe) and 1127 cm^{-1} (cytochrome c), and slightly more intensive is a peak at 1660 cm^{-1} (secondary structure of proteins) in the D4 spectrum. Some discrepancies come from a region around 1335 cm^{-1} , which was assigned to the polynucleotide chain in the D2 spectrum. Although both score plots show distinct grouping, it is more prominent from the score plot PC1–PC3. Nevertheless, the biochemical discrepancy between D2 and D4 cell populations is clearly observed.

A comparison of the averaged Raman spectra of cells from the D2 (blue) and D5 (red) population is presented in Figure 7B. According to the assignation presented in Table 1, cells from the D5 population have higher protein content in both Amide III and Amide I form, as well as free amino acids. A striking clustering of Raman spectra per cell population is obvious from both PCA score plots, confirming the biochemical distinction between D2 and D5.

From Figure 7C, where the averaged spectra of BM-MSCs from D3 and D4 cell populations are displayed, the dominant impression is a higher content of cytochrome c (Raman mode at 1127 cm^{-1}) in the D4 spectrum. Statistically, these two groups show the minimum degree of separation, which is also demonstrated for the spectra of D3 and D5 cell populations presented in Figure 7D.

Finally, Figure 7E shows the last compared pair, the Raman spectra of BM-MSCs from cell populations D4 and D5, giving the conclusion of higher content of cytochrome c in the D4 population, while Amide III $_{\beta}$ content is higher in the D5 population. The separation read from PCA score plots is slightly better than in the previous two groups and more clearly indicates the biochemical discrepancy between D4 and D5.

3. Discussion

The goal of this study was to analyze and compare the main functional features of BM-MSCs derived from five pediatric donors. We evaluated their basal stemness-related properties including morphology, phenotype, multilineage differentiation potential, colony-forming capacity, expression of pluripotency-associated markers and proliferation capacity. In parallel with the use of standard biological methods, single BM-MSCs were examined by Raman spectroscopy in order to identify donor-specific differences at the biochemical level with the aim to test whether this method could be used as an additional technique to characterize MSCs at the single-cell level.

Raman spectroscopy has been utilized to study various physiological and pathological conditions with the purpose of disease diagnosis, surgical guidance, and therapeutic or metabolic monitoring [45,46]. In the field of regenerative medicine and stem cell research, the application of Raman spectroscopy is rapidly increasing [24], whereby it can be noticed that stem cell differentiation at a single cell and tissue level was mostly investigated [37,38]. Regarding the use of Raman spectroscopy for distinguishing cell populations, several studies addressed this issue from different viewpoints. The results of [47] showed that this technique can precisely identify and evaluate prostatic adenocarcinoma (CaP) *in vitro*, based on different degrees of biological aggressiveness between CaP cell lines. Likewise, the distinction and identification of cells from different tissues and species (MDCK, CHO, and NIH 3T3 cells) as well as cells from a single species (NIH 3T3 and Clone 15 cells) were shown in the study of [48], indicating that the slight changes in cell phenotype can be determined based on Raman spectra and used to identify cell type. In addition, confocal Raman micro-spectroscopy was successfully used to delineate immortalized human cell lines derived from lung cancer (A549) and fibroblasts (MRC5) as well as three primary human bronchial epithelial cell (HBEC) lines [49]. Moreover, by using the Fourier Transform Infrared (FTIR) technique together with Raman spectroscopy, a clear distinction between undifferentiated BM-MSCs, their myogenic and osteogenic progeny, and de-differentiated smooth muscle cells were observed based on spectral differences [29] as well as between human ESCs and human MSCs [50]. Raman spectroscopy was shown to be a suitable tool for distinguishing human BM-MSCs and fibroblasts, thus enabling the rapid detection of fibroblastic contaminations in BM-MSC cultures [51]. Recent data also show that MSCs originating from different dental tissues such as apical papilla (SCAP), the dental follicle (DFSC), and pulp (DPSC) can be grouped based on Raman spectra that reveals a subtle distinction between these cells [52]. However, to our best knowledge, no data were published related to the inter-donor variability of MSCs. So, this is the first study that attempted to employ Raman spectroscopy to compare the spectral pattern of undifferentiated BM-MSCs deriving from healthy pediatric donors and to use these data for distinguishing cell populations.

In line with that goal, our first step was to isolate and characterize BM-MSCs by using standard biological tests following the minimal criteria for MSCs identification set by ISCT that include morphologic properties, immunophenotype and multilineage differentiation potential [14]. Our results revealed that plastic-adherent cells derived from the bone marrow of five pediatric donors retain adherence and typical fibroblast-like morphology cells during prolonged cultivation in standard conditions, while no donor-to-donor differences in cells sizes or shape were noticed, as observed under phase contrast microscope. Thus, these findings are in accordance with the first criteria as well as with previous studies related to the BM-MSCs morphology of adults [53–57]. The elongated spindle shape morphology of isolated BM-MSCs of each donor was further confirmed by cytoskeleton visualization. Immunofluorescent staining of the filamentous form of actin (F-actin), a critical structure of the cytoskeleton, revealed a strong expression of branched, multiple-directed F-actin stress bundles distributed through the whole cell, as it has been shown for MSCs derived from human placenta grown in standard adherent conditions [58]. Next, by using flow cytometry, we detected a high expression of surface molecules related to MSCs origin including CD29, CD73, CD90, and CD105, along with

the low expression of leukocyte markers CD45 and HLA-DR amongst all donors. A high expression of CD73, CD90 and CD105 markers was previously reported for BM-MSCs derived from adults [53–57,59], along with a high expression of CD29 observed in [56,59]. In parallel, the low percentage of CD45 and HLA-DR positive cells demonstrated in our study is in line with the results of [54,55,59], confirming that the immunophenotype of BM-MSCs of pediatric donors and adults is similar [60] and comparable with MSCs deriving from other tissue sources [59,61,62]. As the third ISCT requirement for MSCs identification, we examined the multilineage differentiation capacity of isolated cells. Indeed, the BM-MSCs of each pediatric donor were able to differentiate toward osteogenic, chondrogenic and adipogenic lineage, which is in agreement with previous research related to the BM-MSCs of adults [53–56,63], while no spontaneous differentiation in standard media was noticed, as reported in [60,64,65]. Overall, our results confirmed that adherent cells isolated from the bone marrow of all five pediatric donors meet the ISCT criteria for MSCs identification, whereby no significant differences were determined in this study.

Further on, we examined the clonogenic potential of BM-MSCs of each donor as a part of the self-renewal capacity analysis. Our results showed that isolated cells form a typical but heterogenic morphology of CFU-F colonies, while their number was uniform among donors (around 3%). Although clonogenic efficiency may vary depending on the cultivation conditions [55,66] and particularly passage [67,68], our results are comparable with the published data. Namely, approximately 5% of BM-MSCs colonies were formed at the fourth passage in the study of [67], 8% in [68]. Likewise, [69] reported that at the P3-6, around 5% colonies were formed, as well as in [55] for the BM-MSCs of P6 cultivated in the serum-containing in-house medium, which all points to the clonogenic potential of BM-MSCs derived from pediatric donors being similar to the BM-MSCs of adults.

As stem cells, MSCs are characterized by self-renewal ability, which encompasses the division ability with stemness maintaining [3,70]. At the molecular level, the regulation of stemness is mostly mediated via pluripotency-associated transcription factors, such as OCT4, SOX2 and NANOG, as described for embryonic stem cells [71]. Thus, it is assumed that these factors play a similar role also in adult stem cells. However, the molecular basis of MSCs stemness is still poorly understood. Nevertheless, previous studies have shown that MSCs derived from adult tissues do express pluripotency-associated markers [72–77] and that stemness-related processes may be associated with the activity of these markers in MSCs [78–83]. Our results are in line with these data and demonstrate that BM-MSCs derived from pediatric donors constitutively express markers associated with pluripotency (OCT4, NANOG and SOX2), while interestingly, we observed slight differences in the expression of these markers that may potentially indicate the existence of donor-dependent variation of self-renewal.

In the next part of describing BM-MSCs populations, we compared their proliferative capacity. Our study revealed a similar metabolic activity of BM-MSCs derived from different donors that increased during the time, as determined by the MTT test. Equal viability was accompanied by a uniform proliferation rate. Namely, all investigated cell types maintained their growth rate during prolonged in vitro culture, whereby the time needed for population doubling ranged between 60 and 70 h among donors during passaging (up to the 6th passage). Thus, these data agree with PDT observed in studies [55,56,84]. Active proliferative capacity was also supported based on β -galactosidase activity, as the low number of senescent cells has been observed in the fifth passage of BM-MSCs of each donor, which is also in accordance with previously published data [85]. These results are additionally confirmed at a molecular level. At first, we showed the basal expression of proliferation marker Ki67, by using immunofluorescence that also revealed slight differences in Ki67 localization between donors. Namely, donors D1, D2 and D3 expressed Ki67 in the nucleus and cytoplasm, while D4 and D5 showed a more dominant cytoplasmic localization of this marker. Our previous study showed that under basal conditions, Ki67 expression in dental stem cells is predominantly in cell cytoplasm [78], while both cytoplasmic and nuclear Ki67 localization was detected in ASCs [86]. Although

Ki67 has been traditionally considered a cell proliferation marker due to its presence in the nucleus during all active phases of the cell cycle (G1, S, G2 and M), the role of Ki67 has been particularly well described for cancer cells [84,87]. However, recent findings indicate that Ki-67 should not be considered only as a marker of cell proliferation [88,89]. Since differences in the extranuclear pathway of Ki-67 regulation in non-cancer and cancer cells have been identified [90], additional studies will potentially provide answers related to the biological role of nuclear and cytoplasmic Ki67 in adult stem cells.

Along with Ki67 expression, we investigated the expression of p53, which has been widely implicated in cellular senescence and aging [91,92], MSCs differentiation, bone homeostasis [93] as well as other MSCs functions [94]. Our results confirmed the basal expression of p53 in BM-MSCs of pediatric donors and interestingly revealed cellular localization differences. Namely, p53 was localized in the nucleus of donors D4 and D5, while donors D1, D2 and D3 expressed p53 predominantly in the cytoplasm. The regulation of p53 cellular localization is conditioned by many signaling factors that affect its nuclear transport, subnuclear localization, and cytoplasmic sequestration [95–97]. As for stem cells, there are indications that p53 is localized predominantly in the cytoplasm in proliferating embryonic stem cells, while upon DNA damage, the nuclear accumulation of p53 is induced, leading to the transcriptional activation of genes involved in cell cycle arrest [98]. The study of [96] showed that BM-MSCs from systemic lupus erythematosus patients exhibit characteristics of senescence, whereby p53 and p21 were mainly localized in the nuclei of these cells. The higher nuclear localization of p53 was also detected in MSCs derived from the periosteum of old patients [99], indicating potential age-related p53 localization. However, there are still open questions that are related to the p53 functions in different cells and tissues within the human body or how p53 activity is modulated in humans depending on sex, age or metabolic state [100]. Although cellular localization is changeable, further studies are needed to address p53 location in MSCs and its potential correlation with Ki67 expression/localization pattern.

Altogether, these data show that no significant differences between BM-MSCs of examined donors can be observed based on ISCT criteria and the use of standard biological methods for testing clonogenic and proliferative capacity. Nevertheless, variations between BM-MSCs of different donors at the molecular and biochemical level certainly exist [10]. Therefore, we further examined the biochemical composition of these cells at the individual level by using Raman spectroscopy. As expected, our results of BM-MSCs Raman spectra revealed that the dominant contribution to BM-MSCs Raman spectra is related to the nucleic acids (singled out purine and/or pyrimidine bases and DNA/RNA backbone structure), proteins (individual amino acids, amide groups of proteins' secondary structure and various vibrations within C-C or C-N bonding), and lipids (vibrations within the hydrocarbon chain), as described previously [27,36,41,101–104]. A comparison of BM-MSCs spectra did not reveal new vibrational bands; however, changes related to existing bands' intensities are detected. Despite Raman spectra similarities, following their comprehensive direct and statistical analyses, subtle distinctions between the averaged Raman spectra of BM-MSCs of each donor were detected, providing an important indication that this method can be used to clearly distinguish cell populations with a similar biochemical background. Namely, based on PCA score plots, the disjunctions between BM-MSCs populations were observed, whereby clustering between cell populations was most conspicuous when analyzed in pairs. Interestingly, maximum separation was noticed between D2 and D3 BM-MSCs, while the minimum separations were detected between D3 and D4 as well as D3 and D5 BM-MSCs (Figures 6 and 7). Certainly, further biochemical and Raman studies of MSCs populations is needed to understand the specific reasons for the level of variations in donor-specific separations. This issue will be the subject of our future research in order to provide biological validation of Raman spectra analysis. Nevertheless, in the following text, we discuss possible explanations for the obtained differences in the Raman spectra of different BM-MSCs donors.

Regarding the nucleic acid content, our results revealed differences in RNA and DNA content between BM-MSCs, whereby a higher level of RNA was detected in D2, D3, D4 and D5 in comparison to D1, while D4 and D5 donors had a higher content of DNA when compared to D1. Although we did not detect donor-related differences in metabolic activities of BM-MSCs based on MTT, we may only speculate that variations in RNA content detected by Raman spectroscopy are captured due to differences in RNA synthesis, i.e., metabolic activity [105] that cannot be detected by the MTT test. Differences in the DNA level detected by Raman spectroscopy may reflect a different stage of the cell cycle [36,106] or proliferation rate [107]; however, we did not observe differences in BM-MSCs proliferation rate between donors based on population doubling time. Still, during the cell cycle, the DNA level varies [107], so we may assume that detected differences in DNA come from variations in the cell cycle captured at a specific moment. On the other hand, a decrease in spectral features of RNA and DNA has been documented in differentiated murine embryonic cells that can be interpreted by the fact that differentiated cells are more in the G1 phase of the cell cycle and consequently exhibit reduced proliferative capacity [36]. Along with DNA decrease during differentiation, it has been reported that RNA levels also diminish during this process [36]. Indeed, MSCs populations are heterogenic in terms of proliferation dynamics that results in a population of cells that consist of mitotically active (dividing) and mitotically inactive (non-dividing) cells encompassing quiescent cells, differentiated cells and senescent cells [108,109]. Therefore, it should not be neglected that variations in DNA/RNA content determined by Raman spectroscopy may also reflect the heterogeneity of cell population related to the differentiation stage.

Along with changes in nucleic acid content, our results also revealed variations in proteins (1003, 1030, 1250, 1660, 1669 cm^{-1}) and lipids bands (1310 and 1440 cm^{-1}) that can also be implicated in the metabolic activity of the cells [110] or may indicate the existence of spontaneous differentiation, as it has been demonstrated for human pluripotent stem cells [34,110]. As for MSCs, considerable lipid content was detected in dental MSCs (peaks at 1440 and 1650 cm^{-1}) [52]. Although it is not fully clarified, lipid content may be associated with the stemness level, as the study [50] showed by using FTIR spectroscopy that divergence between hESC and hMSCs comes from the increased presence of lipids in the cytoplasm of hESC, while their level progressively decreases during differentiation [50]. Similar findings were observed in the study of [111], showing that mouse embryonic stem cells exhibited a higher intensity of fatty acids (1260 cm^{-1} and 1650 cm^{-1}) and lower amounts of unsaturated lipids (1445 cm^{-1}) than their neural progenitors and reprogrammed counterparts. Interestingly, based on immunofluorescence staining, no differences in the expression of pluripotency markers (Nanog, Oct4 and Sox2) were detected between embryonic and reprogrammed cells; however, Raman spectroscopy revealed significant spectral differences in unsaturated lipids. Since it has been reported that the fatty acid synthesis is important for the cellular stemness regulation [112], additional studies need to be carried out to reveal a correlation between lipids bands and fatty acid synthesis and to address whether this can be a significant spectral marker associated with stemness.

Another interesting finding of our study is related to the variations of band intensities for cytochrome c (1127 cm^{-1}) between BM-MSCs populations. Cytochrome c is a small, multi-functional protein with a significant role in the electron transport, and it is a part of the pathway for ATP synthesis necessary in the energy-production process. Under physiological conditions, it is located in the inner mitochondrial membrane, but upon proapoptotic signal, it is released to the cytoplasm [113–116]. The role of cytochrome c in apoptosis is well established [117,118], and few Raman studies addressed the correlation between cytochrome c and programmed cell death. As for HeLa cells, [119] reported that changes in cytochrome c distribution can be distinguished as a release of cytochrome c from mitochondria, while mitochondrial membrane potential confirmed that the observed cytochrome c release was associated with apoptosis. Likewise, confocal Raman microscopy has been successfully used to detect the apoptosis of the MCF-7 cell line mediated by cytochrome c release from mitochondria [120]. On the other hand, a comparison of cy-

cytochrome c signals within the Raman spectra of human ESC and human iPSCs did not reveal differences between these cell lines, whereby equivalent cytochrome c levels correlated with the level of mitochondria detected by MitoTracker staining [107]. Interestingly, it has been demonstrated that after the differentiation of a mouse neuroblastoma cell-line Neuro2a (N2a) toward neurons and differentiation of the 3T3L1 cell-line into adipocytes, Raman spectroscopy detected an increased amount of cytochrome c in the cytosol in both cell lines [121], indicating that cytochrome c detection also may be dependent on differentiation status. Therefore, due to multiple cellular functions, a cautious interpretation of the cytochrome c signal in the Raman spectra of BM-MSCs is needed. Our biological analysis, along with the detection of other spectral markers (primarily proteins), indicates that these cell populations are viable, so we may assume that the detection of a cytochrome c signal in Raman spectra can be a result of the metabolic variations or even differentiation heterogeneity. Nevertheless, a deeper investigation of cytochrome c localization along with mitochondrial characterization is necessary to determine the biological basis of detected cytochrome c in Raman spectra.

4. Materials and Methods

4.1. Collection, Isolation, Expansion, and Cultivation of MSCs

Bone marrow samples (2 mL) from five healthy donors (age range 2–12 years) (Table 2) were aspirated from iliac bone during the collection of bone marrow for allogeneic transplantation at the Mother and Child Health Care Institute of Serbia. For each sample, informed consent was assigned, and all samples were collected in accordance with the ethical standards of the local ethical committee and the Declaration of Helsinki.

Table 2. The main characteristics of BM-MSCs donors enrolled in the study.

Donor	Sex	Blood Type	Karyotype	Age
D1	male	AB+	46, XY, 20	8 years and 10 months
D2	female	B+	46, XX, 20	12 years and 3 months
D3	female	O+	46, XX, 20	2 years and 5 months
D4	male	AB+	46, XY, 20	12 years and 4 months
D5	female	O+	46, XX, 20	12 years and 2 months

Lymphocyte separation media Lymphocyte Separation Medium 1077 (Capricorn-Scientific, Ebsdorfergrund, Germany) and density gradient centrifugation were used to obtain mononuclear fraction (MNCs) of bone marrow. MNCs were resuspended in growth medium (GM) composed of MEM Alpha Modification medium supplemented with nucleosides (Capricorn-Scientific), 10% Fetal Bovine Serum, certified, United States (FBS, Gibco, Thermo Fisher Scientific, Waltham, MA, USA), 1% Penicillin/Streptomycin (P/S, Gibco, Thermo Fisher Scientific) and 1% L-glutamine (Capricorn-Scientific) and cultured in plastic tissue culture flasks (Greiner Bio-One, Monroe, NC, USA) in GM at 37 °C in a humidified atmosphere containing 5% CO₂ (standard conditions). The GM was replaced twice a week, and non-adherent cells were disposed of. After reaching 80–90% of confluence, adherent BM-MSCs were passaged using 0.25% Trypsin/EDTA solution (Capricorn-Scientific) and replated at concentration of 1×10^4 cells/cm². Cell number was evaluated by Trypan blue solution (Invitrogen, Carlsbad, CA, USA). The morphology of adherent cells was visualized by using the light microscope (Olympus, Tokyo, Japan). All further experiments were performed using BM-MSCs from the 5th passage.

4.2. Immunophenotyping

The detection of BM-MSCs phenotype was determined following the cultivation of cells in GM at standard conditions. Upon reaching confluence, cells were detached using Accutase solution (Biowest, Nuaille, France), and for each cell-surface marker analysis,

2×10^5 BM-MSCs were separated and washed in cold 0.5% BSA/PBS. Then, cells were labeled with fluorescein isothiocyanate (FITC)- or phycoerythrin (PE)-conjugated monoclonal antibodies against human antigens CD29, CD73, CD90, CD45 (all from R&D Systems, Minneapolis, MN, USA), CD105 and HLA-DR (both from Invitrogen, Carlsbad, CA, USA) during 30 min in the dark at +4 °C. For determination of the level of non-specific binding, corresponding FITC- and PE-conjugated isotype control antibodies (R&D Systems) were used. Flow cytometry was conducted using a Cytomics FC 500 (Beckman Coulter, Brea, CA, USA) cytometer, while data were analyzed using WinMDI 2.9 software (J. Trotter, The Scripps Research Institute, La Jolla, CA, USA).

4.3. Multipotent Differentiation

To determine the multilineage differentiation potential, BM-MSCs were plated in a 96-well plate (5×10^3 cells/well) in GM and incubated under standard conditions. GM was changed every 2–3 days until cells reached subconfluence when the GM was replaced with specific differentiation medium (DM), while cells cultivated in GM served as control.

For osteogenic differentiation medium, GM was supplemented with 200 μ M ascorbic acid-2-phosphate (Sigma-Aldrich, St. Louis, MO, USA), 10 mM β -glycerophosphate (AppliChem, Darmstadt, Germany) and 10 nM dexamethasone (Sigma-Aldrich). After 7 days of cultivation, the early stage of osteogenic differentiation was analyzed via assessment of alkaline phosphatase (ALP) activity stained with 5-bromo-4-chloro-3-indolyl phosphate/nitro blue tetrazolium, BCIP/ NBT substrate (Sigma-Aldrich) in alkaline phosphatase buffer (0.1 M Tris, 100 mM NaCl, 5 mM MgCl₂, pH 9.5). Late osteogenic differentiation was confirmed upon visualization of calcified deposits and extracellular matrix mineralization by using 2% Alizarin red dye (Merck Chemicals, Darmstadt, Germany) after three weeks of cultivation.

To determine the chondrogenic differentiation capacity of BM-MSCs, chondrogenic medium containing GM with 200 mM ascorbic acid-2-phosphate (Sigma-Aldrich), 10 nM dexamethasone (AppliChem, Darmstadt, Germany) and 5 ng/mL transforming growth factor (TGF- β) (R&D Systems) was used. Chondrogenic differentiation was estimated via proteoglycans staining with Safranin O (Merck Chemicals, Darmstadt, Germany) following the three weeks of treatment.

For adipogenic differentiation induction, BM-MSCs were cultivated in an adipogenic differentiation medium that contained GM enriched with 1 mM dexamethasone (Sigma-Aldrich), 10 μ g/mL insulin (Sigma-Aldrich) and 100 μ g/mL isobutyl methylxanthine (IBMX, Sigma-Aldrich). After four weeks, the formation of intracellular lipid droplets was confirmed by staining with Oil Red O (Merck Chemicals, Darmstadt, Germany).

Following the incubation period and staining assays, differentiated cells and control groups were analyzed by using the light microscope (Olympus, Tokyo, Japan).

4.4. CFU-F (Colony-Forming Units-Fibroblastic) Assay

To detect the clonogenicity of BM-MSCs, a colony-forming unit–fibroblastic (CFU-F) test was applied. BM-MSCs were plated in a 6-well plate (triplicate) at a seeding density of 250 cells per well. Following the 14 days of culturing in GM at standard conditions, cells were washed two times with PBS and fixed using ice-cold methanol for 5 min at room temperature. After fixation, cells were stained with 0.3% crystal violet (Carlo Erba reagents S.A.S., Emmendingen, Germany) for 15 min, when the cells were washed using distilled water. The number of colonies was determined by a light microscope (Olympus, Tokyo, Japan). Only colonies that were larger than 2 mm in diameter and consisted of more than 50 cells were counted. The ratio of the number of colonies to the number of cells plated was denoted as colony-forming efficiency.

4.5. Cellular Proliferation, Viability and Senescence

The population doubling time (PDT) of BM-MSCs was estimated through passaging. Cells were seeded in flasks at a concentration of 1×10^4 /cm² and grown in GM under

standard conditions until reaching confluency. Further on, BM-MSCs were detached, and cell number was determined by Trypan blue dye. Subsequently, cells were reseeded at the initial density. This process was repeated at every passage, up to passage 6. For calculation of the PDT, the following formula was used: $PDT = (T - T_0) \lg 2 / (\lg N_t - \lg N_0)$, where T_0 corresponds to the starting time of cell culture, T corresponds to the ending time of cell culture, N_0 corresponds to the cell number at the start of culture, and N_t corresponds to the cell number at the end of culture.

To assess the viability of BM-MSCs, the metabolic activity of these cells was analyzed. Cells were seeded in 96-well-plates (5×10^3 /well) and cultivated under standard conditions for 24 h and 48 h. Then, 3-(4,5-dimethylthiazol-2-yl) 2,5-diphenyltetrazolium bromide (MTT) solution (5 mg/mL) (Sigma-Aldrich) was added to each well, and incubation was continued for the next 2 h. Formed formazan crystals were dissolved with isopropanol, and the optical density was measured at 540 nm by the automatic reader for microplates (Labsystems Multiskan PLUS, Nelsirri, Finland).

For BM-MSCs, the senescence activity of the β -galactosidase enzyme was analyzed. Cells were seeded in 96-well plates (2×10^3 cells/well) and cultivated in GM under standard conditions for 24 h. Next, cells were washed with PBS, fixed, and stained using Senescence Cells Histochemical Kit according to the manufacturer's instructions (Sigma Aldrich). Samples were visualized by a light microscope (Olympus).

4.6. Immunofluorescence

To perform immunofluorescent labeling, BM-MSCs were seeded in 24-well plates, over rounded glass coverslips (3×10^3 cells/well) in GM and grown under standard conditions for 24 h to ensure adhesion of the cell. Samples were then washed with PBS twice and fixed in 4% formaldehyde. Subsequently, cells were permeabilized with 0.1% Triton X – 100 in PBS for 10 min, blocked with 1% BSA/PBS (30 min at room temperature) and incubated with primary antibodies: rabbit anti-Ki67 (Abcam, Cambridge, UK), rabbit anti-Oct-4, mouse anti-NANOG, mouse anti-SOX-2 (all from Cell Signaling Technology, Danvers, MA, USA) and mouse anti-p53 (Santa Cruz Biotechnologies, Dallas, TX, USA). Following 2 h of incubation at room temperature, samples were washed with PBS and treated with corresponding FITC-coupled secondary antibodies (Sigma-Aldrich) or Alexa Fluor 555-coupled anti-mouse antibody (Cell Signaling Technology) and 1 ng/mL of nuclear dye DAPI (Sigma-Aldrich) for 2 h. An epi-fluorescent microscope (Olympus, Tokyo, Japan) was used for the examination of mounted cell samples.

4.7. Sample Preparation for Raman Experiment

For the purpose of Raman spectroscopy, BM-MSCs were seeded on rounded CaF_2 slides (Raman grade quality, Crystran, Dorset, UK) in a 24-well plate (5×10^3 cells per slide) and cultivated in GM under standard cultivation conditions for 24 h. After the adhesion, BM-MSCs were washed with saline buffer and fixed with methanol for 10 min at room temperature. Chemical fixation allows samples to be collected at a particular moment, preserving biomolecular distribution within cells and making analysis possible to repeat. Just before Raman spectroscopy was performed, samples were washed with distilled water.

4.8. μ -Raman Spectroscopy

In this research, standard μ -Raman spectroscopy was used. Raman scattering experiments were performed on a TriVista 557 Raman system (Teledyne Princeton Instruments, Trenton, NJ, USA) in backscattering configuration. A coherent Ar^+/Kr^+ ion gas laser of 514.5 nm was used as an excitation source. The focusing on the sample was achieved by using a $\times 50$ Olympus microscope objective, $NA = 0.50$. The laser spot diameter in our experimental configuration was $\approx 20 \mu\text{m}$. Sample damage by overheating was prevented by keeping low levels of the laser power at the sample plain, $\approx 5 \text{ mW}$. It was determined that under these conditions, no laser-induced effects were observed, and the spectra were fully reproducible for the particular cell site. The acquisition time per spectrum was 300 s.

On average, 50 to 100 cells per each cell population (D1–D5) were analyzed. Since cells are heterogeneous dynamical systems, typically for spectral acquisition, several positions are randomly selected per cell to consider a complex chemical and morphological inner structure, which might induce slight variations in Raman spectra, especially in intensities of some Raman bands. To obtain a representative spectrum per each cell, these spectra are averaged. Here, we opted for the alternative approach. By increasing the size of the randomly positioned laser spot (at the expense of the probing acquisition time), a more significant portion of the sample was probed, thus capturing more of its internal inhomogeneity.

4.9. Data Processing and Analysis

The statistical interpretation of the results was completed by using the principal component analysis (PCA) method [36,40,41]. This method is used to reduce the large dimensionality of the Raman dataset in which every wavenumber represents a variable and the light intensity measured at that wavenumber represents a data point. The dimensionality reduction is completed by projecting the data points onto a new set of linearly uncorrelated variables, which are called principal components [42,43]. The PCA method used in this work is based on the singular value decomposition algorithm adopted from the GNU Octave standard library.

The Raman dataset, consisting of spectra collected within one or more donors, was preprocessed before it was forwarded to the PCA algorithm. The preprocessing procedure includes the following steps:

- (i) Removal of the irregular spectra from the datasets;
- (ii) Removal of the background noise from every spectrum in the data set;
- (iii) Spectra normalization.

An irregular spectrum does not have Raman modes characteristic to donor cells. An example would be a spectrum exhibiting high luminescence, which masks the relevant Raman modes or a spectrum without any Raman modes. These types of spectra are omitted from the analysis, since they do not carry any relevant information and are known for introducing unwanted outlier data points when passed through the PCA.

The background removal is completed by subtracting a fourth-degree polynomial function from the measured spectra. The polynomial is tailored to fit the background of every individual spectrum from the dataset.

After the background has been removed, every spectrum from the dataset is normalized to the value of the integral intensity calculated within the considered spectral region.

4.10. Statistical Analysis

All biological assays were repeated at least three times, and the results are presented as mean \pm SEM. Differences between groups were tested for statistical significance by Student's two-tailed *t*-test with *p* values less than 0.05 considered significant. Data analysis and graphical representations were performed by using GraphPad Prism 7 Software, Inc., San Diego, CA, USA.

5. Conclusions

Overall, the results of this study bring new evidence regarding the use of Raman spectroscopy in the field of MSCs exploration at the level of a single cell. Namely, by using standard biological assays analysis of BM-MSCs isolated from five healthy pediatric donors, no significant differences in terms of their MSCs properties, including morphology, phenotype, multilineage differentiation potential, colony-forming capacity, expression of pluripotency-associated markers or proliferative capacity were observed. On the other hand, Raman analysis revealed biochemical variations between these populations, whereby only changes related to peaks intensities were determined. Despite Raman spectra similarities, following the comprehensive analysis, subtle distinctions between averaged Raman spectra of BM-MSCs of each donor were detected, providing an important indication that this method can be used to clearly distinguish cell populations with a similar biochemical

background. Particularly, based on PCA score plots, disjunctions between BM-MSCs populations were observed, whereby clustering between cell populations were most conspicuous when cell populations was analyzed in pairs. Although further studies are needed to elucidate the precise biological validation of Raman results, this study provides an important basis for revealing inter-individual variability between primary MSCs populations at the single-cell level by using this non-invasive, label-free, optical technique.

Author Contributions: Conceptualization, T.K. and J.L.; Methodology, T.K., A.B., J.L. and U.R.; Validation, A.J., D.V., N.L. and D.B.; Investigation, A.B., T.K., J.L. and U.R.; Data curation, T.K., J.L. and U.R. Writing—original draft preparation, T.K., J.L. and A.B.; Review and editing, A.J., N.L., D.V. and D.B.; Supervision, A.J., D.V., N.L. and D.B.; Funding acquisition, N.L. and D.B. All authors have read and agreed to the published version of the manuscript.

Funding: This work was funded by the Ministry of Education, Science, and Technological Development of the Republic of Serbia (contract number 451-03-68/2022-14/200015) and the Institute of Physics Belgrade, through a grant from the Ministry of Education, Science, and Technological Development of the Republic of Serbia. This research is also conducted within the national program “Start up for science” 2019/2020 realized by the Center for Leadership Development and the Philip Morris Company in Serbia.

Institutional Review Board Statement: This study was conducted in accordance with the Declaration of Helsinki and approved by the Ethics Committee of the Mother and Child Health Care Institute of Serbia “Dr. Vukan Čupić” (8/20, 29 June 2018).

Informed Consent Statement: Informed consent was obtained from all subjects involved in the study.

Data Availability Statement: The data presented in this study are available from the corresponding author upon reasonable request.

Acknowledgments: The authors are grateful to Slavko Mojsilović, Group for Hematology and Stem Cells, Institute for Medical Research, National Institute of Republic of Serbia, University of Belgrade, for flow cytometry analysis. In addition, we are thankful to Željko Zečević, Marija Simić, and Borko Gobeljić for tissue collection.

Conflicts of Interest: The authors declare no conflict of interest.

References

- Teixeira, F.G.; Salgado, A.J. Mesenchymal Stem Cells Secretome: Current Trends and Future Challenges. *Neural Regen. Res.* **2020**, *15*, 75–77. [\[CrossRef\]](#)
- Zakrzewski, W.; Dobrzyński, M.; Szymonowicz, M.; Rybak, Z. Stem Cells: Past, Present, and Future. *Stem Cell Res. Ther.* **2019**, *10*, 68. [\[CrossRef\]](#)
- Nava, M.M.; Raimondi, M.T.; Pietrabissa, R. Controlling Self-Renewal and Differentiation of Stem Cells via Mechanical Cues. *J. Biomed. Biotechnol.* **2012**, *2012*, 797410. [\[CrossRef\]](#)
- Wei, X.; Yang, X.; Han, Z.; Qu, F.; Shao, L.; Shi, Y. Mesenchymal Stem Cells: A New Trend for Cell Therapy. *Acta Pharmacol. Sin.* **2013**, *34*, 747–754. [\[CrossRef\]](#)
- Caplan, A.I. Mesenchymal Stem Cells: Time to Change the Name! *Stem Cells Transl. Med.* **2017**, *6*, 1445–1451. [\[CrossRef\]](#)
- Harrell, C.R.; Fellabaum, C.; Jovicic, N.; Djonov, V.; Arsenijevic, N.; Volarevic, V. Molecular Mechanisms Responsible for Therapeutic Potential of Mesenchymal Stem Cell-Derived Secretome. *Cells* **2019**, *8*, 467. [\[CrossRef\]](#)
- Pittenger, M.F.; Discher, D.E.; Péault, B.M.; Phinney, D.G.; Hare, J.M.; Caplan, A.I. Mesenchymal Stem Cell Perspective: Cell Biology to Clinical Progress. *NPJ Regen. Med.* **2019**, *4*, 22. [\[CrossRef\]](#)
- Musiał-Wysocka, A.; Kot, M.; Majka, M. The Pros and Cons of Mesenchymal Stem Cell-Based Therapies. *Cell Transpl.* **2019**, *28*, 801–812. [\[CrossRef\]](#)
- Yin, P.T.; Han, E.; Lee, K.-B. Engineering Stem Cells for Biomedical Applications. *Adv. Health. Mater.* **2016**, *5*, 10–55. [\[CrossRef\]](#)
- Wilson, A.; Hodgson-Garms, M.; Frith, J.E.; Genever, P. Multiplicity of Mesenchymal Stromal Cells: Finding the Right Route to Therapy. *Front. Immunol.* **2019**, *10*, 1112. [\[CrossRef\]](#)
- Lv, F.-J.; Tuan, R.S.; Cheung, K.M.C.; Leung, V.Y.L. Concise Review: The Surface Markers and Identity of Human Mesenchymal Stem Cells. *Stem Cells* **2014**, *32*, 1408–1419. [\[CrossRef\]](#)
- Mo, M.; Wang, S.; Zhou, Y.; Li, H.; Wu, Y. Mesenchymal Stem Cell Subpopulations: Phenotype, Property and Therapeutic Potential. *Cell. Mol. Life Sci.* **2016**, *73*, 3311–3321. [\[CrossRef\]](#)
- Phinney, D.G. Functional Heterogeneity of Mesenchymal Stem Cells: Implications for Cell Therapy. *J. Cell. Biochem.* **2012**, *113*, 2806–2812. [\[CrossRef\]](#)

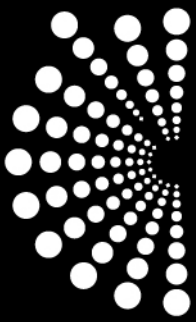
14. Dominici, M.; Le Blanc, K.; Mueller, I.; Slaper-Cortenbach, I.; Marini, F.; Krause, D.; Deans, R.; Keating, A.; Prockop, D.; Horwitz, E. Minimal Criteria for Defining Multipotent Mesenchymal Stromal Cells. The International Society for Cellular Therapy Position Statement. *Cytotherapy* **2006**, *8*, 315–317. [[CrossRef](#)]
15. Ullah, I.; Subbarao, R.B.; Rho, G.J. Human Mesenchymal Stem Cells—Current Trends and Future Prospective. *Biosci. Rep.* **2015**, *35*, e00191. [[CrossRef](#)]
16. Chen, J.-Y.; Mou, X.-Z.; Du, X.-C.; Xiang, C. Comparative Analysis of Biological Characteristics of Adult Mesenchymal Stem Cells with Different Tissue Origins. *Asian Pac. J. Trop. Med.* **2015**, *8*, 739–746. [[CrossRef](#)]
17. Guan, Y.-T.; Xie, Y.; Li, D.-S.; Zhu, Y.-Y.; Zhang, X.-L.; Feng, Y.-L.; Chen, Y.-P.; Xu, L.-J.; Liao, P.-F.; Wang, G. Comparison of Biological Characteristics of Mesenchymal Stem Cells Derived from the Human Umbilical Cord and Decidua Parietalis. *Mol. Med. Rep.* **2019**, *20*, 633–639. [[CrossRef](#)]
18. Sangeetha, K.N.; Vennila, R.; Secunda, R.; Sakthivel, S.; Pathak, S.; Jeswanth, S.; Surendran, R. Functional Variations between Mesenchymal Stem Cells of Different Tissue Origins: A Comparative Gene Expression Profiling. *Biotechnol. Lett.* **2020**, *42*, 1287–1304. [[CrossRef](#)]
19. Xu, L.; Liu, Y.; Sun, Y.; Wang, B.; Xiong, Y.; Lin, W.; Wei, Q.; Wang, H.; He, W.; Wang, B.; et al. Tissue Source Determines the Differentiation Potentials of Mesenchymal Stem Cells: A Comparative Study of Human Mesenchymal Stem Cells from Bone Marrow and Adipose Tissue. *Stem Cell Res. Ther.* **2017**, *8*, 275. [[CrossRef](#)]
20. Costa, L.A.; Eiro, N.; Fraile, M.; Gonzalez, L.O.; Saá, J.; Garcia-Portabella, P.; Vega, B.; Schneider, J.; Vizoso, F.J. Functional Heterogeneity of Mesenchymal Stem Cells from Natural Niches to Culture Conditions: Implications for Further Clinical Uses. *Cell. Mol. Life Sci.* **2021**, *78*, 447–467. [[CrossRef](#)]
21. Lähnemann, D.; Köster, J.; Szczurek, E.; McCarthy, D.J.; Hicks, S.C.; Robinson, M.D.; Vallejos, C.A.; Campbell, K.R.; Beerenwinkel, N.; Mahfouz, A.; et al. Eleven Grand Challenges in Single-Cell Data Science. *Genome Biol.* **2020**, *21*, 31. [[CrossRef](#)]
22. Yuan, G.-C.; Cai, L.; Elowitz, M.; Enver, T.; Fan, G.; Guo, G.; Irizarry, R.; Kharchenko, P.; Kim, J.; Orkin, S.; et al. Challenges and Emerging Directions in Single-Cell Analysis. *Genome Biol.* **2017**, *18*, 84. [[CrossRef](#)]
23. Zheng, G.; Xie, Z.-Y.; Wang, P.; Wu, Y.-F.; Shen, H.-Y. Recent Advances of Single-Cell RNA Sequencing Technology in Mesenchymal Stem Cell Research. *World J. Stem Cells* **2020**, *12*, 438–447. [[CrossRef](#)]
24. Ember, K.J.I.; Hoeve, M.A.; McAughtrie, S.L.; Bergholt, M.S.; Dwyer, B.J.; Stevens, M.M.; Faulds, K.; Forbes, S.J.; Campbell, C.J. Raman Spectroscopy and Regenerative Medicine: A Review. *NPJ Regen. Med.* **2017**, *2*, 12. [[CrossRef](#)]
25. Garcia-Timmermans, C.; Props, R.; Zacchetti, B.; Sakarika, M.; Delvigne, F.; Boon, N. Raman Spectroscopy-Based Measurements of Single-Cell Phenotypic Diversity in Microbial Populations. *mSphere* **2020**, *5*, e00806-20. [[CrossRef](#)]
26. Downes, A.; Mouras, R.; Bagnaninchi, P.; Elfick, A. Raman Spectroscopy and CARS Microscopy of Stem Cells and Their Derivatives. *J. Raman Spectrosc.* **2011**, *42*, 1864–1870. [[CrossRef](#)]
27. Bai, H.; Chen, P.; Fang, H.; Lin, L.; Tang, G.Q.; Mu, G.G.; Gong, W.; Liu, Z.P.; Wu, H.; Zhao, H.; et al. Detecting Viability Transitions of Umbilical Cord Mesenchymal Stem Cells by Raman Micro-Spectroscopy. *Laser Phys. Lett.* **2010**, *8*, 78. [[CrossRef](#)]
28. Azrad, E.; Zahor, D.; Vago, R.; Nevo, Z.; Doron, R.; Robinson, D.; Gheber, L.A.; Rosenwaks, S.; Bar, I. Probing the Effect of an Extract of Elk Velvet Antler Powder on Mesenchymal Stem Cells Using Raman Microspectroscopy: Enhanced Differentiation toward Osteogenic Fate. *J. Raman Spectrosc.* **2006**, *37*, 480–486. [[CrossRef](#)]
29. Molony, C.; McIntyre, J.; Maguire, A.; Hakimjavadi, R.; Burtenshaw, D.; Casey, G.; di Luca, M.; Hennelly, B.; Byrne, H.J.; Cahill, P.A. Label-Free Discrimination Analysis of de-Differentiated Vascular Smooth Muscle Cells, Mesenchymal Stem Cells and Their Vascular and Osteogenic Progeny Using Vibrational Spectroscopy. *Biochim. Biophys. Acta Mol. Cell Res.* **2018**, *1865*, 343–353. [[CrossRef](#)]
30. Butler, H.J.; Ashton, L.; Bird, B.; Cinque, G.; Curtis, K.; Dorney, J.; Esmonde-White, K.; Fullwood, N.J.; Gardner, B.; Martin-Hirsch, P.L.; et al. Using Raman Spectroscopy to Characterize Biological Materials. *Nat. Protoc.* **2016**, *11*, 664–687. [[CrossRef](#)]
31. Rangan, S.; Schulze, H.G.; Vardaki, M.Z.; Blades, M.W.; Piret, J.M.; Turner, R.F.B. Applications of Raman Spectroscopy in the Development of Cell Therapies: State of the Art and Future Perspectives. *Analyst* **2020**, *145*, 2070–2105. [[CrossRef](#)]
32. Geng, J.; Zhang, W.; Chen, C.; Zhang, H.; Zhou, A.; Huang, Y. Tracking the Differentiation Status of Human Neural Stem Cells through Label-Free Raman Spectroscopy and Machine Learning-Based Analysis. *Anal. Chem.* **2021**, *93*, 10453–10461. [[CrossRef](#)]
33. Wang, J.; Qi, G.; Qu, X.; Ling, X.; Zhang, Z.; Jin, Y. Molecular Profiling of Dental Pulp Stem Cells during Cell Differentiation by Surface Enhanced Raman Spectroscopy. *Anal. Chem.* **2020**, *92*, 3735–3741. [[CrossRef](#)]
34. Hsu, C.-C.; Xu, J.; Brinkhof, B.; Wang, H.; Cui, Z.; Huang, W.E.; Ye, H. A Single-Cell Raman-Based Platform to Identify Developmental Stages of Human Pluripotent Stem Cell-Derived Neurons. *Proc. Natl. Acad. Sci. USA* **2020**, *117*, 18412–18423. [[CrossRef](#)]
35. Lazarević, J.J.; Kukolj, T.; Bugarski, D.; Lazarević, N.; Bugarski, B.; Popović, Z.V. Probing Primary Mesenchymal Stem Cells Differentiation Status by Micro-Raman Spectroscopy. *Spectrochim. Acta. A Mol. Biomol. Spectrosc.* **2019**, *213*, 384–390. [[CrossRef](#)]
36. Notingher, I.; Bisson, I.; Bishop, A.E.; Randle, W.L.; Polak, J.M.P.; Hench, L.L. In Situ Spectral Monitoring of mRNA Translation in Embryonic Stem Cells during Differentiation In Vitro. *Anal. Chem.* **2004**, *76*, 3185–3193. [[CrossRef](#)]
37. Ghita, A.; Pascut, F.C.; Sottile, V.; Denning, C.; Notingher, I. Applications of Raman Micro-Spectroscopy to Stem Cell Technology: Label-Free Molecular Discrimination and Monitoring Cell Differentiation. *EPJ Tech. Instrum.* **2015**, *2*, 6. [[CrossRef](#)]
38. Ravera, F.; Efeoglu, E.; Byrne, H.J. Vibrational Spectroscopy for In Vitro Monitoring Stem Cell Differentiation. *Mol. Basel Switz.* **2020**, *25*, 5554. [[CrossRef](#)]

39. Carvalho, M.S.; Silva, J.C.; Hoff, C.M.; Cabral, J.M.S.; Linhardt, R.J.; da Silva, C.L.; Vashishth, D. Loss and Rescue of Osteocalcin and Osteopontin Modulate Osteogenic and Angiogenic Features of Mesenchymal Stem/Stromal Cells. *J. Cell. Physiol.* **2020**, *235*, 7496–7515. [[CrossRef](#)]
40. Wiercigroch, E.; Szafraniec, E.; Czamara, K.; Pacia, M.Z.; Majzner, K.; Kochan, K.; Kaczor, A.; Baranska, M.; Malek, K. Raman and Infrared Spectroscopy of Carbohydrates: A Review. *Spectrochim. Acta. A Mol. Biomol. Spectrosc.* **2017**, *185*, 317–335. [[CrossRef](#)]
41. Clemens, G.; Hands, J.R.; Dorling, K.M.; Baker, M.J. Vibrational Spectroscopic Methods for Cytology and Cellular Research. *Analyst* **2014**, *139*, 4411–4444. [[CrossRef](#)]
42. Czamara, K.; Majzner, K.; Pacia, M.Z.; Kochan, K.; Kaczor, A.; Baranska, M. Raman Spectroscopy of Lipids: A Review. *J. Raman Spectrosc.* **2015**, *46*, 4–20. [[CrossRef](#)]
43. de Gelder, J.; de Gussem, K.; Vandennebeele, P.; Moens, L. Reference Database of Raman Spectra of Biological Molecules. *J. Raman Spectrosc.* **2007**, *38*, 1133–1147. [[CrossRef](#)]
44. Pezzotti, G.; Zhu, W.; Adachi, T.; Horiguchi, S.; Marin, E.; Boschetto, F.; Ogitani, E.; Mazda, O. Metabolic Machinery Encrypted in the Raman Spectrum of Influenza A Virus-Inoculated Mammalian Cells. *J. Cell. Physiol.* **2020**, *235*, 5146–5170. [[CrossRef](#)]
45. Baker, M.J.; Byrne, H.J.; Chalmers, J.; Gardner, P.; Goodacre, R.; Henderson, A.; Kazarian, S.G.; Martin, F.L.; Moger, J.; Stone, N.; et al. Clinical Applications of Infrared and Raman Spectroscopy: State of Play and Future Challenges. *Analyst* **2018**, *143*, 1735–1757. [[CrossRef](#)]
46. Tanwar, S.; Paidi, S.K.; Prasad, R.; Pandey, R.; Barman, I. Advancing Raman Spectroscopy from Research to Clinic: Translational Potential and Challenges. *Spectrochim. Acta. A Mol. Biomol. Spectrosc.* **2021**, *260*, 119957. [[CrossRef](#)]
47. Crow, P.; Barrass, B.; Kendall, C.; Hart-Prieto, M.; Wright, M.; Persad, R.; Stone, N. The Use of Raman Spectroscopy to Differentiate between Different Prostatic Adenocarcinoma Cell Lines. *Br. J. Cancer* **2005**, *92*, 2166–2170. [[CrossRef](#)]
48. Ilin, Y.; Kraft, M.L. Identifying the Lineages of Individual Cells in Cocultures by Multivariate Analysis of Raman Spectra. *Analyst* **2014**, *139*, 2177–2185. [[CrossRef](#)]
49. Surmacki, J.M.; Woodhams, B.J.; Haslehurst, A.; Ponder, B.A.J.; Bohndiek, S.E. Raman Micro-Spectroscopy for Accurate Identification of Primary Human Bronchial Epithelial Cells. *Sci. Rep.* **2018**, *8*, 12604. [[CrossRef](#)]
50. Pijanka, J.K.; Kumar, D.; Dale, T.; Yousef, I.; Parkes, G.; Untereiner, V.; Yang, Y.; Dumas, P.; Collins, D.; Manfait, M.; et al. Vibrational Spectroscopy Differentiates between Multipotent and Pluripotent Stem Cells. *Analyst* **2010**, *135*, 3126–3132. [[CrossRef](#)]
51. Pudlas, M.; Carvajal Berrio, D.; Linneweh, M.; Koch, S.; Thude, S.; Walles, H.; Schenke-Layland, K. Non-Contact Discrimination of Human Bone Marrow-Derived Mesenchymal Stem Cells and Fibroblasts Using Raman Spectroscopy. *Med. Laser Appl.* **2011**, *26*, 119–125. [[CrossRef](#)]
52. Simonović, J.; Toljić, B.; Rašković, B.; Jovanović, V.; Lazarević, M.; Milošević, M.; Nikolić, N.; Panajotović, R.; Milašin, J. Raman Microspectroscopy: Toward a Better Distinction and Profiling of Different Populations of Dental Stem Cells. *Croat. Med. J.* **2019**, *60*, 78–86. [[CrossRef](#)] [[PubMed](#)]
53. Baghaei, K.; Hashemi, S.M.; Tokhanbigli, S.; Asadi Rad, A.; Assadzadeh-Aghdaei, H.; Sharifian, A.; Zali, M.R. Isolation, Differentiation, and Characterization of Mesenchymal Stem Cells from Human Bone Marrow. *Gastroenterol. Hepatol. Bed Bench* **2017**, *10*, 208–213. [[PubMed](#)]
54. Mennan, C.; Garcia, J.; Roberts, S.; Hulme, C.; Wright, K. A Comprehensive Characterisation of Large-Scale Expanded Human Bone Marrow and Umbilical Cord Mesenchymal Stem Cells. *Stem Cell Res. Ther.* **2019**, *10*, 99. [[CrossRef](#)]
55. Bhat, S.; Viswanathan, P.; Chandanala, S.; Prasanna, S.J.; Seetharam, R.N. Expansion and Characterization of Bone Marrow Derived Human Mesenchymal Stromal Cells in Serum-Free Conditions. *Sci. Rep.* **2021**, *11*, 3403. [[CrossRef](#)]
56. Yang, Y.-H.K.; Ogando, C.R.; Wang See, C.; Chang, T.-Y.; Barabino, G.A. Changes in Phenotype and Differentiation Potential of Human Mesenchymal Stem Cells Aging in Vitro. *Stem Cell Res. Ther.* **2018**, *9*, 131. [[CrossRef](#)]
57. Song, Y.; Zhao, H.-Y.; Lyu, Z.-S.; Cao, X.-N.; Shi, M.-M.; Wen, Q.; Tang, F.-F.; Wang, Y.; Xu, L.-P.; Zhang, X.-H.; et al. Dysfunctional Bone Marrow Mesenchymal Stem Cells in Patients with Poor Graft Function after Allogeneic Hematopoietic Stem Cell Transplantation. *Biol. Blood Marrow Transplant.* **2018**, *24*, 1981–1989. [[CrossRef](#)]
58. Zhou, Y.; Chen, H.; Li, H.; Wu, Y. 3D Culture Increases Pluripotent Gene Expression in Mesenchymal Stem Cells through Relaxation of Cytoskeleton Tension. *J. Cell. Mol. Med.* **2017**, *21*, 1073–1084. [[CrossRef](#)]
59. Petrenko, Y.; Vackova, I.; Kekulova, K.; Chudickova, M.; Koci, Z.; Turnovcova, K.; Kupcova Skalnikova, H.; Vodicka, P.; Kubinova, S. A Comparative Analysis of Multipotent Mesenchymal Stromal Cells Derived from Different Sources, with a Focus on Neuroregenerative Potential. *Sci. Rep.* **2020**, *10*, 4290. [[CrossRef](#)]
60. Mareschi, K.; Ferrero, I.; Rustichelli, D.; Aschero, S.; Gammaitoni, L.; Aglietta, M.; Madon, E.; Fagioli, F. Expansion of Mesenchymal Stem Cells Isolated from Pediatric and Adult Donor Bone Marrow. *J. Cell. Biochem.* **2006**, *97*, 744–754. [[CrossRef](#)]
61. Kern, S.; Eichler, H.; Stoeve, J.; Klüter, H.; Bieback, K. Comparative Analysis of Mesenchymal Stem Cells from Bone Marrow, Umbilical Cord Blood, or Adipose Tissue. *Stem Cells Dayt. Ohio* **2006**, *24*, 1294–1301. [[CrossRef](#)] [[PubMed](#)]
62. Araújo, A.B.; Salton, G.D.; Furlan, J.M.; Schneider, N.; Angeli, M.H.; Laureano, Á.M.; Silla, L.; Passos, E.P.; Paz, A.H. Comparison of Human Mesenchymal Stromal Cells from Four Neonatal Tissues: Amniotic Membrane, Chorionic Membrane, Placental Decidua and Umbilical Cord. *Cytotherapy* **2017**, *19*, 577–585. [[CrossRef](#)]
63. Ghaneialvar, H.; Soltani, L.; Rahmani, H.R.; Lotfi, A.S.; Soleimani, M. Characterization and Classification of Mesenchymal Stem Cells in Several Species Using Surface Markers for Cell Therapy Purposes. *Indian J. Clin. Biochem.* **2018**, *33*, 46–52. [[CrossRef](#)]

64. Pittenger, M.F.; Mackay, A.M.; Beck, S.C.; Jaiswal, R.K.; Douglas, R.; Mosca, J.D.; Moorman, M.A.; Simonetti, D.W.; Craig, S.; Marshak, D.R. Multilineage Potential of Adult Human Mesenchymal Stem Cells. *Science* **1999**, *284*, 143–147. [[CrossRef](#)] [[PubMed](#)]
65. Meppelink, A.M.; Wang, X.-H.; Bradica, G.; Barron, K.; Hiltz, K.; Liu, X.-H.; Goldman, S.M.; Vacanti, J.P.; Keating, A.; Hoganson, D.M. Rapid Isolation of Bone Marrow Mesenchymal Stromal Cells Using Integrated Centrifuge-Based Technology. *Cytotherapy* **2016**, *18*, 729–739. [[CrossRef](#)] [[PubMed](#)]
66. Meuleman, N.; Tondreau, T.; Delforge, A.; Dejeneffe, M.; Massy, M.; Libertalis, M.; Bron, D.; Lagneaux, L. Human Marrow Mesenchymal Stem Cell Culture: Serum-Free Medium Allows Better Expansion than Classical Alpha-MEM Medium. *Eur. J. Haematol.* **2006**, *76*, 309–316. [[CrossRef](#)] [[PubMed](#)]
67. Dmitrieva, R.I.; Minullina, I.R.; Bilibina, A.A.; Tarasova, O.V.; Anisimov, S.V.; Zaritskey, A.Y. Bone Marrow- and Subcutaneous Adipose Tissue-Derived Mesenchymal Stem Cells: Differences and Similarities. *Cell Cycle Georget. Tex.* **2012**, *11*, 377–383. [[CrossRef](#)]
68. Vishnubalaji, R.; Al-Nbaheen, M.; Kadalmani, B.; Aldahmash, A.; Ramesh, T. Comparative Investigation of the Differentiation Capability of Bone-Marrow- and Adipose-Derived Mesenchymal Stem Cells by Qualitative and Quantitative Analysis. *Cell Tissue Res.* **2012**, *347*, 419–427. [[CrossRef](#)]
69. Alcayaga-Miranda, F.; Cuenca, J.; Luz-Crawford, P.; Aguila-Díaz, C.; Fernandez, A.; Figueroa, F.E.; Khoury, M. Characterization of Menstrual Stem Cells: Angiogenic Effect, Migration and Hematopoietic Stem Cell Support in Comparison with Bone Marrow Mesenchymal Stem Cells. *Stem Cell Res. Ther.* **2015**, *6*, 32. [[CrossRef](#)]
70. Kolf, C.M.; Cho, E.; Tuan, R.S. Mesenchymal Stromal Cells. Biology of Adult Mesenchymal Stem Cells: Regulation of Niche, Self-Renewal and Differentiation. *Arthritis Res. Ther.* **2007**, *9*, 204. [[CrossRef](#)]
71. Boyer, L.A.; Lee, T.I.; Cole, M.F.; Johnstone, S.E.; Levine, S.S.; Zucker, J.P.; Guenther, M.G.; Kumar, R.M.; Murray, H.L.; Jenner, R.G.; et al. Core Transcriptional Regulatory Circuitry in Human Embryonic Stem Cells. *Cell* **2005**, *122*, 947–956. [[CrossRef](#)] [[PubMed](#)]
72. Riekstina, U.; Cakstina, I.; Parfejevs, V.; Hoogduijn, M.; Jankovskis, G.; Muiznieks, I.; Muceniece, R.; Ancans, J. Embryonic Stem Cell Marker Expression Pattern in Human Mesenchymal Stem Cells Derived from Bone Marrow, Adipose Tissue, Heart and Dermis. *Stem Cell Rev. Rep.* **2009**, *5*, 378–386. [[CrossRef](#)] [[PubMed](#)]
73. Miletic, M.; Mojsilovic, S.; Okić-Dorđević, I.; Kukolj, T.; Jauković, A.; Santibacez, J.F.; Jovčić, G.; Bugarski, D. Mesenchymal Stem Cells Isolated from Human Periodontal Ligament. *Arch. Biol. Sci.* **2014**, *66*, 261–271. [[CrossRef](#)]
74. Tantrawatpan, C.; Manochantr, S.; Kheolamai, P.; U-Pratya, Y.; Supokawej, A.; Issaragrisil, S. Pluripotent Gene Expression in Mesenchymal Stem Cells from Human Umbilical Cord Wharton’s Jelly and Their Differentiation Potential to Neural-like Cells. *J. Med. Assoc. Thail. Chotmaihet Thangphaet* **2013**, *96*, 1208–1217.
75. Park, E.; Patel, A.N. Changes in the Expression Pattern of Mesenchymal and Pluripotent Markers in Human Adipose-Derived Stem Cells. *Cell Biol. Int.* **2010**, *34*, 979–984. [[CrossRef](#)]
76. Jaramillo-Ferrada, P.A.; Wolvetang, E.J.; Cooper-White, J.J. Differential Mesengenic Potential and Expression of Stem Cell-Fate Modulators in Mesenchymal Stromal Cells from Human-Term Placenta and Bone Marrow. *J. Cell. Physiol.* **2012**, *227*, 3234–3242. [[CrossRef](#)]
77. Gao, L.R.; Zhang, N.K.; Ding, Q.A.; Chen, H.Y.; Hu, X.; Jiang, S.; Li, T.C.; Chen, Y.; Wang, Z.G.; Ye, Y.; et al. Common Expression of Stemness Molecular Markers and Early Cardiac Transcription Factors in Human Wharton’s Jelly-Derived Mesenchymal Stem Cells and Embryonic Stem Cells. *Cell Transplant.* **2013**, *22*, 1883–1900. [[CrossRef](#)]
78. Kukolj, T.; Trivanović, D.; Mojsilović, S.; Okić Djordjević, I.; Obradović, H.; Krstić, J.; Jauković, A.; Bugarski, D. IL-33 Guides Osteogenesis and Increases Proliferation and Pluripotency Marker Expression in Dental Stem Cells. *Cell Prolif.* **2019**, *52*, e12533. [[CrossRef](#)]
79. Jauković, A.; Kukolj, T.; Trivanović, D.; Okić-Dorđević, I.; Obradović, H.; Miletic, M.; Petrović, V.; Mojsilović, S.; Bugarski, D. Modulating Stemness of Mesenchymal Stem Cells from Exfoliated Deciduous and Permanent Teeth by IL-17 and BFGF. *J. Cell. Physiol.* **2021**, *236*, 7322–7341. [[CrossRef](#)]
80. Han, S.-M.; Han, S.-H.; Coh, Y.-R.; Jang, G.; Chan Ra, J.; Kang, S.-K.; Lee, H.-W.; Youn, H.-Y. Enhanced Proliferation and Differentiation of Oct4- and Sox2-Overexpressing Human Adipose Tissue Mesenchymal Stem Cells. *Exp. Mol. Med.* **2014**, *46*, e101. [[CrossRef](#)]
81. Piccinato, C.A.; Sertie, A.L.; Torres, N.; Ferretti, M.; Antonioli, E. High OCT4 and Low P16(INK4A) Expressions Determine In Vitro Lifespan of Mesenchymal Stem Cells. *Stem Cells Int.* **2015**, *2015*, 369828. [[CrossRef](#)] [[PubMed](#)]
82. Pitrone, M.; Pizzolanti, G.; Tomasello, L.; Coppola, A.; Morini, L.; Pantuso, G.; Ficarella, R.; Guarnotta, V.; Perrini, S.; Giorgino, F.; et al. NANOG Plays a Hierarchical Role in the Transcription Network Regulating the Pluripotency and Plasticity of Adipose Tissue-Derived Stem Cells. *Int. J. Mol. Sci.* **2017**, *18*, 1107. [[CrossRef](#)] [[PubMed](#)]
83. Lu, Y.; Qu, H.; Qi, D.; Xu, W.; Liu, S.; Jin, X.; Song, P.; Guo, Y.; Jia, Y.; Wang, X.; et al. OCT4 Maintains Self-Renewal and Reverses Senescence in Human Hair Follicle Mesenchymal Stem Cells through the Downregulation of P21 by DNA Methyltransferases. *Stem Cell Res. Ther.* **2019**, *10*, 28. [[CrossRef](#)] [[PubMed](#)]
84. Li, X.; Bai, J.; Ji, X.; Li, R.; Xuan, Y.; Wang, Y. Comprehensive Characterization of Four Different Populations of Human Mesenchymal Stem Cells as Regards Their Immune Properties, Proliferation and Differentiation. *Int. J. Mol. Med.* **2014**, *34*, 695–704. [[CrossRef](#)] [[PubMed](#)]

85. Kundrotas, G.; Gasperskaja, E.; Slapsyte, G.; Gudleviciene, Z.; Krasko, J.; Stumbryte, A.; Liudkeviciene, R. Identity, Proliferation Capacity, Genomic Stability and Novel Senescence Markers of Mesenchymal Stem Cells Isolated from Low Volume of Human Bone Marrow. *Oncotarget* **2016**, *7*, 10788–10802. [[CrossRef](#)] [[PubMed](#)]
86. Nawrocka, D.; Kornicka, K.; Szydłarska, J.; Marycz, K. Basic Fibroblast Growth Factor Inhibits Apoptosis and Promotes Proliferation of Adipose-Derived Mesenchymal Stromal Cells Isolated from Patients with Type 2 Diabetes by Reducing Cellular Oxidative Stress. *Oxid. Med. Cell. Longev.* **2017**, *2017*, 3027109. [[CrossRef](#)]
87. Remnant, L.; Kochanova, N.Y.; Reid, C.; Cisneros-Soberanis, F.; Earnshaw, W.C. The Intrinsically Disorderly Story of Ki-67. *Open Biol.* **2021**, *11*, 210120. [[CrossRef](#)]
88. Sun, X.; Kaufman, P.D. Ki-67: More than a Proliferation Marker. *Chromosoma* **2018**, *127*, 175–186. [[CrossRef](#)]
89. Sales Gil, R.; Vagnarelli, P. Ki-67: More Hidden behind a “Classic Proliferation Marker”. *Trends Biochem. Sci.* **2018**, *43*, 747–748. [[CrossRef](#)]
90. Chierico, L.; Rizzello, L.; Guan, L.; Joseph, A.S.; Lewis, A.; Battaglia, G. The Role of the Two Splice Variants and Extranuclear Pathway on Ki-67 Regulation in Non-Cancer and Cancer Cells. *PLoS ONE* **2017**, *12*, e0171815. [[CrossRef](#)]
91. Hafner, A.; Bulyk, M.L.; Jambhekar, A.; Lahav, G. The Multiple Mechanisms That Regulate P53 Activity and Cell Fate. *Nat. Rev. Mol. Cell Biol.* **2019**, *20*, 199–210. [[CrossRef](#)] [[PubMed](#)]
92. Xia, C.; Jiang, T.; Wang, Y.; Chen, X.; Hu, Y.; Gao, Y. The P53/MiR-145a Axis Promotes Cellular Senescence and Inhibits Osteogenic Differentiation by Targeting Cbfb in Mesenchymal Stem Cells. *Front. Endocrinol.* **2020**, *11*, 609186. [[CrossRef](#)] [[PubMed](#)]
93. Velletri, T.; Xie, N.; Wang, Y.; Huang, Y.; Yang, Q.; Chen, X.; Chen, Q.; Shou, P.; Gan, Y.; Cao, G.; et al. P53 Functional Abnormality in Mesenchymal Stem Cells Promotes Osteosarcoma Development. *Cell Death Dis.* **2016**, *7*, e2015. [[CrossRef](#)] [[PubMed](#)]
94. Boregowda, S.V.; Krishnappa, V.; Strivelli, J.; Haga, C.L.; Booker, C.N.; Phinney, D.G. Basal P53 Expression Is Indispensable for Mesenchymal Stem Cell Integrity. *Cell Death Differ.* **2018**, *25*, 679–692. [[CrossRef](#)] [[PubMed](#)]
95. O’Brate, A.; Giannakakou, P. The Importance of P53 Location: Nuclear or Cytoplasmic Zip Code? *Drug Resist. Updat. Rev. Comment. Antimicrob. Anticancer Chemother.* **2003**, *6*, 313–322. [[CrossRef](#)] [[PubMed](#)]
96. Gu, Z.; Jiang, J.; Tan, W.; Xia, Y.; Cao, H.; Meng, Y.; Da, Z.; Liu, H.; Cheng, C. P53/P21 Pathway Involved in Mediating Cellular Senescence of Bone Marrow-Derived Mesenchymal Stem Cells from Systemic Lupus Erythematosus Patients. *Clin. Dev. Immunol.* **2013**, *2013*, 134243. [[CrossRef](#)]
97. Solozobova, V.; Blattner, C. P53 in Stem Cells. *World J. Biol. Chem.* **2011**, *2*, 202–214. [[CrossRef](#)]
98. Solozobova, V.; Rolletschek, A.; Blattner, C. Nuclear Accumulation and Activation of P53 in Embryonic Stem Cells after DNA Damage. *BMC Cell Biol.* **2009**, *10*, 46. [[CrossRef](#)]
99. Ferretti, C.; Lucarini, G.; Andreoni, C.; Salvolini, E.; Bianchi, N.; Vozzi, G.; Gigante, A.; Mattioli-Belmonte, M. Human Periosteal Derived Stem Cell Potential: The Impact of Age. *Stem Cell Rev. Rep.* **2015**, *11*, 487–500. [[CrossRef](#)]
100. Sullivan, K.D.; Galbraith, M.D.; Andrysik, Z.; Espinosa, J.M. Mechanisms of Transcriptional Regulation by P53. *Cell Death Differ.* **2018**, *25*, 133–143. [[CrossRef](#)]
101. Aksoy, C.; Severcan, F. Role of Vibrational Spectroscopy in Stem Cell Research. *Spectrosc. Int. J.* **2012**, *27*, 167–184. [[CrossRef](#)]
102. Matthews, Q.; Jirasek, A.; Lum, J.; Duan, X.; Brolo, A.G. Variability in Raman Spectra of Single Human Tumor Cells Cultured in Vitro: Correlation with Cell Cycle and Culture Confluency. *Appl. Spectrosc.* **2010**, *64*, 871–887. [[CrossRef](#)] [[PubMed](#)]
103. Movasaghi, Z.; Rehman, S.; Rehman, I.U. Raman Spectroscopy of Biological Tissues. *Appl. Spectrosc. Rev.* **2007**, *42*, 493–541. [[CrossRef](#)]
104. Brauchle, E.; Noor, S.; Holtorf, E.; Garbe, C.; Schenke-Layland, K.; Busch, C. Raman Spectroscopy as an Analytical Tool for Melanoma Research. *Clin. Exp. Dermatol.* **2014**, *39*, 636–645. [[CrossRef](#)] [[PubMed](#)]
105. Hoppe, A. What mRNA Abundances Can Tell Us about Metabolism. *Metabolites* **2012**, *2*, 614–631. [[CrossRef](#)] [[PubMed](#)]
106. Verrier, S.; Notingher, I.; Polak, J.M.; Hench, L.L. In Situ Monitoring of Cell Death Using Raman Microspectroscopy. *Biopolymers* **2004**, *74*, 157–162. [[CrossRef](#)]
107. Parrotta, E.; De Angelis, M.T.; Scalise, S.; Candeloro, P.; Santamaria, G.; Paonessa, M.; Coluccio, M.L.; Perozziello, G.; De Vitis, S.; Sgura, A.; et al. Two Sides of the Same Coin? Unraveling Subtle Differences between Human Embryonic and Induced Pluripotent Stem Cells by Raman Spectroscopy. *Stem Cell Res. Ther.* **2017**, *8*, 271. [[CrossRef](#)]
108. Bogdan, P.; Deasy, B.M.; Gharaibeh, B.; Roehrs, T.; Marculescu, R. Heterogeneous Structure of Stem Cells Dynamics: Statistical Models and Quantitative Predictions. *Sci. Rep.* **2014**, *4*, 4826. [[CrossRef](#)]
109. McLeod, C.M.; Mauck, R.L. On the Origin and Impact of Mesenchymal Stem Cell Heterogeneity: New Insights and Emerging Tools for Single Cell Analysis. *Eur. Cell. Mater.* **2017**, *34*, 217–231. [[CrossRef](#)]
110. Tan, Y.; Konorov, S.O.; Schulze, H.G.; Piret, J.M.; Blades, M.W.; Turner, R.F.B. Comparative Study Using Raman Microspectroscopy Reveals Spectral Signatures of Human Induced Pluripotent Cells More Closely Resemble Those from Human Embryonic Stem Cells than Those from Differentiated Cells. *Analyst* **2012**, *137*, 4509–4515. [[CrossRef](#)]
111. Germond, A.; Panina, Y.; Shiga, M.; Niioka, H.; Watanabe, T.M. Following Embryonic Stem Cells, Their Differentiated Progeny, and Cell-State Changes During IPS Reprogramming by Raman Spectroscopy. *Anal. Chem.* **2020**, *92*, 14915–14923. [[CrossRef](#)] [[PubMed](#)]
112. Wang, L.; Zhang, T.; Wang, L.; Cai, Y.; Zhong, X.; He, X.; Hu, L.; Tian, S.; Wu, M.; Hui, L.; et al. Fatty Acid Synthesis Is Critical for Stem Cell Pluripotency via Promoting Mitochondrial Fission. *EMBO J.* **2017**, *36*, 1330–1347. [[CrossRef](#)] [[PubMed](#)]

113. Ow, Y.-L.P.; Green, D.R.; Hao, Z.; Mak, T.W. Cytochrome c: Functions beyond Respiration. *Nat. Rev. Mol. Cell Biol.* **2008**, *9*, 532–542. [[CrossRef](#)] [[PubMed](#)]
114. Zaidi, S.; Hassan, M.I.; Islam, A.; Ahmad, F. The Role of Key Residues in Structure, Function, and Stability of Cytochrome-c. *Cell. Mol. Life Sci.* **2014**, *71*, 229–255. [[CrossRef](#)] [[PubMed](#)]
115. Kühlbrandt, W. Structure and Function of Mitochondrial Membrane Protein Complexes. *BMC Biol.* **2015**, *13*, 89. [[CrossRef](#)] [[PubMed](#)]
116. Eleftheriadis, T.; Pissas, G.; Liakopoulos, V.; Stefanidis, I. Cytochrome c as a Potentially Clinical Useful Marker of Mitochondrial and Cellular Damage. *Front. Immunol.* **2016**, *7*, 279. [[CrossRef](#)]
117. Cai, J.; Yang, J.; Jones, D.P. Mitochondrial Control of Apoptosis: The Role of Cytochrome c. *Biochim. Biophys. Acta* **1998**, *1366*, 139–149. [[CrossRef](#)]
118. Martínez-Fábregas, J.; Díaz-Moreno, I.; González-Arzola, K.; Díaz-Quintana, A.; De la Rosa, M.A. A Common Signalosome for Programmed Cell Death in Humans and Plants. *Cell Death Dis.* **2014**, *5*, e1314. [[CrossRef](#)]
119. Okada, M.; Smith, N.I.; Palonpon, A.F.; Endo, H.; Kawata, S.; Sodeoka, M.; Fujita, K. Label-Free Raman Observation of Cytochrome c Dynamics during Apoptosis. *Proc. Natl. Acad. Sci. USA* **2012**, *109*, 28–32. [[CrossRef](#)]
120. Salehi, H.; Middendorp, E.; Panayotov, I.; Collart Dutilleul, P.-Y.; Dutilleul, P.-Y.C.; Vegh, A.-G.; Ramakrishnan, S.; Gergely, C.; Cuisinier, F. Confocal Raman Data Analysis Enables Identifying Apoptosis of MCF-7 Cells Caused by Anticancer Drug Paclitaxel. *J. Biomed. Opt.* **2013**, *18*, 56010. [[CrossRef](#)]
121. Ichimura, T.; Chiu, L.; Fujita, K.; Kawata, S.; Watanabe, T.M.; Yanagida, T.; Fujita, H. Visualizing Cell State Transition Using Raman Spectroscopy. *PLoS ONE* **2014**, *9*, e84478. [[CrossRef](#)] [[PubMed](#)]



EDINBURGH
INSTRUMENTS



PRECISION RAMAN

Best-in-class Raman microscopes
for research and analytical requirements
backed with world-class customer
support and service.



edinst.com

RESEARCH ARTICLE

Isotope-like effect in $\text{YVO}_4:\text{Eu}^{3+}$ nanopowders: Raman spectroscopy

Jelena Mitrić¹  | Uroš Ralević¹ | Miodrag Mitrić² | Jovana Ćirković³ | Gregor Križan⁴ | Maja Romčević¹  | Martina Gilić¹ | Nebojsa Romčević¹¹Institute of Physics, University of Belgrade, Belgrade, Serbia²Laboratory for Theoretical Physics and Condensed Matter Physics, Vinca Institute of Nuclear Sciences, University of Belgrade, Belgrade, Serbia³Department for Material Science, Institute for Multidisciplinary Research, University of Belgrade, Belgrade, Serbia⁴AMI d.o.o, Crystal growth, Ptuj, Slovenia**Correspondence**Jelena Mitrić, Institute of Physics, University of Belgrade, Belgrade, Serbia.
Email: jmitric@ipb.ac.rs**Funding information**

Serbian Ministry of Education, Science and Technological Development, Grant/Award Number: Project 45003

Abstract

In this paper, we describe synthesis and characterization of YVO_4 and Eu^{3+} -doped YVO_4 nanopowders. Two methods of preparation were used—solution combustion synthesis (SCS) and classical ceramic method (CCM)—and compared. Morphology and structure of all samples were characterized with atomic-force microscopy (AFM), X-ray diffraction (XRD), and field-emission scanning electron microscopy (SEM). Raman spectroscopy was used to discuss the isotope-like effect. It is confirmed that doping with Eu ions results in a change of Raman spectra of doped samples—new modes arise, and intensity of existing ones change. Influence of different preparation methods on isotope-like effect is presented with detailed calculations of shifted modes.

KEYWORDS

isotope-like effect, nanopowders, phosphor

1 | INTRODUCTION

The revelation of new materials, processes, and phenomena in general within the nanoscale proposes wide opportunities for evolution and expansion of innovative nanosystems and nanostructures. Nanostructured materials attract great attention of researches because of their wide industrial and technological applications. When doped, these kind of materials could exhibit enhanced properties, and when doped with rare-earth (RE) ions specifically oxide nanostructures show improved optical properties when compared with their bulk structures.^[1–3]

The yttrium orthovanadate (YVO_4) belongs to the group of important metal vanadates, MVO_4 ($\text{M} = \text{Bi}, \text{Y}, \text{Fe}, \text{Cr}, \text{In}, \text{etc}$), because of its wide range of applications,

especially in photonics.^[4] Doped YVO_4 is very popular because of its photocatalytic properties^[5,6] and is a very common semiconducting material in photochemistry because of this feature, as well for its enhanced luminescence when doped with RE ions.^[7,8] Excellent thermal stability, robustness, and other physicochemical properties of YVO_4 ensured this nanostructure to be a very used material in optical devices.^[9] Very convenient thing about YVO_4 is that it is an attractive host material (eg, for RE ions) that could be well excited under UV light irradiation; ie, the vanadate group, $\text{V}^{5+} - \text{O}^{2-}$, in $\text{YVO}_4:\text{Eu}^{3+}$ is excited, and in that way, phonon energy is transferred to the doped RE ions. Eu ions exhibit red and orange emission, which corresponds to $^5\text{D}_0 - ^7\text{F}_2$ and $^5\text{D}_0 - ^7\text{F}_1$ transitions, respectively.^[10] There are lot of

examples where nanostructures were doped with Eu ions because of its great luminescent characteristics.^[11] RE ions are well known for their luminescence characteristics, which occur because of inner shell electronic transitions between the 4th energy levels. Yttrium ion in vanadate structure can be easily replaced with RE ions. Because of the similar properties of RE and yttrium ions, the concentration of RE ions can be larger in yttrium oxide than in other hosts. In our earlier work, we showed how doping with Eu ions could result in their replacement with R³⁺ ions in oxide nanopowders (R stands for a trivalent ion in oxide nanopowders, eg, Y³⁺ in YVO₄).^[12] That results in more efficient optical properties of MVO₄ materials.^[13] However, it has been shown that even a small amount of impurity could drastically enhance optical characteristics of these kinds of phosphors.^[1] The inclusion of RE ions may be of a twofold nature: It could cause the shift of the gravity center of the energy levels, which is related to the nephelauxetic effect,^[14] which is a measure of the metal-ligand covalency, and it could cause the splitting of the degenerate energy levels. The difference in size between bulk and nanocrystal cause different impact of the neighborhood on the metal ion, and in that way results in splitting of the energy levels, kinetics of the metastable levels, and metal-ligand covalency.^[15]

There are many methods for nanopowder preparation,^[16–20] and in this paper, we choose solution combustion synthesis (SCS), which is an important technique used for powder preparation, generally used to produce fine complex oxide ceramics. Even though SCS represents one of the simplest techniques, it offers numerous important advantages like homogeneity and high surface area of the samples, as well as high purity in combination with considerably lower temperatures and reduced processing time. Also, with this technique, fine particle size and crystalline samples can be obtained. Another method we used is classical ceramics method (CCM), which also offers significantly reduced time of powder preparation and controlled size of particles with respect only to temperature parameter. The goal was to represent two simple but yet effective methods of nanopowder preparation, which are cheap, fast, and reproducible and can be used for advanced applications. At the same time, they provide an insight in an interesting phenomenon, which we call isotope-like effect where with the use of Raman spectroscopy we observe substitution of Eu with Y ions. This occurrence in oxide nanopowders prepared by SCS and CCM is not explained in details by Raman spectroscopy in the literature yet, and to the best of our knowledge, this is the first report so far.

2 | SAMPLE PREPARATION AND CHARACTERIZATION METHODS

For sample preparation, two methods have been used. First, the solution combustion process is the most frequently used due to the low cost of the synthesis procedures and also due to the possibility of tailoring the size and morphology of particles. Eu³⁺-doped YVO₄ nanopowders were prepared as described in previous research.^[21,22] Eu³⁺ concentration was 1%, and it was obtained using stoichiometric quantities of starting chemicals Y(NO₃)₃·6H₂O, NH₄VO₃, NH₄NO₃, and Eu(NO₃)₃·6H₂O with the purity of 99.99%. Starting chemicals were purchased from ABCR and urea, (NH₂)₂CO, from Sigma-Aldrich. The dry mixture of 0.357 g Eu(NO₃)₃·6H₂O, 4.676 g of NH₃VO₃, and 15.32 g of Y(NO₃)₃·6H₂O was combined with the mixture of 4.8 g of NH₄NO₃ and 3.003 g of (NH₂)₂CO, which were used as organic fuels. When all mixtures were prepared, they were combusted with the flame burner at ~500°C. After the synthesis, the nanopowders were annealed in air atmosphere at 1200°C for 2 hr. The annealing of material is needed in order to achieve the full crystallinity. That sample is labeled with YVO₄:Eu³⁺ (I).

Second sample, YVO₄:Eu³⁺ (II), and the undoped YVO₄ were prepared using simple classic ceramic procedure. Stoichiometric quantities of starting chemicals of Y₂O₅, Y₂O₃, and Eu₂O₃ were used with the purity of 99.99% purchased from ABCR, then powdered and baked on 900°C for 5 hr. Concentration of Eu³⁺ was 1%. In the case of undoped sample, no Eu³⁺ was added, but the rest of the procedure was the same as in preparation of doped sample.

In this way, we got morphologically different samples, and we can also make a comparison regarding two different (but at the same time, simple) preparation methods.

First characterization technique used for examining the topography of obtained samples was atomic force microscopy (AFM). Sample surfaces were investigated using NTMDT's NTEGRA PRIMA atomic force microscope, which operates in semicontact mode. The AFM topography and phase images were acquired simultaneously using NSG01 probes with a typical resonant frequency of 150 kHz and 10 nm curvature radius of the tip apex.

Further structural characteristics were obtained using the X-ray diffraction (XRD) powder technique. All samples were examined under the same conditions, using a Philips PW 1050 diffractometer equipped with a PW 1730 generator, 40 kV × 20 mA, using Ni filtered Co K α radiation of 0.1778897 nm at room temperature. Measurements were carried out in the 2 h range of 10–100° with a

scanning step of 0.05° and 10-s scanning time per step. Crystallite size was determined by using XFIT computing program which is based on fundamental parameter convolution approach.^[23]

Field-emission scanning electron microscopy with energy dispersive X-ray spectrometer, FESEM-EDS, (FEI Scios 2) was used for morphology studies of our samples. The acceleration voltage between cathode and anode was equal to 15 kV. High-resolution SEM images and EDS spectra from the chosen microareas and high-resolution maps were shown elemental composition and surface distribution.

Raman measurements were performed using commercial NTegra Spectra system from NT-MDT with a laser operating at a wavelength of 532 nm. Laser power was set to 2 mW within the $\sim 0.5 \times 0.5 \mu\text{m}$ sized focus with exposure time of 600 s. All the Raman spectra are unpolarized.

3 | RESULTS AND DISCUSSION

3.1 | Atomic force spectroscopy

The results of AFM measurements are shown in Figure 1. The samples of YVO_4 and $\text{YVO}_4:\text{Eu}^{3+}$ (II) have granular surfaces whereas the surface of $\text{YVO}_4:\text{Eu}^{3+}$ (I) has flat domains separated by deep holes with depths up to several hundred nanometers. The lateral size of the flat domains has an average value of 3–4 μm . The grain and domain boundaries are also visible in the corresponding phase images, whose large phase contrast originates mainly from the abrupt changes in the topography at these boundaries. The average grain size cannot be estimated accurately as the AFM tip is not able to penetrate deep enough between the tightly packed grains. Finally, the root-mean-square roughness (RMS) parameter assessed for the YVO_4 and $\text{YVO}_4:\text{Eu}^{3+}$ (II) surfaces has

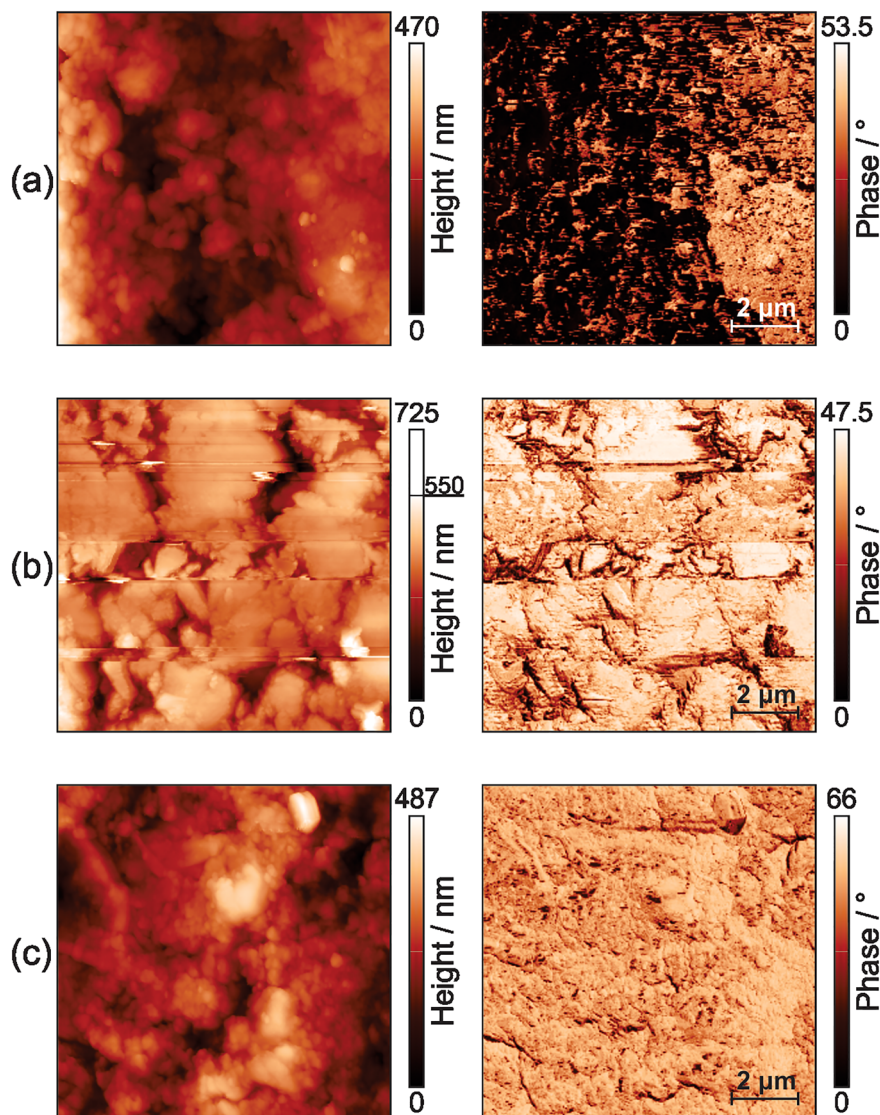


FIGURE 1 AFM topography and corresponding phase images for (a) YVO_4 , (b) $\text{YVO}_4:\text{Eu}^{3+}$ (I) and (c) $\text{YVO}_4:\text{Eu}^{3+}$ (II) [Colour figure can be viewed at wileyonlinelibrary.com]

values of about 67.2 and 67.8 nm, respectively, whereas the morphologically distinctive $\text{YVO}_4:\text{Eu}^{3+}(\text{I})$ surface has smaller RMS of around 64.5 nm.

3.2 | XRD analysis

Structure of synthesized samples of YVO_4 and $\text{YVO}_4:\text{Eu}^{3+}$ nanopowders were identified by XRD patterns as shown in Figure S1. All the observed peaks are in good agreement with the JCPDS card 17-0341. The samples are monophased and they crystallize in body-centered tetragonal lattice in the zircon-type structure (Figure 2). No additional peaks other than ones of YVO_4 , confirm that doping of Eu^{3+} does not change the crystalline structure. Calculated crystallite size for YVO_4 , $\text{YVO}_4:\text{Eu}^{3+}(\text{I})$, and $\text{YVO}_4:\text{Eu}^{3+}(\text{II})$ are 52, 58, and 53 nm, respectively. It was expected that YVO_4 and $\text{YVO}_4:\text{Eu}^{3+}(\text{II})$ have similar crystallite size because of the same method of preparation. It was also showed that using classical ceramic method we get smaller crystallite size of nanopowders when compared with solution combustion method.

3.3 | FESEM analysis

The surface morphology and size of the prepared samples were inspected using field emission scanning electron microscopy (FESEM) equipped with an energy-dispersive X-ray spectrometer (EDX). Results are shown in Figure

S2. All samples have spherical nanoparticles; size of particles are around $2\ \mu\text{m}$ for the samples prepared with classical ceramic method (YVO_4 and $\text{YVO}_4:\text{Eu}^{3+}(\text{II})$) and $3\ \mu\text{m}$ for the sample prepared with solution combustion synthesis ($\text{YVO}_4:\text{Eu}^{3+}(\text{I})$). The particles sizes obtained directly from FESEM images are much bigger than those calculated by XRD patterns, revealing the particle aggregation. However, even after aggregation, particle size is rather similar. It could be said that $\text{YVO}_4:\text{Eu}^{3+}(\text{II})$ crystallized in more fluffier structure, whereas $\text{YVO}_4:\text{Eu}^{3+}(\text{I})$ is more crystalline, but that does not have any impact on aggregation.

EDX spectra confirm that our samples consist only of Y, V, and O for the undoped and Y, V, O and Eu ions for the doped samples.

3.4 | Raman spectroscopy

Primitive cell of YVO_4 consists of 12 atoms (Figure 2), which support 36 modes of vibration of which 12 of them are Raman active can be divided into external and internal modes. External modes originate from translations of the $(\text{VO}_4)^{3-}$ and R^{3+} ions and librational mode of the whole $(\text{VO}_4)^{3-}$ tetrahedra, whereas internal modes occur due to vibrational oxygen modes within the tetrahedral groups $(\text{VO}_4)^{3-}$.^[24] Seven of twelve Raman active modes are labeled as internal – $2A_{1g}$, $2B_{1g}$, $1B_{2g}$, $2E_g$, and four are known as external – $2B_{1g}$, $2E_g$.

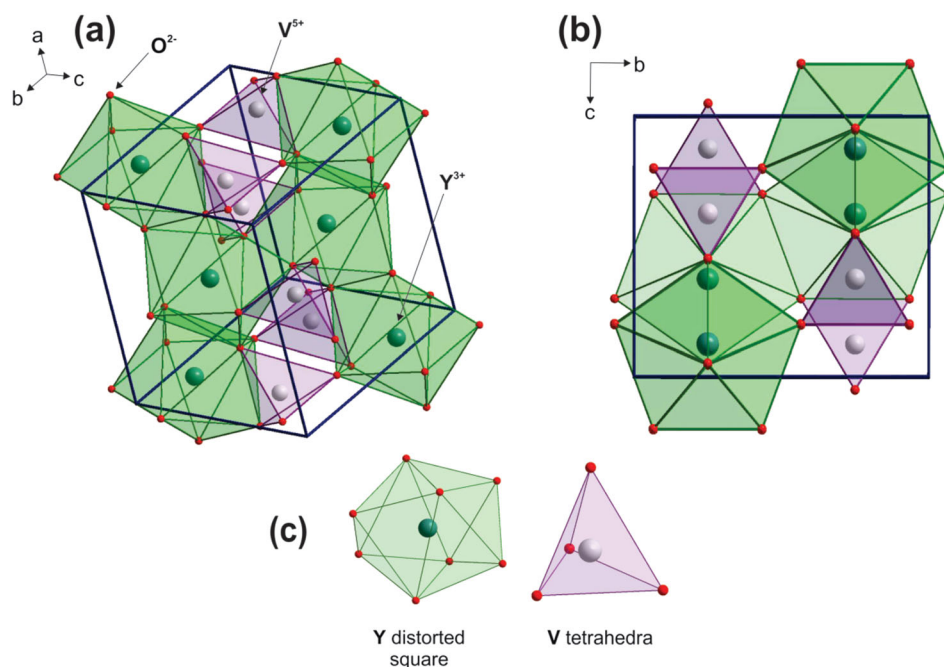


FIGURE 2 Structure of YVO_4 . (a) Pictorial representation of 3D structure of YVO_4 . (b) The same structure along one direction. (c) Polyhedral surroundings of Y and V ions are shown. Y^{3+} has distorted square surrounding eight O^{2-} ions around one Y^{3+} , and V^{5+} has tetrahedral surrounding four O^{2-} ions around one V^{5+} ion [Colour figure can be viewed at wileyonlinelibrary.com]

Figure 3 presents unpolarized Raman spectra obtained for three samples. Assignations of all the modes registered are given in Table 1.

The most of the Raman active modes registered come from YVO_4 structure, external, and internal vibrations, and just couple of them arise or are amplified by doping with Eu^{3+} (see Table 1). In Eu^{3+} doped YVO_4 structure, Eu^{3+} can be regarded as a substitution impurity ion, where Y gets substituted for Eu. The impurity mode could arise due to complex mechanism of electron-phonon interaction^[25] or simply because of the difference between masses of the doping ions and ions of the host material (known as isotope effect).^[26] In our case, there

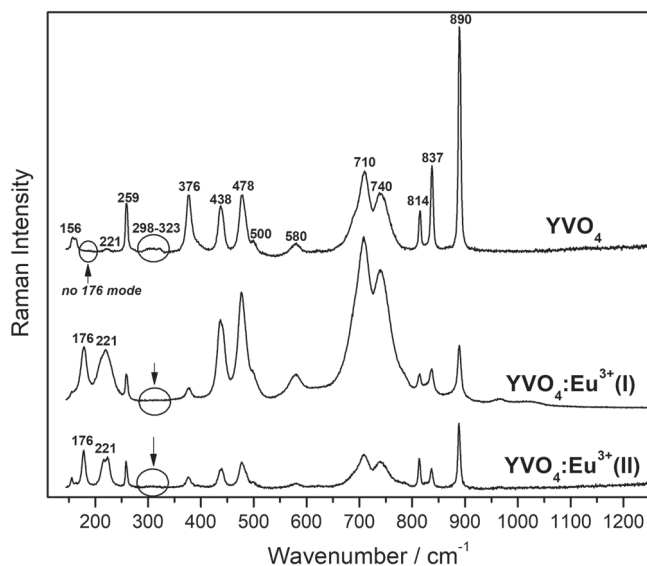


FIGURE 3 Raman spectroscopy of three samples of YVO_4 and $\text{YVO}_4:\text{Eu}^{3+}$ (I) and (II)

TABLE 1 Assignment of $\text{YVO}_4:\text{Eu}^{3+}$ vibrational modes registered by Raman spectroscopy

Vibrational Mode (cm^{-1})	Assignment
156	B_{1g} ; external vibration; vibrational modes of oxygen atoms within $(\text{VO}_4)^{3-}$ tetrahedral group ^[21]
176	vibration caused by doping with Eu^{3+}
221	amplified vibration by doping with Eu^{3+}
259	B_{2g} ; external mode; symmetrical stretching vibration mode ^[4] in $(\text{VO}_4)^{3-}$
376	A_{1g} ; internal mode; symmetrical deformation vibration ^[4] in $(\text{VO}_4)^{3-}$
438	internal mode; amplified in $\text{YVO}_4:\text{Eu}^{3+}$ (I) and weakened in $\text{YVO}_4:\text{Eu}^{3+}$ (II).
478	B_{1g} ; internal mode; antisymmetric stretching vibration mode ^[4] in $(\text{VO}_4)^{3-}$
500	B_{1g} ; internal mode;
580	internal modes; Amplified or weakened vibrations by doping, depending on the method of fabrication. In the $\text{YVO}_4:\text{Eu}^{3+}$ (I) these vibrations are amplified, whereas in the $\text{YVO}_4:\text{Eu}^{3+}$ (II) they are weakened.
710	
740	
814	B_{1g} ; internal mode;
837	E_g ; internal mode; antisymmetric stretching deformation vibration mode in $(\text{VO}_4)^{3-}$
890	A_{1g} ; internal mode;

is no electron-phonon interaction, we have impurity modes that arise due to the difference between mass of ions exchanged. Even though we do not have actual isotopes, we observe a substitution of one ion with a heavier one, with approximation that force constant remains unchanged. Therefore, we call it isotope-like effect.

First, let us define well known equation, which connects force constant and oscillator frequency:

$$k = 4\pi^2 m \omega_{\text{osc}}^2, \quad (1)$$

where k is force constant, m is mass of molecule, and ω_{osc} is an oscillator frequency.

From Equation 1, it is clear that oscillator frequency is proportional to force constant and inversely proportional to the mass. That means that (if we assume that force constant is not changing when impurity is added) change of vibrational (oscillator) frequency depends only on mass of observed molecule.

If we observe molecules with masses m_i ($i = 1, 2, \dots, n$), their corresponding vibrational frequencies, ω_{osc} are given with Equation 2.

$$\omega_{\text{osc}}^i = \frac{1}{2\pi} \sqrt{\frac{k}{m_i}}. \quad (2)$$

If we observe two molecules, their ratio is given with ρ :

$$\frac{\omega_{\text{osc}}^2}{\omega_{\text{osc}}^1} = \sqrt{\frac{\mu_1}{\mu_2}} = \rho. \quad (3)$$

If $m_2 > m_1$, then $\omega_{\text{osc}}^2 < \omega_{\text{osc}}^1$.

In that way, we get the frequency of shifted mode, which appeared when substitution of heavier ion is made.

Mode at 176 cm^{-1} arises when YVO_4 is doped with Eu^{3+} . We explain this with isotope-like effect. Eu ion substitutes Y ion, and as a result mode at 176 cm^{-1} is obtained. Calculation was made using Eq. (1-3). They confirm that mode at 221 cm^{-1} shifted to 176 cm^{-1} within the error limits, but also is significantly amplified. This is due to interaction of modes at 221 and 176 cm^{-1} , also provoked by doping with Eu^{3+} . Also, we have a wide mode in the range $298\text{--}323\text{ cm}^{-1}$ in the sample that is not doped with Eu^{3+} , but it vanishes when doped.

The intensities of modes obtained should also be discussed. Same type symmetry modes, A_{1g} , at 890 cm^{-1} and 376 cm^{-1} are both reduced when YVO_4 nanopowder is doped with Eu ions. Same thing happens with modes at 156 , 259 , and 814 cm^{-1} , which are in B_{1g} and B_{2g} symmetry. E_g mode at 814 cm^{-1} also shows significant reducing in intensity after doping (see Table 1). A_{1g} modes are internal and they represent symmetrical deformation vibrations in $(\text{VO}_4)^{3-}$, whereas B_{1g} and B_{2g} are antisymmetric and symmetric stretching vibrations in $(\text{VO}_4)^{3-}$; E_g represent antisymmetric stretching deformation vibration mode in $(\text{VO}_4)^{3-}$. Irreducible representations noted with A and B are one dimensional, whereas E_g is two dimensional. The modes at 438 , 580 , 710 , and 740 cm^{-1} could not be found in the earlier literature. We think those are internal modes which also arise due to $(\text{VO}_4)^{3-}$ vibrations but are amplified or weakened according to method of fabrication. These modes are amplified when nanopowders are prepared by solution combustion method. As we said earlier, this method results in smaller particles and less grained structure. As a result modes are somewhat wider and more intense when compared with samples prepared by CCM, which have more grained structure. This by no means influence on isotope-like effect in these structures.

4 | CONCLUSION

In this paper, we showed how doping of Eu ions affect on YVO_4 nanopowders. We conclude that Eu ions substitute Y ions in YVO_4 structure and new modes in Raman spectra occur. Detailed calculation of isotope-like effect was presented. Same symmetry modes show the same tendency of reducing intensity which we attribute to the doping with Eu ions, because of the symmetry disturbance of $(\text{VO}_4)^{3-}$ tetrahedra. No effect of method preparation of doped samples on isotope-like effect are observed, which means that the size of crystallites nor morphology of samples affect on substitution of doped ions into YVO_4 nanostructures. It was noticed that particles agglomerate,

but that does not have an impact on isotope-like effect. To our knowledge, there is no similar and more detailed study in the literature concerning this effect, therefore this work is one of the firsts to discuss it.

ACKNOWLEDGMENTS

This research was financially supported by the Serbian Ministry of Education and Science (Project 45003).

ORCID

Jelena Mitrić  <https://orcid.org/0000-0002-1526-3976>

Maja Romčević  <https://orcid.org/0000-0002-5064-175X>

REFERENCES

- [1] S. Thakur, A. K. Gathania, *J. Electronic Mater.* **2015**, *44*, 3444.
- [2] S. M. Rafiaei, A. Kim, M. Shokouhimehr, *Curr. Nanosci.* **2016**, *12*(2), 244.
- [3] S. Rafiaei, T. Isfahani, H. Afshari, M. Shokouhimehr, *Mater. Chem. Phys.* **2018**, *203*, 274.
- [4] M. S. Rabasović, J. Križan, P. Gregorčič, M. D. Rabasović, N. Romčević, D. Šević, *Opt. Quant. Electron.* **2016**, *48*, 163.
- [5] R. M. Mohamed, F. A. Harraz, I. A. Mkhallid, *J. Alloy. Compd.* **2012**, *532*, 55.
- [6] H. Xu, H. Wang, H. Yan, *J. Hazard. Mater.* **2007**, *144*, 82.
- [7] M. Shokouhimehr, S. M. Rafiaei, *Ceram. Int.* **2017**, *43*, 11469.
- [8] S. M. Rafiaei, A. Kim, M. Shokouhimehr, *Nanosci. Nanotechn. Lett.* **2014**, *6*(8), 692.
- [9] X. Xiao, G. Lu, S. Shen, D. Mao, Y. Guo, Y. Wang, *Mater. Sci. Eng. B* **2011**, *176*, 72.
- [10] D. Šević, M. S. Rabasović, J. Križan, S. Savić-Šević, M. Mitrić, M. Gilić, B. Hadžić, N. Romčević, *Mater. Res. Bull.* **2017**, *88*, 121.
- [11] S. Ram, *J. Raman Spectrosc.* **1987**, *18*, 537.
- [12] J. Mitrić, J. Križan, J. Trajić, G. Križan, M. Romčević, N. Paunović, B. Vasić, N. Romčević, *Opt. Mater.* **2018**, *75*, 662.
- [13] Y. Zhou, Q. Ma, M. Lü, Z. Qui, A. Zhang, *J. Phys. Chem. C* **2008**, *112*, 19901.
- [14] C. K. Jorgensen, *Modern Aspects of Ligand Field Theory*, North-Holland, Amsterdam **1971**.
- [15] S. Georgescu, E. Cotoi, A. M. Voiculescu, O. Toma, C. Matei, *Rom. J. Phys.* **2010**, *55*, 750.
- [16] Z. De-Quing, W. Shao-Jun, S. Hong-Shan, W. Xiu-Li, C. Mao-Sheng, *J. Sol-Gel Sci. Techn.* **2007**, *41*, 157.
- [17] W. Feng, L. Mu-Sen, L. Yu-peng, Q. Yong-xin, *Mater. Lett.* **2005**, *59*, 916.
- [18] S. Hua Xiao, W. Fen Jiang, L. Y. Li, X. Jian Li, *Mater. Chem. Phys.* **2007**, *16*, 82.
- [19] C. Xu, L. Ma, X. Liu, W. Qui, Z. Su, *Mater. Res. Bull.* **2004**, *39*, 881.
- [20] K. Zhang, X. Sun, G. Lou, X. Liu, H. Li, Z. Su, *Mater. Lett.* **2005**, *59*, 2729.

- [21] M. S. Rabasović, D. Šević, J. Križan, M. Terzić, J. Mozina, B. P. Marinković, S. Savić –Šević, M. Mitrić, M. D. Rabasović, N. Romčević, *J. Alloy. Compd.* **2015**, *622*, 292.
- [22] J. Križan, M. Mazaj, V. Kančič, J. Bajsić, J. Mozina, *Acta Chim. Slov.* **2014**, *61*, 608.
- [23] R. W. Cheary, A. Coelho, *J. Appl. Cryst.* **1992**, *25*, 109.
- [24] A. Sanson, M. Giarola, B. Rossi, G. Mariotto, E. Cazzanelli, A. Speghini, *Phys. Rev. B* **2012**, *86*, 214305.
- [25] A. A. Gogolin, E. I. Rashba, *Solid State Commun.* **1976**, *19*, 1177.
- [26] N. Romčević, J. Trajić, T. A. Kuznetsova, M. Romčević, B. Hadžić, D. R. Khokhlov, *J. Alloy. Compd.* **2007**, *442*, 324.

SUPPORTING INFORMATION

Additional supporting information may be found online in the Supporting Information section at the end of the article.

How to cite this article: Mitrić J, Ralević U, Mitrić M, et al. Isotope-like effect in YVO₄:Eu³⁺ nanopowders: Raman spectroscopy. *J Raman Spectrosc.* 2019;50:802–808. <https://doi.org/10.1002/jrs.5584>



Photoluminescence spectroscopy of CdSe nanoparticles embedded in transparent glass

M. Gilic¹ · R. Kostic¹ · D. Stojanovic¹ · M. Romcevic¹ · B. Hadzic¹ · M. Petrovic¹ · U. Ralevic¹ · Z. Lazarevic¹ · J. Trajic¹ · J. Ristić-Djurovic¹ · J. Cirkovic² · N. Romcevic¹

Received: 13 October 2017 / Accepted: 23 June 2018 / Published online: 29 June 2018
© Springer Science+Business Media, LLC, part of Springer Nature 2018

Abstract

In this paper we present photoluminescence measurements of CdSe nanoparticles embedded in transparent glass. Sample is prepared using an original technique, which combines both heat treatment and ultraviolet laser irradiation. Photoluminescence spectra displayed one main emission band at 2.14 eV. We identify this bands energy as basic interband transition in CdSe nanoparticle. We calculated energy of basic ($1s_h-1s_c$) transition in spherical CdSe quantum dot (QD), within infinite potential barrier, in effective-mass approximation. On the basis of this model, average radius of synthesized CdSe QDs is about 3 nm, which is in consistence with AFM measurements and UV–VIS absorption measurements.

Keywords Cadmium selenide · Nanoparticles · Photoluminescence · AFM · Effective mass approximation

1 Introduction

Glasses doped with nanosized inclusions of metals or semiconductors are known since a very long time. The first glasses containing metal nanoparticles were fabricated by Roman glassmakers in the fourth century A.D. Mediaval cathedral windows through several European countries witness the attention drawn by stained glasses containing metal aggregates as artistic work (Poole et al. 2003). They exhibit great varieties of beautiful colors owing to the nanosized metal particles which were embedded in the glass matrix.

Semiconductor-doped glasses were, however, not so widespread used. One very important application of semiconductor-doped glasses are sharp cut-off glass filters. In most cases, Cd

This article is part of the Topical Collection on Focus on Optics and Bio-photonics, Photonica 2017.

Guest Edited by Jelena Radovanovic, Aleksandar Krmpot, Marina Lekic, Trevor Benson, Mauro Pereira, Marian Marciniak.

✉ M. Gilic
martina@ipb.ac.rs

¹ Institute of Physics Belgrade, University of Belgrade, Pregrevica 118, Zemun 11080, Serbia

² Institute for Multidisciplinary Research, University of Belgrade, Kneza Visislava 1, Belgrade 11000, Serbia

(S_x, Se_x) nanocrystals are used for this purpose. By varying x the position of the cut-off wavelength can be precisely tuned between ~ 400 and 1000 nm.

These glass filters are easily available from different glassmakers, such as Schott, Corning, Hoya, or Toshiba. This is an import point, as it allowed a great number of optics groups to study this kind of composite material without the need for skills in material preparation.

From technological perspective, CdSe nanoparticles are of significant interest because of their unique quantum confinement properties, bright photoluminescence, narrow emission band, and photostability (Srivastava and Singh 2012). CdSe-polymer nanocomposites find potential applications in the fabrication of devices like photovoltaic cells, laser, thin film transistors, light emitting diodes (Yu et al. 2006; Oertel et al. 2005), catalysis (Ahmadi et al. 1996) and biological fluorescence labels (Bruchez et al. 1998; Chan and Nie 1998). In particular, CdSe nanocrystals have been proposed as working elements for nanotransistors (Klein et al. 1997), electrochromic materials (Wang et al. 2001), and charge-coupling devices (Woo et al. 2002).

In the present paper we studied photoluminescence characteristics of CdSe quantum dots in glass matrix along with investigating surface morphology of the system using AFM measurements.

2 Experimental details

CdSe nanoparticles embedded in transparent silicate-based glasses was successfully fabricated by a novel technique consisting in joined utilization of the thermal annealing below glass crystallization temperature, and the UV continuous wave laser irradiation (Argon laser at 244 nm). This innovative fabrication method exploits adapted combination of thermal annealing and UV laser power density that allows controlling the spatial localization of the nanocrystals formation inside the glass sample. The originality of the technique is that the required thermal energy needed for the precipitation of CdSe into crystals is brought by thermal annealing in association to UV absorption, which leads to the control of the spatial crystallization. Further information about samples fabricating can be found elsewhere (Mekhlouf et al. 2007).

The surface morphology of our sample was investigated by atomic force microscopy (AFM). AFM imaging was done using the NTEGRA Prima system from NT MDT. AFM measurements were performed at room temperature and under ambient conditions.

The UV–VIS absorbance spectrum was recorded on the room temperature in the wavelength range 200–800 nm on a Shimadzu UV-2600 spectrophotometer equipped with an integrated sphere. The absorbance spectrum was measured relative to a reference sample of $BaSO_4$.

Photoluminescence measurements on room temperature were obtained by Jobin-Yvon U1000 spectrometer equipped with RCA-C31034A photomultiplier with housing cooled by Peltier element, amplifiers and counters. As an excitation sources, the 488 and 514.5 nm lines of Argon laser were used.

3 Results and discussion

3.1 Results of AFM surface characterization

The surface morphology of our sample was investigated by atomic force microscopy, in order to determine the general cell wall structure, together with the assembly of particular components into the wall structure as a whole. Areas of 2×2 and 5×5 μm were investigated, and AFM images of our sample are presented in Fig. 1a, b. From Fig. 1 it is clear that the sample is packed and continuous without the presence of porosity and voids. The surface is rather smooth with no cracks observed. The small islands of several nm to several tenths of nm in diameter are distinguished, which corresponds to the nanoparticles of CdSe. According to the height bars at the right side of Fig. 1a, b, the surface height of our sample is up to 14 nm. Figure 1c, d show the histograms of the nanostructure height in 2×2 and 5×5 μm areas of AFM images, respectively. The sample exhibits an ensemble of nanostructures with an average height of (4.9 ± 0.2) nm for chosen area of 2×2 μm , and (6.4 ± 0.2) nm for 5×5 μm area.

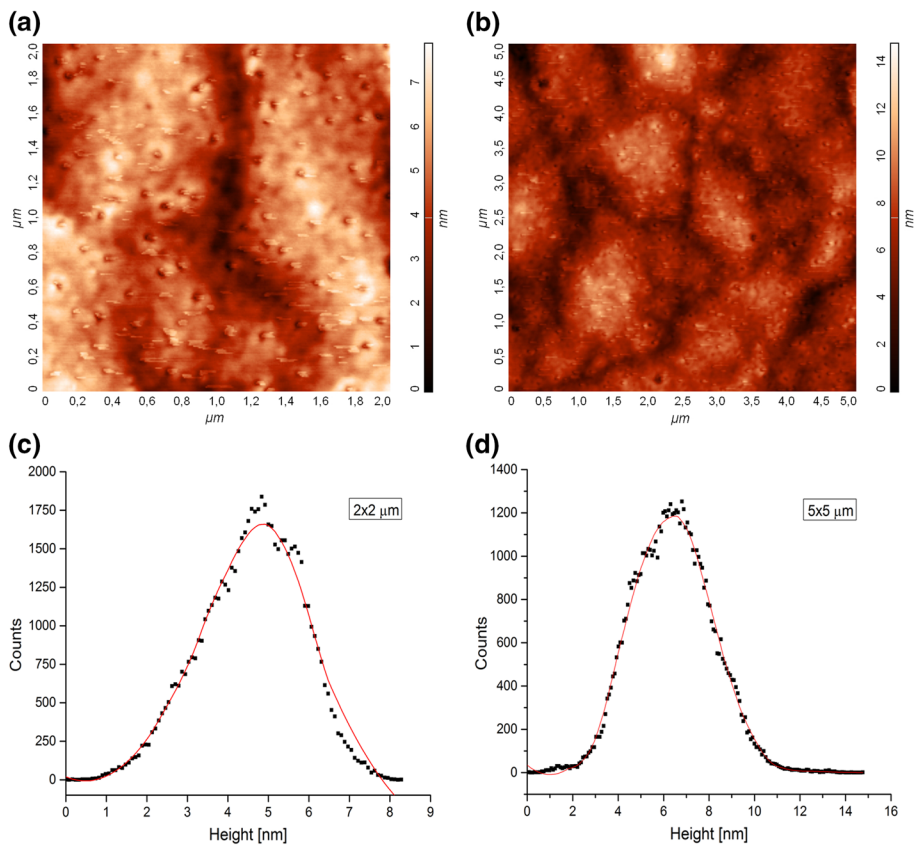


Fig. 1 2D AFM images and histograms of CdSe nanoparticles embedded in transparent silicate-based glasses, **a** 2×2 μm image, **b** 5×5 μm image, **c** 2×2 μm histogram, **d** 5×5 μm histogram

3.2 Optical characterization: photoluminescence and UV–VIS absorbance measurements

UV–VIS absorbance spectrum of our sample is presented in Fig. 2. The position of the first optical transition is at 520 nm. The position of a peak is related to the size of the absorbing nanocrystal and to the band gap. The average size of the nanocrystal of interest can be obtained using the relation (Yu et al. 2003):

$$D = 1.6122 \times 10^{-9} \times \lambda^4 - 2.6575 \times 10^{-6} \times \lambda^3 + 1.6242 \times 10^{-3} \times \lambda^2 - 0.4277 \times \lambda + 41.57 \quad (1)$$

where λ (nm) is the first exciton peak of CdSe absorbance spectrum. From the $\lambda = 520$ nm the calculated size of our nanoparticles is 2.6 nm.

There are several approaches in literature to determine the band gap from the absorbance spectra. In the present study we employ the approach of Yu et al. (2003) and Hegazy and Abd (2014) where the E_g is calculated directly from the absorption maximum of the first exciton absorption peak. Using formula

$$E_g = h\nu = hc/\lambda, \quad (2)$$

the obtained band gap is 2.39 eV.

Normally, the absorption of light by CdSe QDs increases with decreasing wavelength (Kongkanand et al. 2008; Debgupta et al. 2014). In present case, we must conclude that the glass matrix modify the spectrum of CdSe QDs—the absorption spectrum of glass matrix: CdSe QDs hybrid composite differ from those of individual components, as in Dayneko et al. (2016) where the CdSe QDs were incorporated in poly[N-9'-heptadecanyl-2,7-carbazole-alt-5,5-(4',7'-di-2-thienyl-2',1',3'-benzothiadiazole)].

PL spectra of CdSe QDs in glass matrix are presented in Fig. 3. The dominant band in both spectra is very broad and has a maximum at ~ 2.14 eV. Such a broad band implies the existence of vast size distribution of CdSe QDs. We assigned this transition as direct band-to-band transition in CdSe. Due to the Stokes shift, this value is smaller than the band gap observed

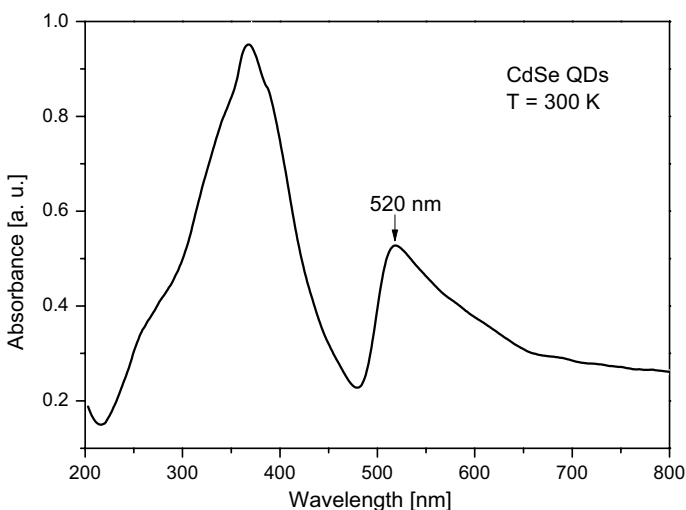


Fig. 2 UV–VIS absorbance spectrum of CdSe QDs

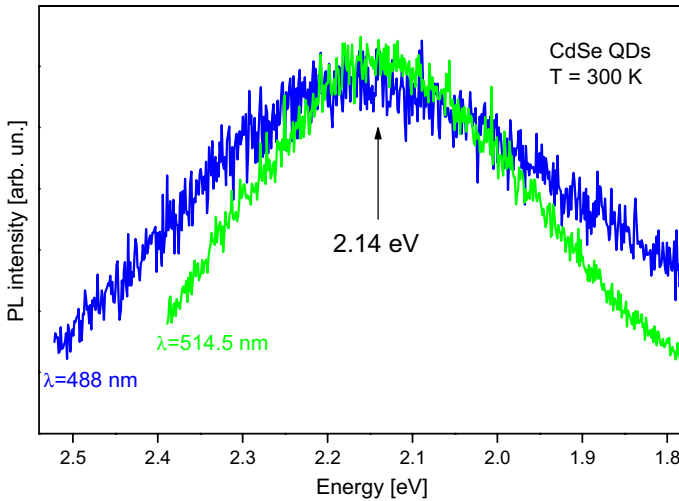


Fig. 3 Photoluminescence spectra of CdSe QDs excited with 488 nm (blue) and 514.5 nm (green) lines of Ar–laser and recorded on the room temperature. (Color figure online)

from absorption spectrum. However, the band gap of bulk CdSe is reported to be 1.75 eV. The observed blue shift of this band is ~0.39 eV, and its position can be explained in the following manner.

3.3 Model

The single quantum dot we consider is spherical CdSe core surrounded by transparent glass. R is the core radius and the dot center is center of coordinates (Schoss et al. 1994; Kostić and Stojanović 2011). Electron and hole i.e. carriers, in such a system are characterized by their effective masses. In this case m_e^* and m_h^* are electron and hole effective masses of CdSe. Rectangular potential through the structure, having in mind that CdSe is surrounded by glass, is assumed as:

$$V(r) = \begin{cases} 0 & r \leq R \\ \infty & r > R \end{cases} \tag{3}$$

Considering that the carrier spectra are mainly formed by size quantization, the stationary Schrödinger equation for a single particle (electron or hole).

$$\left(-\frac{\hbar^2}{2m_i^*} \nabla^2 + V(r) \right) \Psi(\vec{r}) = E_i \Psi_i(\vec{r}), \quad i = e, h \tag{4}$$

is solved in spherically symmetric potential $V(r)$, described by (3). Separation of radial and angular coordinates leads to $\Psi_{lm}(r) = R_l(r)Y_{lm}(\theta, \phi)$. $R_l(r)$ is the radial wave function, and $Y_{lm}(\theta, \phi)$ is a spherical harmonic. l and m are orbital and magnetic quantum numbers. For a spherical potential with stepwise constant value 0, in the core, and ∞ , outside the core, the radial function $R_l(r)$ is given by:

$$R_l(r) = \begin{cases} A_l j_l(kr) & r \leq R \\ 0 & r > R \end{cases}, \tag{5}$$

j_l , are Bessel spherical functions. These solutions already satisfy conditions that the wave function is regular when $r=0$. Each solution must satisfy boundary conditions. In case of infinitely high potential barrier, wave function does not penetrate into the surrounding medium and must satisfy trivial boundary condition: to be zero at $r=R$. This trivial boundary condition leads to equation characteristic for each l ($l=0, 1, 2, \dots$). There is series of solutions (eigenfunctions i.e. eigenenergies) characteristic for each l . Number n numerates eigenenergies E_{nl} . For an electron E_{nl} shows the energy above core conductive band, and for hole energy below valence band of core material.

As it is common, the lowest energy among solution for each l is numerated as $n=1$. Among all states, state $l=0, n=1$ is the lowest energy solution i.e. it is the ground state.

Once the eigenvalues E_{nl} are determined, the coefficients A_{nl} in Eq. (5) are determined by using the normalization condition for $R_{nl}(r)$, $\int_0^{\infty} R_{nl}^2(r) \cdot r^2 dr = 1$. Result of these calculations is the complete information about eigenenergies E_{nl} and corresponding wave functions $R_{nl}(r)$.

One state can be identified by characteristic energy, denoted as E_{nl} and wave function, denoted as ψ_{nl} , or just (n, l) . As it is usual all $l=0$ states are assigned as s , $l=1$ states as p and $l=2$ states as d . In all papers $l=0$ (s) states are assigned: ($l=0, n=1$) as $1s$, ($l=0, n=2$) as $2s$, ($l=0, n=3$) as $3s$ etc. For the $l=1$ (p) states, some authors assigned states in the same manner as for $l=0$, i.e. ($l=1, n=1$) as $1p$, ($l=1, n=2$) as $2p$, ($l=1, n=3$) as $3p$ etc. For the $l=2$ (d) states, assignation is: ($l=2, n=1$) is $1d$, ($l=2, n=2$) is $2d$, ($l=2, n=3$) is $3d$ etc. In this assignation number in front s, p or d numerates if it is the first, second or higher order solution. It is possible, having in mind wave functions properties, to use hydrogen like assignation: ($l=1, n=1$) is $2p$, ($l=1, n=2$) is $3p$, ($l=1, n=3$) is $4p \dots$; ($l=2, n=1$) is $3d$, ($l=2, n=2$) is $4d$, ($l=2, n=3$) is $5d \dots$. Hydrogen like assignation is even more desirable if we deal with charged impurities inside QD.

These calculations were performed for electrons and holes in similar procedure, giving the confinement energies E_{nl}^e and E_{nl}^h , and wave functions R_{nl}^e and R_{nl}^h . Once the electron and hole wave functions are known, radial probability in the system give an illustrative picture, especially in more complex structures, of electron and hole spatial localization.

We focused our analysis to transition between $l=0, n=1$ hole ($1s_h$) and electron ($1s_e$) states, because this is the basic interband transition.

From the electron and hole wave functions, the Coulomb interaction of electron and hole can be calculated. In the frame of perturbation theory energy of Coulomb interaction is given by:

$$E_C = -e^2 \int \int \frac{|R^e(r_e)|^2 |R^h(r_h)|^2}{4\pi\epsilon|r_e - r_h|} r_e^2 r_h^2 dr_e dr_h \tag{6}$$

ϵ is the high energy dielectric permittivity.

The transition electronic energy (E_{10}) is sum of the core gap energy, corresponding electron and hole eigenvalues and the Coulomb energy:

$$E_{10} = E_g + E_{10}^e + E_{10}^h + E_C \tag{7}$$

The parameters characteristic for CdSe bulk are presented in Table 1. Calculation parameters, effective masses of carriers and dielectric permittivity, are transferred from literature (Kostić and Stojanović 2011; Sahin et al. 2009). Calculated transition energy is presented in Fig. 4.

Table 1 The material parameters used in the calculations

Material	m_e^*/m_0	m_h^*/m_0	ϵ_r	E_g (eV)
CdSe	0.13	0.45	9.3	1.75

m_e^* is electron effective mass in material, m_h^* is hole effective mass in material, m_0 is electron mass, ϵ_r is relative dielectric permittivity, E_g is the energy gap of the material

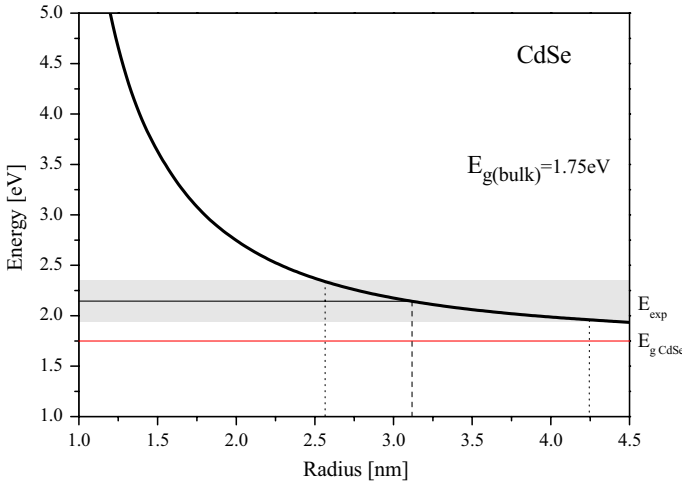


Fig. 4 $1s_h-1s_e$ interband transition energy in CdSe QD as function on the dot radius

Energy of basic interband transition ($1s_h-1s_e$) in the quantum dots increases as the dimension of the dot decreases. Simple model based on effective mass approximation can estimate transition energy of QD. This energy depends on the dimension of the dot, and parameters of the bulk material like energy gap, dielectric permittivity, and electron and hole effective masses. Due to the very broad band, we consider that there is an ensemble of quantum dots with a wide range of sizes. As a provisional borders, we used the energy values of FWHM of the band obtained by 514.5 nm laser line, which is less broad than the one obtained with 488 nm. These borders are 1.94–2.32 eV, and corresponding QD dimensions are 2.5–4.2 nm. The band maximum at 2.14 eV corresponds to the QD size of 3.1 nm. These results are in agreement with the calculations for UV–VIS absorbance.

4 Conclusions

The photoluminescence measurements along with AFM measurements of CdSe nanoparticles embedded in transparent glass are presented. The AFM measurements reveal the presence of small islands of several nm in diameter, which correspond to the nanoparticles of CdSe. The UV–VIS absorbance spectrum displayed the first exciton peak at 520 nm. Calculated size of nanoparticles is about 2.6 nm. The PL measurements display one main broad emission band at ~2.14 eV which is identified as basic interband transition in CdSe nanoparticle. The energy of basic transition in spherical CdSe quantum dot in effective

mass approximation is calculated. Based on this model, the average radius of CdSe QD is found to be ~ 3 nm.

Acknowledgements This work was supported by Serbian Ministry of Education, Science and Technological Development under Project III45003. The authors thank A. Boukenter and F. Goutaland for providing the samples.

References

- Ahmadi, T.S., Wang, Z.L., Green, T.C., Henglein, A., El-Sayed, M.A.: Shape-controlled synthesis of colloidal platinum nanoparticles. *Science* **272**, 1924–1926 (1996)
- Bruchez Jr., M., Moronne, M., Gin, P., Weiss, S., Alivisatos, A.P.: Semiconductor nanocrystals as fluorescent biological labels. *Science* **281**, 2013–2016 (1998)
- Chan, W.C.W., Nie, S.M.: Quantum dot bioconjugates for ultrasensitive nonisotopic detection. *Science* **281**, 2016–2018 (1998)
- Dayneko, S., Linkov, P., Martynov, I., Tameev, A., Tedoradze, M., Samokhvalov, P., Nabiev, I., Christyakov, A.: Photoconductivity of composites based on CdSe quantum dots and low-gap polymers. *Physica E* **79**, 206–211 (2016)
- Debgupta, J., Sadananda, M., Kalita, H., Mohammed, A., Patra, A., Pillai, V.: Photophysical and photoconductivity properties of thiol-functionalized grapheme-CdSe QD composites. *RCS Adv.* **4**, 13788–13795 (2014)
- Hegazy, M., Abd, El-Hameed A.: Characterization of CdSe-nanocrystals used in semiconductors for aerospace applications: production and optical properties. *NRIAG J. Astron. Geophys.* **3**, 82–87 (2014)
- Klein, D.L., Roth, R., Lim, A.K.L., Alivisatos, A.P., McEuen, P.: A single-electron transistor made from a cadmium selenide nanocrystal. *Nature* **389**, 699–701 (1997). <https://doi.org/10.1038/39535>
- Kongkanand, A., Tvrdy, K., Takechi, K., Kuno, M., Kamat, P.V.: Quantum dot solar cells. Tuning photoreponse through size and shape control of CdSe-TiO₂ architecture. *J. Am. Chem. Soc.* **130**, 4007–4021 (2008)
- Kostić, R., Stojanović, D.: Nonlinear absorption spectra for intersubband transition of CdSe/ZnS spherical quantum dots. *J. Nanophotonic* **5**, 051810 (2011)
- Mekhlouf, S.E., Boukenter, A., Ferrari, M., Goutaland, F., Ollier, N., Ouerdane, Y.: UV assisted local crystallization in Er³⁺ doped oxy-fluoride glass. *J. Non-Cryst. Solids* **353**, 506–509 (2007)
- Oertel, D. C., Bawendi, M. G.: Photodetectors based on treated CdSe quantum-dot films. *Appl. Phys. Lett.* **87**, 213505 (2005)
- Poole Charles Jr., P., Owen Frank, J. (ed.): *Introduction to Nanotechnology*, vol. 1, pp. 1–20. Wiley, Hoboken (2003)
- Sahin, M., Nizamoglu, S., Kavruk, A.E., Demir, H.V.: Self-consistent computation of electronic and optical properties of a single exciton in a spherical quantum dot via matrix diagonalization method. *J. Appl. Phys.* **106**, 043704 (2009)
- Schoss, D., Mews, A., Eychmuller, A., Weller, H.: Quantum-dot quantum well CdS/HgS/CdS: theory and experiment. *Phys. Rev. B* **49**, 17072–17078 (1994)
- Srivastava, P., Singh, K.: Synthesis of CdSe nanoparticles by solvothermal route: structural, optical and spectroscopic properties. *Adv. Mater. Lett.* **3**, 340–344 (2012)
- Wang, C., Shim, M., Guyott-Sionnest, P.: Electrochromic nanocrystal quantum dots. *Science* **91**, 2390–2392 (2001)
- Woo, W.K., Shimizu, K.T., Jarosz, M.V., Neuhauser, R.G., Leatherdale, C.A., Rubner, M.A., Bawendi, M.G.: Reversible charging of CdSe nanocrystals in a simple solid-state device. *Adv. Mater.* **14**, 1068–1071 (2002)
- Yu, D., Wehrenberg, B. L., Jha, P., Ma, J., Guyot-Sionnest, P.: Electronic transport of n-type CdSe quantum dot films: effect of film treatment. *J. Appl. Phys.* **99**(10), 104315 (2006)
- Yu, W., Qu, L., Guo, W., Peng, X.: Experimental determination of the extinction coefficient of CdTe, CdSe, and CdS nanocrystals. *Chem. Mater.* **15**, 2854–2860 (2003)

PAPER

Correlation between morphology and local mechanical and electrical properties of van der Waals heterostructures

To cite this article: Borislav Vasi *et al* 2022 *Nanotechnology* **33** 155707

View the [article online](#) for updates and enhancements.

You may also like

- [Impact of a van der Waals interface on intrinsic and extrinsic defects in an MoSe₂ monolayer](#)
Carlos J Alvarez, Minh Tuan Dau, Alain Marty *et al.*
- [Computational screening of MX \(M = Ga, Ge, Sn, In; X = As, Se\) van der Waals heterostructures as suitable candidates for solar cells](#)
Qian Wu, Wei Wei, Fengping Li *et al.*
- [High-efficiency photocatalyst for water splitting: a Janus MoS₂/XN \(X = Ga, Al\) van der Waals heterostructure](#)
Kai Ren, Sake Wang, Yi Luo *et al.*




EDINBURGH INSTRUMENTS

WORLD LEADING MOLECULAR SPECTROSCOPY SOLUTIONS

edinst.com

The advertisement features a red background with the Edinburgh Instruments logo on the left, which consists of a circular pattern of white dots. In the center and right, several pieces of laboratory equipment are displayed, including a spectrometer labeled 'F55', a larger unit labeled 'FLS 1000', and another unit labeled 'FLS 1000'. The text 'EDINBURGH INSTRUMENTS' is written in white, bold, uppercase letters. Below the logo, the text 'WORLD LEADING MOLECULAR SPECTROSCOPY SOLUTIONS' is written in white, bold, uppercase letters. In the bottom right corner, the website 'edinst.com' is displayed in white text on a red rectangular background.

Correlation between morphology and local mechanical and electrical properties of van der Waals heterostructures

Borislav Vasić¹ , Uroš Ralević¹, Sonja Aškričić¹, Davor Čapeta² and Marko Kralj² 

¹Institute of Physics Belgrade, University of Belgrade, Pregrevica 118, 11080 Belgrade, Serbia

²Center of Excellence for Advanced Materials and Sensing Devices, Institute of Physics, Bijenička 46, 10000, Zagreb, Croatia

E-mail: bvasic@ipb.ac.rs

Received 7 October 2021, revised 24 December 2021

Accepted for publication 31 December 2021

Published 21 January 2022



CrossMark

Abstract

Properties of van der Waals (vdW) heterostructures strongly depend on the quality of the interface between two dimensional (2D) layers. Instead of having atomically flat, clean, and chemically inert interfaces without dangling bonds, top-down vdW heterostructures are associated with bubbles and intercalated layers (ILs) which trap contaminations appeared during fabrication process. We investigate their influence on local electrical and mechanical properties of MoS₂/WS₂ heterostructures using atomic force microscopy (AFM) based methods. It is demonstrated that domains containing bubbles and ILs are locally softer, with increased friction and energy dissipation. Since they prevent sharp interfaces and efficient charge transfer between 2D layers, electrical current and contact potential difference are strongly decreased. In order to reestablish a close contact between MoS₂ and WS₂ layers, vdW heterostructures were locally flattened by scanning with AFM tip in contact mode or just locally pressed with an increased normal load. Subsequent electrical measurements reveal that the contact potential difference between two layers strongly increases due to enabled charge transfer, while local I/V curves exhibit increased conductivity without undesired potential barriers.

Keywords: van der Waals heterostructures, two-dimensional materials, atomic force microscopy, Kelvin probe force microscopy, conductive atomic force microscopy, nanofriction, energy dissipation

(Some figures may appear in colour only in the online journal)

1. Introduction

Van der Waals (vdW) heterostructures are vertical stacks of different two dimensional (2D) materials [1–3]. Since individual 2D layers hold together by weak vdW forces without chemical bonding, their stacking is not constrained by the crystal lattice matching. As a result, arbitrary combinations of 2D materials can be fabricated by transferring them on top of each other [4].

Since 2D materials are associated with electronic band-gaps in a broad range, they provide metallic (such as graphene), semiconducting (such as transition metal dichalcogenides (TMDs)) and insulating layers (such as hexagonal

boron nitride). Heterostructures obtained by their combinations bring novel and unique functionalities and devices with properties exceeding those of constituent materials. Characteristic examples are barrier-free electrical contacts [5], efficient substrates for 2D electronic devices with reduced charge scattering [6], and tunneling and field-effect transistors [7–9].

TMDs are 2D semiconductors with the band-gap in the visible and near-infrared domain, with a direct band-gap in the case of the monolayer limit, and correspondingly with a strong photoluminescence [10]. Heterostructures comprising of 2D semiconductors with different band gap are of special importance since they act as atomically sharp vertical

p–n-junctions [11] with obvious applications for rectifying junctions [12, 13]. They are also very interesting for optoelectronics and photovoltaic applications [14] such as atomically-thin photodetectors and solar cells [15–19] and light emitting devices [20, 21].

While recent studies were mainly focused on possible applications in electronics and optoelectronics, vdW heterostructures have interesting mechanical properties as well. They provide robust sliding of adjacent layers through incommensurate states which results in a superlubric state associated with an ultra low dissipation and friction [22–28].

Properties of vdW heterostructures strongly depend on the quality of the interface between 2D layers. In an ideal case, the interface is atomically flat, clean, and chemically inert without dangling bonds. Still, in reality 2D materials are associated with contaminations due to airborne hydrocarbon molecules [29] or intercalated water layers (inevitable under ambient humidity conditions) [30, 31], and due to various residues from polymers employed during fabrication [32] (mechanical exfoliation and transfer). After the transfer process, vdW interaction tends to bring adjacent 2D layers into contact, while the contaminations trapped at the interface are simultaneously squeezed into localized pockets called bubbles [33–39]. Bubbles and layers intercalated between 2D materials (hereafter intercalated layers—ILs) are kind of imperfections and understanding of their formation, chemical composition and physico-chemical properties is essential in order to assess properties of realistic vdW heterostructures.

So far the chemical composition of the contaminations has been investigated using electron microscopy [33, 40], spectroscopic techniques [29, 41, 42] or indirectly, by heating and following morphological changes [34, 43]. Since the thickness of ILs is in the order of nanometer and since bubbles are localized to lateral domains with the size in the order of 100nm, true nanoscale resolution in the chemical identification of these imperfections was achieved by using atomic force microscopy (AFM) based techniques coupled with infrared spectroscopy [44] or by using scanning near-field optical microscopy [45]. AFM was also demonstrated as an efficient tool to manipulate morphology of vdW heterostructures in order to locally flatten and clean them [44, 46–48]. Still, the influence of bubbles and ILs on local mechanical and electrical properties of vdW heterostructures has remained unexplored so far.

Here we investigate the vdW heterostructures consisting of MoS₂ flakes stacked onto WS₂ layers. Using AFM methods, we demonstrate that bubbles and ILs make the heterostructures softer and increase the friction and dissipation of the mechanical energy in dynamic mode (tapping AFM mode). AFM based electrical measurements reveal that bubbles and ILs are obstacles for uniform charge transfer between MoS₂ and WS₂ layers, resulting in a decreased contact potential difference. In a similar way, local electrical current strongly decreases on domains with bubbles which prevent vertical transport of charge carriers between layers. At the end, we provide methods to overcome observed issues. Clean contact between MoS₂ and WS₂ layers is reestablished by AFM based flattening of vdW heterostructures using scanning

in contact mode or by applying an increased normal load from AFM probe at single point. Subsequent measurements of electrical properties prove that both contact potential difference and conductivity are increased.

2. Experimental methods

2.1. Sample preparation

Starting MoS₂ and WS₂ layers were synthesized by chemical vapor deposition (CVD). MoS₂ was grown in homemade CVD system from MoO₃ and S [49]. Sulfur vapor was produced by heating 50–100 mg of S to 150 °C by separate heater, and carried to substrate by 100 SCCM of Ar. Growth substrate, 300 nm SiO₂ on highly doped Si, was placed in center of furnace and heated to 800 °C during growth. For the growth of WS₂, substrates were drop coated with 10 ppm by weight solution of sodium tungstate dihydrate [50]. After drying, they were sulfurized in a similar setup also under 100 SCCM Ar, with substrate temperature 850 °C and S heated at 180 °C. After the growth, the substrate was cooled in furnace to 250 °C in Ar before removal.

vdW heterostructures of MoS₂ and WS₂ layers were then fabricated using a variant of the wet transfer method [51]. The SiO₂/Si substrate carrying the MoS₂ monolayers was covered by Polidimethylsiloxane (PDMS) film and subsequently immersed into aqueous solution of ammonium hydroxide. This solution separates the MoS₂ monolayers and the substrate, leaving the monolayers attached to the PDMS. The PDMS film is then fished out of the ammonium hydroxide, laminated on top of the other SiO₂/Si substrate which carries WS₂ monolayers and finally peeled off slowly using tweezers. The optical image of fabricated vdW heterostructures is depicted in figure 1(a) indicating small MoS₂ triangles deposited onto larger triangular WS₂. We did not apply any post-fabrication technique, such as common post annealing [34], in order to minimize bubbles and ILs, since the aim of the study was to investigate their influence on mechanical and electrical properties of vdW heterostructures.

2.2. Raman characterization

Raman measurements were performed using TriVista 557 spectrometer equipped with a triple monochromator coupled to a microscope and a CCD detector with liquid nitrogen cooling. Raman spectra were excited with 488 nm and 514.5 nm lines of Ar⁺/Kr⁺ laser. Triple monochromator configuration was 900/900/1800 grooves per mm. Low laser power of 0.3 mW was used in order to minimize sample degradation.

2.3. AFM measurements

All AFM measurements were done using NTEGRA Prima system from NT-MDT. Initial morphological measurements of MoS₂/WS₂ heterostructures were always done in tapping mode. Simultaneous phase measurements were used to assess dissipation of the mechanical energy. Namely, the energy dissipation E_{diss} is proportional to the phase lag φ

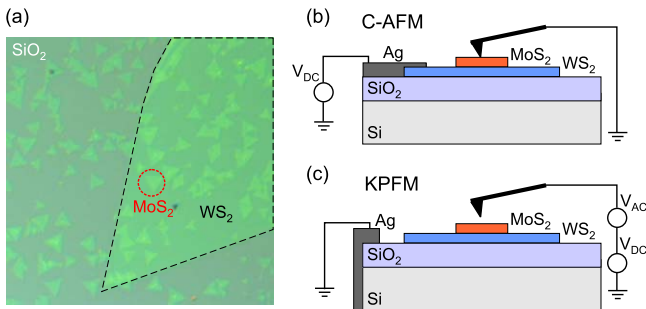


Figure 1. (a) The optical image of fabricated vdW heterostructures. The part of bigger WS₂ triangle is marked by dashed line, while one MoS₂ triangle is encircled by dotted line. The average lateral size of MoS₂ triangles is around 5 μm . Experimental setups for (b) C-AFM and (c) KPFM measurements.

($E_{\text{diss}} \sim \sin(\phi)$) of the AFM cantilever oscillations during the scanning in tapping mode [52].

The local flattening was performed by AFM operating in contact mode [44, 46, 47]. FMG01 probes from NT-MDT (with a typical force constant of 3 N m⁻¹) were employed. After the selection of an appropriate square domain, it was raster scanned for several times (5–10), while the normal load was increased at the beginning of every scan (in the range from ~ 20 nN to ~ 130 nN). After the flattening and scanning in contact mode, we switched back into tapping AFM mode, selected a larger scan area (than the previously chosen squared domain aimed for flattening), and made topographic imaging in order to detect morphological changes.

Distribution of the local stiffness was qualitatively assessed by force modulation microscopy (FMM). In this mode, measurements were performed in contact mode, while an AC voltage was applied to the AFM scanner causing its oscillations in the vertical direction, together with the sample placed on the top of the scanner. The scanner (sample) movement (described with the vertical coordinate z_s) results in the oscillations of AFM tip and cantilever (represented with the vertical coordinate z_c) with the same frequency. Generally, the scanner movement is equal to the sum of the movement of the AFM cantilever and sample indentation δ : $z_s = z_c + \delta$. On hard samples, the indentation is practically zero, therefore, $z_c = z_s$. On the other hand, on locally softer regions, the indentation depth is not negligible and the cantilever oscillations are decreased: $z_c = z_s - \delta$. Therefore, the amplitude of the AFM cantilever oscillations follows the variations of the sample stiffness, implying that larger (smaller) oscillation amplitude is measured on stiffer (softer) regions. FMM measurements were done using CSG10 probes (with a nominal stiffness of 0.11 N m⁻¹) from NT-MDT, while the frequency of the applied oscillations on AFM scanner was around 10 kHz.

Local friction during the sliding of AFM tip on MoS₂/WS₂ heterostructure was measured by friction force microscopy (FFM) using CSG01 probes (with a nominal stiffness of 0.03 N m⁻¹) from NT-MDT. The measurements were done in contact mode by the recording of the lateral

torsion of the AFM cantilever due to local friction between the tip and sample surface. The friction signal was obtained as a half of the difference of the lateral force signal measured in forward and backward scan directions. During the measurements, the fast-scan axis was normal to the AFM cantilever.

Current mapping was performed in contact mode using conductive AFM (C-AFM). During the scanning, DC bias voltage was applied to the sample while the AFM tip was virtually grounded (figure 1(b)). Since the aim of the study was to detect the influence of bubbles and intercalated water layers on properties of vdW heterostructures, the C-AFM imaging was done with very soft probes CSG01/TiN (with a nominal stiffness of 0.03 N/m and TiN conductive coating) and at low normal loads in the order of 1 nN. These probes were selected in order to avoid flattening of vdW heterostructures by the applied normal load from AFM tip [44, 46, 48]. I/V curves were measured at single point, at constant normal load, by sweeping the bias voltage in the range ± 10 V.

Kelvin probe force microscopy (KPFM) was employed in order to map local electrical surface potential of vdW heterostructures. Diamond coated probes DCP11 and NSG01 probes coated with Pt coating NSG01/PT from NT-MDT were employed. The measurements were done using a standard two-pass technique, where the sample morphology was recorded in the first pass, while the contact potential difference (CPD) between the AFM tip and sample surface was measured in the second pass. In the later case, the AFM cantilever was raised by 20 nm in order to measure only electrostatic interaction and avoid the influence of vdW forces. During the second pass, the sum of AC voltage and variable DC voltage (figure 1(c)) was applied on the AFM cantilever (with grounded sample). The applied AC voltage resulted in AFM cantilever oscillations while the electrical feedback loop automatically adjusted the value of variable DC voltage in order to cancel the oscillations. The value of the DC voltage which nullified the AFM cantilever oscillations is equal to the local CPD.

3. Results and discussion

MoS₂/WS₂ vdW heterostructures considered in this study belong to type II of semiconductor heterojunctions which are associated with a staggered band-gap. Excellent rectifying properties, high photo-responsivity [53] and large surface photovoltage [54] make them good candidates for photo-detection [55–58]. Besides interesting optoelectronic properties, MoS₂ and WS₂ are TMDs with excellent elastic [59] and frictional properties [60, 61] as well. Optical properties and absorption of these heterostructures strongly depend on the interlayer coupling and charger transfer between constituent layers [62–64]. At the same time, mechanical properties (elasticity and friction, sliding and deformation) are also strongly influenced by interlayer interactions and stacking [27, 65, 66]. Therefore, MoS₂/WS₂ vdW heterostructure is a

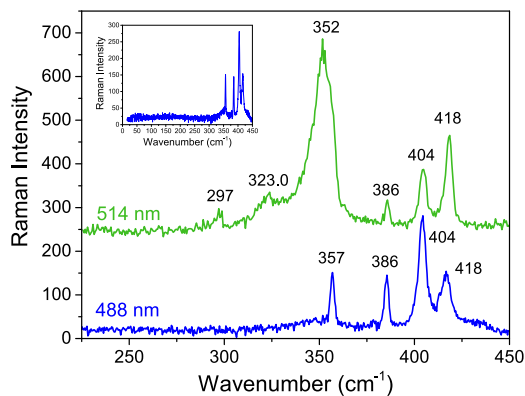


Figure 2. Raman spectra of as-obtained MoS₂/WS₂ heterostructure, excited with 514 nm (green line) and 488 nm (blue line). The inset depicts the Raman spectrum in the low-frequency region (starting from 15 cm⁻¹), excited with 488 nm line.

convenient platform to explore how inhomogeneities, such as bubbles and ILs, influence interlayer interactions and local mechanical and electrical properties.

3.1. Identification of layers

In order to detect the presence of MoS₂ and WS₂ in investigated samples and related interlayer coupling effects, Raman spectroscopy was used. MoS₂ has two Raman active vibrations, E'_{2g} (in-plane), positioned at ~ 386 cm⁻¹, and A'_1/A_{1g} (out-of-plane), positioned at ~ 404 cm⁻¹ [67]. WS₂ has two first order Raman active modes, E_{2g}^1 and A_{1g} , positioned at ~ 357 cm⁻¹ and ~ 418 cm⁻¹ [67, 68]. When a resonant excitation of 514.5 nm is used, second order peaks, mainly acoustic phonons such as 2LA(M) positioned at 297 cm⁻¹, 323 cm⁻¹ and 350 cm⁻¹, become prominent due to phonon–exciton coupling [67, 68]. The 2LA mode of highest intensity is positioned very closely to the E_{2g}^1 mode and the two are superposed into one wide peak at 352 cm⁻¹. When a non-resonant excitation line such as 488 nm is used, only first-order Raman modes appear in spectra of WS₂ [68].

Raman spectra of MoS₂/WS₂ heterostructures, depicted in figure 2, contain both MoS₂ and WS₂ Raman modes which confirms presence of these layers in the heterostructure. The spectrum excited with 488 nm line contains only first-order WS₂ modes, E_{2g}^1 and A_{1g} , whereas the spectrum excited with 514 nm line contains also resonantly enhanced second-order modes. In the low frequency Raman spectrum, which is excited with 488 nm line and displayed in the inset of figure 2, no interlayer modes were observed which suggests scarce coupling between the MoS₂ and WS₂ monolayers [64].

3.2. Bubbles and intercalated layers

AFM topographic image of the characteristic heterostructure (figure 3(a)) consists of the triangular MoS₂ flake on the top of the WS₂ flake. Such geometry with a smaller MoS₂ triangle on a larger WS₂ layer was common for all heterostructures considered in this study. Bright localized domains on the surface of MoS₂ represent bubbles formed at the interface

between MoS₂ and WS₂. The bright lines represent wrinkled MoS₂ domains. Bubbles do not appear below WS₂ since it was directly grown on SiO₂/Si substrate without additional transfer. Small bright dots on WS₂ stand for residues appeared during the transfer process of MoS₂ or adsorbates originating from environment. Previous works already demonstrated that bubbles contain hydrocarbon molecules [33] and/or residues originating from polymers used for the transfer [44]. Taking this information into account, the aim of our work was to study to what extent bubbles and intercalated layers degrade mechanical and electrical properties of vdW heterostructures.

Local flattening based on contact AFM mode was done within the square domain denoted by the dotted line in figure 3(a). Topography recorded in tapping mode after the flattening shown in figure 3(b) reveals that bright domains representing bubbles and wrinkles practically disappeared. During the flattening, surface adsorbates were pushed by AFM tip in a scanning direction and deposited at the rims of the square domain. Height profiles across the MoS₂ flake before and after the flattening in figure 3(c) prove that MoS₂ thickness is decreased from approximately 3 nm to only 1 nm due to squeezing out contaminants trapped between MoS₂ and WS₂. The height of bubbles before the flattening was up to 15 nm. On the other hand, after the flattening, density of all surface corrugations was very low, while their height was less than 2 nm.

Still, after the flattening, the MoS₂ surface contains local depressions which are emphasized in figure 3(d). Characteristic profiles in figure 3(e) taken across local depressions reveal that their depth is around 0.5 nm which corresponds to the thickness of MoS₂. Therefore, the observed depressions represent holes in MoS₂ which appear due to its local tearing at the position of bubbles and wrinkles [47]. The maximal normal loads applied during AFM based flattening were up to around 150 nN. In order to induce wear of mechanically exfoliated 2D materials by AFM tip scratching, the applied normal load should be at least several μ N [69, 70]. Therefore, the threshold force is much higher than the load applied in the current study. However, in the case of layers grown by chemical vapor deposition, wear could start already at normal loads of only several hundreds of nN [71]. In this case, the wear is initiated by AFM tip going across wrinkles which present out-of-plane local deformations and obviously decrease the wear resistance. Since wrinkles and bubbles are similar imperfections (the main difference is that the wrinkles are line deformations), we can expect that wear of vdW heterostructures during AFM based flattening could be also initiated for forces in the order of 100 nN. Therefore, larger normal loads applied during the AFM based flattening give more flat layers and heterostructures, but on the other hand, they could lead to local tearing of bubbles which present local out-of-plane deformations and therefore reduce wear resistance of 2D layers.

In order to further analyze the morphology of bubbles, we used a segment of the heterostructure depicted in figure 4(a) (only the surface of top MoS₂ displayed). We note that smaller bubbles have circular bases, larger ones appear in triangular and trapezoidal bases, while several biggest

bubbles have more complex shapes with polygonal bases. For the sake of simplicity, in our analysis, all bases were approximated with discs described with an effective radius R_{eq} . Relations between bubbles' geometrical parameters are depicted in figure 4(b). Bubbles' maximal height H_{max} approximately linearly increases with effective radius R_{eq} (bottom part of figure 4(b)), while the slope of the linear dependence is around 0.1 (the ratio of H_{max}/R_{eq} as a function of R_{eq} presented in top part of figure 4(b)). The value of the slope agrees well with H_{max}/R_{eq} ratios for bubbles formed in other vdW heterostructures, which are in the range 0.1–0.2 [35, 39]. Since the formation of bubbles is generally governed by the competition between vdW attractive forces (which tend to bring adjacent 2D layers into contact, while the contaminations are simultaneously squeezed into bubbles) and the in-plane stiffness and bending rigidity of the top 2D layer (which try to prevent local bending of the layer and formation of bubbles), H_{max}/R_{eq} depends on the ratio between adhesion energy and Young's modulus of elasticity, and is therefore universal for all bubbles [35].

Although here we considered vdW heterostructures consisting of 2D layers grown by chemical vapor deposition, we expect similar results for the heterostructures made from mechanically exfoliated layers. Possible differences could appear due to applied transfer method. In the wet transfer method, in order to separate MoS₂ from SiO₂/Si substrate, samples were first covered by PDMS and subsequently immersed into aqueous solution of ammonium hydroxide. Nanometric thin fluid layers could then stick to MoS₂ and then become trapped after the transfer onto WS₂. As a result, it is reasonable to expect more pronounced ILs in the heterostructures produced by the wet transfer method, compared to the dry transfer method.

3.3. Stiffness

The imaging in FMM mode reveals that bubbles, represented by brighter contrast in the topographic image (figure 5(a)), correspond to domains with lower magnitude of AFM cantilever oscillations (darker domains in figure 5(b)). The profiles in figure 5(c) display that the bubble represented by a large bump (located at a distance of around 0.4 μm) exactly corresponds to a huge dip in the magnitude signal. Since lower magnitude of the AFM cantilever oscillations in FMM implies softer regions, bubbles present locally softer domains compared to surrounding flat parts.

The mechanical response of layered systems is dominantly determined by the softest layers. In the considered case, the softest layer is the one with trapped contaminations. During the scanning of 2D materials in FMM mode, the local pressure exerted by AFM tip is transferred to the medium below them. Therefore, by scanning across MoS₂ bubbles, the AFM tip locally probes the stiffness of the material trapped within the bubbles. Since they are filled with soft materials such as gases, liquids and polymers (due to trapped air, water, hydrocarbon and/or polymer residues), the AFM tip indents the bubbles and therefore oscillates with decreased magnitude.

The oscillation magnitude image (figure 5(b)) reveals that even flat regions of MoS₂ (which are free of large bubbles) are slightly darker than WS₂. A slight decrease of the oscillation magnitude is indicated by Δmag in the profile in figure 5(c). This implies that MoS₂ and WS₂ are lying on substrates with different stiffness. Since WS₂ was directly grown on SiO₂ and possesses intrinsic growth strain, it is lying on a hard substrate which practically prevents any indentation. As a result, the AFM tip here oscillates with the maximal magnitude determined by the oscillations of AFM scanner. On the other hand, lower oscillation magnitude observed on flat regions of MoS₂ indicates that it is lying on a softer IL. Therefore, both ILs and especially bubbles define local domains in vdW heterostructures with lower stiffness.

3.4. Friction

Friction measurements were done on the MoS₂/WS₂ heterostructure depicted in figure 6(a). Top MoS₂ flake consists of three parts: bright domain 1 in the right-bottom corner, dark domain 2 in the middle, and small bright domain 3 in the left-top corner. The friction map in figure 6(b) reveals brighter contrast on domains 1 and 3, and therefore larger friction than on domain 2. Practically there is no friction contrast between MoS₂ domain 2 and surrounding WS₂ due to similar friction coefficients of two materials [72].

The characteristic height profiles depicted in figure 6(c) illustrate that MoS₂ thickness is $\Delta h_1 \approx 2$ nm for domain 1 and $\Delta h_2 < 1$ nm for domain 2. Domain 1 (and domain 3 as well) is thicker since it is decoupled from the underlying WS₂ by an IL. The friction profile in figure 6(c) displays two force levels while the histogram of the friction map in figure 6(d) exhibits two peaks. The lower peak and lower force level F_2 correspond to domain 2 without IL. On the other hand, the upper peak and higher force level F_1 correspond to domains 1 and 3 which contain ILs. As can be seen, the friction on domains with ILs (1 and 3) is increased by even 50% compared to the friction on domains without them (domain 2).

Increased friction observed on domains with ILs and trapped contaminations is in agreement with previous results obtained on single 2D materials [73–75]. Namely, various contaminations, such as hydrocarbon molecules which are inevitable on surfaces exposed to air, act as 'third bodies' at the interface between two sliding surfaces. They could lock two surfaces into contact or initiate their pristine chemical bonding. Generally, they disturb easy sliding of two contacting surfaces through incommensurate states which results in increased friction. More recently, it has been demonstrated that a water layer intercalated below 2D materials forms hydrogen-bonded clusters which impede easy sliding [76, 77] and increases density of phonon states which provides additional channels for the dissipation of frictional energy [78].

3.5. Energy dissipation in dynamic AFM mode

Friction generally leads to an undesired energy dissipation and losses. In the previous section we considered the case

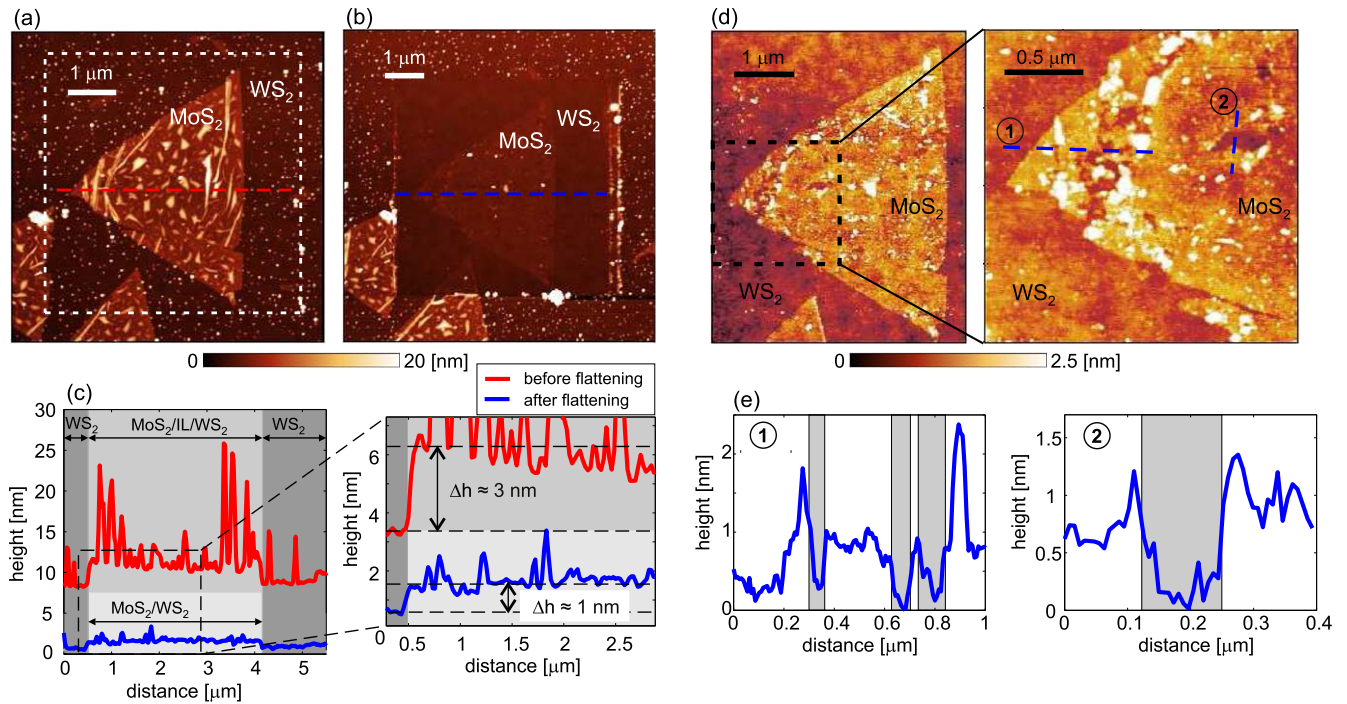


Figure 3. Morphology of the considered MoS₂/WS₂ vdW heterostructure (a) before and (b) after the AFM based flattening. The flattening was performed within the square domain marked in (a). (c) Height profiles along dashed lines in (a) and (b). (d) Morphology of the heterostructure after the flattening with the focus on the area with MoS₂. (e) Height profiles (along dashed lines 1 and 2 in (d)) taken across holes in MoS₂ layer.

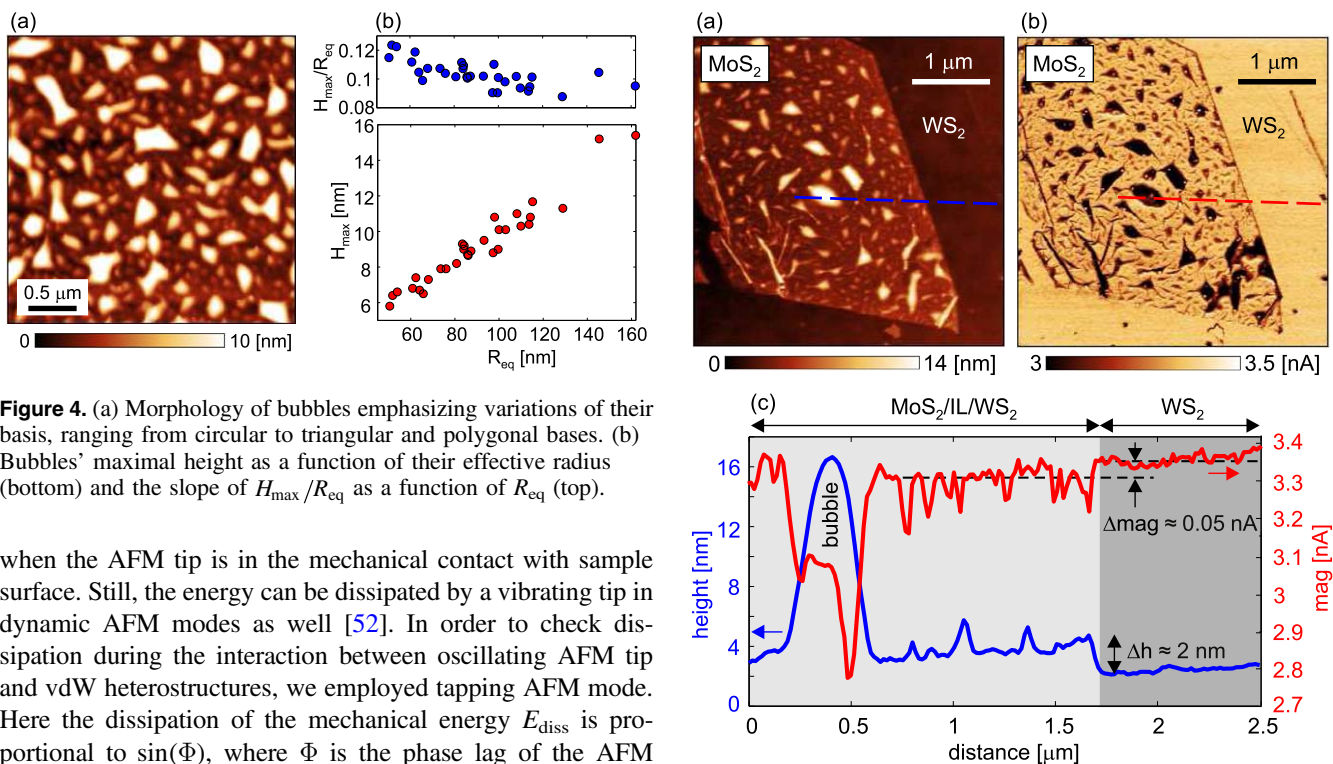


Figure 4. (a) Morphology of bubbles emphasizing variations of their basis, ranging from circular to triangular and polygonal bases. (b) Bubbles' maximal height as a function of their effective radius (bottom) and the slope of H_{max}/R_{eq} as a function of R_{eq} (top).

when the AFM tip is in the mechanical contact with sample surface. Still, the energy can be dissipated by a vibrating tip in dynamic AFM modes as well [52]. In order to check dissipation during the interaction between oscillating AFM tip and vdW heterostructures, we employed tapping AFM mode. Here the dissipation of the mechanical energy E_{diss} is proportional to $\sin(\Phi)$, where Φ is the phase lag of the AFM cantilever oscillations during the tapping mode imaging [52].

Phase maps for the heterostructure in figure 7(a) are presented in figures 7(b) and 7(c), for both the in-phase and out-of-phase oscillations, respectively (the in-phase/out-of-

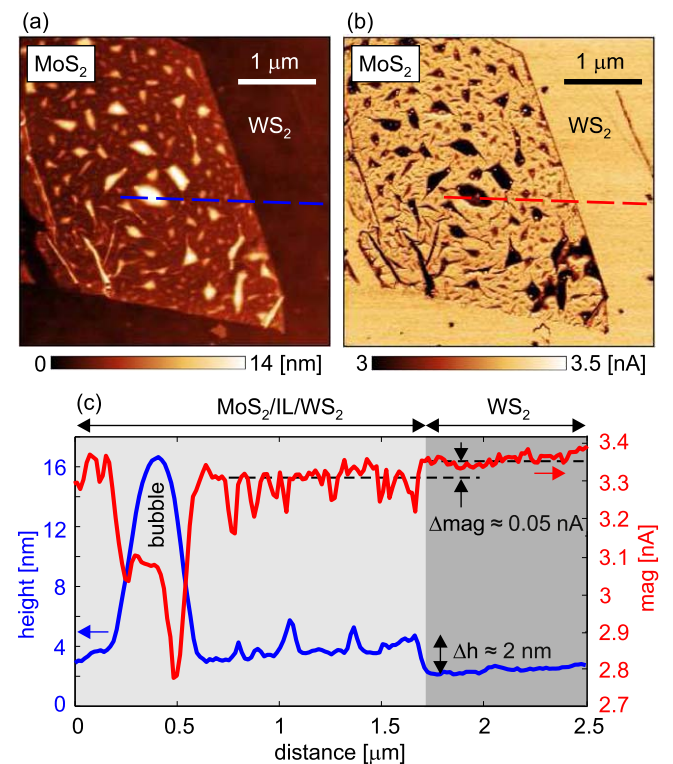


Figure 5. (a) Morphology of MoS₂/WS₂ heterostructure, (b) corresponding magnitude of the AFM cantilever oscillations recorded in FMM mode. (c) Height and magnitude profiles along dashed lines in (a) and (b), respectively.

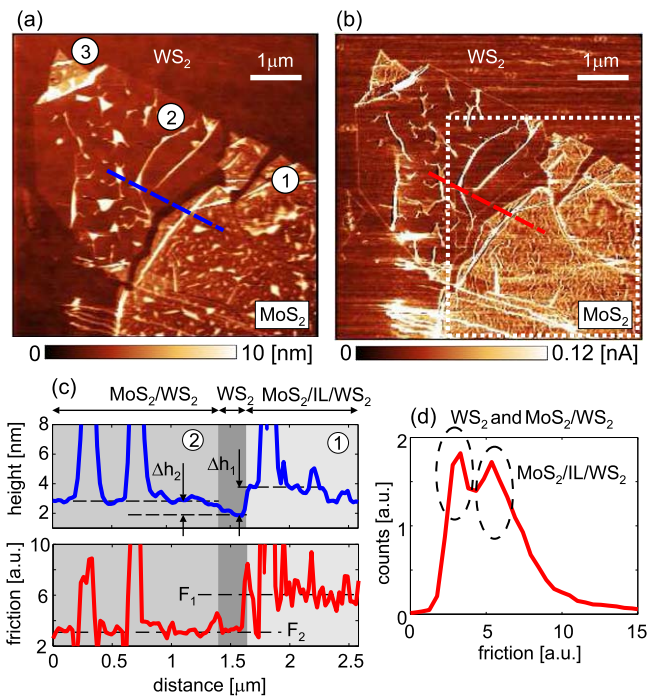


Figure 6. (a) Morphology of MoS₂/WS₂ heterostructure and (b) corresponding friction map. (c) Height and friction profiles along dashed lines in (a) and (b), respectively. (d) Histogram of the friction map calculated for the square domain marked by dotted line in (b).

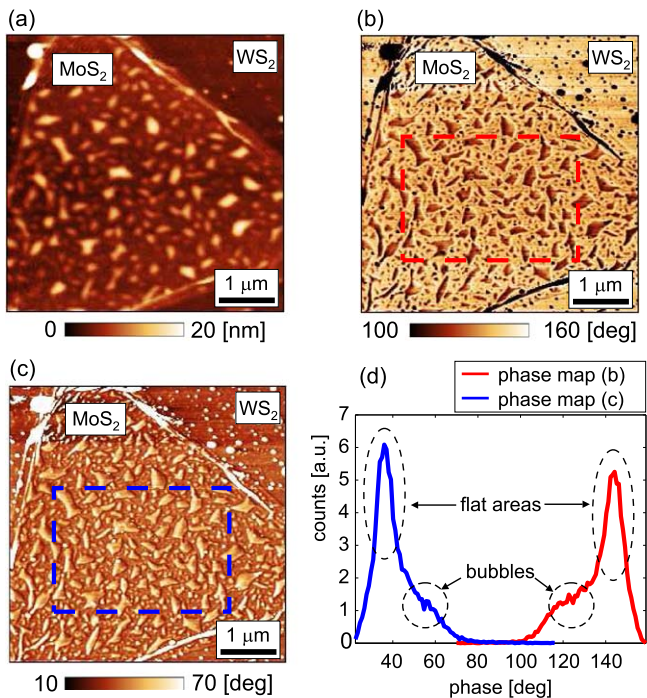


Figure 7. (a) Morphology of MoS₂/WS₂ heterostructure, (b) phase map for the in-phase AFM cantilever oscillations (z-scale from 100° to 160°), (c) phase map for the out-of-phase AFM cantilever oscillations (z-scale from 10° to 70°), (d) histograms of both phase maps.

phase oscillations are associated with increasing/decreasing phase as a function of frequency [79]). In the former (latter) case, the measured phase signal is above (below) 90°, while bubbles are represented by darker (brighter) contrast.

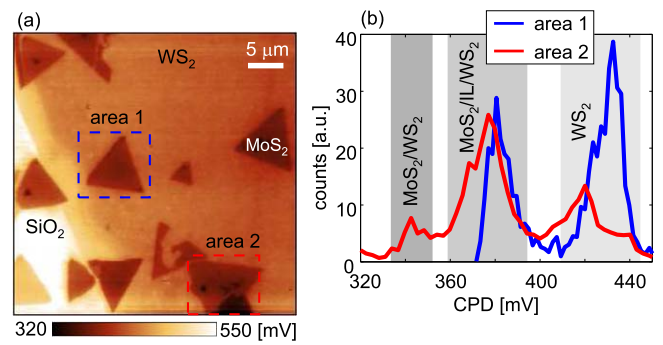


Figure 8. (a) CPD map of MoS₂/WS₂ heterostructures measured by KPFM and (b) corresponding histogram for the indicated areas.

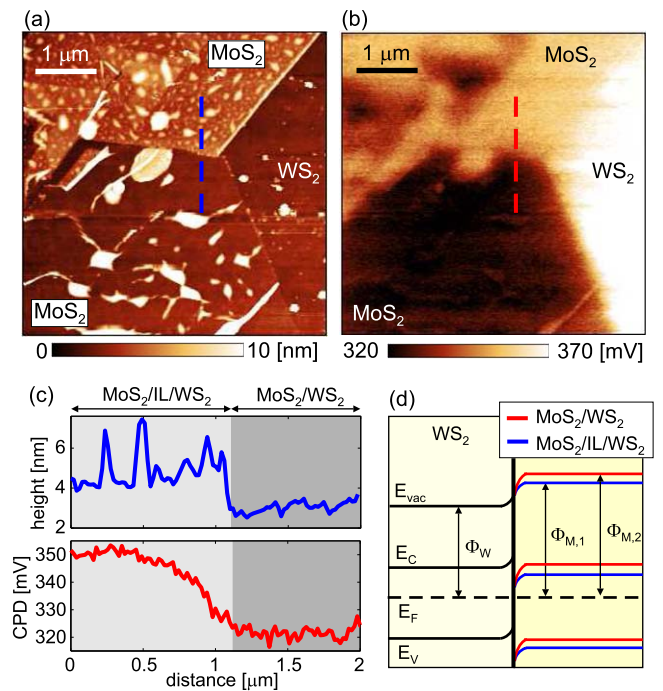


Figure 9. (a) Topography of domain 2 from figure 8(a) and (b) corresponding CPD map. (c) Height and CPD profiles along dashed lines marked in (a) and (b), respectively. (d) Schematic representation of the band structure for domain 2 according to KPFM measurements.

Therefore, lower (higher) phase lag was measured on the bubbles than on their surrounding. The phase contrast was the same in both forward and backward directions, and therefore, it indicates true variations of the local mechanical properties of the vdW heterostructure.

Recently, the phase imaging has been employed in order to study and map local inhomogeneities and bubbles of transferred graphene, while the observed contrast has been explained by variations in local stiffness [80]. Here we relate the observed contrast to variations in energy dissipation. The phase histograms in figure 7(d) reveal two peaks for both cases: around 122° (bubbles) and 144° (surrounding area) for the phase map from figure 7(b), and around 56° (bubbles) and 36° (surrounding area) for the phase map from figure 7(c).

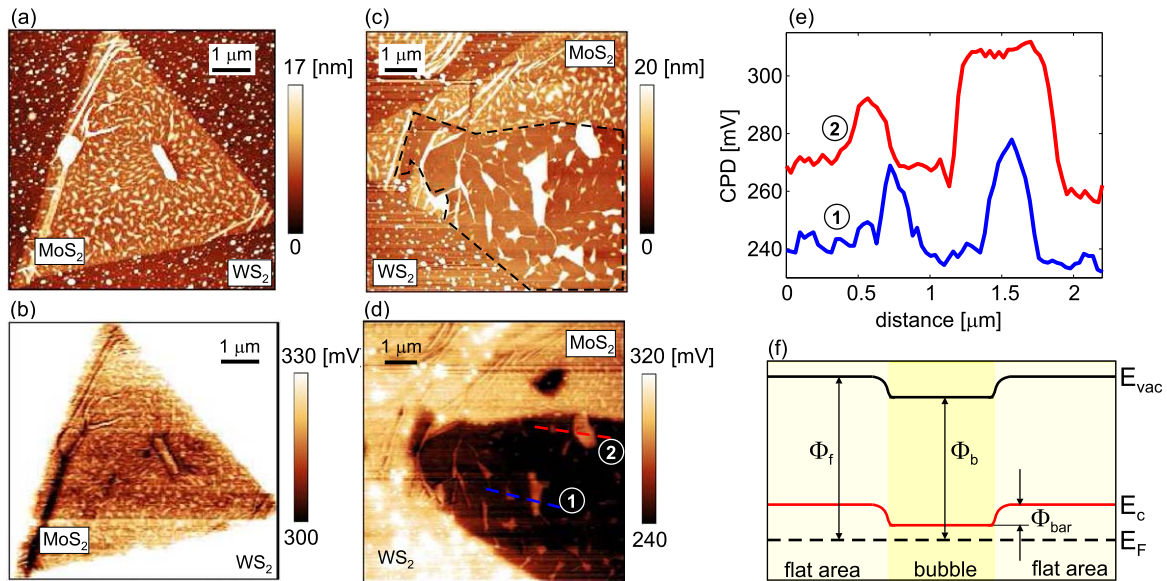


Figure 10. (a) Topography and (b) CPD map of MoS₂/WS₂ heterostructure revealing increased CPD on bubbles. (c) Topography and (d) CPD map of the heterostructure where the bottom part (encircled by the dashed line) is free of ILs and with larger bubbles. (e) CPD profiles along several bubbles from the bottom part of the heterostructure in part (d) (the second profile lifted up by 30 mV for better visibility). (f) Schematic representation of the band diagram indicating local band bending around bubbles.

Since $E_{\text{diss}} \sim \sin(\Phi)$, E_{diss} is larger on the bubbles by around 30% compared to their flat surroundings. The same conclusion holds for both in-phase and out-of-phase oscillations, confirming that the dissipation is independent on the initial scanning conditions [79].

During tapping mode imaging with a vibrating AFM tip, the mechanical energy is usually dissipated due to long- and short-range surface adhesion hysteresis [52]. Still, in the case of vdW heterostructure, the dominant phase contrast is observed across the bubbles which contain trapped fluids and/or polymer residues. Such viscoelastic materials generally introduce an additional dissipation channel due to hysteresis of the viscoelastic force during the tip approach and retract [52]. This seems the main cause of the increased dissipation observed on bubbles.

3.6. Electrical surface potential

The influence of the morphology of MoS₂/WS₂ heterostructures on their local electrical properties was first studied by KPFM. In the CPD map in figure 8(a), top triangular MoS₂ flakes are well resolved. They are represented by darker contrast and lower CPD compared to WS₂. While the potential of MoS₂/WS₂ heterostructure in domain 1 is spatially homogeneous, the heterostructure in domain 2 exhibits an inhomogeneous CPD with two different levels. Histograms for two characteristic domains are given in figure 8(b). Taking into account that $\text{CPD} = \Phi_t - \Phi_s$ (CPD is equal to the difference between the work functions of AFM tip (Φ_t) and sample (Φ_s)), the following relations can be derived. Higher CPD of WS₂ indicates lower work function than on MoS₂/WS₂ heterostructures. Therefore, when MoS₂ is deposited onto WS₂, in order to equilibrate their Fermi levels, electrons are transferred from WS₂ to MoS₂.

The histogram of domain 2 displays two peaks for MoS₂ on WS₂: at around 380 mV (marked by MoS₂/IL/WS₂) and 340 mV (marked by MoS₂/WS₂). In order to clarify the observed inhomogeneity, additional small-scale imaging of this domain was done. Topography in figure 9(a) and characteristic height profiles in figure 9(c) show that the heterostructure consists of two areas with different heights. The upper area (MoS₂/IL/WS₂) is thicker by ~ 2 nm due to an IL between MoS₂ and WS₂. At the same time, these areas are associated with two different CPD levels which are separated by ~ 30 mV as displayed in figures 9(b) and (c).

Previous works demonstrated that water layers intercalated between a substrate and 2D materials prevented commonly observed charge doping from the substrate [81, 82]. Therefore, ILs can be regarded as obstacles for charge transfer. KPFM results can be then interpreted using the schematic representation of the band diagram in figure 9(d) in the following way. The heterostructure without IL (MoS₂/WS₂) has lower CPD. Therefore, it has higher work function $\Phi_{\text{M},2}$ compared to MoS₂/IL/WS₂ with work function $\Phi_{\text{M},1}$. Increased work function $\Phi_{\text{M},2}$ implies larger potential difference compared to WS₂ work function Φ_{W} . As a result, the charge transfer of electrons from WS₂ to MoS₂ is more efficient. Therefore, areas of MoS₂/WS₂ without IL are associated with more pronounced charge transfer leading to larger CPD contrast between MoS₂/WS₂ and bare WS₂.

Bubbles induce inhomogeneous strain in two-dimensional materials and consequently local band bending [83–85]. Possible variations of electrical surface potential across bubbles were explored by KPFM. The comparison of topographic image (Figure 10(a)) and corresponding CPD map (figure 10(b)) reveals that bubbles are represented by brighter domains in the CPD map. This is even more pronounced in the case of heterostructures without ILs and with

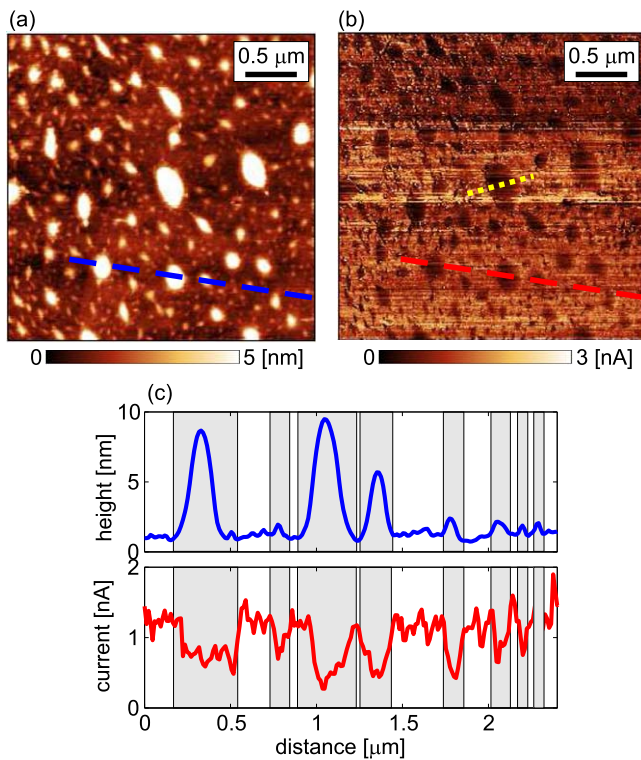


Figure 11. (a) Topography and (b) current map of MoS₂/WS₂ heterostructure. Since the selected scan size was smaller than the size of top MoS₂ flake, surrounding WS₂ flake is not displayed. (c) Corresponding height (top) and current (bottom) profiles taken along dashed lines indicated in (a) and (b), respectively. Shaded domains emphasize overlapping between bubbles and regions with decreased current.

larger bubbles. Such case is presented in the bottom part of the heterostructure presented in figures 10(c) (topography) and 10(d) (CPD map). CPD profiles in figure 10(e) taken across large bubbles with a diameter of several hundreds of nm reveals that the surface potential is increased by several tens of mV. As a result, the band diagram and local band bending around bubbles can be represented by a scheme in figure 10(f). Brighter contrast in CPD maps indicates that bubbles can be considered as local domains with a lower work function Φ_b . They are surrounded by flat areas with a larger work function Φ_f . Therefore, electrons in MoS₂ layer placed on bubbles are sitting in potential wells.

3.7. Electrical conductivity

Local conductivity was investigated on the heterostructure displayed in figure 11(a) presenting only a segment of the top MoS₂ layer. DC bias voltage was applied to the bottom WS₂ layer, while the electrical current was simultaneously measured through the metallic AFM tip in contact with top MoS₂ layer. In the topographic image, bubbles are represented by bright, circular and elliptical domains. As already mentioned, in order to avoid any tip-induced flattening of the heterostructure and to preserve all topographic features such as bubbles, the measurements were done with a soft probe and at a low normal load in the order of 1 nN. The resulting current

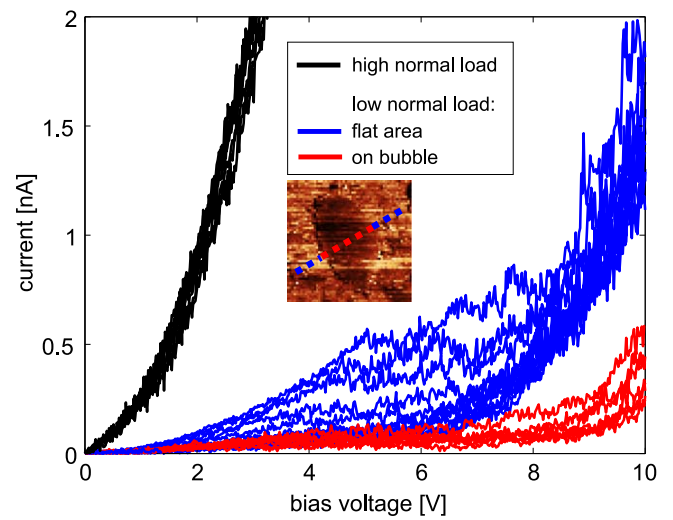


Figure 12. I/V curves measured on MoS₂/WS₂ heterostructure across a bubble (the dotted line indicated in figure 11(b)). The inset depicts the current map measured on the area with the bubble. The line schematically presents the points where the I/V curves were measured. The I/V curves at high normal load were measured on a flat region without bubbles.

map in figure 11(b) displays darker circular and elliptical domains with locally decreased current. Practically the same current maps were measured in both forward and backward directions, thus excluding any tip-shape effects on the obtained results. The observed darker domains correspond exactly to bubbles. This is further proved in figure 11(c) which presents a topographic and corresponding current profile. As can be seen, the electrical current drops exactly on bubbles (shaded regions), and compared to the current measured on flat areas, it decreases by up to $\sim 50\%$.

In order to further explore the origin of a low current measured on bubbles, local I/V curves were measured across them. Characteristic results presented in figure 12 display nonlinear I/V curves with large turn-on voltages. At the same time, the I/V curves are well grouped into two sets. The curves measured exactly on the area with a bubble display much lower currents with increased turn-on voltage of around 9 V. On the other hand, the I/V curves measured on flat areas around the bubble present much larger conductivity and lower turn-on voltage in a wide range of 1–7 V. Therefore, besides lower conductivity, local I/V measurements indicate appearance of an additional potential barrier on bubbles compared to flat areas.

Electrical current measured in C-AFM is dominantly determined by the contact resistance (the resistance between the AFM tip and sample surface) which is proportional to the local resistivity of the sample surface below the AFM tip [86]. Considered MoS₂/WS₂ heterostructures practically consist of two parallel current sheets which can be therefore represented as two parallel resistors with similar resistances. When bubbles are present between two current sheets, the system can be represented with only one resistor corresponding to the top MoS₂ layer. As a result, the total resistance in the latter case is approximately two times larger than in the former case

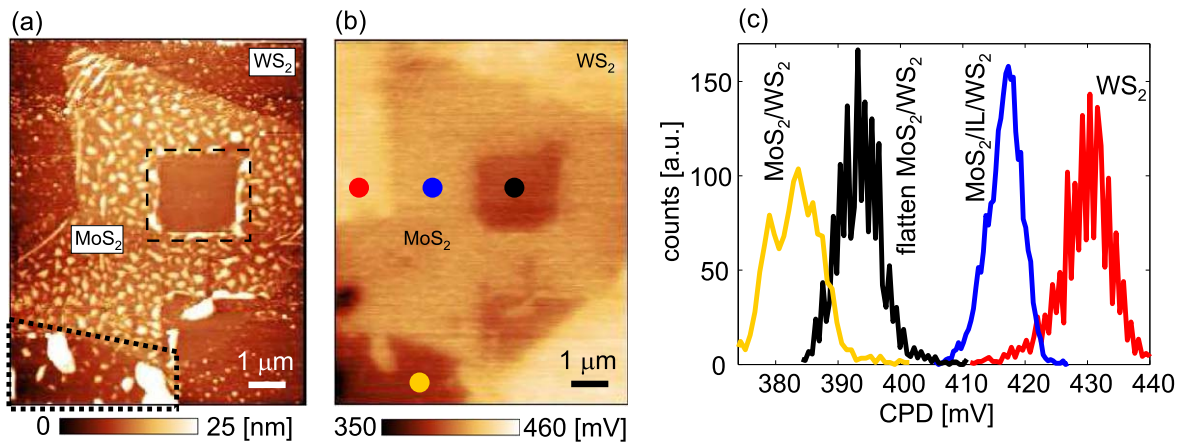


Figure 13. (a) Topography and (b) CPD map of the heterostructure after the AFM based flattening of the square domain marked by dashed line in (a). (c) Histogram of CPD for four areas indicated by dots in part (b): bare WS_2 (domain marked by red dot in (b)), the heterostructure with IL (domain marked by blue dot in (b)), the flatten part of the heterostructure (domain marked by black dot in (b) and by dashed rectangle in (a)), and the heterostructure without IL (domain marked by yellow dot in (b) encircled by dotted line in (a)).

which explains the observed decrease of current in C-AFM by $\sim 50\%$.

C-AFM and I/V curves were measured for the bias voltage applied on bottom WS_2 (figure 1(b)). Therefore, for a high enough positive bias voltage, electrons are transferred from MoS_2 to WS_2 and then into external electrical contact. Still, bubbles prevent direct tunneling of the electrons from MoS_2 to underlying WS_2 . Electrons in these regions first have to reach flat MoS_2 areas. For that purpose, they have to overcome a potential barrier $\Phi_{\text{bar}} = \Phi_f - \Phi_b$ observed in KPFM measurements. After that, they can be transferred from MoS_2 to WS_2 . The potential barriers associated with bubbles could be an additional reason for the observed lower conductivity and larger turn-on voltages (measured in I/V curves) observed on the bubbles.

Figure 12 shows that I/V curves measured on flat regions surrounding bubbles exhibit also rather high turn-on voltages. Still, they practically disappear for high normal load applied on AFM probe during I/V curve measurements as will be discussed in the next section. This indicates that practically whole MoS_2 flake is separated from WS_2 by a thin IL, with a thickness of around 1 nm. Then high enough turn-on voltage is needed to overcome a potential barrier induced by such insulating layer and to initiate electron flow.

3.8. Electrical properties improved by local AFM based flattening

The previous analysis indicates that in order to provide an efficient charge transfer, it is necessary to remove all contaminations between heterostructure's layers. Previous works [44, 46–48] and our results presented in figure 3 demonstrate that AFM based flattening could be an efficient technique for this purpose. The final goal of our study was to explore if the AFM based flattening could improve the efficiency of charge transfer and overall electrical properties of vdW heterostructures.

First we consider the influence of local flattening on electrical surface potential. Topography and CPD map

measured after the flattening of a small square domain within MoS_2/WS_2 heterostructure are presented in figures 13(a) and (b), respectively. We distinguish four levels in CPD which are associated with the following areas: $\text{MoS}_2/\text{IL}/\text{WS}_2$ (thicker part of the heterostructure with IL), MoS_2/WS_2 (thinner part without IL), flattened MoS_2/WS_2 (the central square domain flattened by AFM), and bare WS_2 . The CPD histogram in figure 13(c) shows that CPD of domains with and without IL differs by around 40 mV. The CPD of the area flattened by AFM is decreased compared to non-flattened heterostructure $\text{MoS}_2/\text{IL}/\text{WS}_2$ by ~ 30 mV. Therefore, the CPD of the flattened area approaches the CPD of the heterostructure without IL. In the considered case their difference was decreased to only ~ 10 mV which indicates that AFM based flattening can be really employed as an efficient method for removing contaminations and facilitating charge transfer between layers in vdW heterostructures.

In a similar way, we have tested the influence of the normal force applied during I/V curve measurements on resulting currents. Figure 12 depicts also I/V curves measured at the normal load increased above ~ 100 nN. As can be seen, resulting curves are still nonlinear, but the turn-on voltage practically disappeared. Therefore, for a high enough normal load, contaminations were expelled from the interface between MoS_2 and WS_2 . As a result, potential barriers for charge carriers were removed and high conductivity was reestablished.

4. Conclusions

In a summary, using AFM methods, we have demonstrated that bubbles and ILs deteriorate both mechanical and electrical properties of vdW heterostructures. These imperfections with trapped contaminations prevent direct contact between constituent 2D layers and interlayer interactions. As a result, from a mechanical point of view, they behave as a third body which prevents easy sliding of 2D layers one over each other thus leading to increased friction. In addition, bubbles and ILs

present locally softer domains which open additional dissipation channels, probably due to viscoelastic damping. In an analogous way, from an electrical point of view, bubbles and ILs behave as insulating layers and potential barriers which block charge transfer between constituent 2D layers. As a result, local electrical conductivity on domains with bubbles and ILs decreases, while the difference of the surface potential between constituent layers is lowered.

In order to improve properties of vdW heterostructures after the transfer process, we have demonstrated that it is necessary to apply high enough normal load by AFM probe in order to locally remove contaminations trapped in bubbles and ILs. We illustrated two approaches. The first one is based on AFM flattening of square areas where constituent 2D layers are returned back into a close contact by a scanning in contact AFM mode. As a result, due to reestablished charge transfer between constituent layers, the flattened areas exhibit increased difference of surface potential approaching the levels measured on areas without bubbles and ILs. In the second approach, local I/V curves measured at increased normal load exhibit significantly improved electrical conductivity of vdW heterostructures.

Acknowledgments

B V, U R and S A acknowledge funding provided by the Institute of Physics Belgrade, through the grant of the Ministry of Education, Science, and Technological Development of the Republic of Serbia, and funding provided by the Science Fund of the Republic of Serbia, through the grant PROMIS 6062710 (PV-Waals). D Č and M K acknowledge financial support by the Center of Excellence for Advanced Materials and Sensing Devices (ERDF Grant KK.01.1.1.01.0001).

Data availability statement

All data that support the findings of this study are included within the article (and any supplementary files).

ORCID iDs

Borislav Vasić  <https://orcid.org/0000-0002-1575-8004>

Marko Kralj  <https://orcid.org/0000-0002-9786-3130>

References

- [1] Geim A K and Grigorieva I V 2013 Van der Waals heterostructures *Nature* **499** 419–25
- [2] Liu Y, Weiss N O, Duan X, Cheng H-C, Huang Y and Duan X 2016 Van der Waals Heterostructures and Devices *Nat. Rev. Mater.* **1** 16042
- [3] Li M-Y, Chen C-H, Shi Y and Li L-J 2016 Heterostructures based on two-dimensional layered materials and their potential applications *Mater. Today* **19** 322–35
- [4] Frisenda R, Navarro-Moratalla E, Gant P, Pérez De Lara D, Jarillo-Herrero P, Gorbachev R V and Castellanos-Gomez A 2018 Recent progress in the assembly of nanodevices and van der Waals heterostructures by deterministic placement of 2D materials *Chem. Soc. Rev.* **47** 53–68
- [5] Liu Y *et al* 2015 Toward barrier free contact to molybdenum disulfide using graphene electrodes *Nano Lett.* **15** 3030–4
- [6] Dean C R *et al* 2010 Boron nitride substrates for high-quality graphene electronics *Nat. Nanotechnol.* **5** 722–6
- [7] Britnell L *et al* 2012 Field-effect tunneling transistor based on vertical graphene heterostructures *Science* **335** 947–50
- [8] Yu W J, Li Z, Zhou H, Chen Y, Wang Y, Huang Y and Duan X 2013 Vertically stacked multi-heterostructures of layered materials for logic transistors and complementary inverters *Nat. Mater.* **12** 246–52
- [9] Roy T, Tosun M, Kang J S, Sachid A B, Desai S B, Hettick M, Hu C C and Javey A 2014 Field-effect transistors built from all two-dimensional material components *ACS Nano* **8** 6259–64
- [10] Jariwala D, Sangwan V K, Lauhon L J, Marks T J and Hersam M C 2014 Emerging device applications for semiconducting two-dimensional transition metal dichalcogenides *ACS Nano* **8** 1102–20
- [11] Frisenda R, Molina-Mendoza A J, Mueller T, Castellanos-Gomez A and van der Zant H S J 2018 Atomically thin p-n junctions based on two-dimensional materials *Chem. Soc. Rev.* **47** 3339–58
- [12] Chuang S, Kapadia R, Fang T, Chia Chang H, Yen W-C, Chueh Y-L and Javey A 2013 Near-ideal electrical properties of InAs/WSe₂ van der Waals heterojunction diodes *Appl. Phys. Lett.* **102** 242101
- [13] Deng Y, Luo Z, Conrad N J, Liu H, Gong Y, Najmaei S, Ajayan P M, Lou J, Xu X and Ye P D 2014 Black phosphorus-monolayer MoS₂ van der waals heterojunction p-n diode *ACS Nano* **8** 8292–9
- [14] Jariwala D, Davoyan A R, Wong J and Atwater H A 2017 Van der Waals materials for atomically-thin photovoltaics: Promise and outlook *ACS Photonics* **4** 2962–70
- [15] Britnell L *et al* 2013 Strong light-matter interactions in heterostructures of atomically thin films *Science* **340** 1311–4
- [16] Furchi M M, Pospischil A, Libisch F, Burgdöfer J and Mueller T 2014 Photovoltaic effect in an electrically tunable van der waals heterojunction *Nano Lett.* **14** 4785–91
- [17] Lee C-H *et al* 2014 Atomically thin p-n junctions with van der Waals heterointerfaces *Nat. Nanotechnol.* **9** 676–81
- [18] Ahn J, Jeon P J, Raza S R A, Pezeshki A, Min S-W, Hwang D K and Im S 2016 Transition metal dichalcogenide heterojunction PN diode toward ultimate photovoltaic benefits *2D Mater.* **3** 045011
- [19] Wong J, Jariwala D, Tagliabue G, Tat K, Davoyan A R, Sherrott M C and Atwater H A 2017 High photovoltaic quantum efficiency in ultrathin van der waals heterostructures *ACS Nano* **11** 7230–40
- [20] Cheng R, Li D, Zhou H, Wang C, Yin A, Jiang S, Liu Y, Chen Y, Huang Y and Duan X 2014 Electroluminescence and photocurrent generation from atomically sharp WSe₂/MoS₂ heterojunction p-n diodes *Nano Lett.* **14** 5590–7
- [21] Lopez-Sanchez O, Alarcon Llado E, Koman V, Fontcuberta i Morral A, Radenovic A and Kis A 2014 Light generation and harvesting in a van der waals heterostructure *ACS Nano* **8** 3042–8
- [22] Feng X, Kwon S, Park J Y and Salmeron M 2013 Superlubric sliding of graphene nanoflakes on graphene *ACS Nano* **7** 1718–24
- [23] Leven I, Krepel D, Shemesh O and Hod O 2013 Robust superlubricity in graphene/h-BN heterojunctions *J. Phys. Chem. Lett.* **4** 115–20
- [24] Sheehan P E and Lieber C M 2017 Friction between van der Waals solids during lattice directed sliding *Nano Lett.* **17** 4116–21

- [25] Song Y, Mandelli D, Hod O, Urbakh M, Ma M and Zheng Q 2018 Robust microscale superlubricity in graphite/hexagonal boron nitride layered heterojunctions *Nat. Mater.* **17** 894–9
- [26] Vasić B, Stanković I, Matković A, Kratzer M, Ganser C, Gajić R and Teichert C 2018 Molecules on rails: Friction anisotropy and preferential sliding directions of organic nanocrystallites on two-dimensional materials *Nanoscale* **10** 18835–45
- [27] Ru G, Qi W, Tang K, Wei Y and Xue T 2020 Interlayer friction and superlubricity in bilayer graphene and MoS₂/MoSe₂ van der Waals heterostructures *Tribol. Int.* **151** 106483
- [28] Gao E, Wu B, Wang Y, Jia X, Ouyang W and Liu Z 2021 Computational prediction of superlubric layered heterojunctions *ACS Appl. Mater. Interfaces* **13** 33600–8
- [29] Li Z et al 2013 Effect of airborne contaminants on the wettability of supported graphene and graphite *Nat. Mater.* **12** 925–31
- [30] Xu K, Cao P and Heath J R 2010 Graphene visualizes the first water adlayers on mica at ambient conditions *Science* **329** 1188–91
- [31] He K T, Wood J D, Doidge G P, Pop E and Lyding J W 2012 Scanning tunneling microscopy study and nanomanipulation of graphene-coated water on mica *Nano Lett.* **12** 2665–72
- [32] Rezaia B, Dorn M, Severin N and Rabe J P 2013 Influence of graphene exfoliation on the properties of water-containing adlayers visualized by graphenes and scanning force microscopy *J. Colloid Interface Sci.* **407** 500–4
- [33] Haigh S J, Gholinia A, Jalil R, Romani S, Britnell L, Elias D C, Novoselov K S, Ponomarenko L A, Geim A K and Gorbachev R 2012 Cross-sectional imaging of individual layers and buried interfaces of graphene-based heterostructures and superlattices *Nat. Mater.* **11** 764–7
- [34] Uwanno T, Hattori Y, Taniguchi T, Watanabe K and Nagashio K 2015 Fully dry PMMA transfer of graphene on h-BN using a heating/cooling system *2D Mater.* **2** 041002
- [35] Khestanova E, Guinea F, Fumagalli L, Geim A K and Grigorieva I V 2016 Universal shape and pressure inside bubbles appearing in van der Waals heterostructures *Nat. Commun.* **7** 12587
- [36] Ghorbanfekr-Kalashami H, Vasu K S, Nair R R, Peeters F M and Neek-Amal M 2017 Dependence of the shape of graphene nanobubbles on trapped substance *Nat. Commun.* **8** 15844
- [37] Sanchez D A, Dai Z, Wang P, Cantu-Chavez A, Brennan C J, Huang R and Lu N 2018 Mechanics of spontaneously formed nanoblisters trapped by transferred 2D crystals *Proc. Natl. Acad. Sci.* **115** 7884–9
- [38] Sanchez D A, Dai Z and Lu N 2021 2D Material Bubbles: Fabrication, characterization, and applications *Trends Chem.* **3** 204–17
- [39] Blundo E, Yildirim T, Pettinari G and Polimeni A 2021 Experimental adhesion energy in van der Waals crystals and heterostructures from atomically thin bubbles *Phys. Rev. Lett.* **127** 046101
- [40] Algara-Siller G, Lehtinen O, Wang F C, Nair R R, Kaiser U, Wu H A, Geim A K and Grigorieva I V 2015 Square ice in graphene nanocapillaries *Nature* **519** 443–5
- [41] Vasu K S et al 2016 Van der Waals pressure and its effect on trapped interlayer molecules *Nat. Commun.* **7** 12168
- [42] Gasparutti I, Song S H, Neumann M, Wei X, Watanabe K, Taniguchi T and Lee Y H 2020 How clean is clean? recipes for van der Waals heterostructure cleanliness assessment *ACS Appl. Mater. Interfaces* **12** 7701–9
- [43] Pizzocchero F, Gammelgaard L, Jessen B S, Caridad J M, Wang L, Hone J, Bøggild P and Booth T J 2016 The hot pick-up technique for batch assembly of van der Waals heterostructures *Nat. Commun.* **7** 11894
- [44] Schwartz J J, Chuang H-J, Rosenberger M R, Sivaram S V, McCreary K M, Jonker B T and Centrone A 2019 Chemical identification of interlayer contaminants within van der Waals heterostructures *ACS Appl. Mater. Interfaces* **11** 25578–85
- [45] Vincent T, Hamer M, Grigorieva I, Antonov V, Tzalenchuk A and Kazakova O 2020 Strongly absorbing nanoscale infrared domains within strained bubbles at hbn-graphene interfaces *ACS Appl. Mater. Interfaces* **12** 57638–48
- [46] Rosenberger M R, Chuang H-J, McCreary K M, Hanbicki A T, Sivaram S V and Jonker B T 2018 Nano-‘Squeegee’ for the creation of clean 2D Material interfaces *ACS Appl. Mater. Interfaces* **10** 10379–87
- [47] Tan B H, Zhang J, Jin J, Ooi C H, He Y, Zhou R, Ostrikov K, Nguyen N-T and An H 2020 Direct measurement of the contents, thickness, and internal pressure of molybdenum disulfide nanoblisters *Nano Lett.* **20** 3478–84
- [48] Kim Y, Herlinger P, Taniguchi T, Watanabe K and Smet J H 2019 Reliable postprocessing improvement of van der Waals heterostructures *ACS Nano* **13** 14182–90
- [49] Delač Marion I, Čapeta D, Pielich B, Faraguna F, Gallardo A, Pou P, Biel B, Vujičić N and Kralj M 2018 Atomic-scale defects and electronic properties of a transferred synthesized MoS₂ monolayer *Nanotechnology* **29** 305703
- [50] Lau C S et al 2021 Gate-defined quantum confinement in CVD 2D WS₂ *Adv. Mater.* **33** 2103907
- [51] Niehues I, Blob A, Stiehm T, Schmidt R, Jadriško V, Radatović B, Čapeta D, Kralj M, de Vasconcellos S M and Bratschitsch R 2018 Strain transfer across grain boundaries in MoS₂ monolayers grown by chemical vapor deposition *2D Mater.* **5** 031003
- [52] García R, Gómez C J, Martínez N F, Patil S, Dietz C and Magerle R 2006 Identification of nanoscale dissipation processes by dynamic atomic force microscopy *Phys. Rev. Lett.* **97** 016103
- [53] Huo N, Kang J, Wei Z, Li S-S, Li J and Wei S-H 2014 Novel and enhanced optoelectronic performances of multilayer MoS₂-WS₂ heterostructure transistors *Adv. Funct. Mater.* **24** 7025–31
- [54] Kim B, Kim J, Tsai P-C, Choi H, Yoon S, Lin S-Y and Kim D-W 2021 Large Surface Photovoltage of WS₂/MoS₂ and MoS₂/WS₂ Vertical Hetero-bilayers *ACS Appl. Electron. Mater.* **3** 2601–6
- [55] Xue Y et al 2016 Scalable production of a few-layer MoS₂/WS₂ vertical heterojunction array and its application for photodetectors *ACS Nano* **10** 573–80
- [56] Wang G, Li L, Fan W, Wang R, Zhou S, Lü J-T, Gan L and Zhai T 2018 Interlayer coupling induced infrared response in WS₂/MoS₂ heterostructures enhanced by surface plasmon resonance *Adv. Funct. Mater.* **28** 1800339
- [57] Ye K et al 2019 Lateral bilayer MoS₂-WS₂ heterostructure photodetectors with high responsivity and detectivity *Adv. Opt. Mater.* **7** 1900815
- [58] Kanade C K, Seok H, Kanade V K, Aydin K, Kim H-U, Mitta S B, Yoo W J and Kim T 2021 Low-temperature and large-scale production of a transition metal sulfide vertical heterostructure and its application for photodetectors *ACS Appl. Mater. Inter.* **13** 8710–7
- [59] Bertolazzi S, Brivio J and Kis A 2011 Stretching and breaking of ultrathin MoS₂ *ACS Nano* **5** 9703–9
- [60] Vazirisereshk M R, Hasz K, Zhao M-Q, Johnson A T C, Carpick R W and Martini A 2020 Nanoscale friction behavior of transition-metal dichalcogenides: Role of the chalcogenide *ACS Nano* **14** 16013–21
- [61] Rapuc A, Wang H and Polcar T 2021 Nanotribology of transition metal dichalcogenide flakes deposited by chemical vapour deposition: The influence of chemical composition and sliding speed on nanoscale friction of monolayers *Appl. Surf. Sci.* **556** 149762

- [62] Hong X, Kim J, Shi S-F, Zhang Y, Jin C, Sun Y, Tongay S, Wu J, Zhang Y and Wang F 2014 Ultrafast charge transfer in atomically thin MoS₂/WS₂ heterostructures *Nat. Nanotechnol.* **9** 682–6
- [63] Tongay S et al 2014 Tuning interlayer coupling in large-area heterostructures with CVD-Grown MoS₂ and WS₂ monolayers *Nano Lett.* **14** 3185–90
- [64] Zhang J et al 2016 Observation of strong interlayer coupling in MoS₂/WS₂ heterostructures *Adv. Mater.* **28** 1950–6
- [65] Liu K et al 2014 Elastic properties of chemical-vapor-deposited monolayer MoS₂, WS₂, and their bilayer heterostructures *Nano Lett.* **14** 5097–103
- [66] Susarla S, Manimunda P, Morais Jaques Y, Hachtel J A, Idrubo J C, Syed Amnulla S A, Galvão D S, Tiwary C S and Ajayan P M 2018 Deformation mechanisms of vertically stacked WS₂/MoS₂ heterostructures: The role of interfaces *ACS Nano* **12** 4036–44
- [67] Cong X, Liu X-L, Lin M-L and Tan P-H 2020 Application of Raman spectroscopy to probe fundamental properties of two-dimensional materials *Npj 2D Mater. Appl.* **4** 13
- [68] Berkdemir A et al 2013 Identification of individual and few layers of WS₂ using Raman Spectroscopy *Sci. Rep.* **3** 1755
- [69] Vasić B, Matković A, Ralević U, Belić M and Gajić R 2017 Nanoscale wear of graphene and wear protection by graphene *Carbon* **120** 137–44
- [70] Özoğul A, Gnecco E and Baykara M Z 2021 Nanolithography-induced exfoliation of layered materials *Appl. Surf. Sci. Adv.* **6** 100146
- [71] Vasić B, Zurutuza A and Gajić R 2016 Spatial variation of wear and electrical properties across wrinkles in chemical vapour deposition graphene *Carbon* **102** 304–10
- [72] Fang L, Liu D-M, Guo Y, Liao Z-M, Luo J-B and Wen S-Z 2017 Thickness dependent friction on few-layer MoS₂, WS₂, and WSe₂ *Nanotechnology* **28** 245703
- [73] He G, Müser M H and Robbins M O 1999 Adsorbed layers and the origin of static friction *Science* **284** 1650–2
- [74] Dietzel D, Ritter C, Mönninghoff T, Fuchs H, Schirmeisen A and Schwarz U D 2008 Frictional duality observed during nanoparticle sliding *Phys. Rev. Lett.* **101** 125505
- [75] Dietzel D, Brndiar J, Štich I and Schirmeisen A 2017 Limitations of structural superlubricity: chemical bonds versus contact size *ACS Nano* **11** 7642–7
- [76] Khare H S and Burriss D L 2013 The effects of environmental water and oxygen on the temperature-dependent friction of sputtered molybdenum disulfide *Tribol. Lett.* **52** 485–93
- [77] Stella M, Lorenz C D and Righi M C 2021 Effects of intercalated water on the lubricity of sliding layers under load: a theoretical investigation on MoS₂ *2D Mater.* **8** 035052
- [78] Lee H, Jeong H, Suh J, Doh W H, Baik J, Shin H-J, Ko J-H, Wu J, Kim Y-H and Park J Y 2019 Nanoscale friction on confined water layers intercalated between MoS₂ flakes and silica *J. Phys. Chem. C* **123** 8827–35
- [79] Vasić B, Matković A and Gajić R 2017 Phase imaging and nanoscale energy dissipation of supported graphene using amplitude modulation atomic force microscopy *Nanotechnology* **28** 465708
- [80] Xu C, Yao Q, Du H, Hong C, Xue T, Kang Y and Li Q 2021 Abnormal raman characteristics of graphene originating from contact interface inhomogeneity *ACS Appl. Mater. Interfaces* **13** 22040–6
- [81] Shim J, Lui C H, Ko T Y, Yu Y-J, Kim P, Heinz T F and Ryu S 2012 Water-gated charge doping of graphene induced by mica substrates *Nano Lett.* **12** 648–54
- [82] Lee H, Ko J-H, Song H C, Salmeron M, Kim Y-H and Park J Y 2018 Isotope- and thickness-dependent friction of water layers intercalated between graphene and mica *Tribol. Lett.* **66** 36
- [83] Feng J, Qian X and Huang C-W 2012 Strain-engineered artificial atom as a broad-spectrum solar energy funnel *Nat. Photon.* **6** 866–72
- [84] Li H et al 2015 Optoelectronic crystal of artificial atoms in strain-textured molybdenum disulphide *Nat. Commun.* **6** 7381
- [85] Tyurnina A, Bandurin D A, Khestanova E, Kravets V G, Koperski M, Guinea F, Grigorenko A N, Geim A K and Grigorieva I V 2019 Strained bubbles in van der waals heterostructures as local emitters of photoluminescence with adjustable wavelength *ACS Photonics* **6** 516–24
- [86] Moerman D, Sebaihi N, Kaviyil S E, Leclère P, Lazzaroni R and Douhéret O 2014 Towards a unified description of the charge transport mechanisms in conductive atomic force microscopy studies of semiconducting polymers *Nanoscale* **6** 10596–603